Nacre-inspired ceramic-based composite materials via bi-directional freeze casting

By

HONGBO WAN

Bristol Dental School
UNIVERSITY OF BRISTOL

Supervisors
Prof. Bo Su
Prof. Hua-xin Peng

A dissertation submitted to the University of Bristol in accordance with the requirements for award of the degree of

Doctor of Philosophy

in the Faculty of Health Sciences

November 2020

Word count: 49,158

Abstract

Natural nacre is well known for its significant improvements in strength and toughness compared to its monolithic constituents because of its unique layered architecture. The toughening mechanisms of nacre have drawn considerable research interest. To synthesize materials with good mechanical properties of high strength and toughness, nacre-like materials were developed to replicate the architecture of nacre.

In this work, manufacturing techniques based on bi-directional freeze casting and densification process were employed to prepare nacre-like ceramic (alumina, zirconia and hydroxyapatite) scaffolds. Two densification methods, namely one-step and two-step method, were investigated to produce nacre-like ceramic scaffolds with micro-layered (μL) and brick-and-mortar (BM) architecture, respectively. Afterwards, nacre-like ceramic scaffolds were infiltrated with different polymers (acrylates, epoxy, polyurethane) or metals (aluminium, magnesium) as the compliant phase to generate nacre-like ceramic/polymer or ceramic/metal composites. By tuning of processing parameters such as sintering temperature, binder content, cooling rate, compressive distance and solid loading, the resulting ceramic scaffolds exhibited various architecture and microstructure which were retained in the nacre-like ceramic/polymer or ceramic/metal composites.

To understand the strengthening and toughening mechanisms in these nacre-like composites, mechanical characterization was systematically conducted on composites with different processing methods and parameters. Nacre-like composites with relatively lower ceramic fractions (<85%) revealed various intrinsic toughening (plasticity) and extrinsic toughening mechanisms (crack deflection, pull-out, frictional sliding, and ceramic bridges breakage). The difference in mechanical performance of composites manufactured from different processing parameters were attributed to their microstructure and strengthening/toughening mechanisms. The μL composite exhibited superior mechanical properties to those of the BM composite due to its better stress-transfer and crack deflection effects. The manufacturing method of one-step densification also had advantages of shorter processing time and more flexible control in microstructure. The novel μL composites with different combinations of ceramics and polymers or metals could potentially be used in many engineering and biomedical applications.

Acknowledgements

My first sincere acknowledgment goes to my supervisor, Prof. Bo Su. It was his dedication, passion and rigorous attitude to the research that influenced me deeply. Thanks go for his continuous support and guidance during my PhD study that let me to be a better researcher and a better person. My thanks also go to my co-supervisor Prof. Hua-Xin Peng for his guidance and encouragement.

I would like to thank my parents for their love and support both financially and mentally during my PhD study.

I am grateful to my collaborators: Dr. Tan Sui, Nathanael Leung (Department of Mechanical Engineering Sciences, University of Surrey, UK), Dr. Xiao-Dong Xu (Bristol Composites Institute, University of Bristol, UK), Dr. Dong Liu, and Paul Forna Kreutzer (Department of physics, University of Bristol, UK) for their assistance on fracture toughness testing and calculation.

I would like to acknowledge my lab mates in our Biomaterials Engineering Group (bioMEG): Dr. Sana Algharaibeh, Dr. Sarah Al-Jawoosh, Eric Ho. Thanks for their help and support whenever I had a doubt. Thanks go to our lab technician Mr. Mark Ginty who did a fantastic work to maintain lab instruments and secure every lab member. It was an unforgettable experience to work with them.

Finally, I would very much like to thank Dr. Qiang Liu (School of Materials Science and Engineering, Harbin Institute of Technology, China) for his valuable technical advice on ceramic preparation while visiting the bioMEG.

Author’s declaration

I declare that the work in this dissertation was carried out in accordance with the requirements of the University's Regulations and Code of Practice for Research Degree Programmes and that it has not been submitted for any other academic award. Except where indicated by specific reference in the text, the work is the candidate's own work. Work done in collaboration with, or with the assistance of, others, is indicated as such. Any views expressed in the dissertation are those of the author.

SIGNED:  ……. DATE: ……11/11/2020.……

Table of contents

List of figures

Chapter 1

Chapter 2

Chapter 3

Chapter 4

Chapter 5

Chapter 6

List of Tables

Chapter 2

Chapter 3

Chapter 4

Chapter 5

Abbreviations

µL	Micro-layered
BM	Brick-and-mortar
HA	Hydroxyapatite
γ-MPS	3-(trimethoxysilyl)propyl methacrylate
APS	3-aminopropyl triethoxysilane
PMMA	Polymethyl methacrylate
PU	Polyurethane
TEDGMA	Triethylene glycol dimethacrylate
UDMA	Urethane dimethacrylate
PDMS	Polydimethylsiloxane
micro-CT	Micro computerized tomography
CNC	Computer numeric-controlled
SEM	Scanning electron microscopy
XRD	X-ray diffraction
FTIR	Fourier-transform infrared spectroscopy
3D	Three-dimension
°C	Cellulose degrees
nm	Nanometer
µm	Micrometer
mm	Millimeter
cm	Centimeter
g	Gram
MPa	Gigapascal
GPa	Megapascal
s	Second
min	Minute
h	Hour
vol.	Volume
wt.	Weight

Chapter 1

Introduction and literature review

1.1 Introduction

It has always been a technical challenge to design and fabricate synthetic materials with both high strength and toughness because they are often mutually exclusive [1]. Nevertheless, some natural materials, such as bone, wood, and shells exhibit remarkable functional and mechanical properties [2, 3]. As a result, many researchers have started to investigate how natural materials obtain their exceptional mechanical properties (strength, stiffness, fracture toughness, impact resistance etc.). Due to the limited sources of chemical elements from nature (e.g. C, H, O, N, P, Si, Na, K, Si) [4], most natural materials are essentially composites of proteins, fibres, and minerals built into specific architectures [5]. These architectures are obtained by combining different features: interface between phases; hierarchical structures that span from nanoscale to macroscale; combinations of soft and hard materials within layered, columnar or fibrous arrangements, each with different mechanical response and properties etc. Therefore, studies have led to the beginning of a new branch of material engineering, usually referred to biomimetics. The main objective of biomimetics is to understand the principle behind the creation of the complex architectures of natural materials, then design and synthesize nature-inspired materials. For instance, nacre, also known as mother of pearl, composed of inorganic aragonite and organic biopolymer, is an excellent example of natural composite materials with both high strength and toughness. The exceptional mechanical performances of nacre are attributed to the specific multi-layered architectures composed of hard aragonite and soft proteins. Thus, to mimic the structure of nacre, researchers have developed nacre-like synthetic composite materials comprising hard phase (ceramic or silica) and soft phase (polymer, glass,

or metal). In particular, biomimetics will allow scientists and engineers to optimise nacre-like composites with alternative compositions, architectures, microstructures, and fabrication techniques. Here, as the source of inspiration, the microstructure and mechanical properties of natural materials especially nacre will be firstly reviewed. Next, based on the toughening principles of nacre-like materials, the mechanical response of nacre-like synthetic composites will be highlighted regarding to their architecture, interface, and mineral bridges. Finally, to generate nacre-like composites, fabrication techniques related to freeze casting will be reviewed.

1.2 Nature materials: the hierarchical architecture and properties

1.2.1 Nacre

In general, nacre refers to the inner layer of abalone shell (**Fig.1-1a**). Because of the harsh living conditions, this nacre layer in the shells of mollusks has exceptional mechanical performance to protect their soft bodies against external aggression from predators, rocks, or debris displaced by currents or waves [6]. Nacre is composed of ~95 vol.% highly aligned inorganic aragonite platelets and ~5% organic biopolymer with a complex architecture known as the 'brick-and-mortar' (**Fig.1-1b**). The 'brick' is the major load-bearing constituent composed of aragonite platelets (thickness: ~0.3-0.5 μm; diameter: ~5-8 μm), while the 'mortar' acts as the lubricant for bricks, which is the bio-polymer (~20 nm thick) [7]. In the case of an appropriate interface [8], this brick-and-mortar architecture offers high toughness by dissipating energy therefore natural nacre exhibited at least one order of magnitude tougher than the monolithic aragonite [9]. For example, the fracture toughness (K_J) of aragonite does not exceed ~1 MPa $m^{½}$, whereas the toughness of nacre reaches 9 MPa $m^{½}$ [10-12].

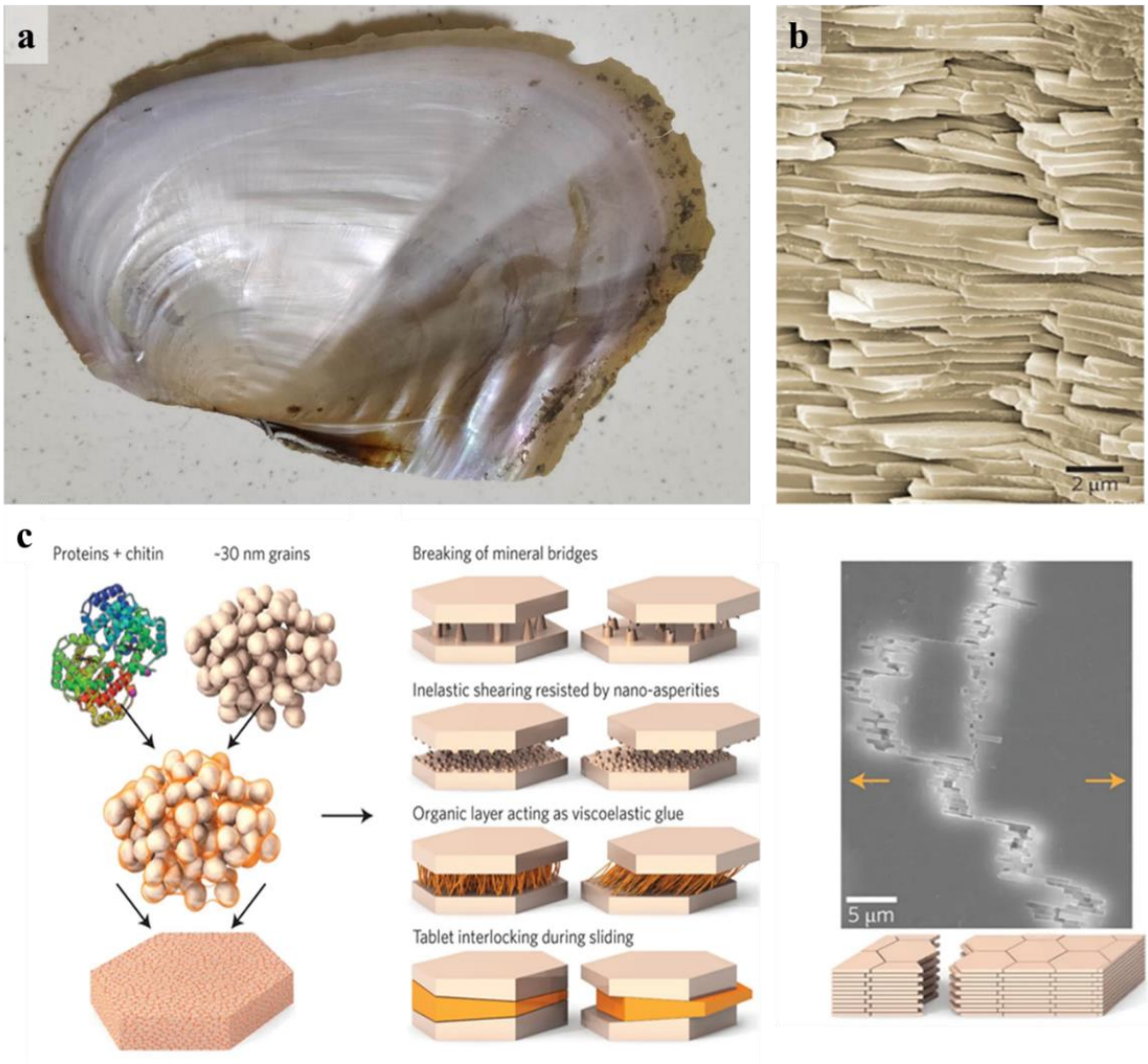

Fig.1-1 *View of the inner nacreous layer of red abalone shell* ***a)****. SEM images of fracture surface of nacre* ***b)****. The hierarchical structure of nacre and its toughening mechanisms* ***c)****. Adapted from [2].*

Hierarchical architecture in nacre is complex and ranged from nano to macro scales showing multiple toughening mechanisms (**Fig.1-1c**). On the nanoscale, as the building block in nacre, each aragonite brick is formed by calcium carbonate nanograins (diameter: ~30 nm) glued by biopolymer. During mechanical testing, the bricks exhibited deformability due to the rotating and deformation of nanograins [13]. When the aragonite bricks are highly aligned, the micro-

interaction between them plays a key role in toughening and strengthening. Four main mechanisms have been observed: mineral bridges, nano-asperities, viscoelastic organic layers, and platelet interlocking. All of performances above allow the relief of local stresses and provide inelasticity. On the macroscale, the brick-and-mortar material shows a typical crack deflection after crack initiates, which is a typical toughening mechanism that earlier research has focused on [12]. It is suggested that the toughening mechanism of nacre is a combination of the above mechanisms from multi-scales in a synergetic and harmonious fashion. However, recent research mainly focused on the micro-scale toughening which is the inspiration of nacre-like synthetic composites.

The mineral bridges immersed in organic phase and connecting the bricks were first reported by Schäffer *et al*. [14]. To observe the mineral bridges and study their effect on mechanical properties, TEM was employed on the cross-section of nacre (**Fig.1-2a** and **b**). Nano-indentation and three-point bending were performed for mechanical testing. The mechanical performance and analysis of nacre indicated that the existence of mineral bridges led to improvements in stiffness, strength, and toughness [15-17].

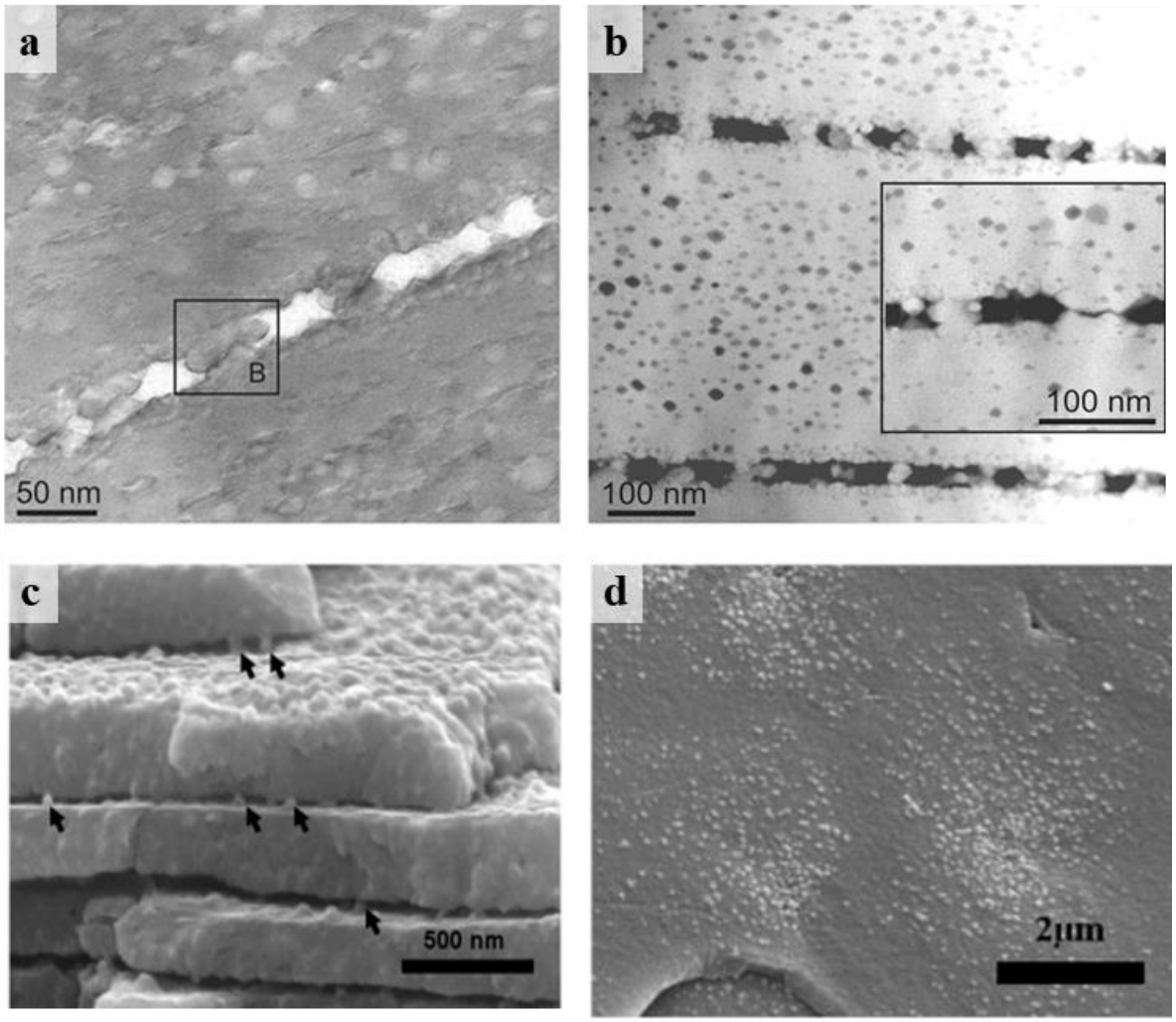

Fig.1-2 *High-resolution and high-quantification electron microscope images of nacre taken after deproteination.* ***a)*** *and* ***b)*** *are TEM images illustrating mineral bridges between aragonite platelets in Gibbula umbilicalis. SEM images were taken from profile* ***c)*** *and top* ***d)*** *of aragonite bricks showing the nanoasperities. Adapted from [15] and [18].*

The nano asperities were believed to be the principal source of shear resistance by increasing sliding friction between bricks. At the onset of plastic deformation, broken mineral bridges may play an important role in forming the asperities that subsequently resist shear.

The biopolymer in nacre consisting of beta-pleated sheets folded into cross-linked polymer-like glue could adhere to the bricks and provide toughness through many sacrificial bonds

between them [19]. **Fig.1-3a** showed that the biopolymer could be stretched out and extended up to 150% since the organic polymer chains could be elastically elongated to redistribute the applied stress. The ductile biopolymer provides additional deformation before failure, resulting in high fracture toughness [20].

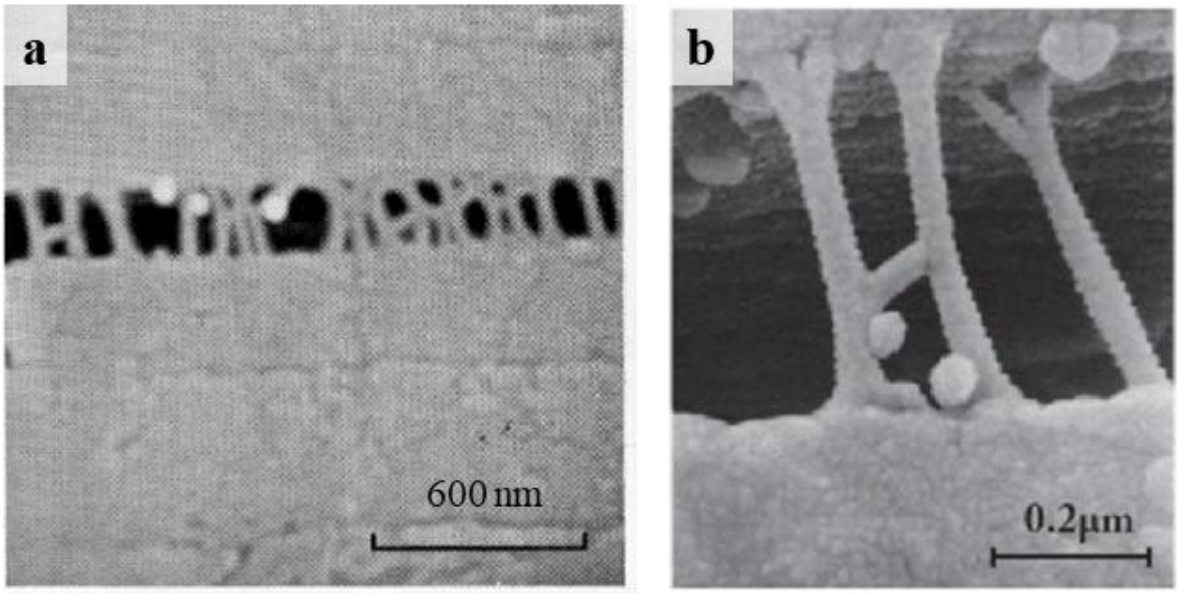

Fig.1-3 SEM images of crack illustrating the fibril of biopolymer in nacre at low magnification and ***a)*** *high magnification* ***b)****. Adapted from [10].*

The interlocking of bricks was first observed by Katti *et al.* in certain nacres [21]. As shown in **Fig.1-4**, bricks were wrapped and tacked together to build up an interlocking structure. Thus, the sliding or rotation of between bricks could be hindered, leading to crack resistance.

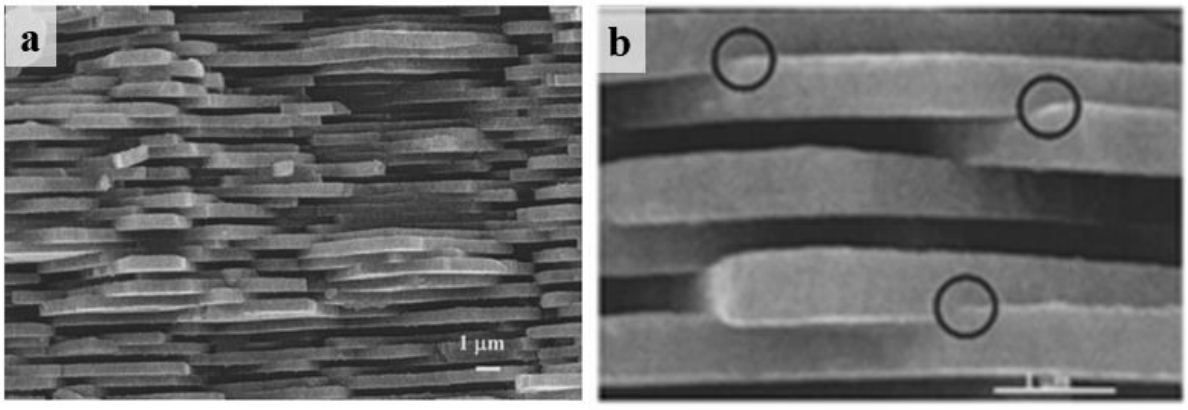

Fig.1-4 *SEM images showing the fracture surface of nacre at low and* ***a)*** *high magnification* ***b)****. Adapted from [21].*

1.2.2 Other natural materials

The properties and functions of natural materials are always dependent on their living environments. Thus, natural materials found from different creatures show various mechanical properties. A material-property chart has been developed in **Fig.1-5** representing sections through the multidimensional property space of materials and their mechanical performance. Besides, almost all the natural materials are composites of soft biopolymers and hard building-blocks with complex architectures. Hence, apart from nacre, some other natural composite materials with remarkable mechanical properties would be introduced in this section. As lightweight natural plant materials with high hardness and strength per unit of weight, bamboo, wood or palm consisting of lignin, hemicellulose and cellulose fibres are shaped into hollow prismatic cells of varying layer width [5, 22-24]; keratin is the main component of creatures' hair, nails, horns, reptilian scales, wool, and hooves, which demonstrate astonishing tensile strength. The structural characterisation of human hair reveals that it has a compact architecture with the scales on the surface [25, 26]. The dactyl club of a stomatopod known as the aggressive "biological hammer" of the ocean can penetrate or even smash the strong and tough natural materials like nacre and crab exoskeletons with a strike force up to 1334 N at 90 Hz. It also

exhibited extraordinary damage-tolerance and exceptional impact force resistance [27, 28]. Based on microstructural characterisation and simulation, the club illustrates a pitch-graded helicoidal architecture constructed from mineralized chitin fibres that can dissipate the energy released by propagating microcracks [29].

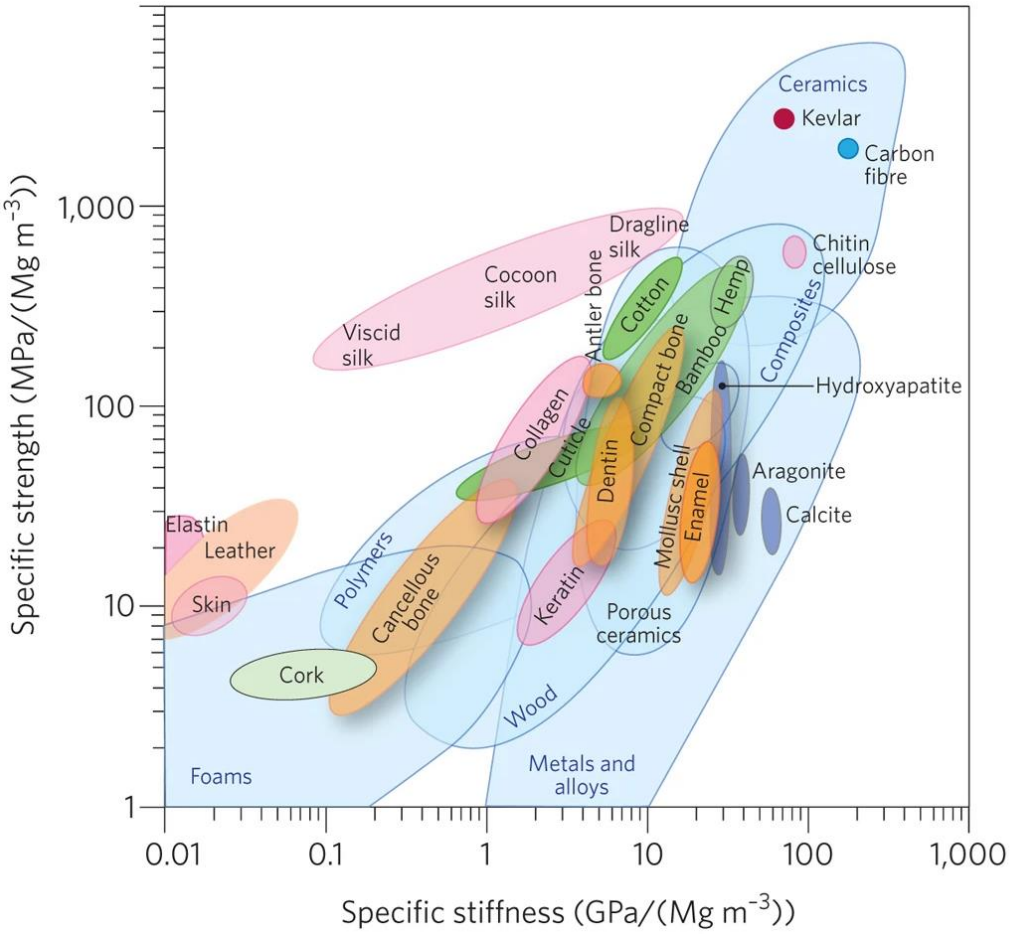

Fig.1-5 *Ashby plot of the specific stiffness vs. specific strength for various natural and synthetic materials. Adapted from [5].*

In human body, tooth and bone are prime examples of natural composites with mechanical properties that far exceed those of their constituents. Mature bones consist of compact bone and sponge bone, where compact bone covered the bone surface to protect structure inside the bone, and sponge bone can only be found in the interior of bones (**Fig.1-6**). Similar to nacre, compact bone and sponge bone are also highly mineralized composite materials of

hydroxyapatite (HA) nanocrystals (95% dry weight [30]) and type-I collagen. Hydroxyapatite is a hydrated calcium phosphate ceramic providing strength for bones to support and protect the body and organs, but it also participates in metabolism as a source of calcium [30]. Collagen is the most abundant biopolymer in the body of animals, and it is a basic structural element in soft tissues that results in improvement of the fracture toughness of bone. The architecture and multi-scale structures of bone are illustrated in **Fig.1-6**.

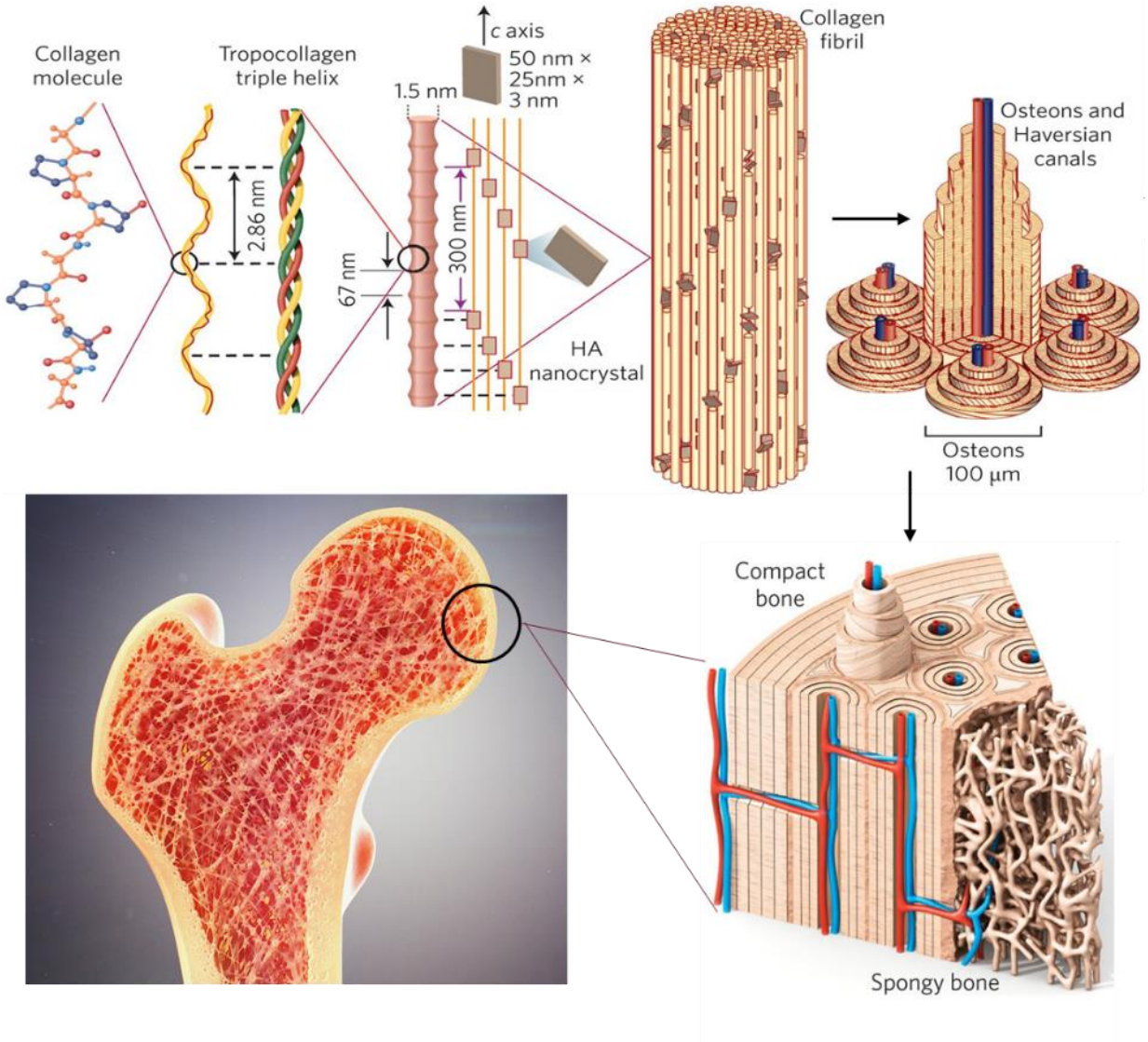

Fig.1-6 *The hierarchical structure of bone. Adapted from [5].*

1.3 Mechanical properties: natural materials vs. nature inspired synthetic materials

As reviewed in section 1.2, some natural composite materials exhibited remarkable mechanical properties with a combination of high strength and high toughness. Nacre, the outer layer of abalone shell, has been proven as an excellent example of biological composite materials with both high strength and high toughness because of its unique layered architecture of organic and inorganic phases. Hence, learning from the nacre, a variety of nacre-inspired synthetic materials have been created to replicate the architecture of nacre, which are aimed at overcoming the conflict between toughness and strength. This section will focus on toughening mechanisms of nacre-like synthetic materials and the factors that affect their mechanical properties.

1.3.1 Fracture toughness

In theory, toughness is defined as the ability of a material to resist fracture under a load, thus both initiation and subsequent extension of a crack are taken into account. In the schematic illustration of crack propagation within materials (**Fig.1-7**), fracture toughness can be improved extrinsically and intrinsically. The intrinsic toughening is achieved by increasing the microstructural resistance, e.g. dislocation accumulations or interfacial debonding to suppress damage in the form of microcracking ahead of a crack tip. This mechanism is more effective for ductile materials like polymers or metals. However, for brittle materials, toughness is mostly achieved via the extrinsic toughening of microstructures that act principally behind the crack tip to reduce the 'driving force' at the crack tip. This is also known as the crack-tip shielding effect, which occur by such mechanisms as crack bridging. In fact, fracture toughness is the result of a competition between intrinsic (damage) mechanisms ahead of the crack tip

that promote cracking and extrinsic (shielding) mechanisms behind the tip that try to impede it [31].

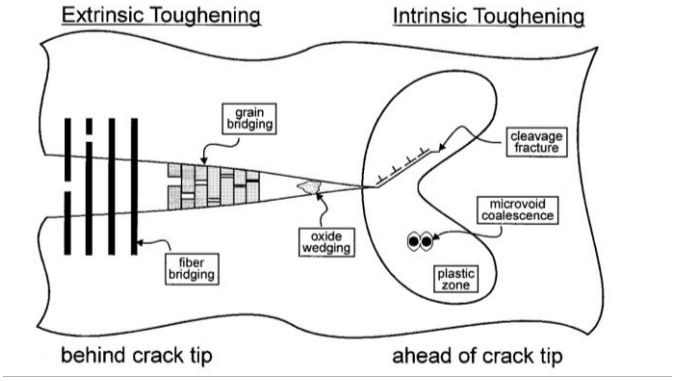

Fig.1-7 *Schematic illustration of intrinsic and extrinsic toughening mechanisms. Adapted from [32].*

From the fracture mechanics perspective, it is apparent that most biological materials derive their fracture resistance through the action of a series of extrinsic toughening mechanisms. Inspired by this, J. Cook and J.E. Gordon reported that when introducing weak interfaces transverse to brittle materials, the materials were toughened due to extrinsic toughening such as the crack bridging effect [33]. For engineering materials, the resistance (*R*)-curve behaviour has vital implications in characterising the toughness of materials since it is developed while toughening during crack growth, rather than crack initiation. *R*-curve is frequently used to evaluate fracture toughness of nacre or nacre-like composite materials. It is defined as the plot of crack extension versus fracture resistance [34]. The exceptional fracture resistance of nacre-like composites results from the fact that these materials do not exhibit catastrophic failure where the fracture energies increase as the crack extended.

1.3.2 Architectures

Microstructure generally defines mechanical properties of materials. For bioinspired materials, the mechanical properties are derived from architectural design that spans multiple scales.

Nacre's exceptional mechanical properties are attributed to its layered microstructure because its main toughening mechanism is crack deflection along interface between layers, resulting in high energy dissipation. Nacre-inspired materials possess normally layered microstructures such as lamellar [35] and brick-and-mortar architecture [36, 37]. The SEM images **Fig.1-8** revealed that the crack propagation behaviours are similar in nacre and nacre-inspired synthetic materials.

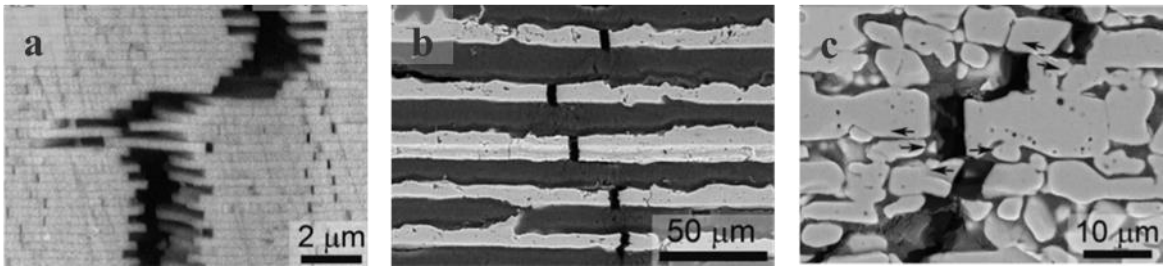

Fig.1-8 *SEM images taken during stable crack propagation of natural nacre* ***a)****, nacre-like lamellar* ***b)****, and brick-and-mortar* ***c)*** *composite materials. Adapted from [36].*

The nacre-like ceramic based composite materials were first reported in 1990 by Clegg *et al.* [38]. In their work, layer-by-layer silicon carbide/graphite composites were fabricated. A decade later, laminated silicon nitride/boron nitride composites were prepared and the resulting composites displayed a fracture toughness of 24 MPa $m^{1/2}$ without the obvious sacrifice of composite strength [39]. More recently, a novel brick-and-mortar ceramic/polymer composite was prepared by compressing the lamellar ceramic scaffolds created by freeze casting [40]. Launey *et al.* reported that the brick-and-mortar alumina/polymethyl methacrylate (PMMA) composite materials achieved very high fracture toughness over 30 MPa $m^{1/2}$ [36]. A comparison of lamellar and brick-and-mortar structured composites revealed that the latter with high ceramic content resulted in better mechanical properties. Moreover, some advanced nacre-like composites were developed based on these two architectures. For instance, nano brick-and-mortar composite was manufactured from ceramic nanoplatelets instead of particles [41],

while a brick-bridges-mortar composite synthesised by modified freeze casting displayed high strength at low ceramic content [42]. Another multi-layered brick-and-mortar composite was obtained by combining brick-and-mortar composite layers with epoxy layers [43].

1.3.3 Interface

The interface in composite materials was also known as a key factor to affect its mechanical properties. Since the extrinsic toughening of nacre-like composite is dependent on crack deflection between layers, optimal interface could lead to a higher fracture toughness. For instance, in nacre-like ceramic/polymer composites, when ceramic surface was modified by silane coupling agent before polymer infiltration, organic phase and ceramic phase were connected by covalent bond. Therefore, interfacial strength was enhanced. Not only flexural strength but also fracture toughness were improved in both lamellar or brick-and-mortar alumina/PMMA composite materials [36]. Apart from covalent bonding between phases, the interface could be enhanced by other methods such as laser engraving [44] and compliant phase crystallization [45]. The resulting nacre-like composite materials demonstrated improved mechanical performance in both strength and toughness.

However, too strong interface also led to lower fracture toughness since it may prevent crack deflection. For instance, Wat *et al.* fabricated alumina/BMG nacre-like composite materials, in which the interface was formed at various infiltration temperatures [45]. From the micro-cantilever tests (**Fig.1-9a**), infiltration at a lower temperature (1153K) resulted in a stronger interface. This was also supported by the high-magnification SEM images, clearly showing erosion behaviour at the interface, with a rough boundary (**Fig.1-9d**). For both brick-and-mortar and lamellar structures, a weaker interface (1273 K) led to an approximate fourfold decrease in flexural strength (**Fig.1-9b**). However, fracture toughness showed opposite results (**Fig.1-9c**). For the lamellar composites, the fracture toughness improved slightly with a weaker interface. Conversely, the brick-and-mortar samples with a stronger interface failed

catastrophically without stable crack growth resulting in a lower fracture toughness. The toughening mechanism of crack deflection no longer existed in the brick-and-mortar alumina/BMG composites (1153K) with a strong interface as shown in SEM images taken after fracture (**Fig.1-9e**).

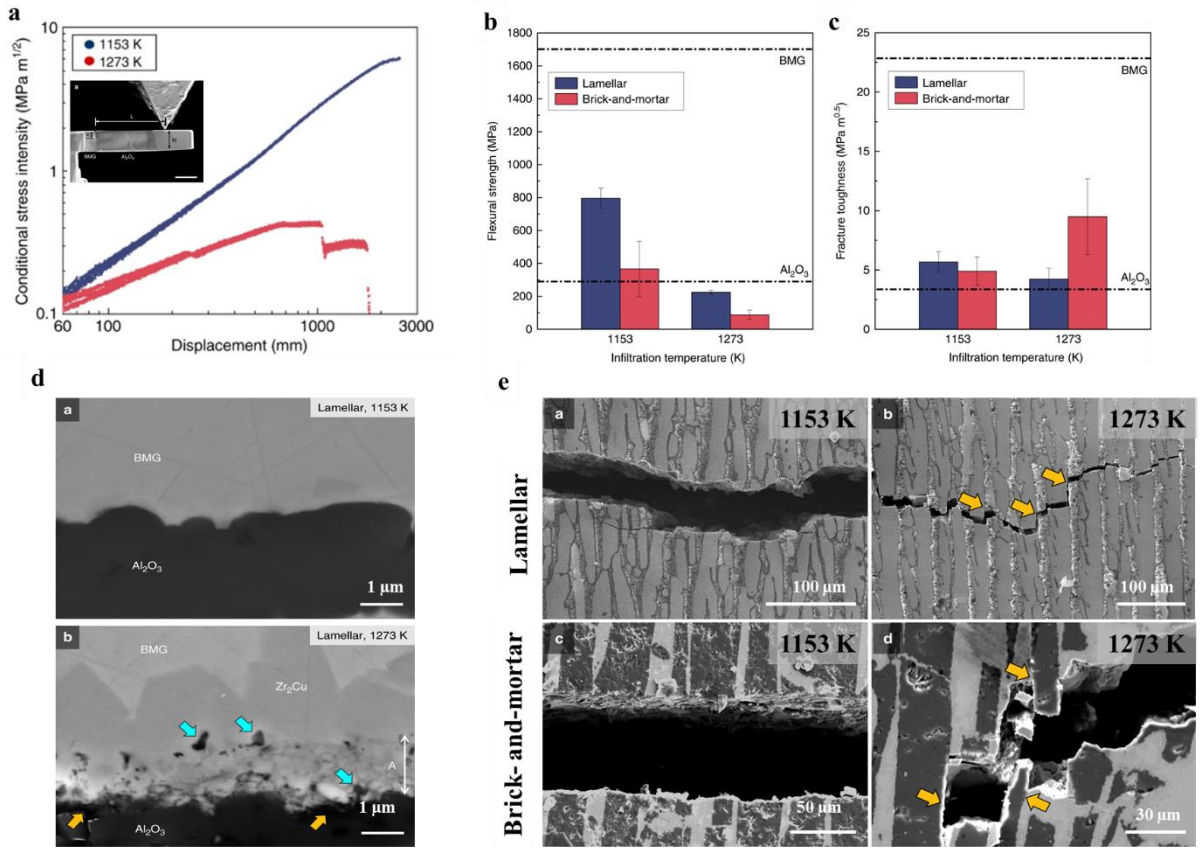

Fig.1-9 *Conditional stress intensity–displacement curves for alumina/BMG composites processed at different infiltrating temperatures* ***a)****; flexural strength* ***b)*** *and fracture toughness* ***c)****; SEM images of interface* ***d)*** *crack propagation* ***e)*** *of nacre-like alumina/BMG composites. Adapted from [45].*

1.3.4 Mineral bridges

The introduction of inorganic bridges in nacre-inspired bulk materials could promote their mechanical properties. The inorganic, stiff bridges could be introduced by magnetic assisted slip casting (MASC) [41, 46], vacuum-assisted magnetic alignment (VAMA) [47, 48], 3D

printing [49], and controlled freezing conditions in freeze casting [42]. It was found that the composite materials obtained impressive mechanical properties with the addition of mineral bridges. For example, as demonstrated by Grossman *et al.*, brick-and-mortar composite materials with mineral bridges were fabricated successfully via VAMA of titania-coated alumina micro-platelets (**Fig.1-10b**). The titania particle coated on surface alumina platelets were consolidated into mineral bridges connecting adjacent layers during the sintering process in a spark plasma sintering process. The effects of mineral bridges on the mechanical response of the resulting nacre-like composites were quantified. As a result, the bridges-reinforced composite showed a remarkable combination of flexural strength and toughness. Moreover, the mechanical properties were almost linearly dependent on the density of the ceramic bridges (**Fig.10b-f**), which could be explained by the ceramic bridges impeding interface shearing and promoting stress redistribution [42].

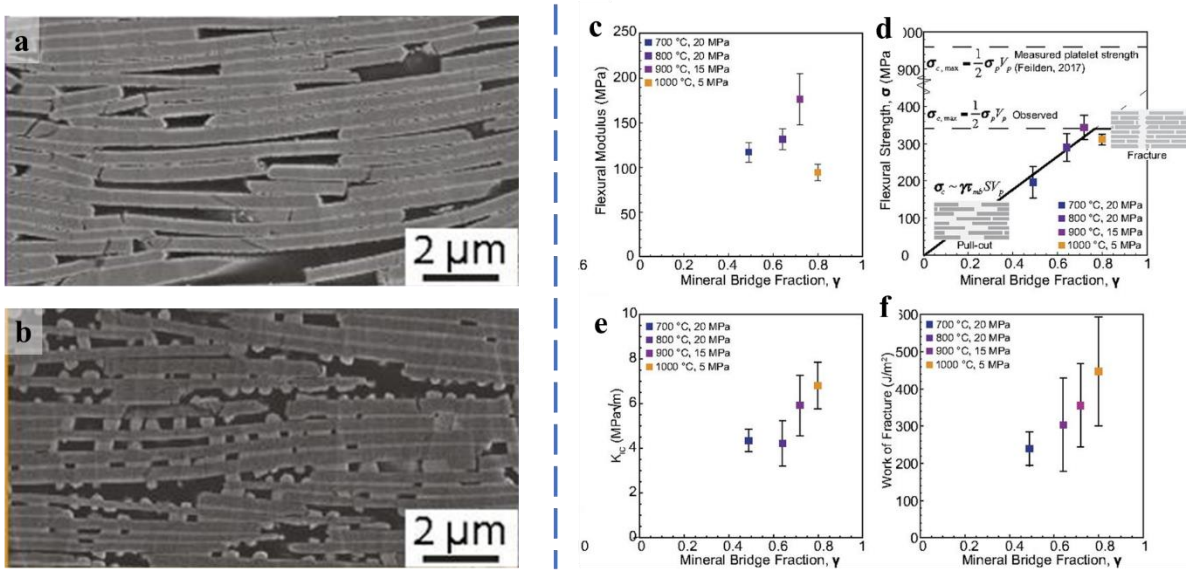

Fig.1-10 *SEM images showing brick-and-mortar composites before* ***a)*** *and after* ***b)*** *the introduction of mineral bridges (titania nanoparticles). Effect of mineral bridges fraction on flexural modulus* ***c)****, flexural strength* ***d)****, fracture toughness* K_{IC} ***e)****, and work of fracture* ***f)****. Adapted from [48].*

1.4 Fabrication process

Accordingly, the idea of replicating the natural designs in synthetic composite materials has attracted enormous interests [2, 50, 51]. The generation of synthetic bioinspired materials with intricate, hierarchical architectures is a challenge that requires not only the design of optimum microstructures but also the development of fabrication procedures to implement these designs [52]. To mimic the structure and achieve similar mechanical behaviour of nacre, synthetic composite materials with nacre-like architecture were synthesised via a variety of fabrication techniques such as freeze casting [35, 36], 3D printing [49], magnetic assisted alignment [37], biomineralization [53, 54], hot pressed assisted slip casting [55], gravitational sedimentation [56], layer-by-layer deposition [57-59], or by direct gluing ceramic layers [38]. The resultant nacre-like composite materials with multi-layered architectures displayed extraordinary flexural or tensile strength and a rising *R*-curve behaviour due to their nacre-mimicking architecture. However, it is difficult with most of these fabricating methods to generate biomimetic composites with structural hierarchy in large dimensions. Freeze casting can produce bulk materials with micro-scale architecture and relatively large size (>cm). This technique is also flexible, cost-effective and environmentally friendly.

1.4.1 Freeze casting

Freeze casting is a versatile technique to build up 3D porous scaffold structure by assembling particles suspended in liquid into ordered microstructure, which is also known as an ice-templating mechanism [60]. This phenomenon was first found by Lottermoser [61] in 1908, where cellular structures were formed by freezing hydrosols. Furthermore, this process was developed on other solutions or slurries to prepare more complex structures. Currently, freeze casting is attracting an increasing interest because of its flexibility and cost-effectiveness. As a result, by 2016, over 900 papers had been published on this technique to fabricate well-controlled porous scaffolds or composite materials [62]. This method could be used on all

classes of materials, especially ceramics. The porosity, microstructure and architecture of scaffolds created by freeze casting can be tailored by altering slurries and freezing conditions resulting in different physical or mechanical properties of final products [60, 63]. Therefore, freeze casting has been widely employed to produce high-performance bioinspired materials mimicking natural materials in various application fields.

The complete fabrication process of freeze casting of ceramics or composites shown in **Fig.1-11** is generally composed of four steps: (a) ceramic slurry preparation, (b) freeze casting, (c) freeze drying and (d) sintering. In the first step, ceramic powder is suspended in a liquid freezing agent with additional dispersant and organic binder to produce a colloidal suspension or slurry (a). In the second step, the as-prepared slurry is frozen under controlled temperature field, where the solidification of the freezing agent induces a freezing front of crystals that segregate the ceramic particles (b). When the slurry is frozen completely, the solidified liquid is sublimed under vacuum (c). The green body scaffold is obtained, and the structure of pores replicates the shape and location of the solidified liquid formed during freezing process. Finally, green body scaffold is sintered at high temperature to consolidate the ceramic particles to form the final scaffold with retained architecture (d). In some studies, there may be a fifth step, i.e. the post-processing step (e). The aim of this step is to fabricate composite materials, where infiltration of a second phase such as polymer [35, 36, 64], metal [45, 65], or glass [66, 67] is carried out. The resultant ceramic-based composite materials with bioinspired architecture demonstrate excellent mechanical properties [36, 40].

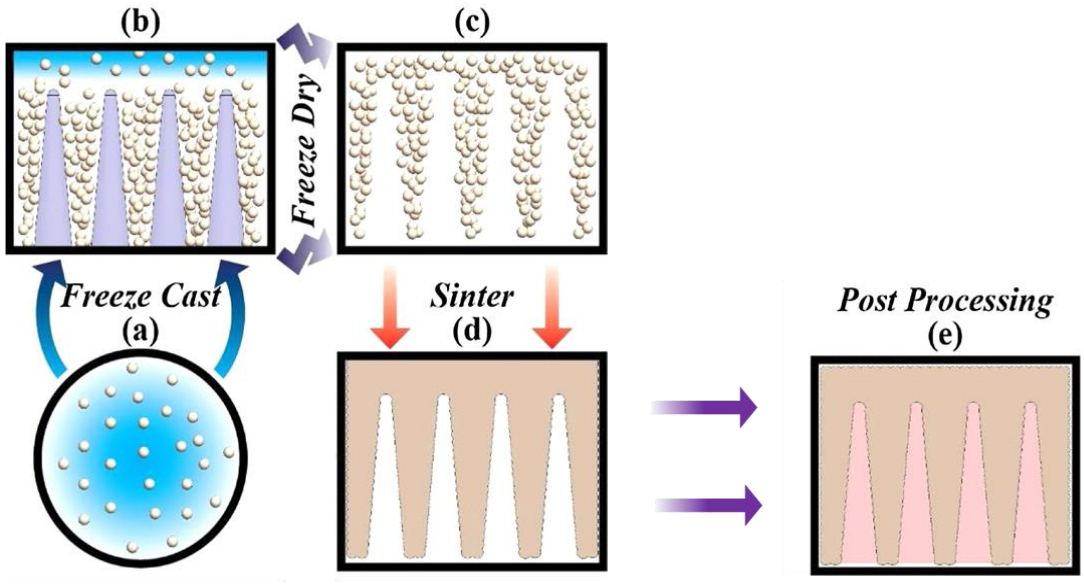

Fig.1-11 *Schematic diagram of the complete freeze-casting process, which occurs in four distinct steps, i.e. slurry preparation* ***a)****, freeze casting* ***b)****, freeze drying* ***c)****, sintering* ***d)*** *and post processing* ***e)****. Adapted from [63].*

The most widely used liquid freezing agent is water, in addition to other organic solvents such as camphene, camphor-naphthalene, and tert-butyl alcohol [68], as it is more economic and environmentally friendly. The aim of using dispersant is to provide stable slurries, avoid aggregation/sedimentation of particles, and alter the interface free energy between particles and solvent during freeze casting process [63]. The dispersive ability of dispersant governs the resistance to flow and fluidity of suspension during ice growth. To exam the dispersive ability of additive dispersant, rheological properties (i.e. viscosity) of slurries were characterised where the optimal dispersant was obtained with lowest viscosity and homogeneous structures and improved mechanical properties in the final sintered porous scaffolds [69]. Organic additive has been proven to be an important factor in ice solidification on freeze cast scaffolds by altering the properties of slurries (e.g. viscosity, pH value, and chemical structures). Many studies discussed how the viscosity affect the nucleation of ice crystal during freeze casting resulting in different pore size and morphology. Different amounts and types of organic

additive such as polyvinyl alcohol (PVA) [69-71], glycerol [72], and sucrose [73] were investigated on controlling the viscosity of slurries and generating scaffolds with different microstructures. At the same time, pH value of slurries determined by additive acid compounds has been shown to alter the pore size. In addition of citric acid [73], hydrochloric acid/sodium hydroxide [70], or acetic acids [74], the ice crystal displayed different morphologies. Dispersed chemical structures were formed in slurries offering a way to control scaffold structures. For instance, with addition of alcoholic organic compound such as ethanol, propanol and butanol, cage-like clathrate hydrates that can hold particles within were formed by hydrogen-bonded alcohol and water [75, 76]. This leads to drastically increased pore sizes. Another noticeable way with a similar mechanism to control microstructure of pores was to use antifreezes [68]. Fish gelatine and frog gelatine were used as antifreezes that directly bind to the surface of ice crystal by Van der Waals interaction or hydrogen bond thus blocking the ice growth resulting in ice recrystallisation inhibition, thermal hysteresis and ice shaping/crystal habit modification [77]. Inspired by this, zirconium acetate was added into slurries before freeze casting to modify the shape of ice. Deville *et al.* indicated that the zirconium acetate will adopt a hydroxyl-bridges polymer structure which would connect to the surface of ice crystals leading to reducing growing speed and manipulate the shape of ice crystals, thus the final ceramic scaffolds exhibited homogeneous honeycomb-like hexagonal pores [78].

Besides slurry composition, the freezing conditions could also affect the porosity and pore structure in scaffolds. The basic mechanism of aqueous freeze casting to generate lamellar porous structure is shown in **Fig.1-12**. Solid particles in suspension are rejected by the moving solidification front and repositioned between the growing lamellar ice crystals. Thus, varying the freezing conditions could alter different architecture features. To control the microstructure of scaffolds, efforts have been made to adjust the freezing conditions such as cooling rate [79, 80], cooling temperature [81], ice growth speed [82, 83], cooling field [63], and external field

[84]. The resultant scaffolds exhibited different microstructure with various layer thickness and porosity gradient.

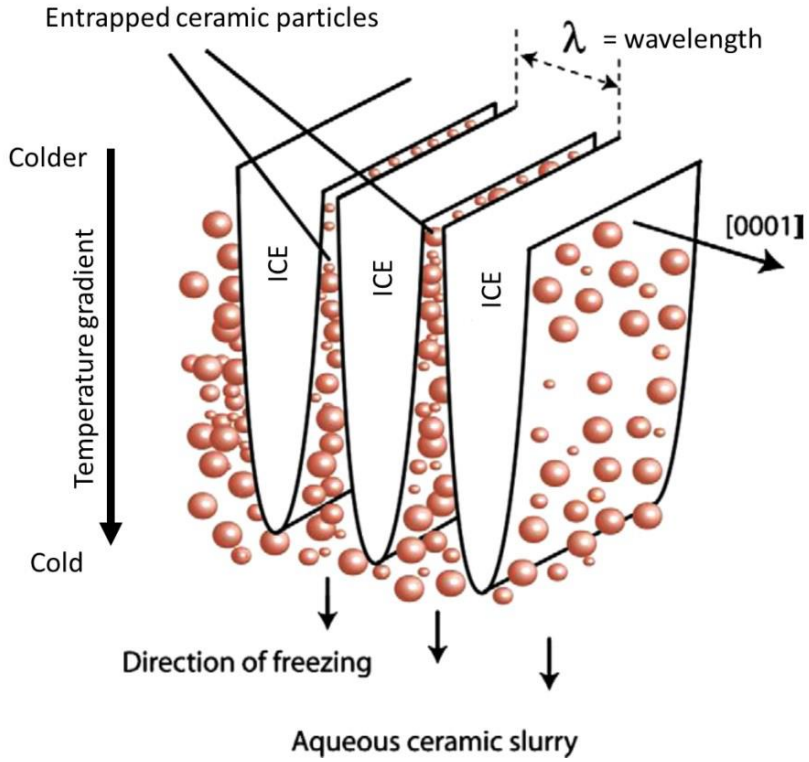

Fig.1-12 *Schematic of freeze casting process in aqueous suspension. Adapted from [82].*

1.4.2 Fabrication of orderly aligned porous structures via freeze casting

1.4.2.1 Altering cooling field

Currently, a number of freeze casting techniques (**Fig.1-13**) with complex cooling fields have been reported to align lamellar walls in scaffolds. Those freeze casting techniques provided different cooling fields that rely on geometries and set-up of cold fingers to manipulate the freezing process. According to the configuration of different cold fingers, freeze casting techniques could be classified into multidirectional and templated freeze casting. Uni-directional, bi-directional [85-88], tri-directional [89], infinite-directional (radial) freezing [90], infinite-directional (radial) concentric [91], and templated freeze casting [36, 73] have been developed to control the architecture and microstructure of final freeze-cast scaffolds.

In the case of conventional uni-directional freezing, there was a unique temperature gradient thus the nucleation of ice crystals occurred randomly on the surface of cold finger where the freezing initiated within the aqueous slurry [92]. Consequently, the freezing slurry media consisted commonly of ice crystals that oriented preferentially along the direction of the temperature gradient, resulting in scaffolds with fine-scale lamellar structures (**Fig.1-13a**). However, when a slurry was frozen at complex cooling fields offered by alternative freeze-casting configurations, the suspended particles assembled into different microstructures since the nucleation of ice crystals was changed. For example, bi-directional freeze casting was able to produce highly aligned scaffolds from the freezing aqueous suspension. In this case, the bi-directional freeze casting technique provided two temperature gradients: vertical and horizontal to the cold finger, where the ice crystals grew along two directions mutually [85-88] (**Fig.1-13b**). When the number of temperature gradient was increased to three, the lamellar walls aligned into three distinct regions [89] (**Fig.1-13c**). Likewise, a cylinder freeze casting copper mould, surrounded by the slurry could provide a radial cooling field with infinite temperature

gradient in which the lamellar ice crystals were distributed along the radius of cylindrical mould, leading to the formation of centrosymmetric aligned lamellar structures [90] (**Fig.1-13d**). Besides, based on the cylinder copper mould, a copper rod inserted into the slurry at the central of cylinder can supply additional temperature gradients, resulting in the formation of concentric structure of the porcupine fish spine in the final scaffold [91] (**Fig.1-13e**). In addition, by scratching the flat surface of cold finger uni-directionally with a sandpaper, the cooling field became templated. When the slurry was frozen on this templated cold finger surface, aligned lamellar architecture was obtained in the scaffold [36, 73] (**Fig.1-13f**). This implied that the templated cooling field could manipulate the nucleation and growth direction of ice crystals.

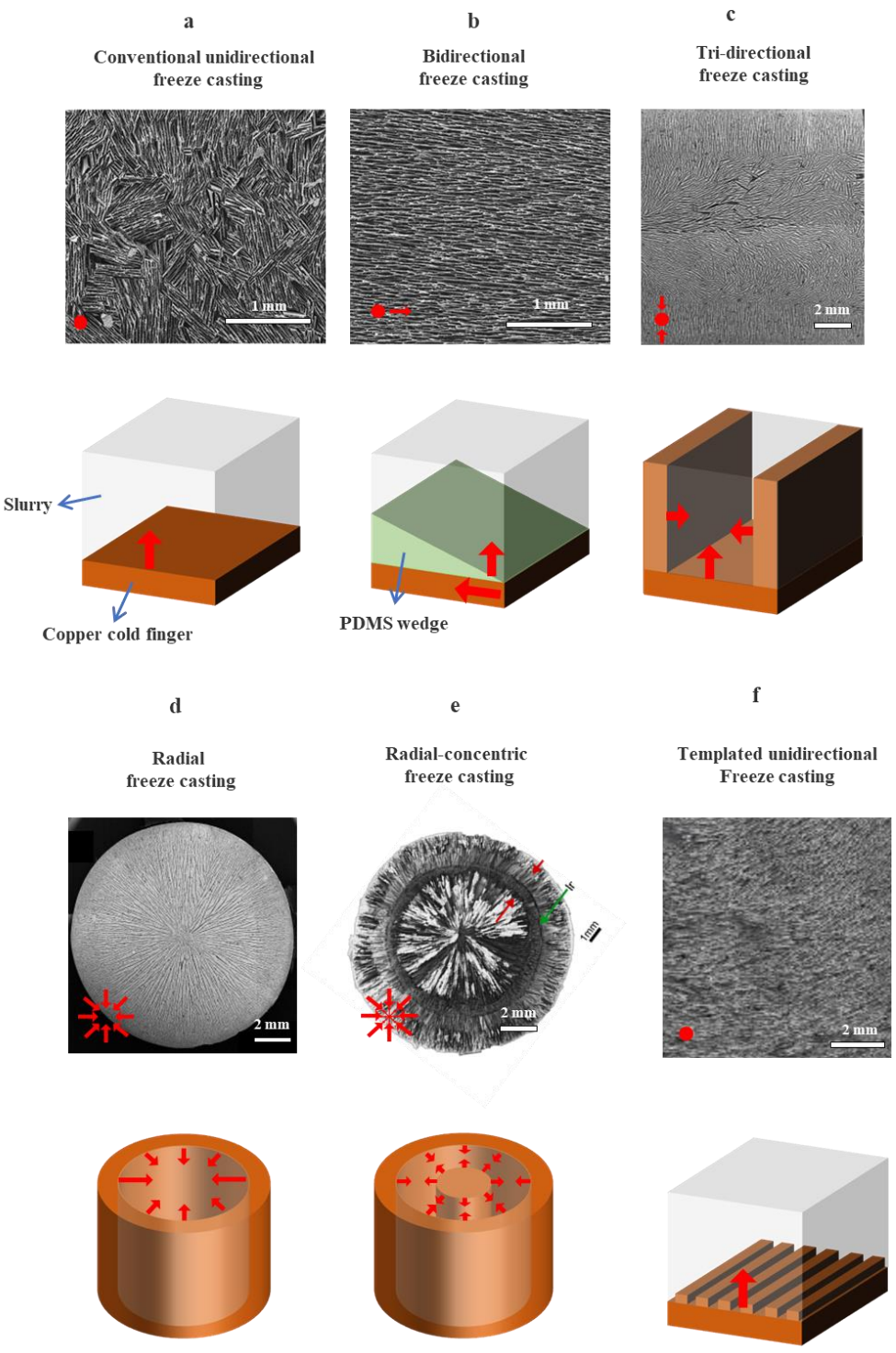

Fig.1-13 *Freeze casting techniques based on different cooling fields applied and SEM images of cross-section of the resultant scaffolds. Examples are given with uni-directional* ***a)****, bi-directional* ***b)****, tri-directional* ***c)****, radial* ***d)****, radial-concentric* ***e)****, and templated uni-directional cooling* ***f)****. The red arrows indicate the direction of temperature gradient. SEM images are adapted from [85], [89], [90], [91] and [73].*

1.4.2.2 Altering external field

The freeze casting process could be altered by not only temperature field but also external forces. It has been reported that when slurries were frozen under external force such as dynamic flow [93], electric [94], magnetic [95], or ultrasound field [96, 97], the final scaffolds exhibited aligned architecture with various microstructure and mechanical properties. Compared with the conventional uni-directional freeze casting, the microstructure of resultant scaffolds fabricated by freeze casting assisted with external fields is shown in **Fig.1-14.**

To obtain aligned ceramic walls during freeze casting, alumina nanoplatelet slurry was frozen as it flowed dynamically over the freezing surface [93]. The resultant scaffolds exhibited a large region of aligned structure and a small randomly oriented region compared with the samples prepared using conventional freeze casting at static condition (**Fig.1-14a**). From the thermal measurements on slurries during freezing under flow [94], the temperature gradient along flowing direction was formed depending on flow velocity, implying that the dynamic flow field offered a horizontal temperature gradient to create aligned structure where the principle was similar to that in bi-directional freeze casting. In another study, the symmetrical structure of porous ceramics was obtained after applying an electrostatic field with an intensity of 150 kV/m (**Fig.1-14b**). This study demonstrated that electric fields could rearrange the water molecule in slurries. As water is a polar molecule with a permanent dipole moment, the electric field was able to alter the preferential orientation and nucleation of ice crystals, hence redirecting ice growth [89, 94, 98]. It was also reported that a Helmholtz coil or permanent magnets could be employed to produce magnetic field in the freeze casting process to alter the microstructure during ice growth (**Fig.1-14c**). In aqueous solution, the magnetic field could affect both water molecules and suspended particles [95]. The hydrogen bonds between water molecules were strengthened by the magnetic field leading to the formation of ice crystals with smaller size during solidification, therefore reduced porous size in the final scaffolds. For

instance, lamellar spacing in sintered alumina scaffolds increased around 60% from 52 to 88 μm when the intensity of magnetic field decreased from 12.75 to 11 kV/m [89]. The effect of magnetic field on the alignment of particles was also dependent on the interaction energy between the suspended particles. The magnetic field affected particle aggregation and chain formation before ice nucleation during freeze casting. Recent studies on magnetic-assisted freeze casting demonstrated the utility of diverse types of magnets and magnet positioning techniques. As a typical diamagnetic particle, alumina had ignorable interaction with magnetic field. Frank *et al.* [93] used the ferrofluid-coated alumina (paramagnetic) particles to produce aligned alumina scaffolds via magnetic-assisted freeze casting. The results indicated that best alignment of lamellar ceramic wall was obtained when the alumina particle size was 350 nm and static magnetic field was perpendicular to freezing direction at an intensity of 75 mT. When the magnetic field was too strong (150 mT), the scaffolds displayed angled lamellar wall alignment. Ultrasound was also reported to assist the freeze casting process. Ultrasound pressure waves could orient and reposition particles suspended in slurries (**Fig.1-14d**). The particles suspended in slurries absorbing or reflecting the acoustic radiation force were more likely to agglomerate, the process of orienting and repositioning these particles was known as ultrasound directed self-assembly process. Scaffolds generated by freeze casting under ultrasound exhibited distribution of alternating dense/porous concentric rings, where the number of rings was dependent on operating frequency of ultrasound transducer [96]. Consequently, by altering either cooling field or external field provided routine to obtained samples with aligned architectures. Next, the bi-directional freeze casting would be further investigated as its great potential to create nacre-like materials.

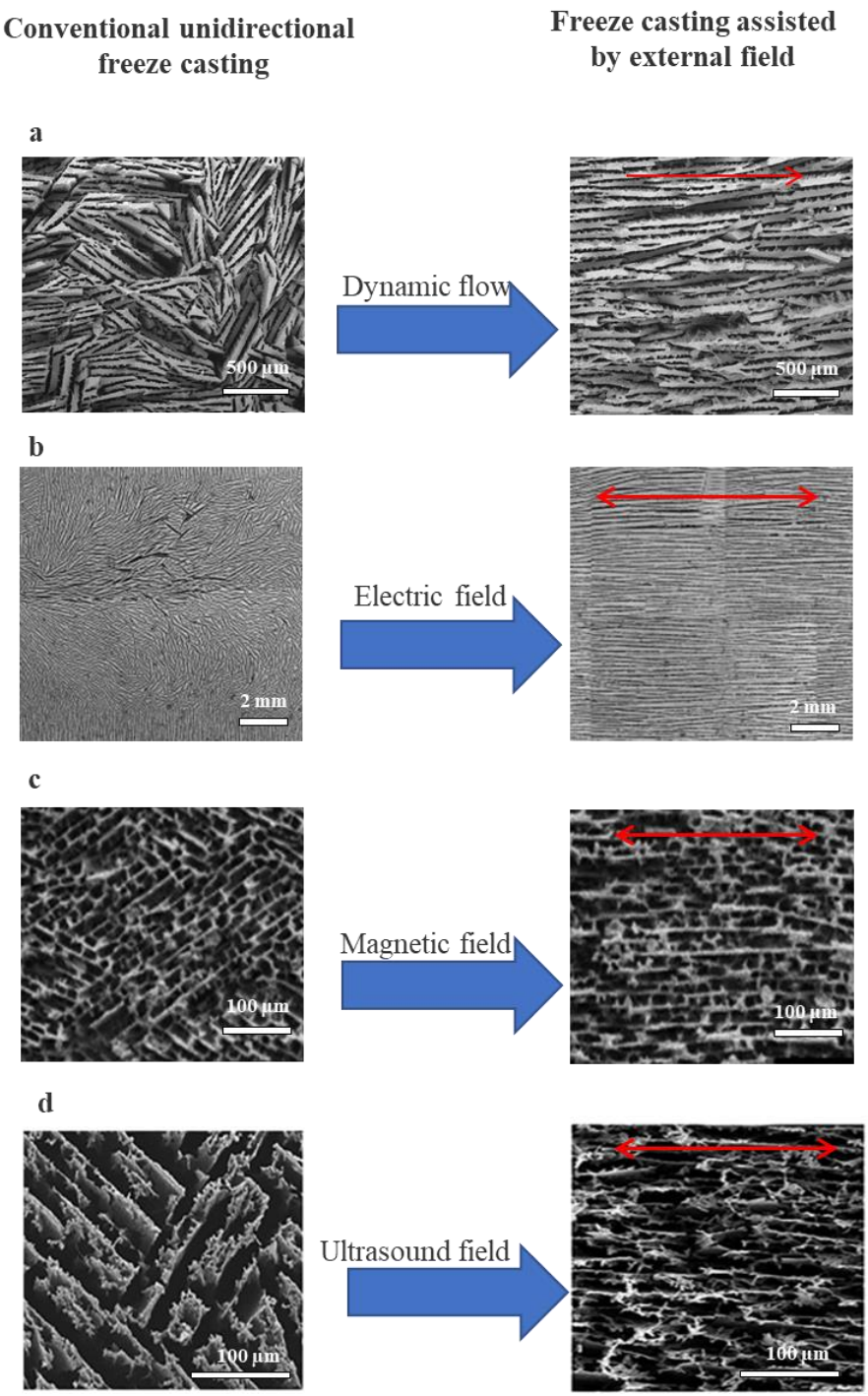

Fig.1-14 *Effect of external field on microstructure of freeze casting scaffolds. Examples of aligned microstructure of scaffolds via freeze casting under dynamic flow* ***a)****, electric* ***b)****, magnetic* ***c)****, and ultrasound* ***d)*** *fields. Red arrows indicate the direction of the applied external field. All images show transverse cross-sectional view perpendicular to the ice growth direction. Adapted from [93], [94], [95] and [96].*

1.4.2.3 Bi-directional freeze casting

Bi-directional freeze casting is one of the most effective techniques to prepare scaffolds with aligned microstructure. It was first reported in 2015, by Bai *et al.* [85], who fabricated large-scale lamellar ceramic scaffolds by freezing hydroxyapatite (HA) suspension under dual temperature gradients. To add an additional temperature gradient, the uni-directional freeze casting mould was modified as shown in **Fig.1-15b.** Cold finger were separated by an insulating polydimethylsiloxane (PDMS) wedge with various angles. Due to relatively low thermal conductivity of PDMS, temperature field was dependent on the thickness of the PDMS at different positions. Therefore, changes in PDMS thickness lead to horizontal temperature gradient (**Fig.1-15d**). As a result, one more temperature gradient was formed at left-right (horizontal) in addition to top-down (vertical) directions. To confirm this, the slurry temperature at different positions shown in **Fig.1-15d** was measured using a thermocouple inserted into the mould and plotted as a function of time during freeze casting (**Fig.1-15f**). Compared with the uni-directional freeze casting (**Fig.1-15a, c,** and **d**), the ΔT indicated that a horizontal temperature gradient was established. The aligned microstructure was obtained (**Fig.1-13b**).

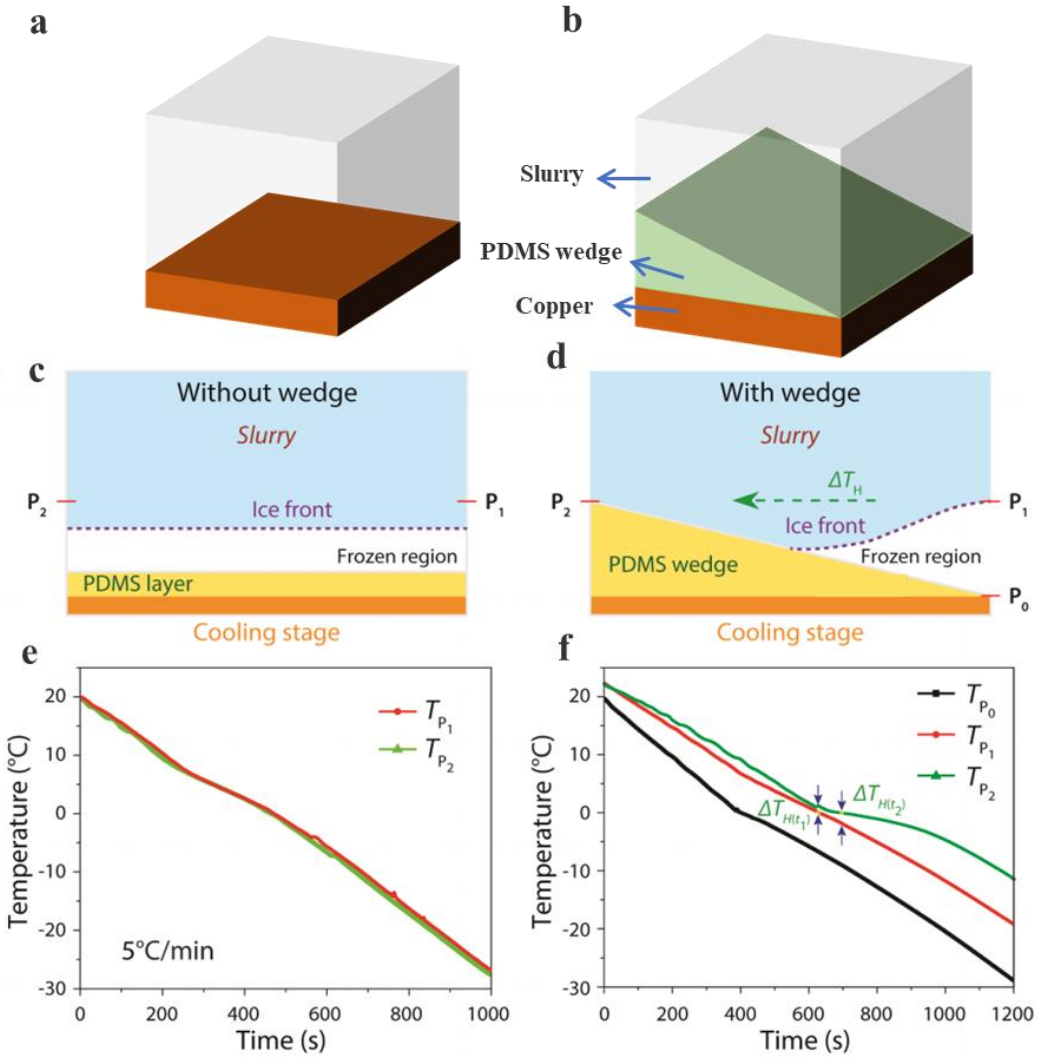

Fig.1-15 *Comparison between uni-directional and bi-directional freeze casting. Schematic of the freeze casting moulds* ***a)*** *and* ***b)****; profiles illustrating the ice-front within different moulds* ***c)*** *and* ***d)****; the time vs. temperature plot exhibiting temperature gradient* ***e)*** *and* ***f)****. Adapted from [85].*

Therefore, this technique can be used to control the alignment of ice crystal growth under dual temperature gradients. To evaluate the ice crystal nucleation and propagation processes, HA slurries frozen under the bi-directional freezing field at a cooling rate of 5 °C/min were recorded by the real-time optical images of profile at different stages (**Fig.1-16b**). When the freezing started, ice crystals nucleated at the thinnest part of the wedge and then propagated along the

PDMS surface not only horizontally but also vertically due to effect of the particles and the constitutional supercooling [60, 82]. During this process, the temperature on the PDMS surface also decreased, which accelerated freezing process of ice crystal along the PDMS. When the slurries on the PDMS surface were all frozen, the ice profile propagated upwards until reaching the slurries top surface.

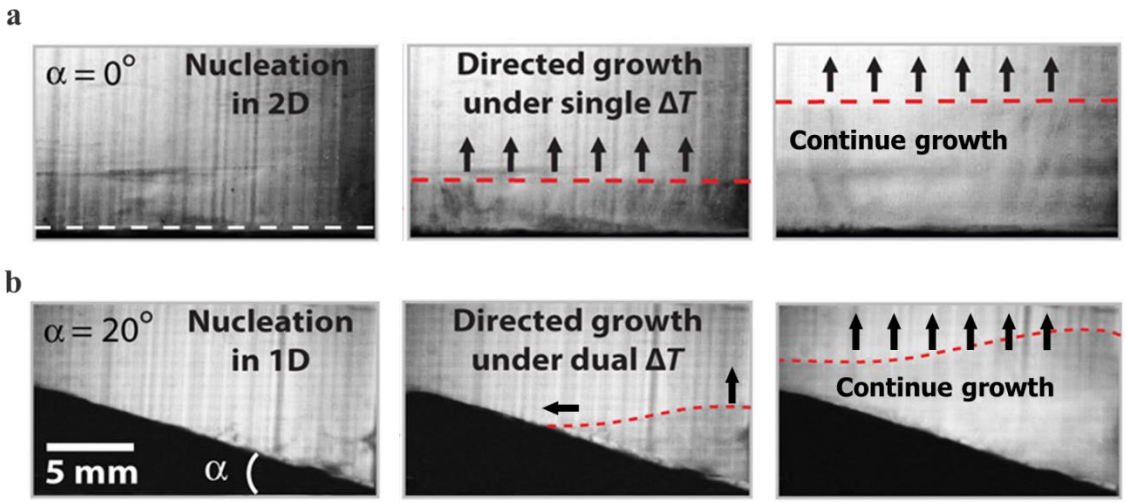

Fig.1-16 *Ice-profile propagation during uni-directional* ***a)*** *and bi-directional freeze casting* ***b)*** *in different stages from left to right hand side: Nucleation, directed growth, continue growth. Red dash line assign to the ice front and the black arrows indicate ice growing direction. Adapted from [85].*

However, the scaffold produced using the above mould had a slope because of the use of the PDMS wedge. Two more bi-directional freeze casting moulds were developed to produce more regular shaped scaffolds as shown in **Fig.1-17**. A recent work by our group reported a modified configuration of mould using the similar principle [87]. Instead of the PDMS wedge sitting on the flat copper plate (**Fig.1-17a**) [85, 99], the modified mould was composed of a wedged copper plate back-filled with PDMS to form a flat surface in the mould (**Fig.1-17b)**. The advantage of this mould configuration was that it could produce ceramic scaffolds with aligned microstructure and regular shape, e.g. cubic or cuboid block which allowed use of simple

uniaxial pressing in the subsequent densification process. This mould will therefore be used in this work. Another alternative mould was composed of two different materials with different thermal conductivity to provide two cooling rates in two directions (**Fig.1-17c)** [54]. In this method, the PDMS gasket was placed at the bottom of slurry. It could also be replaced by other thermal insulating materials like Teflon [86]. Thermal conducting copper plate was used as a sidewall of the mould. Two temperature gradients (vertical and horizontal) were generated at the same time when the freeze casting initiated. One of the drawbacks of this mould was that the freezing of slurries was slower at the same cooling condition because the relatively thermal insulating PDMS was in direct contact with the cooling source, leading to higher loss of cooling energy.

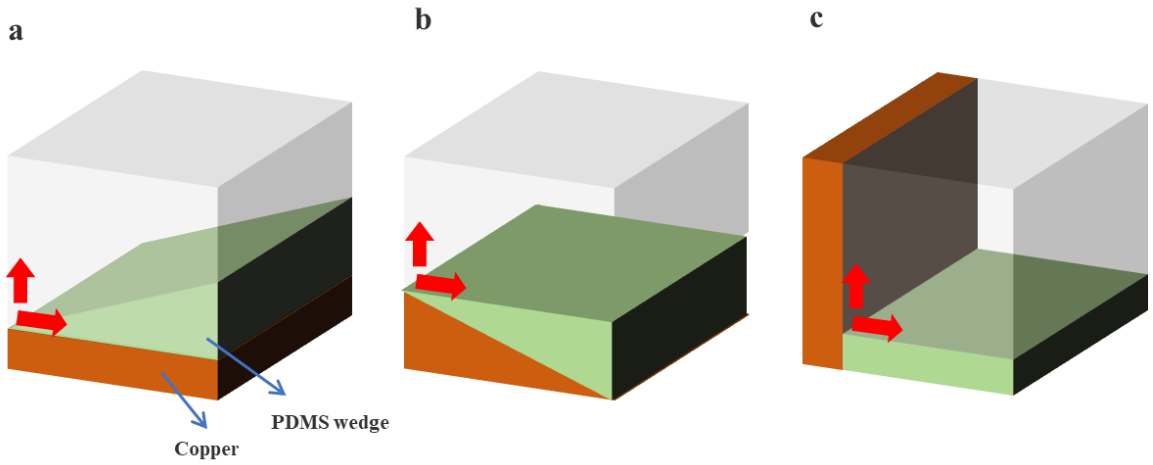

*Fig.1-17 Schematics of three different bi-directional freeze casting moulds: Flat copper mould covered by a PDMS wedge **a)**; copper wedge covered by a PDMS wedge to form a flat surface **b)**; copper and PDMS plates placed on left and bottom side respectively **c)**.*

Fig.1-18 showed the arrangement of ice crystal (white) and ceramic particles (blue) during freeze casting under unidirectional and bi-directional cooling conditions (a, d) and their respective optical (b, e), SEM (c, f) and micro-CT images (g, h) of scaffolds . It can be seen that the scaffolds prepared using bi-directional freeze casting exhibited highly aligned

microstructure (uniform blue coloured region in e), compared with the initial disordered region (multi-coloured region in e) and those from unidirectional freeze casting (b).

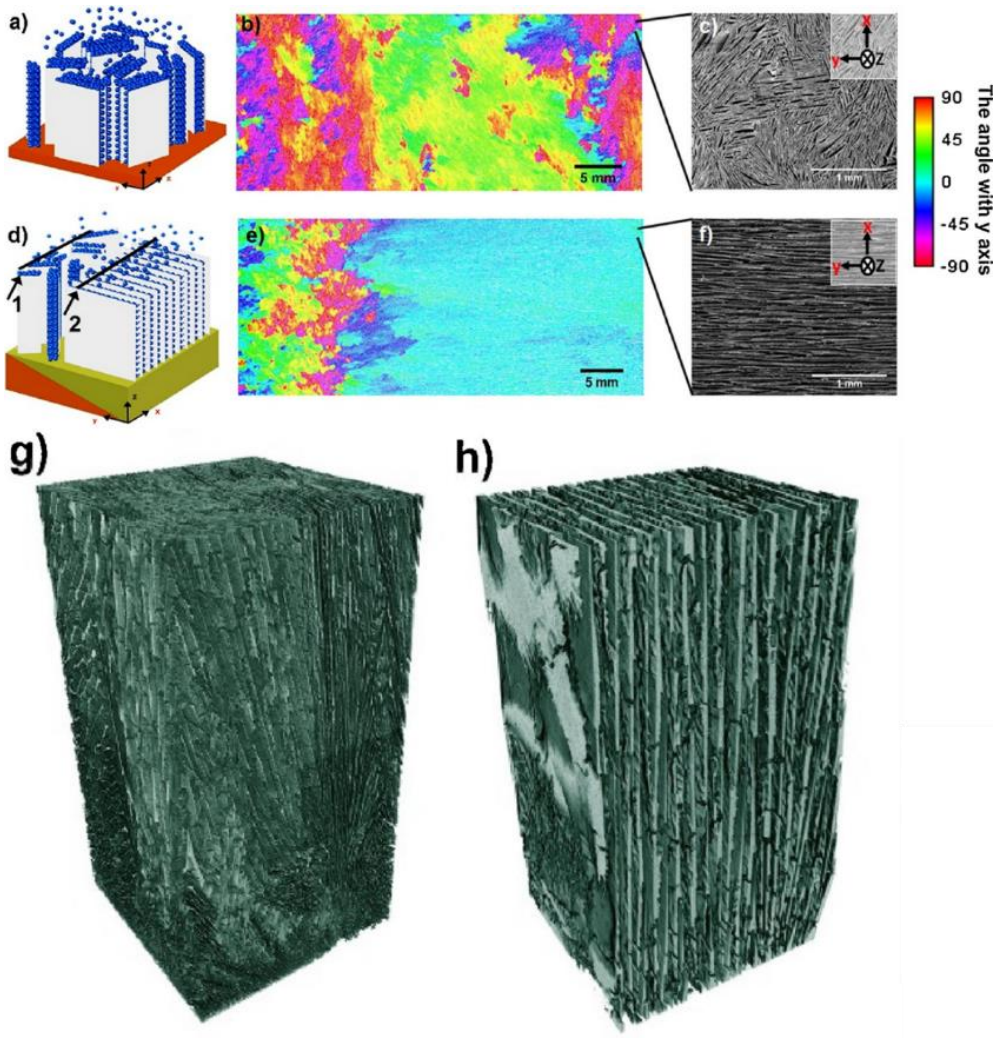

Fig.1-18 *Schematic of the uni-directional* ***a)*** *and bi-directional* ***d)*** *freeze casting processes. Coloured stitched light microscope images taken along z-direction from resultant scaffolds of uni-directional* ***b)*** *and bi-directional* ***e)****. SEM images of randomly* ***c)*** *and highly aligned* ***f)*** *areas in scaffolds. Reconstructed 3D tomography of uni-directional freeze casting product* ***g)*** *and highly aligned scaffolds* ***h)*** *generated using bi-directional freeze casting. Adapted from [87].*

When bi-directional freeze casting was performed at various cooling rates and different slope angles of wedge, the light microscope 2D top-view images indicated that the cooling rate and temperature gradient significantly affected the microstructural alignment within the scaffolds

(**Fig.1-19**). Therefore, the slope angle of 10° and the highest cooling rate (10 °C/min) resulted in the longest aligned region as shown in **Fig.1-19k**. Other processing parameters such as solid loading and additive organic binder, had also influence on microstructure (e.g. lamellar thickness and interlamellar spacing, density of ceramic bridges) [86, 87].

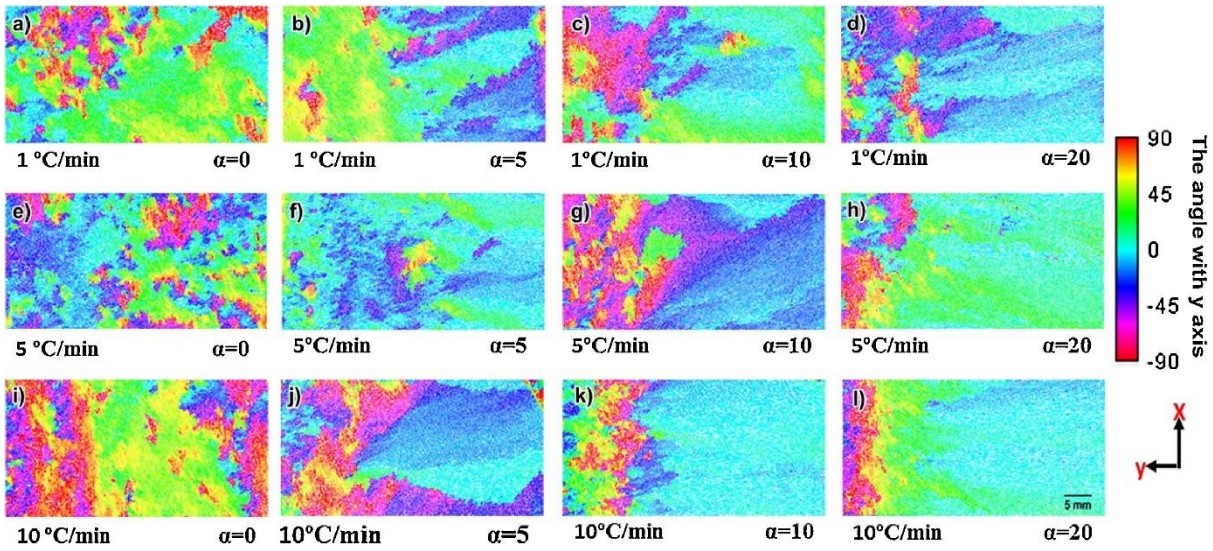

Fig.1-19 *Microstructural change of scaffolds created by bi-directional freeze casting. Domain orientations of alumina scaffolds fabricated under different cooling rates (from 1 to 10 °C/min) and slope angles (α from 0° to 20°) of PDMS wedge. Adapted from [87].*

1.4.2.4 Application of bi-directional freeze casting

Based on the successful fabrication of long-range and highly aligned scaffolds, bi-directional freeze casting was widely used in different applications. For example, long-range and highly aligned lamellar TiO_2 scaffolds with improved mechanical properties compared to conventional freeze casting [72]; β-chitin lamellar matrix to support mineralisation of nacre-mimetic materials [54]; boron nitride nano-sheet (BNNS)/epoxy lamellar composites were fabricated as a thermal insulation material [100]; and carbon-based layered materials such as graphene was obtained with aligned porous structures exhibiting shape memory properties [101, 102]. Furthermore, the freeze-cast highly aligned ceramic scaffolds were post-treated with

infiltration of polymer, glass, or metal to produce nacre-mimicking composite materials with brick-and-mortar microstructure. They exhibited excellent mechanical properties, particularly fracture toughness. Materials combinations included HA/PMMA [99], alumina/ Zr-based bulk-metallic glass (BMG) [45], zirconia/methacrylate resin [103], and silica platelets/epoxy [104].

1.5 Aims and objectives

This work is aimed at fabricating and characterising nacre-like ceramic-based composite materials. The ceramic phases are alumina, zirconia or HA, and the compliant phases are either polymers (PMMA, PU, UDMA/TEDGMA and PU) or metals (aluminium and magnesium alloys). The intention was to obtain the composites replicating the nacre-like architecture found in nature and to achieve a good combination of mechanical properties of high strength and high fracture toughness.

The specific objectives of this project were as follows:

- Prepare nacre-like ceramic scaffolds using bi-directional freeze casting and densification process.
- Study densification methods (i.e. one-step and two-step method) to generate ceramic scaffolds with micro-layered (μL) and brick-and-mortar (BM) architectures, respectively.
- Investigate the effect of different manufacturing parameters on microstructure of ceramic scaffolds.
- Produce nacre-like ceramic/polymer composites by salinization and polymer infiltration into as-obtained nacre-like ceramic scaffolds.
- Systematically characterise mechanics and microstructure of the resultant composites to understand the toughening and strengthening mechanisms.
- Develop nacre-like ceramic/metal composites through metal pressureless infiltration into as-prepared ceramic scaffolds.
- Investigate the relationship between ceramic fraction, microstructure, and mechanical properties of ceramic/metal composites.
- Investigate coating and its roles during infiltration process of metal alloy into ceramic scaffolds.

1.6 References

[1] R.O. Ritchie, The conflicts between strength and toughness, Nature Materials 10(11) (2011) 817-822.

[2] U.G.K. Wegst, H. Bai, E. Saiz, A.P. Tomsia, R.O. Ritchie, Bioinspired structural materials, Nature Materials 14(1) (2015) 23-36.

[3] C. Ortiz, M.C. Boyce, Bioinspired Structural Materials, 319(5866) (2008) 1053-1054.

[4] A.R. Studart, Towards High-Performance Bioinspired Composites, Advanced Materials 24(37) (2012) 5024-5044.

[5] U.G.K. Wegst, M.F. Ashby, The mechanical efficiency of natural materials, Philosophical Magazine 84(21) (2004) 2167-2186.

[6] F. Barthelat, D. Zhu, A novel biomimetic material duplicating the structure and mechanics of natural nacre, Journal of Materials Research 26(10) (2011) 1203-1215.

[7] K.S. Katti, D.R. Katti, S.M. Pradhan, A. Bhosle, Platelet interlocks are the key to toughness and strength in nacre, Journal of Materials Research 20(5) (2005) 1097-1100.

[8] F. Barthelat, Z. Yin, M.J. Buehler, Structure and mechanics of interfaces in biological materials, Nature Reviews Materials 1(4) (2016) 16007.

[9] H.D. Espinosa, A.L. Juster, F.J. Latourte, O.Y. Loh, D. Gregoire, P.D. Zavattieri, Tablet-level origin of toughening in abalone shells and translation to synthetic composite materials, Nature Communications 2 (2011) 173.

[10] A.P. Jackson, J.F.V. Vincent, R.M. Turner, R.M. Alexander, The mechanical design of nacre, Proceedings of the Royal Society of London. Series B 234(1277) (1988) 415-440.

[11] M. Sarikaya, K.E. Gunnison, M. Yasrebi, I.A. Aksay, Mechanical Property-Microstructural Relationships in Abalone Shell, MRS Proceedings 174 (1989) 109.

[12] J.-y. Sun, J. Tong, Fracture Toughness Properties of Three Different Biomaterials Measured by Nanoindentation, Journal of Bionic Engineering 4(1) (2007) 11-17.

[13] X. Li, Z.-H. Xu, R. Wang, In Situ Observation of Nanograin Rotation and Deformation in Nacre, Nano Letters 6(10) (2006) 2301-2304.

[14] T.E. Schäffer, C. Ionescu-Zanetti, R. Proksch, M. Fritz, D.A. Walters, N. Almqvist, C.M. Zaremba, A.M. Belcher, B.L. Smith, G.D. Stucky, D.E. Morse, P.K. Hansma, Does Abalone Nacre Form by Heteroepitaxial Nucleation or by Growth through Mineral Bridges?, Chemistry of Materials 9(8) (1997) 1731-1740.

[15] A.G. Checa, J.H.E. Cartwright, M.-G. Willinger, Mineral bridges in nacre, Journal of Structural Biology 176(3) (2011) 330-339.

[16] F. Barthelat, C.-M. Li, C. Comi, H.D. Espinosa, Mechanical properties of nacre constituents and their impact on mechanical performance, Journal of Materials Research 21(8) (2006) 1977-1986.

[17] S. Fan, B. Yilong, Mineral bridges of nacre and its effects, Acta Mechanica Sinica 17(3) (2001) 251.

[18] A.Y.-M. Lin, P.-Y. Chen, M.A. Meyers, The growth of nacre in the abalone shell, Acta Biomaterialia 4(1) (2008) 131-138.

[19] B.L. Smith, T.E. Schäffer, M. Viani, J.B. Thompson, N.A. Frederick, J. Kindt, A. Belcher, G.D. Stucky, D.E. Morse, P.K. Hansma, Molecular mechanistic origin of the toughness of natural adhesives, fibres and composites, Nature 399(6738) (1999) 761-763.

[20] Structural and functional biological materials: Abalone nacre, sharp materials, and abalone foot adhesion, A.Y.-M. Lin, (Author). 24 Mar 2008 Student thesis: Doctoral Thesis › Doctor of Philosophy (PhD).

[21] K.S. Katti, D.R. Katti, S.M. Pradhan, A. Bhosle, Platelet interlocks are the key to toughness and strength in nacre, Journal of Materials Research 20(5) (2005) 1097-1100.

[22] U.G.K. Wegst, M.F. Ashby, The structural efficiency of orthotropic stalks, stems and tubes, Journal of Materials Science 42(21) (2007) 9005-9014.

[23] U.G.K. Wegst, Bending efficiency through property gradients in bamboo, palm, and wood-based composites, Journal of the Mechanical Behavior of Biomedical Materials 4(5) (2011) 744-755.

[24] U.G.K. Wegst, Bamboo and Wood in Musical Instruments, Annual Review of Materials Research 38(1) (2008) 323-349.

[25] Y. Yu, W. Yang, B. Wang, M.A. Meyers, Structure and mechanical behavior of human hair, Materials Science and Engineering: C 73 (2017) 152-163.

[26] J. McKittrick, P.-Y. Chen, S.G. Bodde, W. Yang, E.E. Novitskaya, M.A. Meyers, The Structure, Functions, and Mechanical Properties of Keratin, Journal of the Minerals, Metals and Materials Society 64 (2012) 449.

[27] S.N. Patek, R.L. Caldwell, Extreme impact and cavitation forces of a biological hammer: strike forces of the peacock mantis shrimp Odontodactylus scyllarus, Journal of Experimental Biology 208(19) (2005) 3655.

[28] S.N. Patek, W.L. Korff, R.L. Caldwell, Deadly strike mechanism of a mantis shrimp, Nature 428(6985) (2004) 819-820.

[29] J.C. Weaver, G.W. Milliron, A. Miserez, K. Evans-Lutterodt, S. Herrera, I. Gallana, W.J. Mershon, B. Swanson, P. Zavattieri, E. DiMasi, D. Kisailus, The Stomatopod Dactyl Club: A Formidable Damage-Tolerant Biological Hammer, Science 336(6086) (2012) 1275.

[30] K. Hing, Bone repair in the twenty-first century: Biology, chemistry or engineering?, Philosophical transactions. Series A, Mathematical, physical, and engineering sciences 362 (2004) 2821-50.

[31] R.O. Ritchie, Mechanisms of fatigue-crack propagation in ductile and brittle solids, International Journal of Fracture 100(1) (1999) 55-83.

[32] M.E. Launey, R.O. Ritchie, On the Fracture Toughness of Advanced Materials, Advanced Materials 21(20) (2009) 2103-2110.

[33] J. Cook, G.J. E., A mechanism for the control of crack propagation in all-brittle systems, Proceedings of the Royal Society of London. Series A. Mathematical and Physical Sciences 282(1391) (1964) 508-520.

[34] R. Pippan, Fatigue Thresholds for Engineering Applications, in: K.H.J. Buschow, R.W. Cahn, M.C. Flemings, B. Ilschner, E.J. Kramer, S. Mahajan, P. Veyssière (Eds.), Encyclopedia of Materials: Science and Technology, Elsevier, Oxford, 2001, pp. 3001-3005.

[35] V. Naglieri, B. Gludovatz, A.P. Tomsia, R.O. Ritchie, Developing strength and toughness in bio-inspired silicon carbide hybrid materials containing a compliant phase, Acta Materialia 98 (2015) 141-151.

[36] M.E. Launey, E. Munch, D.H. Alsem, H.B. Barth, E. Saiz, A.P. Tomsia, R.O. Ritchie, Designing highly toughened hybrid composites through nature-inspired hierarchical complexity, Acta Materialia 57(10) (2009) 2919-2932.

[37] F. Bouville, E. Maire, S. Deville, Self-Assembly of Faceted Particles Triggered by a Moving Ice Front, Langmuir 30(29) (2014) 8656-8663.

[38] W.J. Clegg, K. Kendall, N.M. Alford, T.W. Button, J.D. Birchall, A simple way to make tough ceramics, Nature 347(6292) (1990) 455-457.

[39] C.-a. Wang, Y. Huang, Q. Zan, H. Guo, S. Cai, Biomimetic structure design — a possible approach to change the brittleness of ceramics in nature, Materials Science and Engineering: C 11(1) (2000) 9-12.

[40] E. Munch, M.E. Launey, D.H. Alsem, E. Saiz, A.P. Tomsia, R.O. Ritchie, Tough, Bio-Inspired Hybrid Materials, Science 322(5907) (2008) 1516-1520.

[41] H. Le Ferrand, F. Bouville, T.P. Niebel, A.R. Studart, Magnetically assisted slip casting of bioinspired heterogeneous composites, Nature Materials 14 (2015) 1172.

[42] H. Zhao, Y. Yue, L. Guo, J. Wu, Y. Zhang, X. Li, S. Mao, X. Han, Cloning Nacre's 3D Interlocking Skeleton in Engineering Composites to Achieve Exceptional Mechanical Properties, Advanced Materials 28(25) (2016) 5099-5105.

[43] M. Grossman, D. Pivovarov, F. Bouville, C. Dransfeld, K. Masania, A.R. Studart, Hierarchical Toughening of Nacre-Like Composites, Advanced Functional Materials 29(9) (2019) 1806800.

[44] S.M.M. Valashani, F. Barthelat, A laser-engraved glass duplicating the structure, mechanics and performance of natural nacre, Bioinspiration & Biomimetics 10(2) (2015) 026005.

[45] A. Wat, J.I. Lee, C.W. Ryu, B. Gludovatz, J. Kim, A.P. Tomsia, T. Ishikawa, J. Schmitz, A. Meyer, M. Alfreider, D. Kiener, E.S. Park, R.O. Ritchie, Bioinspired nacre-like alumina with a bulk-metallic glass-forming alloy as a compliant phase, Nature Communications 10(1) (2019) 961.

[46] R. Libanori, D. Carnelli, N. Rothfuchs, M.R. Binelli, M. Zanini, L. Nicoleau, B. Feichtenschlager, G. Albrecht, A.R. Studart, Composites reinforced via mechanical interlocking of surface-roughened microplatelets within ductile and brittle matrices, Bioinspiration & Biomimetics 11(3) (2016) 036004.

[47] M. Grossman, F. Bouville, F. Erni, K. Masania, R. Libanori, A.R. Studart, Mineral Nano-Interconnectivity Stiffens and Toughens Nacre-like Composite Materials, 29(8) (2017) 1605039.

[48] M. Grossman, F. Bouville, K. Masania, A.R. Studart, Quantifying the role of mineral bridges on the fracture resistance of nacre-like composites, Proceedings of the National Academy of Sciences 115(50) (2018) 12698-12703.

[49] G.X. Gu, F. Libonati, S.D. Wettermark, M.J. Buehler, Printing nature: Unraveling the role of nacre's mineral bridges, Journal of the Mechanical Behavior of Biomedical Materials 76 (2017) 135-144.

[50] A. Sellinger, P.M. Weiss, A. Nguyen, Y. Lu, R.A. Assink, W. Gong, C.J. Brinker, Continuous self-assembly of organic–inorganic nanocomposite coatings that mimic nacre, Nature 394(6690) (1998) 256-260.

[51] J. Peng, Q. Cheng, High-Performance Nanocomposites Inspired by Nature, Advanced Materials 29(45) (2017) 1702959.

[52] H.D. Espinosa, J.E. Rim, F. Barthelat, M.J. Buehler, Merger of structure and material in nacre and bone – Perspectives on de novo biomimetic materials, Progress in Materials Science 54(8) (2009) 1059-1100.

[53] Y. Oaki, A. Kotachi, T. Miura, H. Imai, Bridged Nanocrystals in Biominerals and Their Biomimetics: Classical Yet Modern Crystal Growth on the Nanoscale, Advanced Functional Materials 16(12) (2006) 1633-1639.

[54] L.-B. Mao, H.-L. Gao, H.-B. Yao, L. Liu, H. Cölfen, G. Liu, S.-M. Chen, S.-K. Li, Y.-X. Yan, Y.-Y. Liu, S.-H. Yu, Synthetic nacre by predesigned matrix-directed mineralization, Science 354(6308) (2016) 107.

[55] O. Oner Ekiz, A.F. Dericioglu, H. Kakisawa, An efficient hybrid conventional method to fabricate nacre-like bulk nano-laminar composites, Materials Science and Engineering: C 29(6) (2009) 2050-2054.

[56] S. Behr, U. Vainio, M. Müller, A. Schreyer, G.A. Schneider, Large-scale parallel alignment of platelet-shaped particles through gravitational sedimentation, Scientific Reports 5 (2015) 9984.

[57] Z. Tang, N.A. Kotov, S. Magonov, B. Ozturk, Nanostructured artificial nacre, Nature Materials 2(6) (2003) 413-418.

[58] L.J. Bonderer, A.R. Studart, L.J. Gauckler, Bioinspired Design and Assembly of Platelet Reinforced Polymer Films, Science 319(5866) (2008) 1069.

[59] P. Podsiadlo, A.K. Kaushik, E.M. Arruda, A.M. Waas, B.S. Shim, J. Xu, H. Nandivada, B.G. Pumplin, J. Lahann, A. Ramamoorthy, N.A. Kotov, Ultrastrong and Stiff Layered Polymer Nanocomposites, Science 318(5847) (2007) 80.

[60] S. Deville, S. Meille, J. Seuba, A meta-analysis of the mechanical properties of ice-templated ceramics and metals, Science and Technology of Advanced Materials 16(4) (2015) 043501.

[61] A. Lottermoser, Über das Ausfrieren von Hydrosolen, Berichte der deutschen chemischen Gesellschaft European Journal of Inorganic Chemistry 41(3) (1908) 3976-3979.

[62] K.L. Scotti, D.C. Dunand, Freeze casting – A review of processing, microstructure and properties via the open data repository, FreezeCasting.net, Progress in Materials Science 94 (2018) 243-305.

[63] I. Nelson, S.E. Naleway, Intrinsic and extrinsic control of freeze casting, Journal of Materials Research and Technology 8(2) (2019) 2372-2385.

[64] S. Al-Jawoosh, A. Ireland, B. Su, Fabrication and characterisation of a novel biomimetic anisotropic ceramic/polymer-infiltrated composite material, Dental Materials 34(7) (2018) 994-1002.

[65] A. Shaga, P. Shen, C. Sun, Q. Jiang, Lamellar-interpenetrated Al–Si–Mg/SiC composites fabricated by freeze casting and pressureless infiltration, Materials Science and Engineering: A 630 (2015) 78-84.

[66] F. Bouville, E. Maire, S. Meille, B. Van de Moortèle, A.J. Stevenson, S. Deville, Strong, tough and stiff bioinspired ceramics from brittle constituents, Nature Materials 13(5) (2014) 508-514.

[67] Z. Yin, F. Hannard, F. Barthelat, Impact-resistant nacre-like transparent materials, Science 364(6447) (2019) 1260.

[68] S. Deville, Ice-templating, freeze casting: Beyond materials processing, Journal of Materials Research 28(17) (2013) 2202-2219.

[69] Y. Zhang, K. Zhou, Y. Bao, D. Zhang, Effects of rheological properties on ice-templated porous hydroxyapatite ceramics, Materials Science and Engineering: C 33(1) (2013) 340-346.

[70] M.M. Porter, R. Imperio, M. Wen, M.A. Meyers, J. McKittrick, Bioinspired scaffolds with varying pore architectures and mechanical properties, Advanced Functional Materials 24(14) (2014) 1978-1987.

[71] K.H. Zuo, Y.-P. Zeng, D. Jiang, Effect of polyvinyl alcohol additive on the pore structure and morphology of the freeze-cast hydroxyapatite ceramics, Materials Science and Engineering: C 30(2) (2010) 283-287.

[72] Y. Zhang, L. Hu, J. Han, Z. Jiang, Freeze casting of aqueous alumina slurries with glycerol for porous ceramics, Ceramics International 36(2) (2010) 617-621.

[73] E. Munch, E. Saiz, A.P. Tomsia, S. Deville, Architectural Control of Freeze-Cast Ceramics Through Additives and Templating, Journal of the American Ceramic Society 92(7) (2009) 1534-1539.

[74] D. Clearfield, M. Wei, Investigation of structural collapse in unidirectionally freeze cast collagen scaffolds, Journal of Materials Science: Materials in Medicine 27(1) (2016) 15.

[75] S.E. Naleway, C.F. Yu, R.L. Hsiong, A. Sengupta, P.M. Iovine, J.A. Hildebrand, M.A. Meyers, J. McKittrick, Bioinspired intrinsic control of freeze cast composites: Harnessing hydrophobic hydration and clathrate hydrates, Acta Materialia 114 (2016) 67-79.

[76] S.E. Naleway, C.F. Yu, M.M. Porter, A. Sengupta, P.M. Iovine, M.A. Meyers, J. McKittrick, Bioinspired composites from freeze casting with clathrate hydrates, Materials & Design 71 (2015) 62-67.

[77] R. Peltier, C.W. Evans, A.L. DeVries, M.A. Brimble, A.J. Dingley, D.E. Williams, Growth Habit Modification of Ice Crystals Using Antifreeze Glycoprotein (AFGP) Analogues, Crystal Growth & Design 10(12) (2010) 5066-5077.

[78] S. Deville, C. Viazzi, C. Guizard, Ice-Structuring Mechanism for Zirconium Acetate, Langmuir 28(42) (2012) 14892-14898.

[79] T. Waschkies, R. Oberacker, M.J. Hoffmann, Control of Lamellae Spacing During Freeze Casting of Ceramics Using Double-Side Cooling as a Novel Processing Route, Journal of the American Ceramic Society 92(s1) (2009) S79-S84.

[80] V. Naglieri, H.A. Bale, B. Gludovatz, A.P. Tomsia, R.O. Ritchie, On the development of ice-templated silicon carbide scaffolds for nature-inspired structural materials, Acta Materialia 61(18) (2013) 6948-6957.

[81] Y. Chino, D.C. Dunand, Directionally freeze-cast titanium foam with aligned, elongated pores, Acta Materialia 56(1) (2008) 105-113.

[82] S. Deville, E. Saiz, A.P. Tomsia, Ice-templated porous alumina structures, Acta Materialia 55(6) (2007) 1965-1974.

[83] S.M. Miller, X. Xiao, K.T. Faber, Freeze-cast alumina pore networks: Effects of freezing conditions and dispersion medium, Journal of the European Ceramic Society 35(13) (2015) 3595-3605.

[84] P. Niksiar, Y.F. Su, B.M. Frank, A.T. Ogden, E.S. Naleway, A.M. Meyers, J. McKittrick, M.M. Porter, External Field Assisted Freeze Casting, Ceramics 2(1) (2019).

[85] H. Bai, Y. Chen, B. Delattre, A.P. Tomsia, R.O. Ritchie, Bioinspired large-scale aligned porous materials assembled with dual temperature gradients, Science Advances 1(11) (2015).

[86] S.-L. Geng, P. Shen, Z.-J. Hu, R.-F. Guo, Q.-C. Jiang, Formation mechanism and control of a large-scale lamellar structure in freeze-cast Al2O3 ceramics under dual temperature gradients, Journal of the European Ceramic Society 38(6) (2018) 2605-2611.

[87] S. Algharaibeh, A.J. Ireland, B. Su, Bi-directional freeze casting of porous alumina ceramics: A study of the effects of different processing parameters on microstructure, Journal of the European Ceramic Society 39(2) (2019) 514-521.

[88] Z.-J. Hu, X.-T. Shen, S.-L. Geng, P. Shen, Q.-C. Jiang, 3D long-range ordered porous ceramics prepared by a novel bidirectional freeze-casting technique, Ceramics International 44(5) (2018) 5803-5806.

[89] Y. Tang, S. Qiu, Q. Miao, C. Wu, Fabrication of lamellar porous alumina with axisymmetric structure by directional solidification with applied electric and magnetic fields, Journal of the European Ceramic Society 36(5) (2016) 1233-1240.

[90] Y. Tang, Q. Miao, S. Qiu, K. Zhao, L. Hu, Novel freeze-casting fabrication of aligned lamellar porous alumina with a centrosymmetric structure, Journal of the European Ceramic Society 34(15) (2014) 4077-4082.

[91] F.Y. Su, J.R. Mok, J. McKittrick, Radial-Concentric Freeze Casting Inspired by Porcupine Fish Spines, Ceramics 2(1) (2019) 161-179.

[92] M.-A. Shahbazi, M. Ghalkhani, H. Maleki, Directional Freeze-Casting: A Bioinspired Method to Assemble Multifunctional Aligned Porous Structures for Advanced Applications, Advanced Engineering Materials (2020) 2000033.

[93] F. Bouville, E. Portuguez, Y. Chang, G.L. Messing, A.J. Stevenson, E. Maire, L. Courtois, S. Deville, Templated Grain Growth in Macroporous Materials, Journal of the American Ceramic Society 97(6) (2014) 1736-1742.

[94] W. Sun, Z. Chen, S.-y. Huang, Effect of an external electric field on liquid water using molecular dynamics simulation with a flexible potential, Journal of Shanghai University (English Edition) 10(3) (2006) 268-273.

[95] M.B. Frank, S.E. Naleway, T. Haroush, C.-H. Liu, S.H. Siu, J. Ng, I. Torres, A. Ismail, K. Karandikar, M.M. Porter, O.A. Graeve, J. McKittrick, Stiff, porous scaffolds from magnetized alumina particles aligned by magnetic freeze casting, Materials Science and Engineering: C 77 (2017) 484-492.

[96] T.A. Ogden, M. Prisbrey, I. Nelson, B. Raeymaekers, S.E. Naleway, Ultrasound freeze casting: Fabricating bioinspired porous scaffolds through combining freeze casting and ultrasound directed self-assembly, Materials & Design 164 (2019) 107561.

[97] M. Prisbrey, J. Greenhall, F. Guevara Vasquez, B. Raeymaekers, Ultrasound directed self-assembly of three-dimensional user-specified patterns of particles in a fluid medium, Journal of Applied Physics 121 (2017) 014302.

[98] K. Carpenter, V. Bahadur, Influence of Electric Fields and Surface Chemistry on Ice Nucleation Kinetics, 2015.

[99] H. Bai, F. Walsh, B. Gludovatz, B. Delattre, C. Huang, Y. Chen, A.P. Tomsia, R.O. Ritchie, Bioinspired Hydroxyapatite/Poly(methyl methacrylate) Composite with a Nacre-Mimetic Architecture by a Bidirectional Freezing Method, Advanced Materials 28(1) (2016) 50-56.

[100] J. Han, G. Du, W. Gao, H. Bai, An Anisotropically High Thermal Conductive Boron Nitride/Epoxy Composite Based on Nacre-Mimetic 3D Network, Advanced Functional Materials 29(13) (2019) 1900412.

[101] N. Zhao, M. Yang, Q. Zhao, W. Gao, T. Xie, H. Bai, Superstretchable Nacre-Mimetic Graphene/Poly(vinyl alcohol) Composite Film Based on Interfacial Architectural Engineering, ACS Nano 11(5) (2017) 4777-4784.

[102] C. Huang, J. Peng, Y. Cheng, Q. Zhao, A. Tomsia, Y. Du, S. Dou, D. Wagner, L. Jiang, Q. Cheng, Ultratough Nacre-inspired Epoxy-Graphene Composites with Shape Memory Property, Journal of Materials Chemistry A 7 (2019).

[103] G. Tan, J. Zhang, L. Zheng, D. Jiao, Z. Liu, Z. Zhang, R.O. Ritchie, Nature-Inspired Nacre-Like Composites Combining Human Tooth-Matching Elasticity and Hardness with Exceptional Damage Tolerance, Advanced Materials 31(52) (2019) 1904603.

[104] G. Du, A. Mao, J. Yu, J. Hou, N. Zhao, J. Han, Q. Zhao, W. Gao, T. Xie, H. Bai, Nacre-mimetic composite with intrinsic self-healing and shape-programming capability, Nature Communications 10(1) (2019) 800.

Chapter 2

Materials and experimental techniques

2.1 Raw materials

2.1.1 Slurries preparation

Alumina powder (CT3000SG, Almatis GmbH, Germany), 3% yttria-stabilized zirconia powder (OZ-3Y, Orient Zirconic Ind, China), hydroxyapatite (HA, Captal S, Plasma biotal, UK), Dolapix CE64 (ZSCHIMMER&SCHWARZ Germany), Darvan 821A (R. T. Vanderbilt Co., Norwalk, US), magnesium oxide (MG-OX-04-P, American element, US), polyvinyl alcohol (PVA powder, MW: 30,000-70,000, Sigma Aldrich), octanol-1 (Fisher Scientific, US).

2.1.2 Composite fabrication

Duplication silicone (Elite double 32, Zhermack, UK), paraffin wax (Henry Schein, 900-1514, US), hydrogen peroxide (35 wt.% solution in water, stabilized, Sigma Aldrich), sulfuric acid (97.5+%, A.R. Grade, Sigma Aldrich), γ-methacryloxypropyl trimethoxy silane (γ-MPS, Sigma Aldrich), toluene (99.85%, extra dry, AcroSeal, UK), 3-Aminopropyl triethoxysilane (APS, Sigma Aldrich), methyl methacrylate (MMA, Sigma Aldrich), azobisisobutyronitrile (AIBN, Sigma Aldrich), polyurethane (Xencast P6 toughened polyurethane, Easycomposite, UK), triethylene glycol dimethacrylate (TEGDMA, Sigma Aldrich), urethane dimethacrylate (UDMA, Sigma Aldrich), epoxy resin (Specifix, Struers, UK), Silica suspension (LUDOX AS-40, Sigma Aldrich), Aluminium alloy (5083, Shropshire stainless and aluminium, UK) and Magnesium alloy (AZ31, Goodfellow, UK).

2.2 Fabrication process of ceramics and composites

2.2.1 Ceramic slurries preparation

Ceramic slurries for freeze-casting were prepared by dispersing submicrometric ceramic powders into deionized water (DI water). The mixture of ceramic powder/dispersant/DI water was transferred into polyethylene (PE) bottle with zirconia milling balls (two sizes of zirconia milling ball (diameter:10 mm and 5 mm) in the ratio of 1:1 by weight) and then processed 24-hour ball milling (1600-VS-A, Pascall engineering, UK) at ambient temperature and high speed (˜200 rpm) to break down the coarse powder or aggregates into fine particles. To strengthen the ceramic scaffolds after demoulding, organic binder polyvinyl alcohol (PVA) in the form of 10 vol. % solution was added before the ball milling process.

After ball milling, the slurries were de-gassed under the vacuum following the addition of 0.1 ml of octanol (de-bubbling agent by increasing surface tension of slurries) for 10 min to remove air bubbles generated during high-speed ball-milling. The ceramic slurries were then further treated in an ultrasonic water bath (XUB5, Grant, UK) at ambient temperature and 38 kHz/150 W ultrasonic power for 30 min until homogeneous mixing of ceramic particles and water.

Organic binder, PVA is dissolved in DI water to synthesize aqueous solution before being added into ceramic slurries. Here, 10 vol.% PVA solution was prepared. Firstly, 59.5 g (50 ml) of PAV powder (density:1.19 g/cm^3) was mixed with 450 ml cold DI water in a glass flask. The mixture is then placed on a multifunctional hot plate (Isotemp, Fisher Scientific, US) and magnetically stirred without heating-up, as the PVA/water mixture becomes sticky and tends to form lumps at elevated temperature. After 12-hour stirring, the PVA/water mixture becomes a clear and viscous solution which is then heated to 90 ℃ to increase dissolving rate of PVA. When the PVA solution was completely dissolved at 90 ℃ for 2 h, it was then cooled down

and stored in a refrigerator at 4 ℃ to inhibit bacteria growth. The PVA solution has to be consumed with 8 weeks.

2.2.2 Ceramic dry pressing

Ceramic discs were prepared by dry pressing method for comparison with composites. As the most economic and fast process for ceramic production, dry pressing is formed by ceramic powder compaction at uniaxial presses.

Ceramic powder, ethanol, and 10 vol.% PVA solution were mixed in 40:3:3 ratio by weight. After violently stirring by a glass rod, the mixture was transferred into a steel pressing die and pressed at 150 MPa for 5 min. A ceramic disc green body was obtained after demoulding from the die. The green bodies were then sintered as described in 2.2.4.

2.2.3 Freeze casting

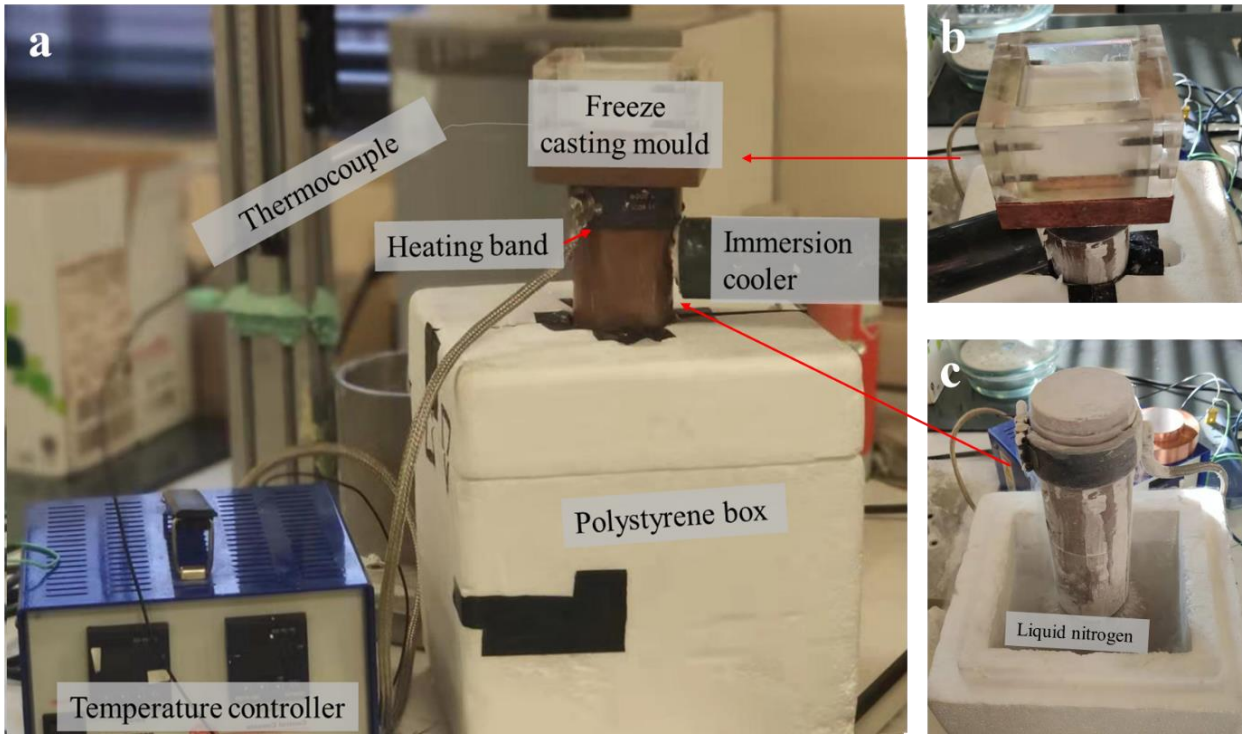

Fig.2-1 *Set-up for the freeze casting process* ***a)****, PMMA mould* ***b)*** *and cooling stage with heating band immersed in liquid nitrogen* ***c)****.*

The main purpose of freeze casting apparatus (**Fig.2-1**) is to provide a temperature field that controls the freezing of slurries. When as-prepared ceramic slurry (in 2.1.1) is poured into a custom-made freeze casting mould (**Fig.2-1b**), it is then transferred on the top of a pre-cooled cooling stage (**Fig.2-1c**), and the freezing of the ceramic slurry initiates.

Fig.2-2 and **Fig.2-3** showed schematically configurations of freeze casting apparatus for the control of temperature field and cooling stage, respectively. In this project, freeze casting moulds were made of a copper bottom block surrounded with an insulating polymer wall. A detachable, 20 mm thick polymethyl methacrylate (PMMA) material was used to produce a square mould to insulate ceramic slurries from the surrounding environment. The dimension of inner square of mould is 60 mm x 60 mm x 20 mm. Since top of the mould was opening to air, the top temperature of the slurries was equivalent to ambient temperature (ca. 25 ℃). On the bottom side of the mould, the copper block was the key to provide the cooling field within the slurries for the control of ice crystals' nucleation and growth during freezing. To produce the ceramic scaffolds with controlled architectures, two types of mould constructions were commissioned to render uni-directional (**Fig.2-2a**) and bi-directional (**Fig.2-2b**) freeze casting.

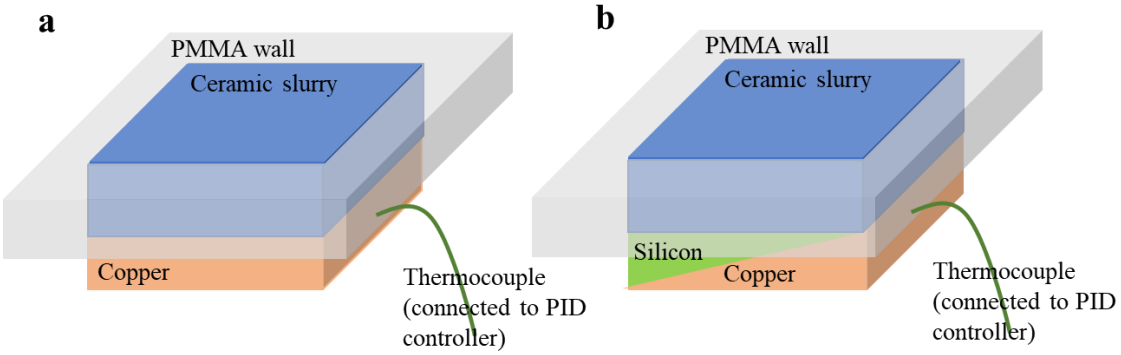

*Fig.2-2 Schematics for uni-directional **a)** and bi-directional **b)** freeze casting mould.*

For the uni-directional freeze casting, the bottom of the mould was a flat copper block (**Fig.2-2a**), thus the direction of temperature gradient was perpendicular to the bottom surface during

freezing. By contract, the bottom of the mould for bi-directional freeze casting was made of a copper wedge covered by equivalent duplication silicone (**Fig.2-2b**). A base silicone (Elite double 32) was weighted and mixed by 1:1 (base : catalyst) weight ratio and stirred by a blending machine (RZR, Heidoph, UK) for 30 s to mix the two parts completely. The mixture was then poured down onto the wedge and cured for 20 min at ambient temperature. When the freezing initiated, apart from the bottom-top direction, the temperature gradient also formed along the horizontal direction along the wedge slope due to gradual thickness of the thermal insulating silicone. Therefore, the slurry started to freeze from the top line of copper wedge and ended at the other side of the mould. In the previous work published by our group [1], it was found that the copper wedge with an angle of 10° produced highly aligned lamellar ceramic scaffolds, therefore the wedge slope angle of 10° was chosen for the bi-directional freeze casting of ceramics in this work.

When the mould was transferred on the top of pre-cooled cooling stage (**Fig.2-1c**), the freeze process began. As shown in **Fig.2-3**, the cooling stage was made of a heating band (MI, Watlow, US), an immersion cooler (polyscience, US) and liquid nitrogen. The proportional–integral–derivative (PID) temperature controller (TCP-200, Tempco, US) was used to control and monitor the real-time temperature of the copper base through a thermocouple (Type J, Watlow, US) inserted in the freeze casting moulds (**Fig.2-2a** and **b**). Within the closed loop of the heating band, thermocouple and PID controller, the cooling stage was able to regulate the cooling rate of the copper base of the moulds from 1 to 40 °C/min by the feedback mechanism.

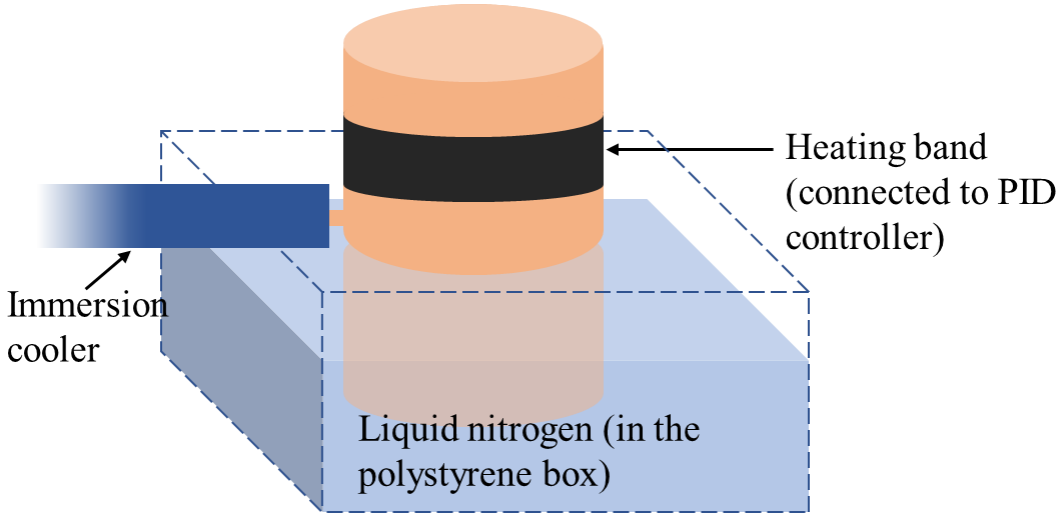

Fig.2-3 *Schematic of the cooling stage used to control the cooling rate during freeze casting.*

When the slurry was completely frozen, the ice formed in the frozen samples was sublimated in a freeze dryer (Edwards, Modulyo freeze dryer, UK) at -60 ºC for at least 24 hours under a vacuum pressure of 0.03 mbar. Freeze-dried samples were de-moulded from the PMMA square mould. Finally, ceramic scaffolds were obtained with a dimension of PMMA mould (60 mm x 60 mm x 20 mm).

2.2.4 Densification and sintering

To control the ceramic fraction in the final composite materials, highly aligned lamellar ceramic scaffolds obtained from bi-directional freeze casting were densified by a simple axial pressing. Before the densification process, the ceramic scaffolds were infiltrated with a paraffin wax (Henry Schein, 900-1514, US) at 80 ℃. The wax-filled ceramic scaffolds were cut to blocks with a cross-sectional dimension of 23 mm x 36 mm to fit in pressing mould shown in **Fig.2-4**.

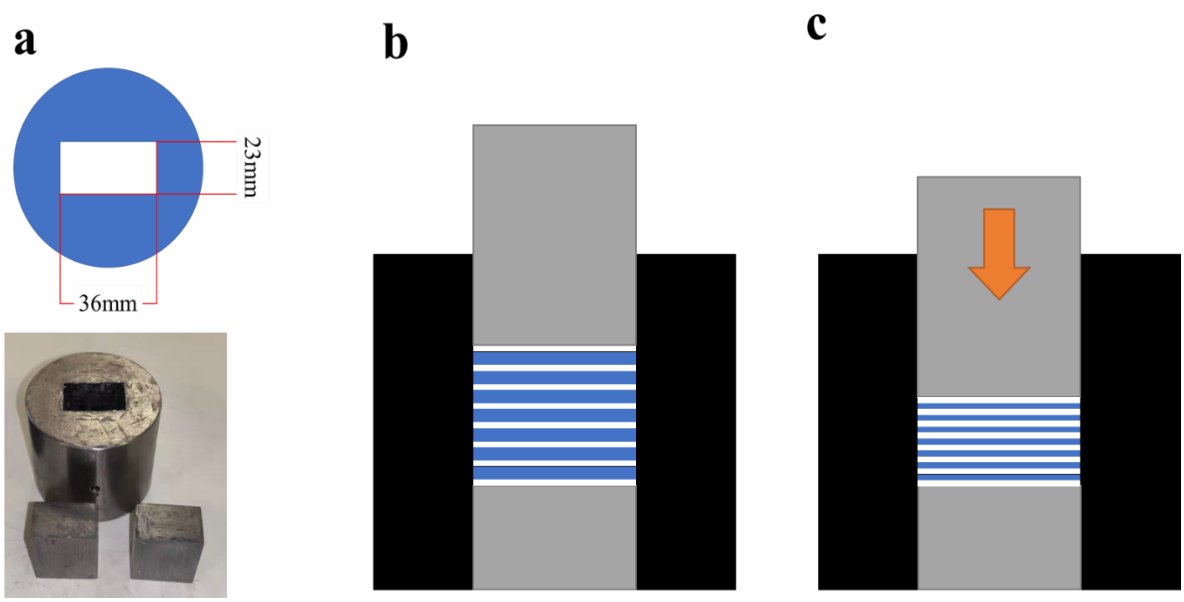

*Fig.2-4 The pressing mould made of steel with high carbon content with a cross-sectional dimension of 23 mm×36 mm **a)**. The schematic shows the ceramic scaffolds before **b)** and after **c)** densification.*

The pressing mould was firstly heated up to 90 ℃ for 30 min to ensure that the wax in ceramic scaffolds was melted. Densification was carried out by uniaxial pressing through the control of pressure using a hydraulic press (PerkinElmer, USA) (**Fig.2-5a**) or the compression distance using a mechanical testing machine (Zwick/Roell, Z020, Germany) (**Fig.2-5b**)

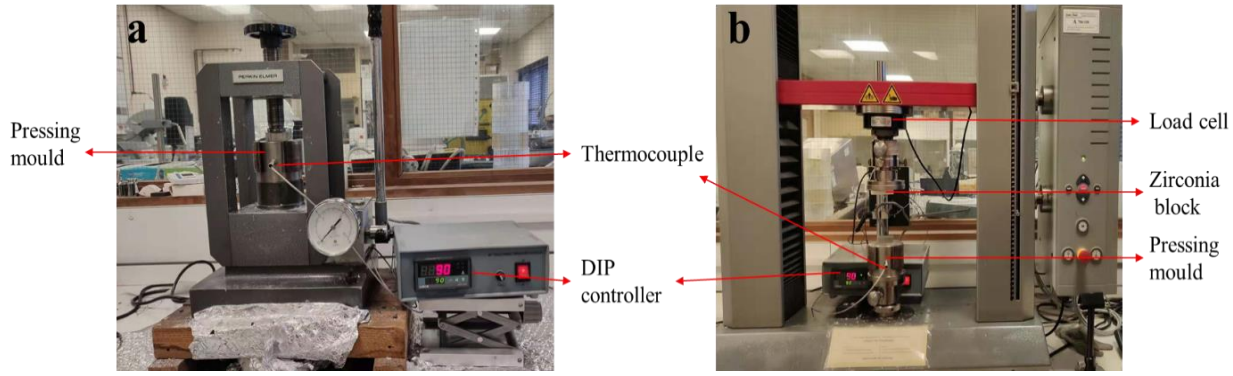

*Fig.2-5 Set-up for ceramic scaffold densification by uniaxial pressing at 90 ºC for 30 min: hydraulic press **a)** and mechanical testing machine **b)**.*

Finally, pressureless sintering of densified ceramic scaffolds with pre-designed compaction densities was carried out in a high temperature chamber furnace (Elite Thermal, UK). The samples were placed inside a cylindrical porous alumina crucible of 70 mm in diameter and 15 mm in height. The sintering process was comprised of two cycles: binder-burning process and ceramic sintering process. In the binder-burning process, temperature raised to 600 ℃ with a heating rate of 2 ℃/min avoid the bloating of wax and polymer binder in ceramic scaffolds. The temperature was held for 2 hours to ensure the complete removal of organic compounds. Afterwards, ceramic were sintered at a higher temperatures (from 1350 to 1550 ℃ for 2 hours) at a heating rate of 10 ℃/min. The sintering temperature for high-temperature process was determined by the type of ceramics: alumina (1550 ℃), zirconia (1550 ℃), and HA (1350 ℃)

2.2.5 Infiltration of compliant phase

The nacre-like composite materials were prepared by infiltration of the compliant phase into open pores in ceramic scaffolds. In this work, both polymers and metal were employed to make different composites. The fabrication processing details of ceramic/polymer and ceramic/metal composites will be described in Chapter 4 and Chapter 5, respectively.

Briefly, short chain polymers (oligomers or monomers) were infiltrated into the ceramic scaffolds first and then cured by *in situ* polymerization to create nacre-like ceramic/polymer composite materials. For nacre-like ceramic/metal composite materials, molten metals were pressureless infiltrated into ceramic scaffolds by capillary force and then solidified at room temperature.

2.2.6 Surface treatment of ceramic scaffolds

For nacre-like ceramic/polymer or ceramic/metal composites, to alter the adhesion between ceramic and the compliant phase, surface treatment on the ceramic scaffolds was essential before the infiltration process. For instance, organic silane coupling agent was grafted on the

ceramic surface prior to polymerization resulted in the formation of covalent bonds between ceramic and polymer. For ceramic/metal system, ceramic scaffolds were coated a new layer such as silica minimise the interfacial reactions and promote the wettability between ceramic and molten metal phase.

The grafting of organic silane on the ceramic surface was achieved via a simple immersion silanization process. As schematically shown in **Fig.2-7**, when ceramic scaffolds were immersed in a solution of silane coupling agent at ambient temperature, the silane molecule chemically bonded to the ceramic molecule. Subsequently, oligomers/monomers were infiltrated into ceramic scaffolds. In the polymerization process, covalent bonds were formed between the organic compounds where oligomers/monomers were not only polymerised into long-chain molecules but also reacted with silane coupling agent on the ceramic surface. Consequently, grafted ceramic scaffolds were connected with polymer via covalent bonds.

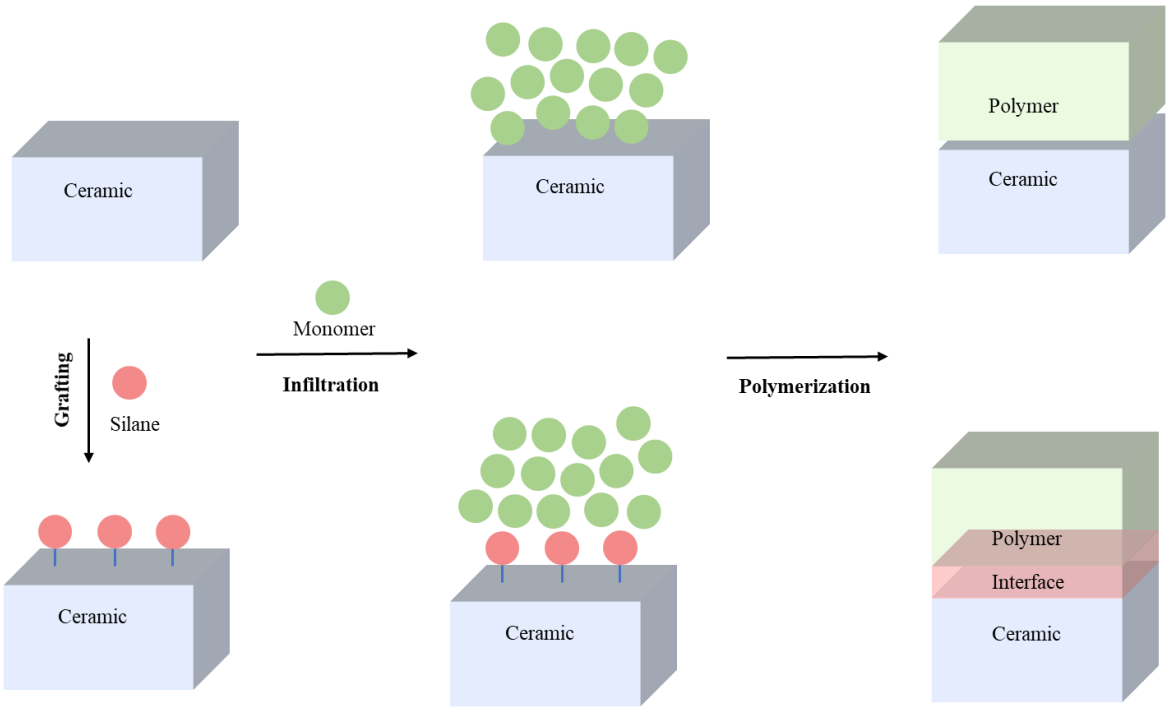

Fig.2-6 Schematic of silane coupling agent grafting, oligomer/monomer infiltration and polymerization process.

For facilitating metal infiltration and minimising the interactions of ceramic/metal composites, a colloidal silica (Ludox AS-30, Grace, UK) was used to form a silica coating on the ceramic surface [2]. Ludox AS-30 was a widely used commercial silica colloidal solution (stabilized by ammonia) containing 30 vol.% silica nanoparticles. Firstly, the Ludox AS-30 was infiltrated into ceramic scaffolds to introduce silica nanoparticles into scaffolds. Then the ceramic scaffolds were dried and calcined at high temperature. On drying, the colloidal silica nanoparticles were fused together at elevated temperature through silanol-silanol and silanol-metal oxide reactions. Consequently, colloidal silica particles were attached to the ceramic surface and formed a thin layer (**Fig.2-7**).

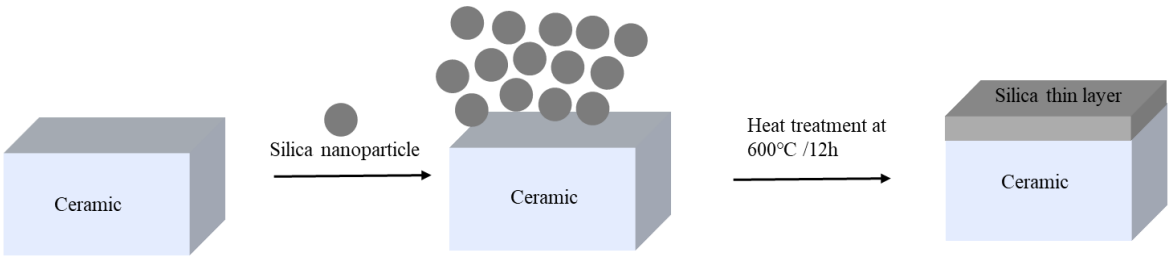

Fig.2-7 *Schematic of silica nanoparticle coating mechanism.*

The pressureless infiltration of metals was carried out in a tube furnace (Elite Thermal, TSH15/100/750-2416CG, UK) as shown in **Fig.2-8a**. Unlike the chamber furnace for ceramic sintering, the tube furnace operated in an oxygen-free atmosphere (N_2 or Ar) at high temperature to prevent oxidation reaction of metal. As shown in **Fig.2-8b**, a metal ingot was placed on the top of sintered ceramic scaffolds in a crucible. An extra crucible containing the same metal foil or powder was placed as an external getter to consume the extra oxygen before infiltration [3]. Next, the tube furnace was heated to the infiltration temperature (over the melting temperature of metals) for 20-180 min to complete the infiltration. Afterwards, the protective gas flowing was maintained until the temperature was cooled down to 150 ℃.

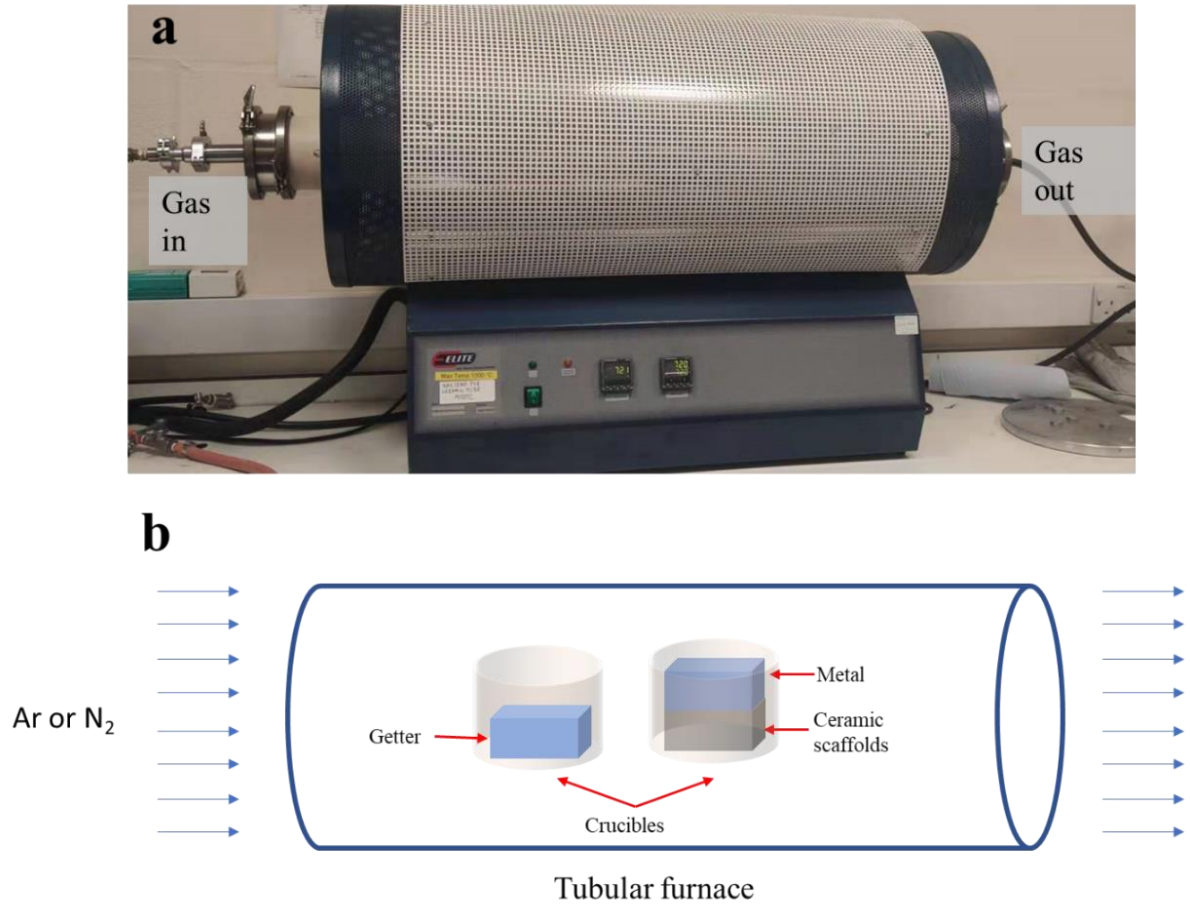

*Fig.2-8 Tubular furnace for pressureless infiltration of metal **a)** and schematic of pressureless infiltration of metal **b)**.*

2.2.7 Cutting and polishing

2.2.7.1 Cutting and CNC machining

Cutting and notching were performed using a water-cooled high-speed precise cutting machine (Accutum-50, Struers, Germany). Drilling was carried out using a 3D computer numeric-controlled (CNC) milling machine (Modela pro MDX-600, Roland, Japan).

For the cutting procedure, different saw blades and programs were used for different materials (**Table.2-1)**. All the diamond-coated blades were dressed by a dressing block at 1000 rpm and 0.7 mm/min prior to cutting.

Materials	Purposes	Blades	Spin speed (rpm)	Feeding speed (mm/min)
Ceramic	Cutting	Diamond wafering blade 15LC,(152 x 0.4 mm) Buehler US	2700	0.005-0.02
Metal	Cutting	Silicon carbide cut-off wheel 10S15, Struers Germany	2700	0.005-0.02
Ceramic-based composite	Cutting	Diamond wafering blade 15LC,(152 x 0.4 mm) Buehler US	2700	0.005-0.02
Polymer	Cutting	Toothed saw blades SAW13, Struers Germany	1200	0.2
Ceramic-based composite	Notching	Diamond wafering blade 15LC, (127 x 0.4 mm) Buehler US	2700	0.005

Table 2-1 *Saw blades used in different materials and cutting procedures.*

CNC milling machine was used to drill holes (diameter: 4 mm) on the composite samples to produce compact tension specimens for fracture toughness. Before cutting, the specimen was clamped on the T-slot table and a silicon carbide-coated bur (2071-4E, Industrial tooling, UK) was fixed in the high-speed spindle. Using a specific software (Modela 4), the cutting program was exported to CNC machine to drill holes at a spin speed of 4000 rpm and a feeding speed of 1 mm/min.

2.2.7.2 Polishing

After cutting, all samples were polished to achieve smooth surface (< 1 μm). This step can minimise the stress concentration in mechanical testing. In this work, a polishing machine (Tegra Pol 15, Struers, Denmark) was employed to drive resin bonded silicon carbide sandpapers (#80 to #2000) to grind sample surface or remove extra materials at a high spin speed (200 rpm). Afterwards, samples were further polished using a maintenance-free disc (MD-Largo, Struers, Denmark) with the aid of 3-μm diamond suspension and then finished by soft cloth disc (MD-Nap, Struers, Denmark) immersed in 1-um diamond suspension at low

spin speed (100 rpm). Finally, well-polished samples were cleaned in an ultrasonic bath (XUB5, Grant, UK).

2.3 Physical and chemical characterization

2.3.1 Rheometry

Rheometry generally refers to an experimental technique used to define the rheological properties of fluid or soft material, e.g. a solution, slurry, and gel. It determines the relationships between strain and stress during flow. Rheology is the science that studies the viscosity or the viscoelastic response of fluid under different stress or external stimuli that could be oscillatory, steady, squeeze or pull. Rheology is perhaps the most frequently used technique to determine the dispersion properties of concentrated ceramic powder suspension. Hence, the rheological measurement technique can be conveniently employed to determine the optimum type and concentration of the dispersant for each slurry system [4]. Freeze casting of ceramic slurries with high viscosity produced scaffolds with poor quality lamellar structure and even delamination in freeze casting direction [5]. According to fluid mechanics, the suspension with fewer aggregates or interactions exhibited lower viscosity. To optimise the freeze-casting ceramic slurries, the viscosities of slurries with various amounts of dispersant were measured using a rheometer (Kinexus pro Rheometer, UK) at 25 ºC and a shear rate from 1 to 1000 s^{-1} with a cone-plate geometry (diameter 40 mm). A 20 vol.% solid loading without addition of PVA was used.

2.3.2 Linear shrinkage

To study the effect of sintering temperature on the level of sintering, linear shrinkage at one the direction was used since the density of ceramics increased gradually during the high temperature sintering process [6]. The linear shrinkage is expressed as following (2.1):

$$Linear\ shrinkage\ ratio = (L_b - L_a)/L_b \times 100\% \quad (2.1)$$

where L_b and L_a are the length of ceramic scaffolds before and after sintering process, respectively.

The length of scaffold was measured from the direction perpendicular to the lamellar direction using a digital calliper (Absolute Digimatic, Mitutoyo, UK).

2.3.3 Porosity and ceramic fraction

The Archimedes' method was used to evaluate the porosity and ceramic fraction of the sintered ceramic scaffolds according to ASTM C373 [7]. The mass of the scaffolds was taken in three different states: dry mass (m_{dry}), mass in water (m_{water}) and wet mass (m_{wet}), which were evaluated as shown in **Fig.2-9.**

The m_{dry} was taken after drying in an oven at 120 °C for 2 hours. To measure the m_{water} and m_{wet}, the ceramic scaffolds were boiled in DI water for 4 hours to ensure all open porous were infiltrated by water. When it cooled down, scaffolds immersed in water were weighted and the results were named as m_{water}. Afterwards, ceramic scaffolds were taken out of the water and wiped by a damp chamois cloth to remove water outside the scaffolds. Following this, scaffolds were weighted immediately, and the resulting value was m_{wet}.

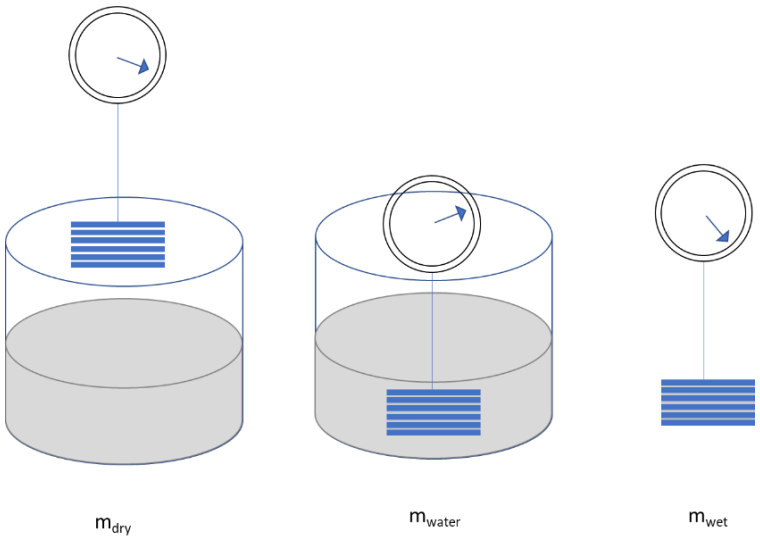

Fig.2-9 *Schematic of measurements of dry mass (m_{dry}), mass in water (m_{water}) and wet mass (m_{wet}).*

Once all the three measurements were taken, the following formulae were used to calculate the density (2.2), closed porosity (2.3), open porosity (2.4), and the ceramic fraction (2.5):

$$Density = \frac{m_{dry}}{m_{dry} - m_{water}} * density\ of\ water \tag{2.2}$$

$$Closed\ porosity = \left(1 - \frac{density}{density\ of\ 100\%\ solid}\right) * 100\% \tag{2.3}$$

$$Open\ porosity = \frac{m_{wet} - m_{dry}}{m_{wet} - m_{water}} * 100\% \tag{2.4}$$

$$Ceramic\ fraction = 1 - open\ porosity - closed\ porosity \tag{2.5}$$

All the specimens were weighted using an electronic analytical balance (Ac 120S, Sartorius analytic, Germany). All the values represented at least an average of three measurements per configuration.

2.3.4 Fourier-transform infrared spectroscopy (FT-IR)

Fourier-transform infrared spectroscopy (FTIR) characterisation of the grafted ceramic surface was performed using a FTIR spectrometer (PerkinElmer, spectrum-one FTIR, US) with an attenuated total reflection attachment (ATR). ATR-FTIR is a powerful tool to investigate silane-coated ceramic surface [8]. Hence, to characterise the surface chemistry on grafted ceramic scaffolds, alumina scaffolds prepared by bi-directional freeze casting were grafted by different silane (γ-MPS or APS). Afterwards, ATR probe was loaded on the direction perpendicular to lamellar of grafted alumina scaffolds. The resulting FTIR spectrum can provid the information to confirm the existence of the organic functional groups.

As illustrated in **Fig.2-10**, the ATR-FTIR technique uses the total internal reflection property of a trapezoidal high refractive index crystal (ATR crystal) that, when passing through by an infrared beam, results in an evanescent wave. The sample is placed directly onto the crystal surface so that it can absorb the evanescent wave which penetrates it between 0.5 μm and 2 μm. This experiment is usually performed by using a broadband IR beam light source with

wavenumber ranged from (10000-200 cm^{-1}). Before it was collected by the detector, IR beam went through the surface of the sample where functional groups on sample absorbed lights with certain wavelength.

The raw data of beams collected by detector named interferogram is a plot of mirror position vs. light, which is converted into the format of wavenumbers vs. light absorption using the Fourier transform. The resulting plot is the FTIR spectrum.

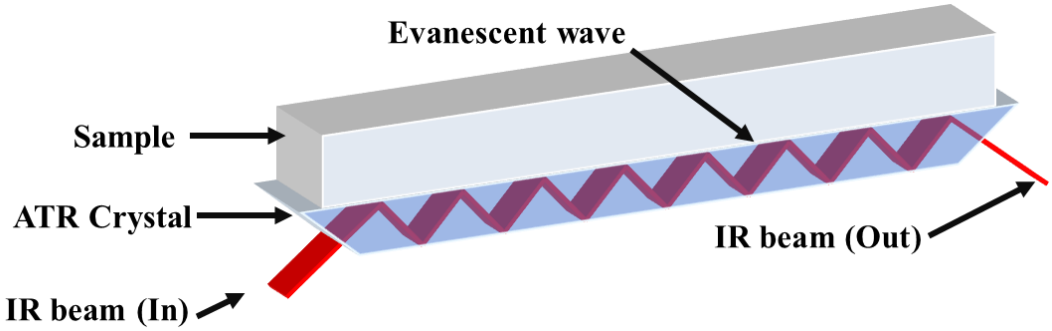

Fig.2-10 *Schematic representation of an ATR-FTIR system. The infrared beam passes through the ATR crystal covered on the top by the sample.*

Prior to testing, a polished pure ceramic block was used to set the infrared baseline of FTIR characterization. Next, ATR probe was placed on the top surface of sample and loaded to 30 N to make sure the ATR crystal contacted tightly with sample surface. 120 scans were collected and accumulated for each measurement in the spectral range of 4000-400 cm^{-1} with a resolution of 2 cm^{-1} at room temperature. Each measurement was repeated 3 times, and the results were analysed using the software of OPUS™ 6.5. The ATR probe was cleaned by ethanol after testing.

2.3.5 X-ray diffraction

X-ray diffraction (XRD) was widely used to identify the different phases in composite materials on the cell dimensions [9]. Here, the phases analysis of HA/magnesium composite

materials were performed by X-ray powder diffraction (XRD, Bruker D8 Advance, US), in which the sample powders of HA/magnesium composites was used. Scan data were collected with Cu-K_a (λ=1.54 Å) radiation at a step size of 0.2° and 0.5 s for each step.

An X-ray diffractometer is composed of an X-ray source, a sample stage, and an X-ray detector. When the tests initiate, an X-ray beam generated from X-ray source was collimated to concentrate towards the sample on the stage which is rotated as an angle θ from the X-ray beam direction where the X-ray scattered secularly. The X-ray detector is placed at an angle of 2θ to collect scattered beam. Constructive interference was generated by the interaction of the incident rays when the condition satisfies the Bragg's law (2.6):

$$\lambda=2dsin\theta \quad (2.6)$$

where λ is the wavelength of the incident X-ray, d is the spacing between the planes in the atomic lattice and θ is the diffraction angle (the angle between the incident X-ray and the scattering planes).

The Bragg's law relates the wavelength of radiation to the lattice spacing. As a result, the collected data was processed by this law to produce a spectrum illustrating all possible diffraction angle of lattice. Comparing the positions and then intensities of measured diffraction with measured pattern with the entries in reference databases using a search-match algorithm allows identification of single or multiple phases.

2.3.6 Microstructural characterization

2.3.6.1 Optical microscopy

Optical microscope (DMI6000, Leica, Germany) was used to provide the optical images of samples at magnification ranging from 4× to 100× to analyse the microstructure of specimens. The well-polished samples were placed on the sample stand in the microscope, an external light source and a set of lenses were employed to observe the top surface of samples at different

magnifications. The digital images produced by the optical microscope were captured by a camera (Prime 95B sCMOS camera, Teledyne Photometrics, US). A scale bar was burned in using a software (Cellsens Entry, US).

2.3.6.2 Scanning electron microscopy (SEM)

Scanning electron microscopy (SEM) was utilised to observe surface morphologies or fracture surface of scaffolds and composites at micro-scale. SEM was a more versatile and powerful technique to produce images with higher quality and high resolution to characterise the microstructure of materials.

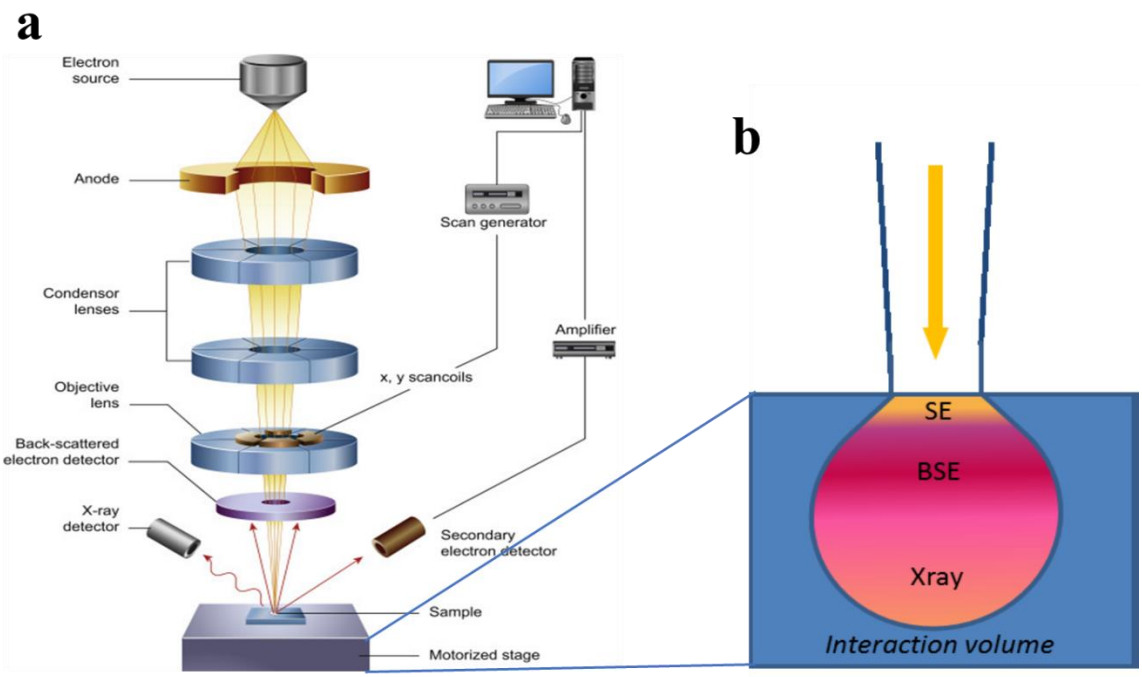

Fig.2-11 *Schematic of SEM representation of the SEM functioning* ***a)*** *and the teardrop-shaped volume interaction* ***b)*** *of the electron beam with the sample surface. Adapted from [10].*

The schematic of a typical SEM (**Fig.2-11a**) reveals the scanning process. An electron beam is collimated from the electron source and then focused by condenser lenses and objective lenses into a single beam (with a diameter of ≈0.4-5 μm). Once the electron beams interact the sample surface, energy of electrons reduced by repeating random scattering and absorption with a

teardrop-shaped interaction volume on the specimen surface. The depth of the interaction volume varies from 0.1 to 5 µm and determined by different factors including acceleration voltage, atomic number, and specimen's density. According to the schematic of interaction volume (**Fig.2-11b**), when the electron interacts with specimen surface, various signals were generated including secondary electrons (SE), back-scattered electrons (BSE), X-rays, and cathodoluminescence radiation which were detected and collected to produce different types of SEM images.

Slight differences in surface topography lead to significant variations in the strength of the secondary electrons which are used to reconstruct the image in a scanning pattern synchronized with the electron beam scan of the sample surface [11]. This analysis allows a topographic evaluation of the sample surface and due to the depth of field of the SEM. The SEM has the measuring depth much larger than a normal optical microscope that rises from the geometry of the beam optics. The depth of field is the space between the best plane of focus where the image results still sharp and being larger in the SEM it allows the observation of rough surfaces.

Backscattered electrons are generated by elastic energetic interactions of the primary electrons with the nuclei of the samples' atoms. The intensity of the BSE signal depends on the average atomic number and density of the sample; images obtained with BSE electrons offers the compositional information. The inelastic interaction of the beam with the K-shell of the sample's atoms, besides producing secondary electrons, generates Auger electrons, X-rays, and cathodoluminescence. The acquisition of the generated X-rays allows a localized chemical analysis, also known as energy dispersive spectroscopy (EDS).

The microstructural characterization was mainly performed using a Quanta scanning electron microscope (Quanta 200F, FEI, US). To minimise the surface charging effect, specimens were loaded on an aluminium SEM stub via a conductive carbon taps adhesive and coated with 10-20 nm thick platinum or gold by sputtering (K575X sputter coater, Quorum technologies, UK)

in a vacuum chamber. Silver paint was applied on the edge of specimen to improve the electrical connection between the specimen surface and the aluminium SEM stub. The SEM images of microstructure were further analysed by imageJ.

2.3.6.3 X-ray microtomography

The X-ray tomography is a non-destructive method to image bulk samples. While the X-ray going through the sample, it records the information inside materials via 2D images. The number of images is dependent on resolution of scanner. Once scanning finished, the 2D images would be combined and constructed into a 3D numerical microtomographic images using Avizo 8.1 (Thermo Fisher Scientific, US). The composite materials were also examined using a micro-CT scanner (Nikon XTH 225 ST, Japan) at 120 kV and 3 μm resolution.

In this work, the X-ray microtomography was used to determine the internal 3D geometries of composites and monitor the crack propagation during *in situ* fracture toughness testing.

2.3.7 Mechanical characterization

2.3.7.1 Compressive strength

Compression strength (σ_f) is the capacity of a material to withstand uniaxial compressive loads per unit area, it can be calculated by:

$$Compressive\ strength, \sigma_c = \frac{P}{A} \tag{2.7}$$

Where *P* is the maximum load, *A* is the area of specimens.

The compressive strength was measured using a universal mechanical testing machine (Zwick/Roell, Z020, Germany) with a load cell of 20 kN. Following the ASTM 1358 standard, all the tests were performed at ambient temperature at a loading rate of 1 mm/min. The compressive area was 4 mm×4 mm=16 mm^2 and height of specimen was 6 mm. All values represented an average of at least three measurements per configuration.

2.3.7.2 Flexural strength

Flexural strength (σ_f) of materials is the force to withstand an applied load on its longitudinal axis between the supporting points. Three-point-bending test was employed to evaluate flexural strength in this work. When loaded to the central point, the three-point-bending specimen was under a combined stress of tensile, compression and shear, the maximum stress achieved during the bending test was called flexural strength.

According to the ASTM D790 standard [12], the flexural strength was calculated using the following equation (2.8):

$$Flexural\ strength, \sigma_f = \frac{3PS}{2bd^2} \tag{2.8}$$

Where P is the maximum bending load, S is the support span, b is specimen width, d is specimen thickness.

The specimen geometry is shown in **Fig.2-12.**

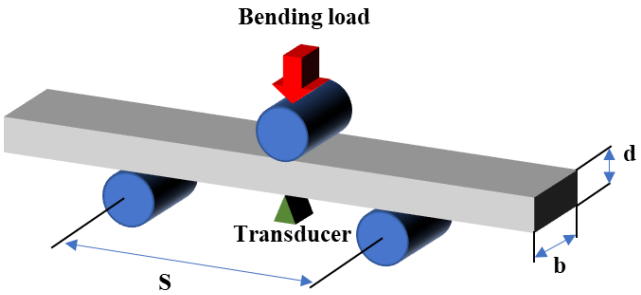

Fig.2-12 *Schematic of three-point-bending specimen. The red arrow illustrates the loading direction.*

Specimens were polished in the lengthwise direction before testing. Two load cells with the maximum limit of 500 N and 20 kN were used for ceramic/polymer and ceramic/metal composites, respectively. The support span of 12.5 mm and testing speed of 0.1 mm/s were used. A displacement transducer (Travel transducer, Zwick/Roell, Germany) was placed at

midspan of the specimen to measure vertical deflection (**Fig.2-12**). All values represented an average of at least three measurements per configuration.

2.3.7.3 Modulus

Young's modulus is defined as the stiffness of solid materials and is calculated by the relation between stress and strain in the elastic linear regime of a uniaxial deformation:

$$Youngs\ modulus, E = \frac{\sigma}{\varepsilon} \tag{2.9}$$

Where σ is stress, ε is strain.

Ultrasonic testing was conducted to determine elastic modulus of pure polymer and pure ceramic. The ultrasonic waves were defined as elastic waves propagating in the materials with higher frequency. In this test, ultrasonic wave would be collected after propagating through materials and the Young's modulus were calculated as the equation (2.10).

$$E = \frac{V_l \rho (1+v)(1-2v)}{1-v} \tag{2.10}$$

Where E is Young's modulus, ρ is density of material obtained in 2.3.3, V_l is ultrasonic longitudinal wave velocity, v is Poisson's ratio.

Specimens for ultrasound testing are bulk cubes in the dimension of 10 mm×10 mm×10 mm produced by CNC or cutter. The surface has to be polished down to 1 μm. Handyscope HS3 (Tiepie engineering, Netherlands) was employed to do ultrasound testing at three different frequency of probe at 1, 2, and 4 MHz.

In the case of anisotropic materials such as nacre-like composites, elastic properties vary with direction, and so do longitudinal and shear wave sound velocity which will affect the measurements via ultrasound. In addition, ultrasonic waves provided by our equipment are hard to access nacre-like composites which may attributed to its high attenuation in shear mode. Thus, this method was only employed on pure polymer, metal, and ceramic, and the modulus

of composites were estimated by the rule of mixture (RoM). RoM was often used to predict the elastic modulus of composite materials by combining the modulus of monolithic constituents. In this work, the RoM was employed to estimate the modulus of nacre-like ceramic-based composite materials in the calculation of fracture toughness. Commonly, there are upper- and lower- bound limits for composites moduli which are calculated using following equations:

$$E_{Upper} = E_1 f_1 + E_2(1 - f_1) \tag{2.11}$$

$$E_{Lower} = \left(\frac{f_1}{E_1} + \frac{(1 - f_1)}{E_2}\right)^{-1} \tag{2.12}$$

Where E_{Upper} is Upper-bound modulus, E_{Lower} is Lower-bound modulus, E_1 is modulus of ceramic phase, E_2 is modulus of compliant phase material, f_1 is volume fraction of ceramic phase.

$$E' = \frac{E_{Upper} + E_{Lower}}{2} \tag{2.13}$$

Where E' is the mid-point of upper-bound and lower-bound modulus which is used in the calculation of fracture toughness K_J (2.3.7.4.2).

2.3.7.4 Fracture toughness

Fracture toughness is the capability of a material to resist to a crack propagation. In this work, two different factors, i.e. K_{IC} and *R*-curve were used to evaluate the fracture toughness of nacre-like composite materials. K_{IC} represents the critical stress intensity factor of crack initiation. On the other hand, the *R*-curve reveals fracture toughness regarding to crack propagation. Fracture toughness was measured using three-point bending on a single-edged notched bending specimen (SEB) or tensile test on a single edge-notched compact tension specimen (CT). In accordance with the ASTM E1820 standard [13], samples were cut into a certain geometry. Next, a pre-notch was cut and sharpened in a custom-made micro-notching machine, designed to offer a sharper notch with a narrow tip to promote early crack initiation in fracture toughness

tests. A schematic shown in **Fig.2-13a** and **b** reveals the micro-notching process alongside the optical images of a sharpened notch (**Fig.2-13c** and **d**). In the micro-notching process, a razor blade was sliding at a speed of 3 times/s under a loading of 10 N on the tip of notch immersed in a 1-µm diamond suspension (DiaPro Largo3, Struers, Denmark) for 2 hours. The radius of the sharpened notch was about 50 µm and the depth about 200 µm.

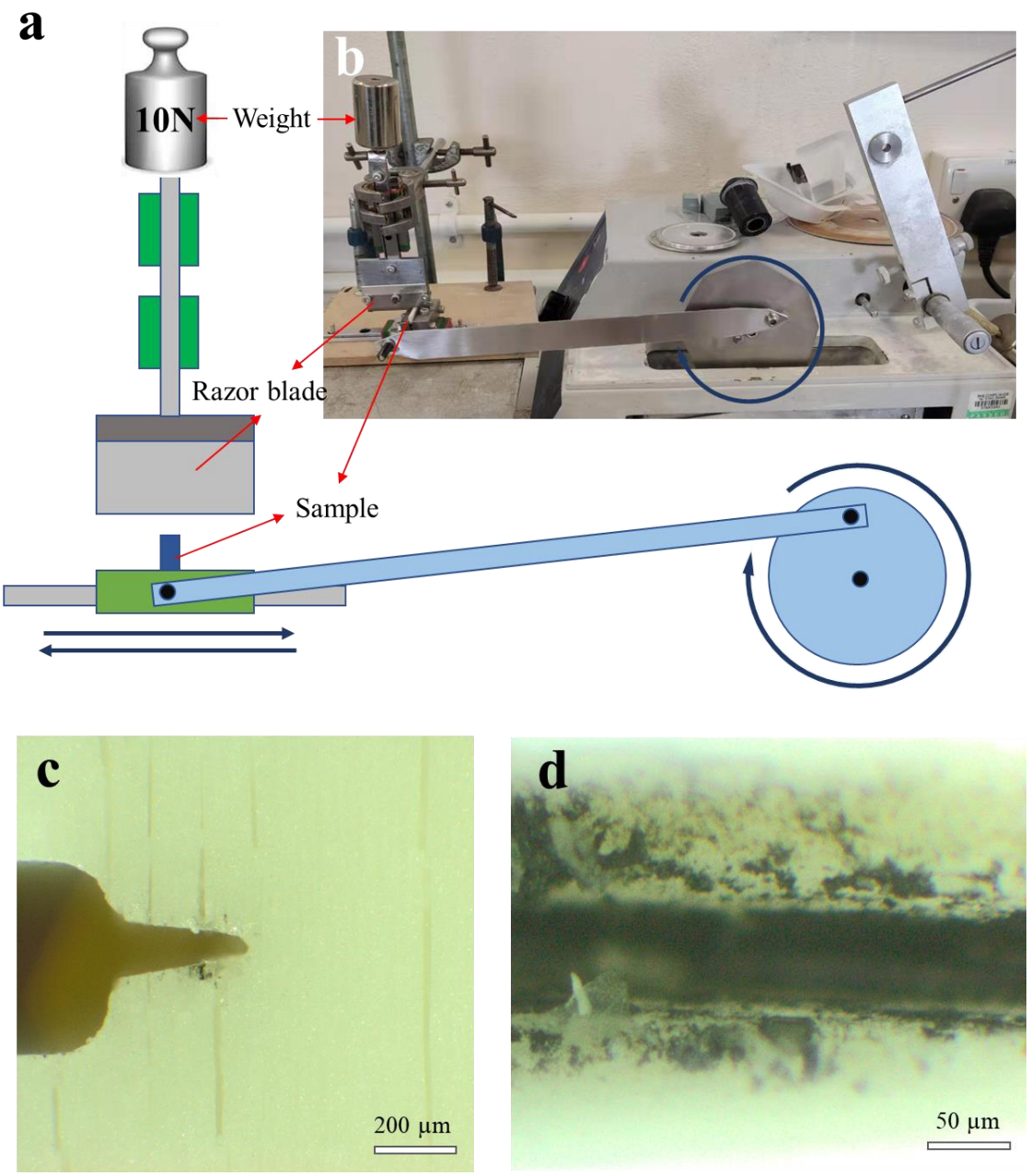

*Fig.2-13 Schematic **a)** and set-up **b)** of micro-notching process. Optical side view **c)** and top view **d)** of a micro-notch. Blue arrows indicate moving/rotating directions.*

2.3.7.4.1 Fracture toughness K_{IC}

To evaluate the fracture toughness K_{IC} of composite materials, as-prepared SEB specimens were tested using a Zwick Roell Z1020 universal testing machine at ambient temperature. The test was conducted with a load cell of 500 N and a loading speed of 1 µm/s.

According to the ASTM 1820 standard [13], the K_{IC} is calculated as:

$$K_{IC} = \frac{PS}{BW^{\frac{3}{2}}} f\left(\frac{a}{w}\right) \tag{2.14}$$

$$f\left(\frac{a}{W}\right) = \frac{3\left(\frac{a}{W}\right)^{\frac{1}{2}}\left[1.99 - \left(\frac{a}{W}\right)\left(1 - \frac{a}{W}\right)\left(2.15 - 3.93\left(\frac{a}{W}\right) + 2.7\left(\frac{a}{W}\right)^{2}\right)\right]}{2\left(1 + 2\frac{a}{W}\right)\left(1 - \frac{a}{W}\right)^{\frac{3}{2}}} \tag{2.15}$$

Where P is the maximum force during testing (N), S is the support span (mm), B is the thickness of specimens (mm), W is the width of specimen (mm) and a is the crack length (mm), as shown in **Fig.2-14**.

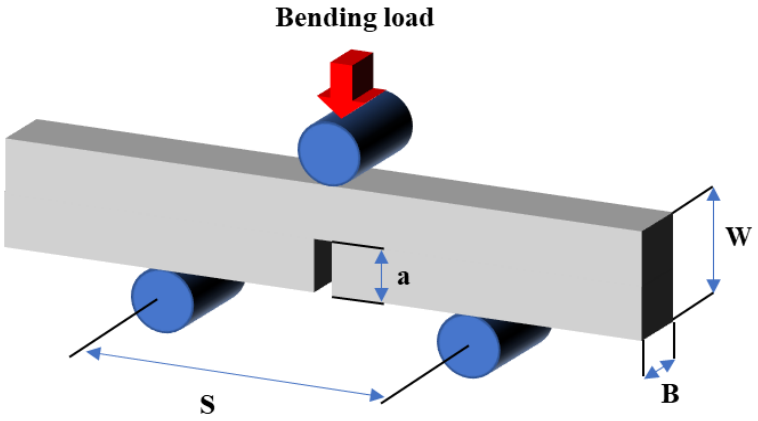

Fig.2-14 *Schematic of fracture toughness SEB specimen. Red arrow illustrates the loading direction.*

For different testing methods and equipment (SEM or Micro-CT), the SEB specimens were fabricated into three specimen size in this work: W=3 mm, B=1.5 mm, S=12.5 mm, a=1.5 mm; W=4 mm, B=2 mm, S=16 mm, a=2 mm; W=5 mm, B=2.5 mm, S=20 mm, a=2.5 mm.

2.3.7.4.2 *R*-Curve

The K_{IC} is the initiation fracture toughness, which is independent on the crack propagation. Thus, K_{IC} is typically used to characterize brittle materials such as traditional ceramics and glasses because they exhibited catastrophically failure once reach maximum loading. In this case, theses brittle materials display flat *R*-curves where $K_J=K_{IC}$=constant. However, the nacre-like composites in this work exhibited rising *R*-curves because these materials produced a slow and stable crack propagation resulting in energy dissipation. As a result, the K_{IC} was no longer enough to describe the fracture toughness of the nacre-like composites. K_J was therefore introduced into the fracture mechanics to account for changes in fracture resistance as a function of crack length. The plots of fracture toughness, K_J vs. crack extension, also known as *R*-curves were described as follows.

Two different specimens were used in this work: SEB specimen and compact tension (CT) specimen. The SEB specimen was the same as that used in the K_{IC} measurements (2.3.7.4.1). The CT specimen geometry is shown in **Fig.2-15**.

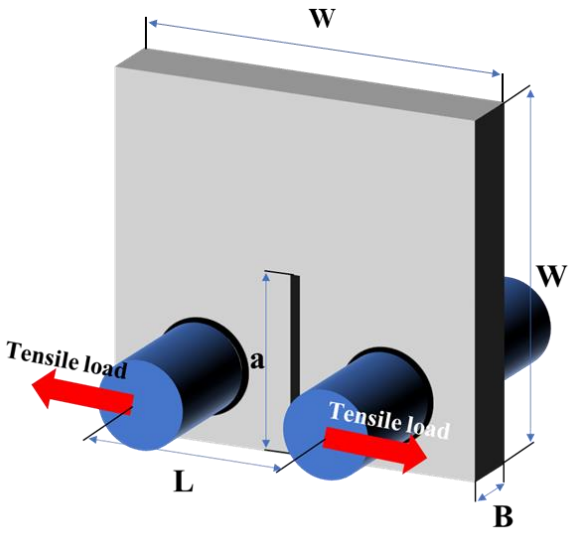

Fig.2-15 *Schematic of CT specimen for fracture toughness measurement. Red arrows illustrate the loading direction.*

The CT specimens were fabricated as the following dimensions, i.e. W=20 mm; B=2 mm; L=10 mm; a=10 mm.

In situ SEM and *in situ* Micro-CT technique were employed to monitor and record the crack propagation on specimen during fracture toughness testing by importing 2D image and 3D tomography, respectively. As-prepared specimens were loaded in customer-designed jigs on an *in situ* Deben Microtest-150 N stage (Deben, UK) mounted within the SEM chamber as shown in **Fig.2-16.**

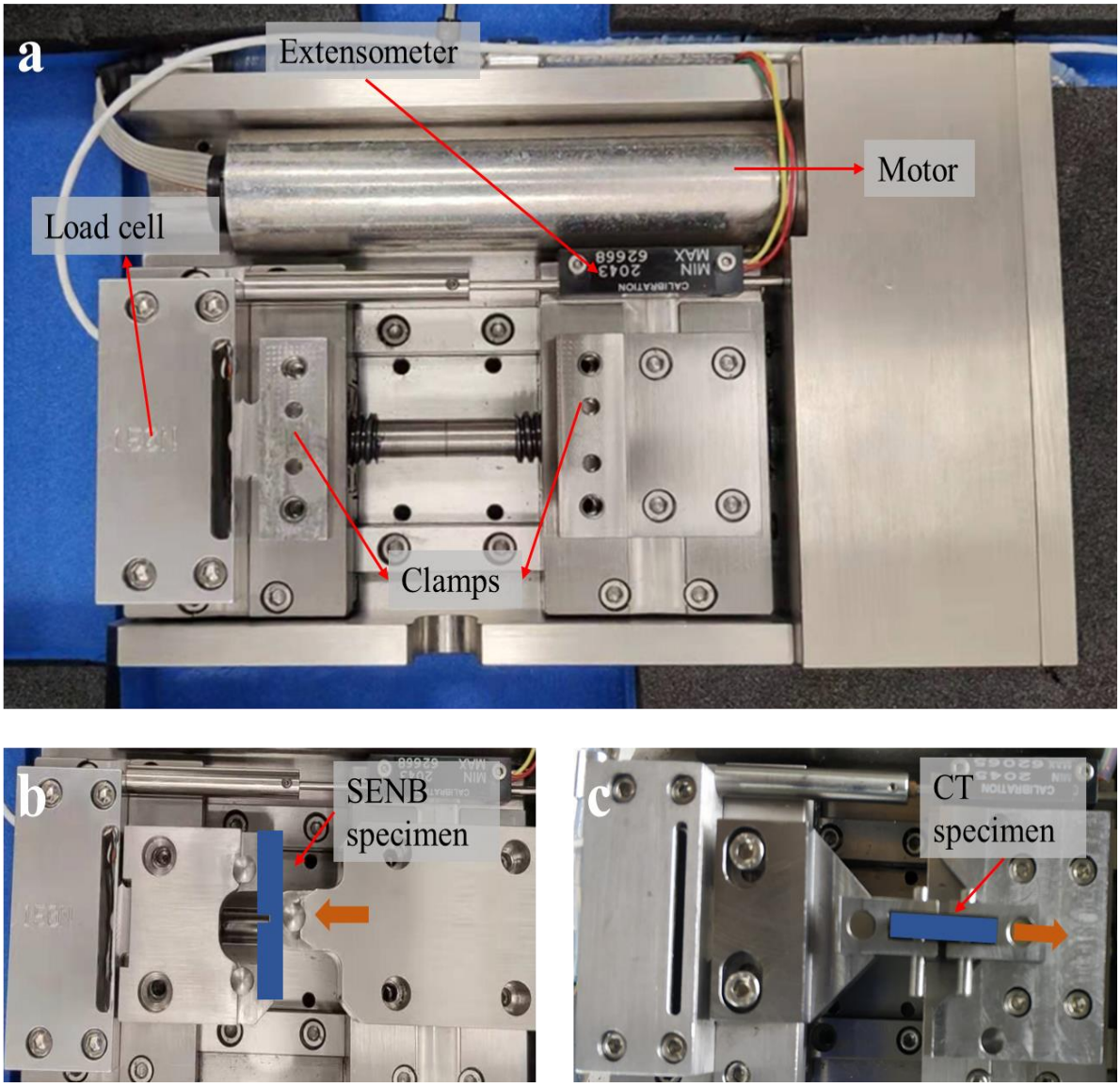

Fig.2-16 *Pictures of Deben Microtest-150N stage* ***a)****, jigs for SEB specimen bending tests* ***b)*** *and CT specimen tensile tests* ***c)****. Orange arrows assign to the loading direction and blue bars indicate specimens.*

Two methods, i.e. cyclic loading-unloading and monotonic loading methods were used to evaluate the fracture toughness.

For the cyclic loading-unloading method, prior to testing, the specimen was preloaded to around 2 N to fix the specimen in the Deben stage and initially loaded into 50% of maximum

force (obtained from the K_{IC} measurement), high-quality images were recorded via a slow scanning mode until the specimen was unloaded up to 80% of the current load. The specimen was then reloaded until the displacement reached more than 0.05 mm, when the motor was stable, unloaded it and took an image. The specimen was loaded and unloaded cyclically until the sample failed. The feeding speed for loading and unloading was 1 mm/min. The cyclic loading-unloading process was recorded by video, SEM images and load-displacement curves. For the monotonic loading method, the specimen was loaded at a feeding speed of 1 mm/min while a video was recorded to monitor the crack propagation in a fast-scanning mode of SEM.

To evaluate the fracture toughness resistance regarding the *J*-integral as a function of crack extension, nonlinear–elastic fracture mechanics measurements were utilized to determine stress intensities, K_J. The crack-resistance curves (*R*-curve) which represented an energy dissipation rate as a function of crack extension was a trend line attained by accumulating points for at least three samples [15]. Fracture toughness K_J were determined by the back-calculated from these measured *J* values using the standard mode I *J*–*K* equivalence ($K_J = \sqrt{JE'}$). Where the E' was the Young's modulus of composites obtained from the rule of mixture (2.3.7.3).

In according with the ASTM E1820 standard, the J was composed of both elastic and plastic component, i.e.

$$J = J_{el} + J_{pl} \tag{2.16}$$

Where

$$J_{el} = \frac{Kel^2}{E'} \tag{2.17}$$

Using the loading P and specimen size, the mode I stress-intensity factor was calculated:

$$K_{el} = \frac{PS}{BW^{\frac{3}{2}}} f(\frac{a}{w}) \tag{2.18}$$

Where B and W were the thickness and width of specimen, respectively, a was the crack length, P was the load, S was the support span, and f was a non-dimensional function of the crack length a.

$$f\left(\frac{\mathrm{a}}{\mathrm{w}}\right)=\frac{3\left(\frac{a}{w}\right)^{\frac{1}{2}}\left[1.99-\left(\frac{a}{w}\right)\left(1-\frac{a}{w}\right)\left(2.15-3.93\left(\frac{a}{w}\right)+2.7\left(\frac{a}{w}\right)^{2}\right)\right]}{2\left(1+2\frac{a}{w}\right)\left(1-\frac{a}{w}\right)^{\frac{3}{2}}} \tag{2.19}$$

Considering the load-displacement, J_{pl} for plastic portion was determined by

$$J_{Pl}=\frac{1.9A_{pl}}{Bb} \tag{2.20}$$

Where b was the uncrack ligament, the A_{pl} was the area under load vs. plastic displacement (V_{pl}) curve.

$$A_{pl(i)}=\frac{\left(P_{(i)}+P_{(i-1)}\right)\left(V_{pl(i)}-v_{pl(i-1)}\right)}{2} \tag{2.21}$$

and the V_{pl} was given by

$$v_{pl(i)}=v_{(i)}-\left(P_{(i)}\,C_{(i)}\right) \tag{2.22}$$

According to loading-unloading curve. $C_{(i)}$ was the compliant of un-loading part and $v_{(i)}$ was the displacement of load cell for cyclic loading mode (CLM).

By coupling the decreasing b with the crack propagation, the incremental definition of J_{pl} calculation was obtained:

$$J_{Pl(i)}=\left[J_{pl(i-1)}+\frac{1.9\left(A_{pl(i)}-A_{pl(i-1)}\right)}{b_{(i-1)}B}\right]\times\left[1-\frac{0.9\left(a_{(i)}-a_{(i-1)}\right)}{b_{(i)}}\right] \tag{2.22}$$

2.4 References

[1] S. Algharaibeh, A.J. Ireland, B. Su, Bi-directional freeze casting of porous alumina ceramics: A study of the effects of different processing parameters on microstructure, Journal of the European Ceramic Society 39(2) (2019) 514-521.

[2] G. Davison, LUDOX® Colloidal Silica Ceramic Shell Investment Casting, (2008).

[3] M.K. Aghajanian, M.A. Rocazella, J.T. Burke, S.D. Keck, The fabrication of metal matrix composites by a pressureless infiltration technique, Journal of Materials Science 26(2) (1991) 447-454.

[4] B.P. Singh, J. Jena, L. Besra, S. Bhattacharjee, Selection and Optimization of Dispersant in Ceramic Slurry Processing by Different Techniques: Comparison, Correlation, and Standardization, Journal of Dispersion Science and Technology 28(7) (2007) 1044-1052.

[5] A. Preiss, B. Su, S. Collins, D. Simpson, Tailored graded pore structure in zirconia toughened alumina ceramics using double-side cooling freeze casting, Journal of the European Ceramic Society 32(8) (2012) 1575-1583.

[6] F. Yang, C. Li, Y. Lin, C.-A. Wang, Effects of sintering temperature on properties of porous mullite/corundum ceramics, Materials Letters 73 (2012) 36–39.

[7] ASTM C373-18. Annual book of ASTM standards, ASTM International; 2018.

Y. Okuda, M. Noda, H. Kono, M. Miyamoto, H. Sato, S. Ban, Radio-opacity of core materials for all-ceramic restorations, Dental Materials Journal 29(1) (2010) 35-40.

[8] J.R.C. Queiroz, P. Benetti, M. Özcan, L.F.C. de Oliveira, A.D. Bona, F.E. Takahashi, M.A. Bottino, Surface characterization of feldspathic ceramic using ATR FT-IR and ellipsometry after various silanization protocols, Dental Materials 28(2) (2012) 189-196.

[9] V.K. Volkova, L.F. Kalistratova, X-ray diffraction analysis of structure of composite materials based on polytetrafluoroethylene during thermal exposure, Inorganic Materials: Applied Research 6(4) (2015) 411-413.

[10] D. McMullan, Scanning electron microscopy 1928–1965, Scanning 17(3) (1995) 175-185.

[11] K.C.A. Smith, C.W. Oatley, The scanning electron microscope and its fields of application, British Journal of Applied Physics 6(11) (1955) 391-399.

[12] ASTM D790-16. Annual book of ASTM standards, ASTM International; 2016.

[13] ASTM E1820-17. Annual book of ASTM standards, ASTM International; 2017.

[14] V. Naglieri, B. Gludovatz, A.P. Tomsia, R.O. Ritchie, Developing strength and toughness in bio-inspired silicon carbide hybrid materials containing a compliant phase, Acta Materialia 98 (2015) 141-151.

Chapter 3

Nacre-like ceramic scaffolds

Results in section 3.3.3.2.3 and 3.3.3.2.4 were published:

H. Wan, N. Leung, S. Algharaibeh, T. Sui, Q. Liu, H.-X. Peng, B. Su, Cost-effective fabrication of bio-inspired nacre-like composite materials with high strength and toughness, Composites Part B: Engineering 202 (2020) 108414.

3.1 Introduction

Prior to the infiltration of polymers (Chapter 4) and metals (Chapter 5) to fabricate ceramic-based composites, the preparation of ceramic scaffolds with nacre-like architectures was presented in this chapter. The fabrication procedure of scaffolds was followed by slurries preparation, bi-directional freeze casting and densification/sintering. Here, ceramic scaffolds with various architectures/microstructure and mechanical properties were investigated as a function of processing conditions.

Beginning with the freeze-casting suspension, aqueous ceramic slurries were prepared by mixing ceramic powder, organic additives, and water. The organic additives i.e. dispersants and binders were shown to have significant impact on the microstructure of final scaffolds. The organic additives could influence the rheological properties of slurries resulting in various growth velocities and morphologies of ice crystals. Therefore, ceramic slurries were prepared with different amounts of dispersant and then characterised using a rheometer.

Next, the as-prepared ceramic slurries were frozen under dual temperature gradients, freeze-dried and sintered to prepare lamellar ceramic scaffolds. The surface morphologies were investigated.

Since natural nacre is a highly mineralised (about 96 vol.%) composite material, it is necessary to densify the freeze-cast ceramic scaffolds into nacre-like scaffolds with higher ceramic fractions. From lamellar ceramic green bodies obtained by bi-directional freeze casting, two different densification methods were investigated to produce sintered nacre-like ceramic scaffolds, namely, one-step and two-step method where the resultant scaffolds exhibited two different nacre-like architectures, respectively. In this case, both alumina and zirconia were used. The dependence of microstructure of nacre-like ceramic scaffolds was investigated on processing parameters such as first-step sintering temperature, polymer binder content, ceramic solid loading, and compressive distance. Finally, the densified nacre-like ceramic scaffolds with μL and BM architectures exhibited good but anisotropic mechanical properties. They were suitable for the subsequent fabrication of nacre-like ceramic/polymer or ceramic/metal composites.

3.2 Materials and methods

3.2.1 Preparation of ceramic slurries

Ceramic slurries were prepared by dispersing sub-micro commercial ceramic powder into deionized (DI) water using an organic dispersant and binder. In this work, three ceramic powders were utilised: alumina, 3% yttria-stabilized zirconia, and hydroxyapatite (HA). Two different dispersants used were the commercial carbonic acid-based polyelectrolyte dispersant (Dolapix CE64) and ammonium polyacrylate (Darvan 821A) depending on the type of ceramics. They were reported to be effective when preparing different ceramic slurries as shown in **Table 3-1**. where Dolapix CE64 was used as a dispersant for alumina [1] and zirconia [2, 3] while Darvan 821A was used for hydroxyapatite (HA) [4]. To determine the effect of dispersant concentration on viscosity, ceramic slurries were prepared with different amounts

of dispersant as shown in **Table 3-1**. Optimal dispersant content was determined using rheological measurement for different ceramic slurry systems.

	Alumina	Zirconia	Hydroxyapatite
Solid loading	20 vol.%	20 vol.%	20 vol.%
Type of dispersant	Dolapix CE64	Dolapix CE64	Darvan 821A
Amounts of dispersant tested	0.7 wt.%, 0.8 wt.%, 0.9 wt.%, 1 wt.%	0.2 wt.%, 0.3 wt.%, 0.4 wt.%, 0.5 wt.%	0.6 wt.%, 0.8 wt.%, 1 wt.%, 1.2 wt.%

Table 3-1 *Slurries composition.*

3.2.2 Bi-directional freeze casting

85 ml of as-prepared ceramic slurries were poured into a freeze casting mould for bi-directional freeze casting as described in 2.2.3. The freeze casting mound used was shown in **Fig.2-1b.** Accordingly, bi-directional freeze casting were widely used to generate ceramic scaffolds with highly aligned structures and their microstructural features could be controlled by applying the physics of ice formation. Based on the configuration of copper wedge covered by Polydimethylsiloxane (PDMS) shown in **Fig.2-2** in Chapter 2, ceramic slurries were frozen under dual temperature gradients. The effects of slope angle (5-20°) and cooling rate (1-10 ℃/min) on scaffold alignments and microstructure were studied in our previous work [5]. In this study, the slope angle of the wedge used was chosen to be 10° because the obtained scaffolds exhibited the best alignment. However, the investigation here was conducted at higher cooling rates in the range of 5-40 ℃/min. Because the maximum cooling rate provided by the PID/immersion cooler system is around 5 ℃/min, three cooling liquids with various cooling temperatures were used to pre-cool the cooling stage of freeze casting (**Fig.2-3**): ethanol (-50 ℃), ethanol (-100 ℃), and liquid nitrogen (-196 ℃). Meanwhile, the real-time

temperature of cold fingers was measured during the freeze casting process. **Fig.3-1** reveals the time vs. temperature plot demonstrating the cooling process in the first 5 min of freeze casting. Accordingly, starting from room temperature, all samples were fast cooled in the first 180 s until the temperature became stable. The cooling rate was calculated by equation 3.1:

$$cooling\ rate = \frac{\Delta T}{\Delta t} \tag{3.1}$$

where the ΔT is the temperature difference between 0s and 180s; Δt is 180s.

As a result, the cooling rates were measured as 11 ℃/min, 20 ℃/min and 40 ℃/min for ethanol (-50 ℃), ethanol (-100 ℃) and liquid nitrogen (-196 ℃) cooling liquids, respectively.

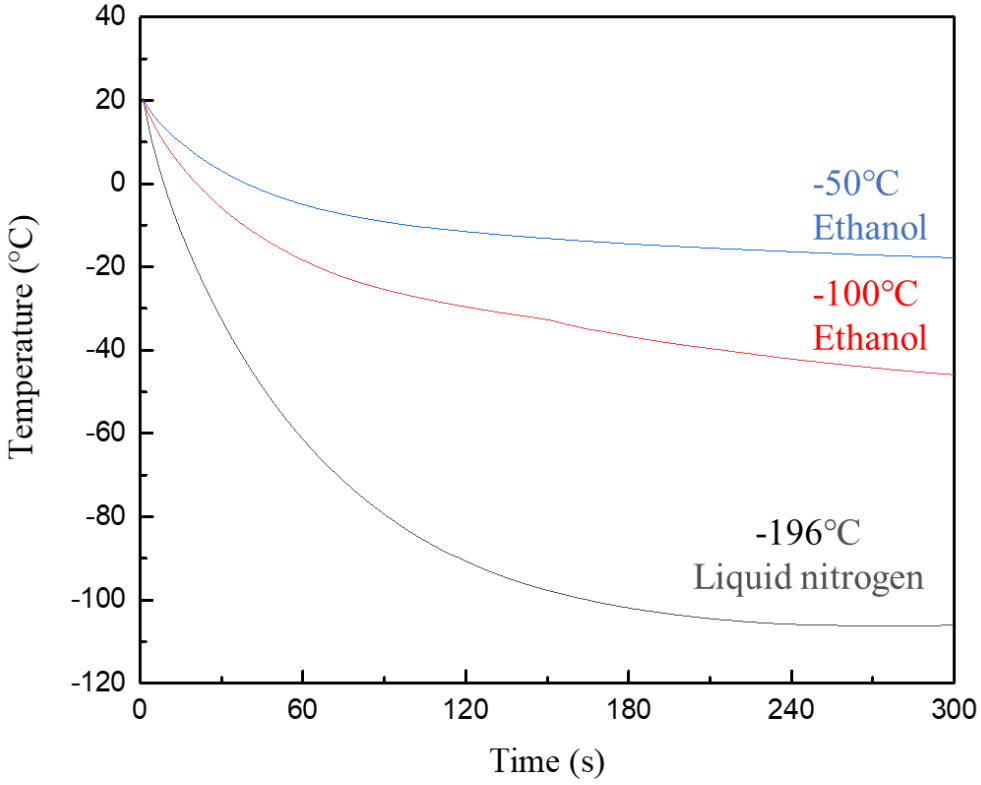

Fig.3-1 *Temperature of cold stage during freeze casting when the cold stages were placed in cooling liquids with different temperature (-50 ℃, -100 ℃, and -196 ℃).*

3.2.3 Densification: One-step method and two-step method

To acquire the scaffolds with nacre-like architecture and high ceramic fractions, two densification methods based on uniaxial pressing were investigated as schematically shown in **Fig.3-2**. These methods were named as ‘two-step method’ and ‘one-step method’ according to the number of their sintering steps.

In the two-step densification method, ceramic scaffold green bodies prepared by bi-directional freeze casting were fired at a low temperature for the de-binder process (550 ℃ for 2 hours at a heating rate of 2 ℃/min) and then sintered at a relatively lower temperature (1150-1450 ℃ for 2 hours at a heating rate of 10 ℃/min) for first-step sintering. The partially sintered scaffolds were subsequently infiltrated by paraffin wax. To increase the ceramic content and further reduce the spacing between ceramic layers, the wax-infiltrated and partially sintered ceramic scaffolds were subject to uniaxial compression under 100 MPa pressure perpendicular to the lamellar layer direction at 90 ℃ and sintered at 1550 ℃ for 2 hours at a heating rate of 10 ℃/min for the second time.

In the one-step densification method, paraffin wax was infiltrated into the green ceramic scaffold directly without pre-sintering. A universal mechanical testing machine (Zwick/Roell Universal testing machine Z020, Germany) was used to control the compression distance to alter the ceramic fraction and spacing between the ceramic lamellar during pressing at 90 ℃. Finally, the compressed ceramic scaffolds with wax were fired in a furnace at 550 ℃ for 2 hours at a heating rate of 2 ℃/min and then sintered at 1550 ℃ for 2 hours at a heating rate of 10 ℃/min.

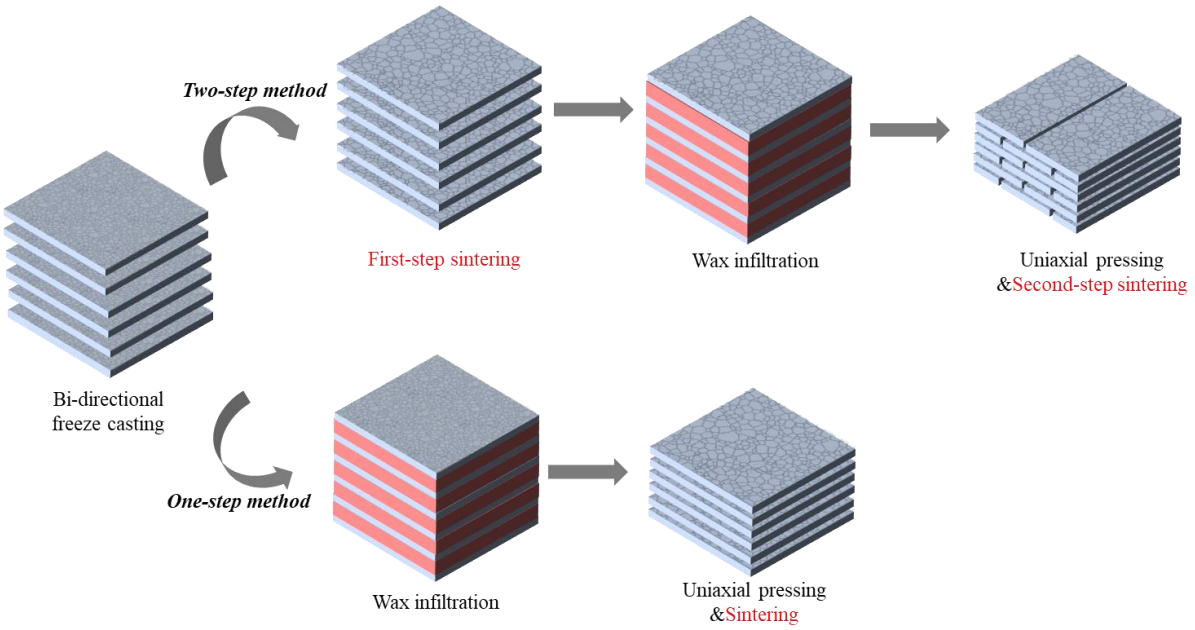

Fig.3-2 *Flowchart illustrating the fabrication processes of nacre-like ceramic scaffolds. The green ceramic scaffolds with highly aligned lamellar structure from bi-directional freeze casting undergo two different densification routes: two-step method and one-step method. The resultant densified ceramic scaffolds displayed different architectures.*

3.2.4 Microstructural characterization

The microstructure of ceramic scaffolds was characterised using a scanning electron microscope (SEM). Here, a fractured surface of scaffolds was performed under SEM to characterise the microstructure of scaffolds. Meanwhile, to examine the microstructural features, such as ceramic wall thickness and length, SEM images of polymer (polymethyl methacrylate or epoxy resin)-infiltrated scaffolds were analysed using ImageJ. Over 3 different images were used to estimate the dimensions of ceramic walls.

3.2.5 Mechanical characterization

The compressive strength of densified scaffolds was measured in two different directions: parallel and perpendicular to the ceramic lamellar in scaffolds. The specimen size was 4 mm×4 mm×6 mm where the loading area was 4×4 mm and height was 6 mm.

3.3 Results and discussion

3.3.1 Rheological behaviours of the ceramic slurries

Prior to freeze casting, the rheological properties of ceramic slurries were investigated with different amounts of dispersant at 25 ℃ to determine the optimal content of dispersant in different ceramic slurry systems. The results of viscosities for the alumina and zirconia slurries with various amounts of dispersant are shown in **Fig.3-3**. Both alumina/Dolapix CE64 (**Fig.3-3a**) and zirconia/Dolapix CE64 (**Fig.3-3b**) suspension displayed similar behaviours with a viscosity ranging from 0.01 to 1 Pa·s at a shear rate of 1-200 s^{-1}. The viscosities of slurries decrease gradually as the shear rate increases, demonstrating a non-Newtonian flow. The ceramic slurries exhibited a shear-thinning behaviour, which is attributed to the broken polymeric links between the nanoparticles provided by the absorbed organic polymeric dispersant [6].

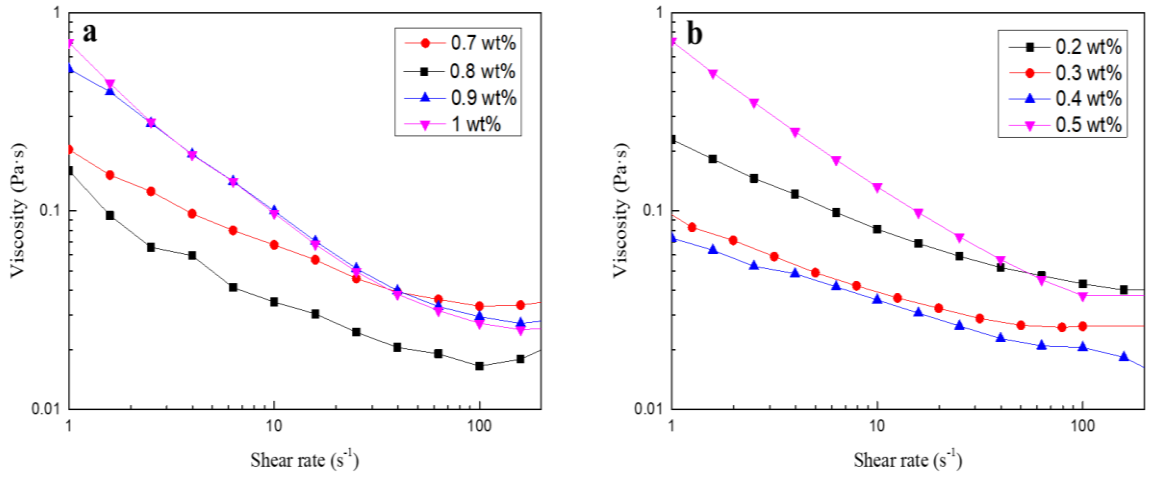

Fig.3-3 Viscosity as a function of shear rate for alumina/Dolapix CE64 ***a)*** *and zirconia/DolapixCE64* ***b)****.*

Furthermore, viscosities of slurries vary with the amount of additive dispersant. Viscosity at the shear rate of 100 s^{-1} is often used to optimise the freeze-casting ceramic slurries [7, 8],

therefore, viscosities of ceramic slurries with different dispersant content were summarised at such a shear rate (**Fig.3-4)**. It can be seen that, for alumina/Dolapix CE64 slurries (**Fig.3-4a**), the viscosity decreased when the dispersant concentration increased from 0.7 to 0.8 wt.%. However, when more dispersant was added with an increasing concentration above 0.9 wt.%, the slurries became more viscous due to the entanglement of the polymeric chains on the organic dispersant [9]. Therefore, the optimal dispersant concentration for alumina was 0.8 wt.%. Similarly, for zirconia and HA slurries (**Fig.3-4b** and **c),** the optimal dispersant concentration with the lowest slurry viscosity was 0.4 wt.% and 1.0 wt.%, respectively.

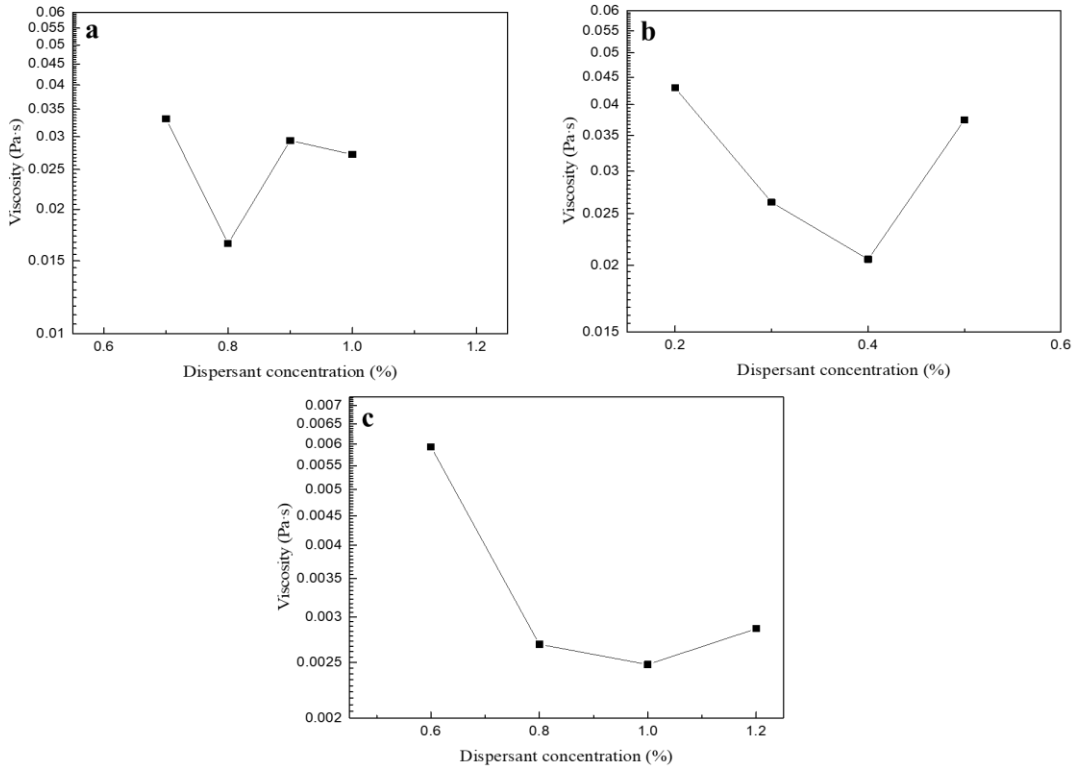

Fig.3-4 *Viscosity as a function of dispersant concentration at a shear rate of 100s^{-1} for alumina/Dolapix CE64* ***a)****; zirconia/DolapixCE64* ***b)*** *and HA/Darvan 821A* ***c)****.*

Previous studies showed that the viscosity of slurry significantly contributed to the quality of the freeze-casting scaffold [10-12]. At a lower viscosity, freeze casting ceramic slurries

produced samples with a better quality of lamellae structure and avoided delamination along the freeze direction. Therefore, this work is aimed to produce ceramic slurries with the lowest viscosity. The temperature of slurries near the freezing ice front was around 5 ℃ and the viscosity of ceramic slurries was not greatly affected by temperatures between 5 ℃ and 25 ℃. Therefore, the rheological properties were measured at 25 ℃ to ensure the regular growth of ice crystals during freezing in a given ceramic slurry. Dolapix CE64 provided both electrostatic and steric effects to stabilise the ceramic particles in slurries and the effects were determined by the ratio of dispersant and particles, thus, the optimal amount of dispersant indicated the best suspension dispersion resulting in the lowest viscosity of slurry [10]. Although viscosity is proportionate to the solid loading of suspension and the amount of organic binder, the influence of dispersant concentration was equivalent at diverse solid loadings or binder contents. Consequently, the optimal dispersant concentration of alumina/Dolapix CE64, zirconia/Dolapix CE64, and HA/Darvan 821A systems were 0.8 wt.%, 0.4 wt.% and 1 wt.%, respectively.

3.3.2 Morphology and microstructure of freeze casting scaffolds

Bi-directional freeze casting was processed on alumina slurries with 20% solid loading at a cooling rate of 5 ℃/min. SEM images of scaffolds in **Fig.3-5b, c,** and **d** showed the surface morphologies of ceramic lamellae. The ceramic walls displayed obvious dendritic-like features on one side and are smooth on the other side. According to the work reported by Deville's group [13], this phenomenon resulted from the balance between the imposed and preferred growth of ice crystals. As shown in **Fig.3-5a**, two growth directions for the ice crystals were defined: temperature gradient and preferred growth direction. The temperature gradient was determined by the cold and hot sides and the preferred growth direction was determined by the crystallographic interfacial energies. The ice crystals growth tilted towards the preferred growth direction showing a featured side to the temperature gradient with a smooth surface on

the other side. When water-based slurries containing alumina powders are frozen directionally, the ice crystals preferentially propagate and repel ceramic particles to form ordered structure and the morphologies of ice crystal reflect on the ceramic lamellae microstructure with the opposite effect.

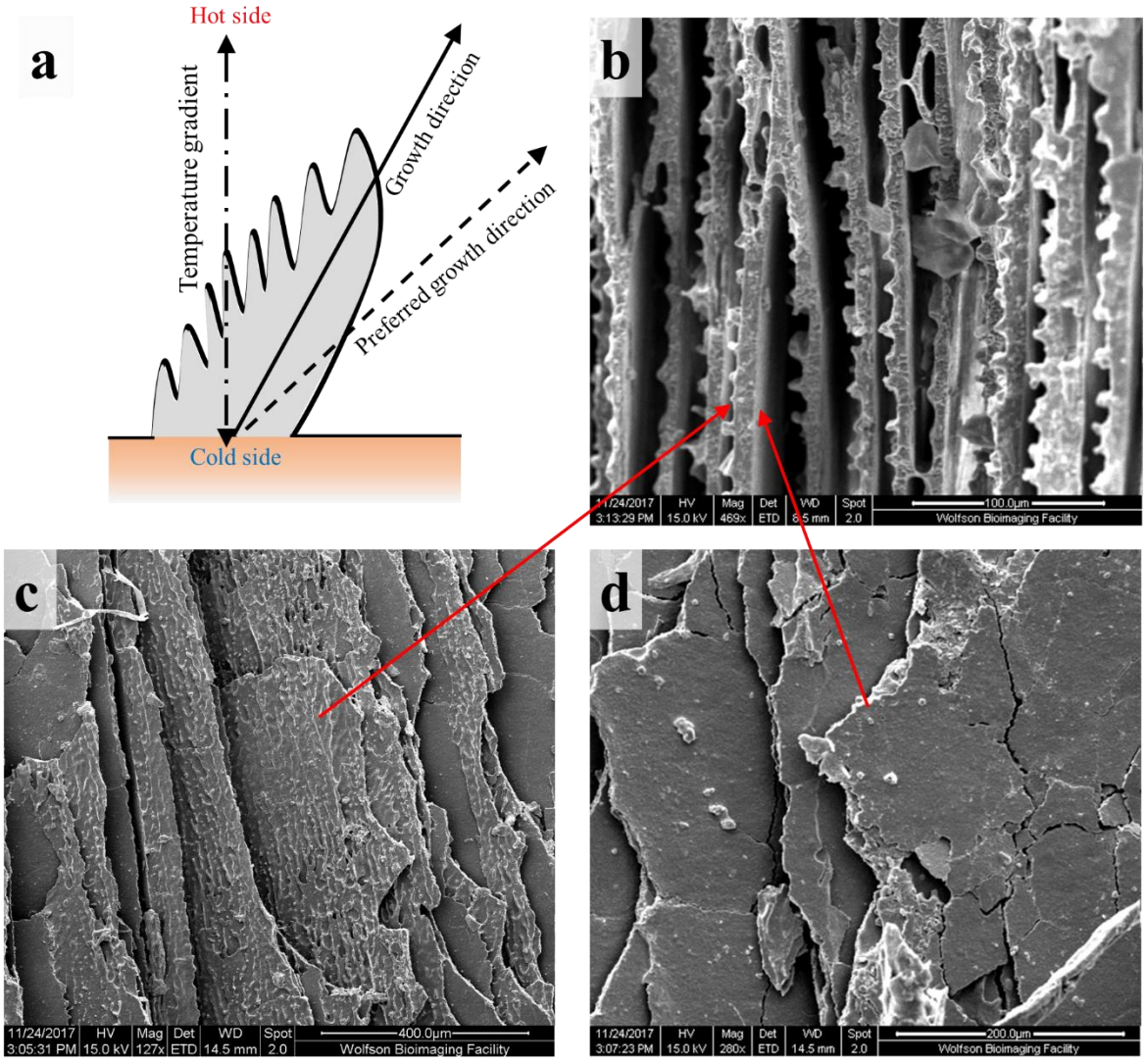

Fig.3-5 Schematic illustration showing ice growth direction ***a)****. SEM images illustrates the cross-section* ***b)****, rough surface* ***c)****, and smooth surface* ***d)*** *of ceramic lamellae.*

3.3.3 One-step vs. two-step densification method

Since nacre has a high mineral content (96 vol.%), the densification of freeze-casting scaffolds was needed to mimic its architecture. Alumina lamellar scaffold green bodies were prepared

by bi-directional freeze casting of 10 vol.% alumina slurries at cooling rate of 40 ℃/min. Two densification methods using a simple uniaxial pressing and pressureless sintering, namely two-step method and one-step method, were employed to build up nacre-like alumina scaffolds (**Fig.3-6**). The resulting ceramic scaffolds were observed under SEM. Although both densified ceramic scaffolds exhibited nacre-like layer-by-layer architecture, the microstructure of each ceramic layer was different. From the top view (**Fig.3-6a** and **c**), scaffolds made using the one-step method exhibited ceramic layers of higher integrity (**Fig.3-6a**). Massive broken ceramic bricks were found in the scaffolds generated from the two-step method (**Fig.3-6c**). From the side-view, while the scaffolds from the two-step method in **Fig.3-6b** were composed of separated ceramic bricks, **Fig.3-6d** displayed a one-step method densified scaffold consisting of long micro-scale ceramic layer. Hence, the architecture produced by the two-step, and one-step methods are named as “brick-and-mortar (BM)” and “micro-layered (μL)”, respectively.

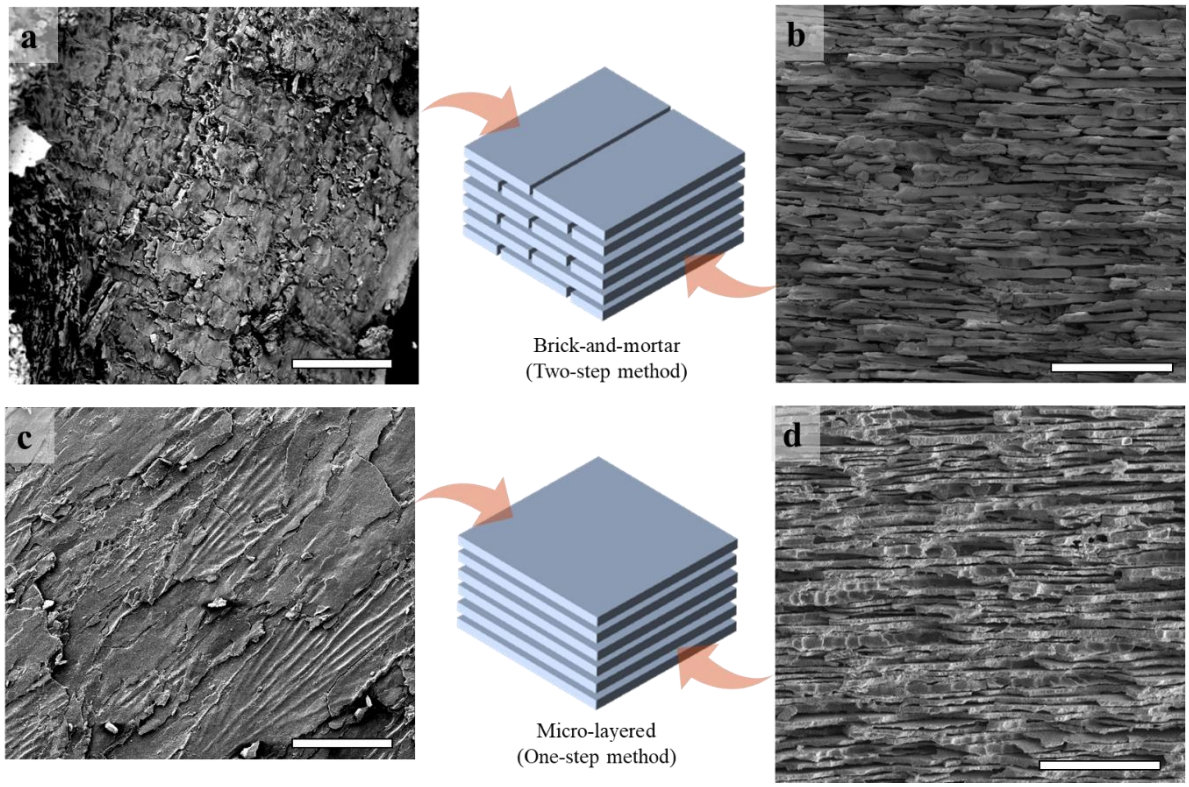

Fig.3-6 *SEM images of the fracture surface of ceramic scaffolds from two-step and one-step method, respectively.* ***a)*** *and* ***c)*** *are top view images perpendicular to the lamellar structure,* ***b)*** *and* ***d)*** *are side view images parallel to lamellar structure. Scale bars:* ***a)*** *and* ***c)*** *200 µm;* ***b)*** *and* ***d)*** *100 µm.*

The two-step method is the most commonly reported fabrication method for BM ceramic scaffolds [14-16] while the one-step method is newly developed in this work and has not been reported before. The key distinction between these two methods is that partially sintered and brittle ceramic scaffolds were uniaxially pressed in the two-step method, while unsintered and ductile ceramic scaffolds were uniaxially pressed in the one-step method. This has significant implications, not only for their overall fabrication time (a sintering cycle typically takes a day) but also for their resultant microstructure (as shown in **Fig.3-6**) and mechanical properties. During conventional uniaxial pressing, the pre-sintered ceramic layers in scaffolds were broken down into ceramic platelets (bricks) as they were relatively weak and brittle and easily to be

fractured under uniaxial pressing loads. Consequently, the densified scaffolds displayed an assembly of aligned ceramic platelets or bricks. After infiltration of the compliant phase (mortar), the classic brick-and-mortar materials were obtained. Conversely, the objective of the one-step method was to preserve the lamellar (micro-layered) structure in the final densified ceramic scaffolds. Uniaxial pressing was employed to reduce the spacing between ceramic layers that were relatively intact after the densification of green ceramic scaffolds. Owing to the relatively high plasticity of the green scaffolds, instead of brittlely fracturing, the ceramic layers plastically deformed under uniaxial pressing load. The plasticity and toughness of green scaffolds are attributed to the organic polymer binder (polyvinyl alcohol, PVA) used. The pressing densification was carried out at 90 ℃ which is slightly above the glass transition temperature (T_g) of PVA (~80 ℃) [17], therefore PVA shows high plasticity at this processing temperature. Additionally, in the one-step method, even though the ceramic walls cracked or broke down during the pressing process, they could still heal and recover during the high-temperature sintering stage as ceramic powders in green scaffolds still maintained a high sintering activity. After uniaxial pressing, the scaffolds underwent a single de-binding/sintering step. The fabrication time for the one-step densification route was therefore significantly shortened.

Next, the study will focus on the effect of processing parameters on the microsutrcture of BM and μL scaffolds, respectively. The first-step sintering temperature for BM architecture will be investigated. Moreover, slurries composition such as binder content and solid loading, the extent of compression during densification would effectively manipulate the microstructure of μL scaffolds.

3.3.3.1 Two-step method

Zirconia brick-and-mortar scaffolds were prepared using the two-step method. Scaffold green bodies were produced by bi-directional freeze casting of 10% zirconia slurries at a cooling rate

of 40 ℃/min. The scaffold green bodies were then partially sintered (first-step sintering) at a relatively lower temperature ranging from 1150-1450 ℃. All the partially sintered scaffolds were then densified under uniaxial press at 100 MPa and finally sintered again (second-step sintering) at 1550 ℃ for 2 hours to build up scaffolds with brick-and-mortar structure.

Ceramic scaffolds sintered at different temperatures shrink differently. Hence, two linear shrinkage values were measured after the first-step sintering and second-step sintering in the two-step method. The sintering temperature for the first-step sintering varied from 1150-1450 ℃ and the second-step sintering temperature was constantly kept at 1550 ℃. **Fig.3-7** showed that linear shrinkage increased dramatically from ~3% to 23% as the first-step sintering temperature increased from 1150 to 1300 ℃. However, when the sintering temperature continued to increase above 1400 ℃, the linear shrinkage was kept steady at ~25%. Following the first-step sintering, the partially-sintered ceramic scaffolds were densified by uniaxial pressing and then sintered again at 1550 ℃ to facilitate further densification and formation of inorganic (ceramic) bridges between the ceramic bricks. After the second-step sintering, the shrinkage behaviours exhibited an opposite trend where the linear shrinkage was smaller for the scaffolds sintered at a higher temperature in the first-step sintering. The shrinkage was almost negligible for the scaffolds sintered above 1400 ℃ in the first-step sintering. Therefore, it could be concluded that the degree of sintering zirconia scaffolds increased when the sintering temperature increased from 1150 to 1400 ℃ and then remained stable until fully sintered (1550 ℃).

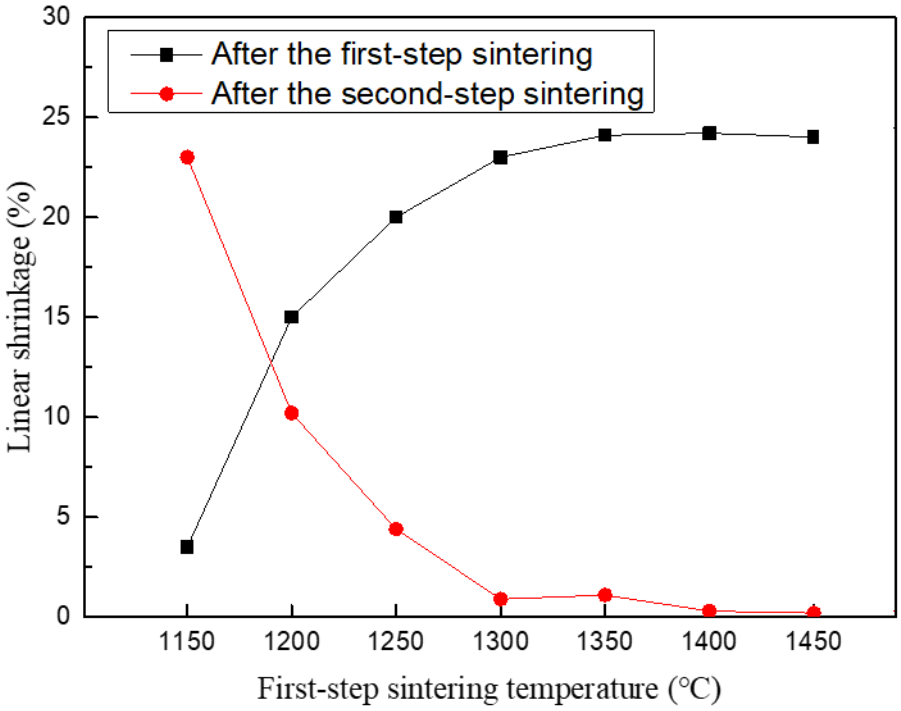

Fig.3-7 *Mean linear shrinkage ratio for zirconia scaffolds after the first-step sintering and second-step sintering at different first-step sintering temperatures ranging from 1150 to 1450 ℃.*

Subsequently, ceramic fractions of scaffolds were measured after the second-step sintering using Archimedes methods and the results are shown in **Fig.3-8**. The ceramic fraction decreased from ~84% to ~58% when the first-step sintering temperature increased from 1150 to 1450 ℃. However, this was a nonlinear process. The ceramic fraction dropped from 84.8% to 62.4% when the first-step sintering temperature increased from 1150 to 1300 ℃ then it continues to decrease until reach 58% when the temperature increased to 1450 ℃.

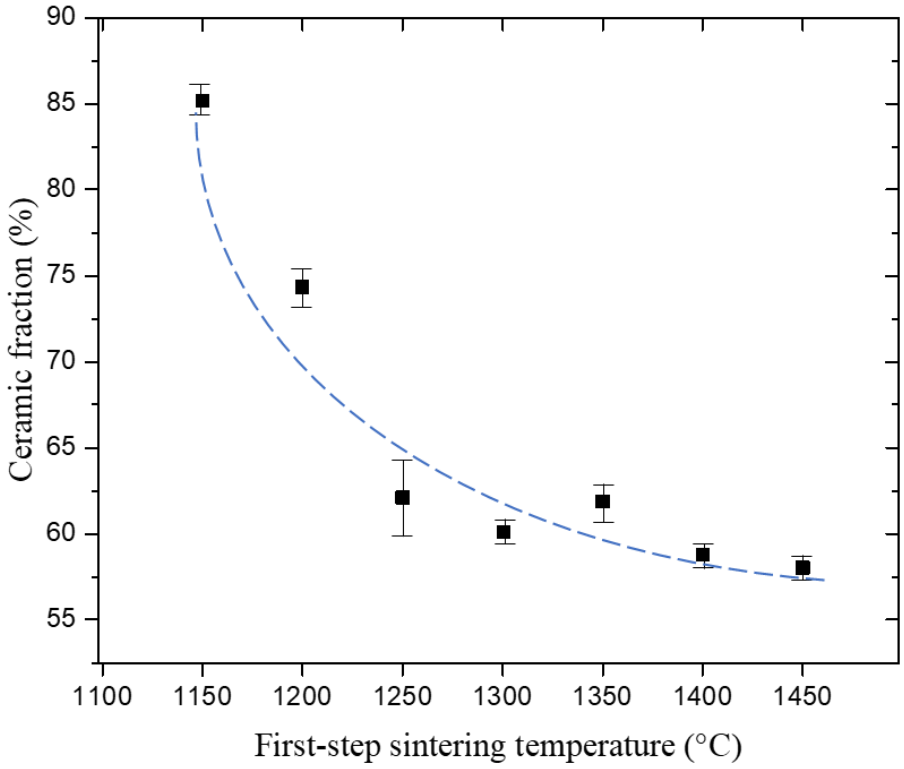

Fig.3-8 The average ceramic fraction of BM zirconia scaffolds as a function of different first-step sintering temperature from 1150 to 1450 ℃.

Fig.3-9 illustrates the microstructure of polymer-infiltrated zirconia scaffold with different first-step sintering temperatures (1150 ℃, 1250 ℃,1350 ℃, and 1450 ℃). When the first-step sintering temperature was 1150 ℃, the ceramic phase displayed a high integrity where the ceramic bricks were connected, resulting in the formation of long ceramic bricks and abundant ceramic bridges between adjacent ceramic layers. This was because the scaffolds obtained at a low first-step sintering temperature of 1150 ℃ still had relatively high sintering activity therefore ceramic layers within a short distance could fuse mutually during second step sintering leading to more connections in the layered structure. In this case, the scaffolds also resulted in a high linear shrinkage after the second-step sintering (**Fig.3-7**) and a higher ceramic

fraction (**Fig.3-8**). At higher first-step sintering temperatures (1250 ℃, 1350℃, and 1450 ℃), scaffolds exhibited separated short bricks imbedded into the polymer phase, also known as a typical brick-and-mortar architecture. The ceramic layers broke down during uniaxial pressing and had a lower sinter ability during the second-step sintering, thus scaffolds exhibited low ceramic fraction and low linear shrinkage after the second-step sintering.

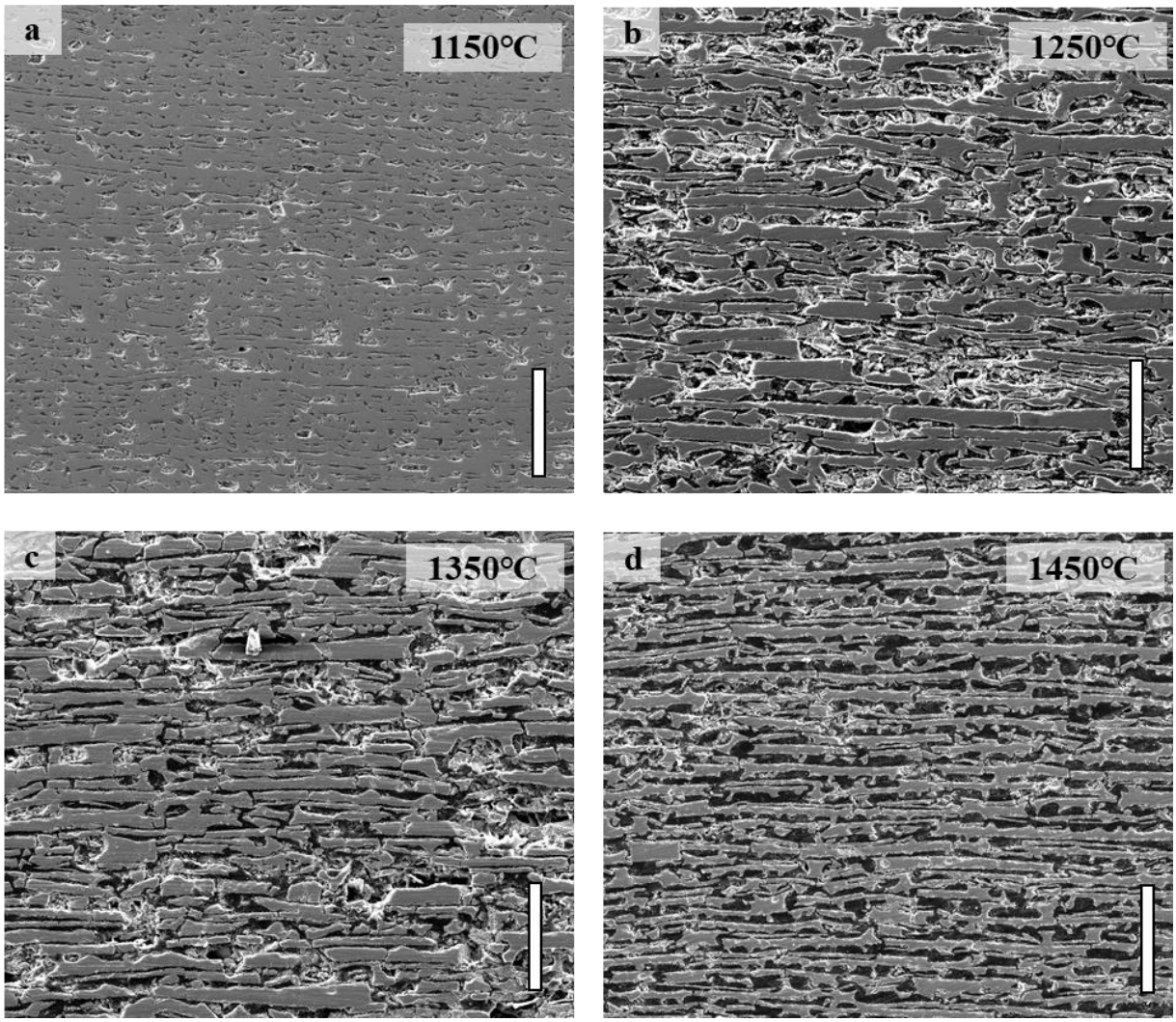

Fig.3-9 *SEM images of polymer-infiltrated zirconia scaffolds produced by the two-step method at first-step sintering temperature of 1150 ℃* ***a)****,1250 ℃* ***b)****, 1350 ℃* ***c)****, and 1450 ℃* ***d)****. Scale bars: 100 µm*

3.3.3.2 One-step method

Three processing parameters were investigated in the one-step method, i.e. binder content, cooling rate, and compressive distance. Their effects on the microstructure of scaffolds were discussed.

3.3.3.2.1 Effect of binder content

Organic binder plays a key role in the one-step method as it can provide strength and elasticity to the ceramic green bodies to maintain the structure during pressing. Different amounts of organic binder (PVA) were added to zirconia slurries with 10% solid loading, where PVA accounted for 1 wt.%, 2 wt.%, 4 wt.%, and 8 wt.% in the freeze-cast slurries. All of the zirconia slurries were frozen at a cooling rate of 40 ℃/min and the resultant scaffolds were densified by one-step method into μL architecture with 72% ceramic fraction. To observe the polished surface and microstructure, all scaffolds were infiltrated with polymer before SEM imaging. The micrographs of polymer-infiltrated zirconia scaffolds are illustrated in **Fig.3-10**. It can be seen that when the binder content was 1 wt.%, 2 wt.% and 4 wt.%, the scaffolds exhibited a distinctive micro scale layered structure. However, the scaffolds obtained from frozen slurries containing 8 wt.% PVA (**Fig.3-10d**) showed a nonuniform net-like microstructure where the layers were linked randomly to adjacent layers and the layer thickness was various from ~10-50 μm. The organic binder of PVA influenced the slurries viscosity, which manipulated the ice growth process, resulting in different morphologies of the lamellar structure. High viscosity slurries produced more ceramic bridges and less homogeneous alignments [11]. It suggests that ceramic scaffolds generated from slurries containing 8 wt.% PVA will produce large amounts of ceramic bridges and poorly aligned lamellar structure that prevented densification under axial-pressing and then generated a net-like nonuniform layered structure.

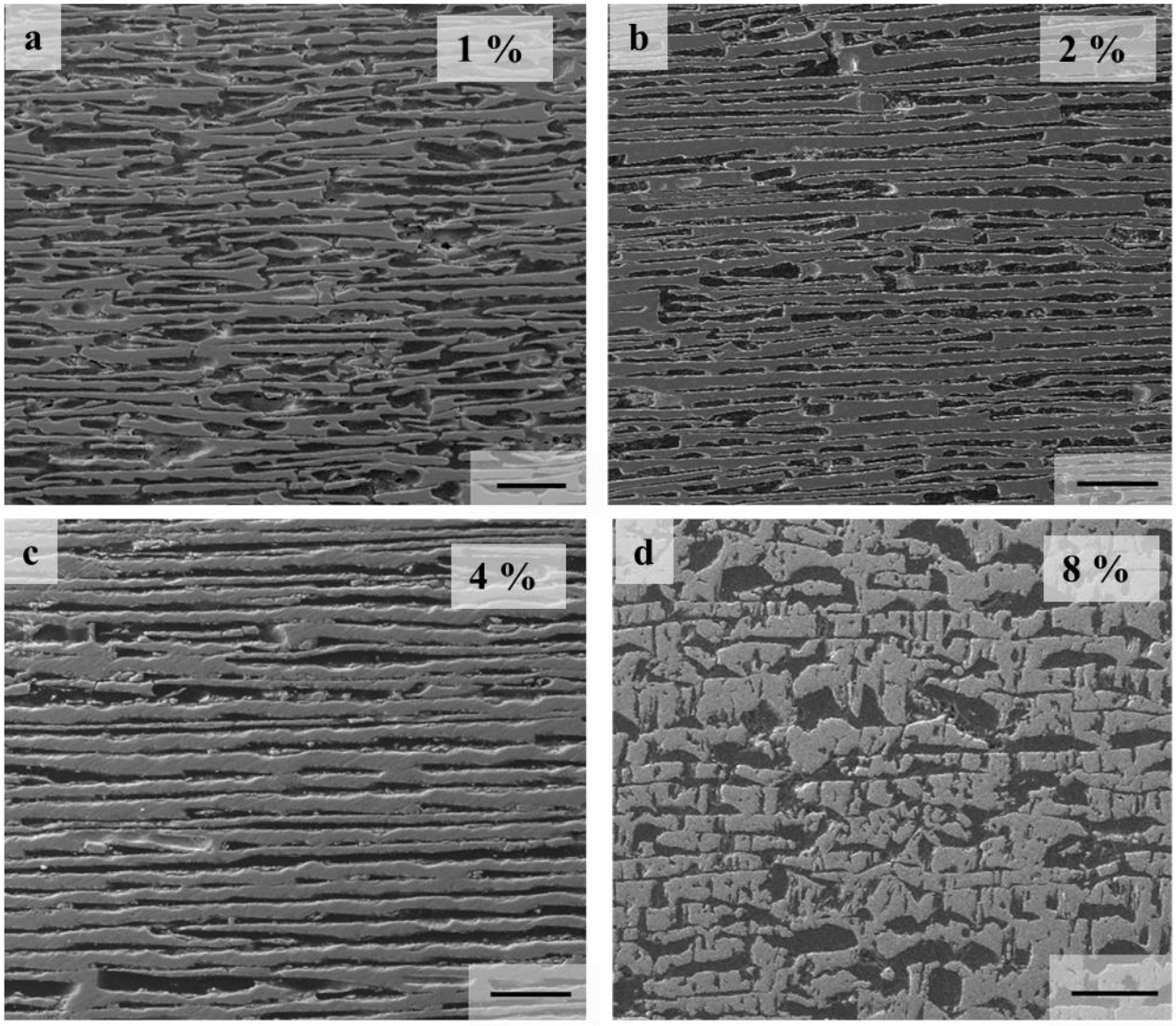

Fig.3-10 *SEM images of µL polymer-infiltrated zirconia scaffolds fabricated with different amounts of PVA content of 1%* ***a)****, 2%* ***b)****,4%* ***c)*** *and 8%* ***d)****. Scale bars: 50 µm*

The ceramic wall lengths in samples with 1 wt.%, 2 wt.% and 4 wt.% binder content were measured, and the histogram analyses are summarised in **Fig.3-11**. At 1 wt.% PVA concentration, the polymer-infiltrated scaffolds (**Fig.3-10a**) displayed a relatively short ceramic walls where the majority of ceramic length value is in the range of 100-200 µm. In this case, a small quantity of binder led to weak ceramic walls in ceramic scaffold green bodies which were not strong enough to maintain the lamellar structure during uniaxial pressing. This

resulted in a brick-and-mortar-like instead of micro-layered architecture. When the binder content was increased to 2 wt.%, the ceramic scaffold green bodies were strengthened resulting in fewer layer breakage during uniaxial densification and the longer ceramic layers were obtained (500 µm). Furthermore, by freezing 4 wt.% binder slurries, the strength of scaffolds was further improved and 38.1% of ceramic walls achieved the length around 2500 µm. It implies that PVA could effectively increase the length of a ceramic wall in the µL scaffolds produced by the one-step method. Similar results were obtained for other ceramic systems such as alumina. Therefore, ceramic slurries with 4 wt.% binder content will be used in the future work to produce the µL scaffolds.

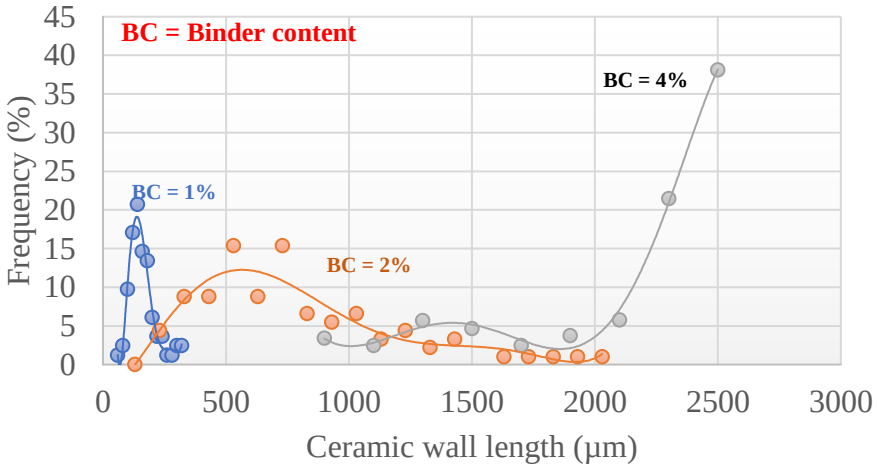

Fig.3-11 *The statistical results of ceramic wall length in micro-layered structure with various binder content.*

3.3.3.2.2 Effect of cooling rate

As shown in 3.2.2, 10% zirconia slurries were frozen bi-directionally with different cooling rates (11 °C/min, 20 °C/min and 40 °C/min) to produce lamellae scaffolds altering ceramic wall thickness. Afterwards, the ceramic lamellar scaffolds were processed by freeze-drying and densification using the one-step method. Nacre-like zirconia scaffolds with µL architecture and 72% ceramic fraction were obtained. According to the SEM images in **Fig.3-12**, all samples

exhibited continuous and highly aligned lamellae structure along the scaffolds and finer dendritic morphology and thinner ceramic walls at a high cooling rate. Specifically, the high cooling rate not only produced controlled structure with defined lamellae thickness, but also changed the ice morphology from large lamellar to small dendritic crystals due to supercooling effects [18]. Using ImageJ analyse, **Fig.3-13** illustrates that the ceramic wall thickness was reduced by half from around 16 to 8 µm when the cooling rate increased from 10 ℃/min to 40 ℃/min. Although the results exhibited large standard errors, this also agreements in the nature of freeze casting according to the previous work reported in 2019 [5].

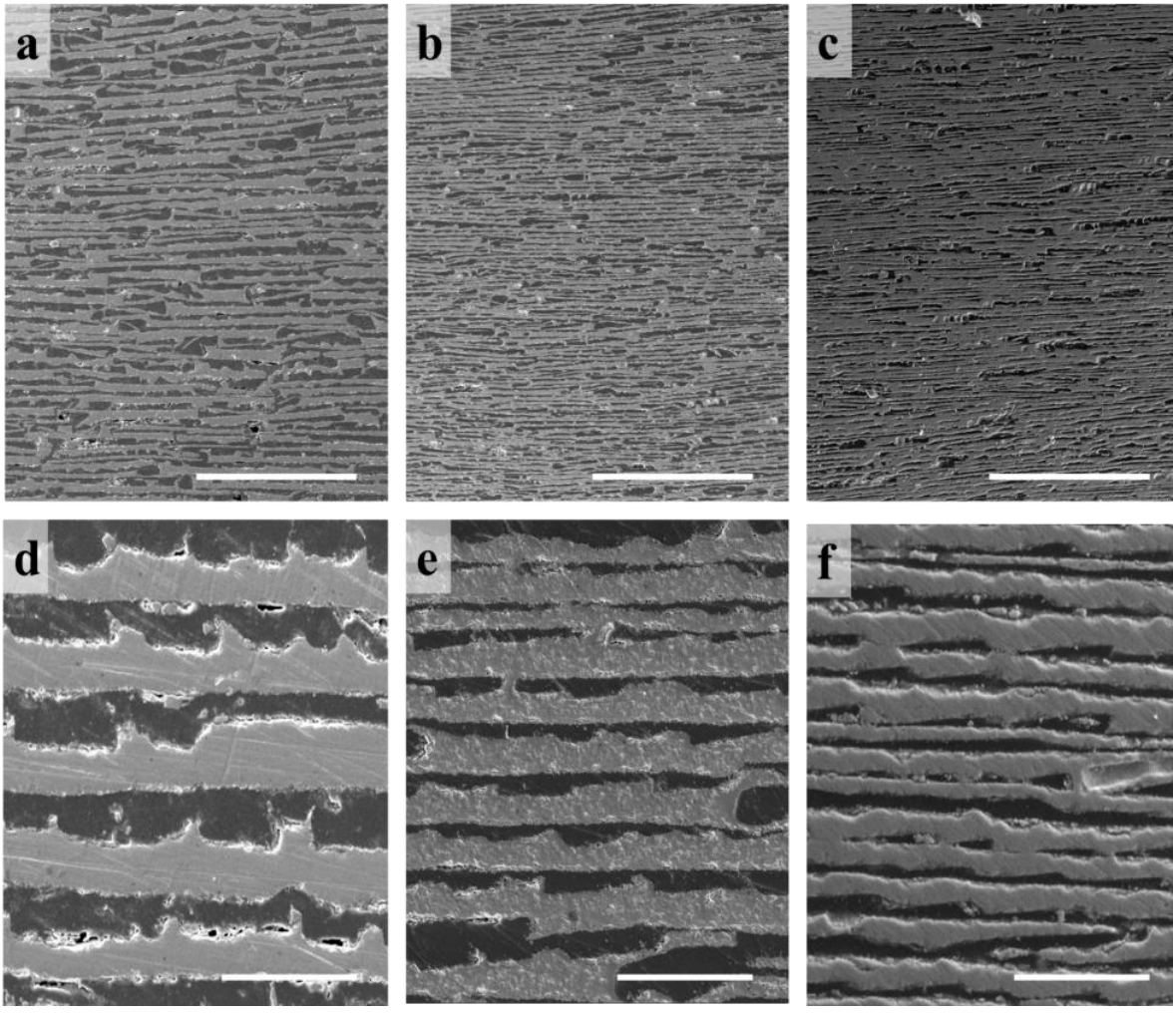

Fig.3-12 *SEM micrographs of polymer-infiltrated µL zirconia scaffolds from 10% zirconia slurries processed at increasing freezing rates of 11 ℃/min* ***a)***, ***d)***, *20 ℃/min* ***b)***, ***e)***, *and 40 ℃/min* ***c)***, ***f)***. *Scale bars:* ***a)***, ***b)***, *and* ***c)*** *500 µm;* ***d)***, ***e)***, *and* ***f)*** *50 µm.*

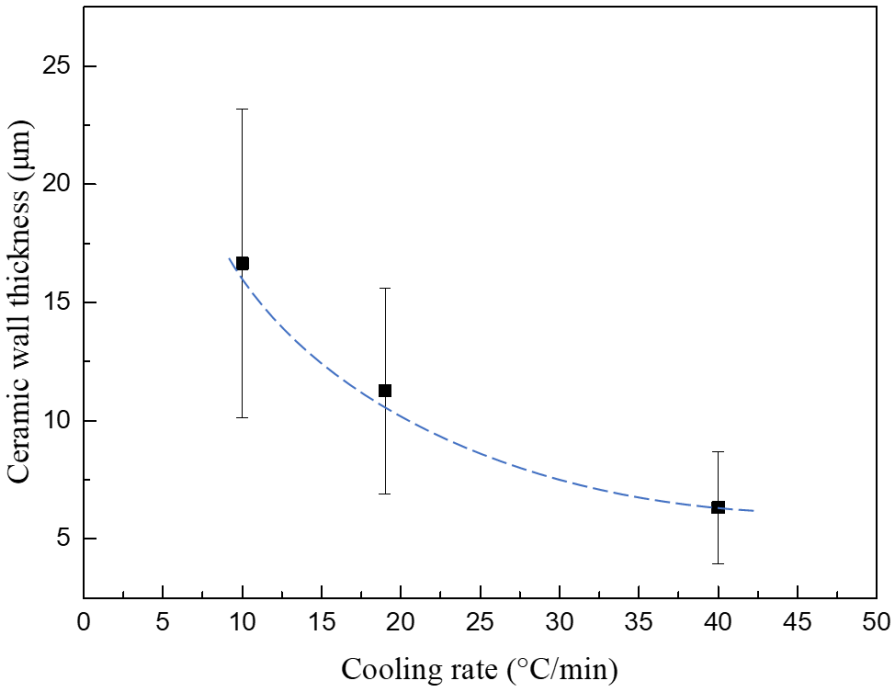

Fig.3-13 *The average ceramic wall thickness as a function of the cooling rate.*

3.3.3.2.3 Compressive distance

One of the most distinct advantages of the one-step method is that the ceramic fraction of μL scaffolds could be simply controlled by uniaxial pressing. Here, ceramic scaffolds were obtained from 10% alumina or zirconia slurries at a cooling rate of 40 ℃/min. To follow the bi-directional freeze casting, the scaffolds were infiltrated with a wax without sintering and pressed using a mechanical testing machine at various compressive distances as shown in **Fig.3-14.** The relation between the compressive distance and ceramic fraction was determined by the equation 3.2:

$$D = T - (T \times C_b)/C_a \quad (3.2)$$

where D is the compression distance; T is the thickness of green scaffold/wax before compression, and C_b and C_a are ceramic fractions before and after compression, respectively. Since the size of the freeze casting mound in this work is 60×60 mm, T=60 mm.

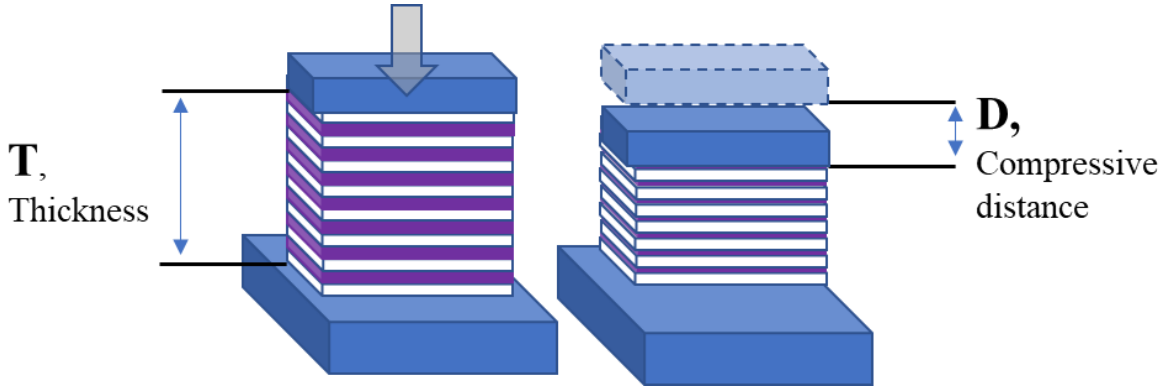

Fig.3-14 Schematics of the densification process in the one-step method.

Fig.3-15 showed the ceramic fraction (measured by Archimedes principle after sintering) of scaffolds produced by altering the compressive distance. As can be seen, the zirconia and alumina scaffolds were prepared with different ceramic fractions from 60 to 72 vol.% and 50 to 85 vol.%, respectively. There was a maximum compression distance for the μL scaffolds. i.e. the scaffolds displayed a maximum ceramic fraction of 72 vol.% for zirconia and 85 vol.% for alumina. The distinctive layered microstructure disappeared when the ceramic fraction was above the maximum compressive distance where the adjacent ceramic walls were too close after pressing; they fused mutually and lost distinct layered microstructure in the subsequent sintering stage.

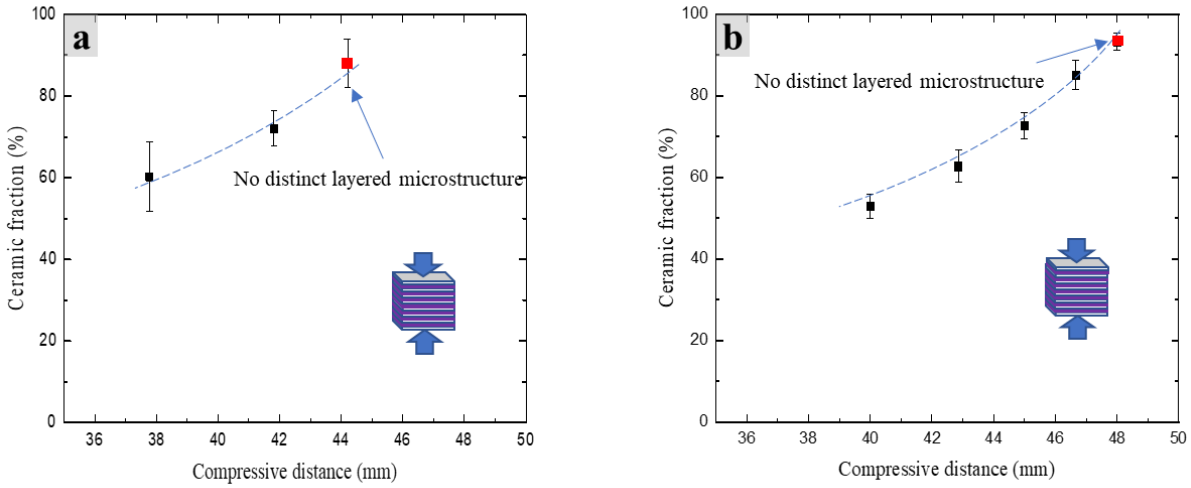

Fig.3-15 *The average ceramic fraction of zirconia* ***a)*** *or alumina* ***b)*** *scaffolds vs. compressive distance after densification. The maximum ceramic fractions of the µL architectures are indicated with red squares in the graphs.*

3.3.3.2.4 Effect of solid loading

Alumina was used to investigate the effect of solid loading because of the relative high radio-opacity of zirconia compared to alumina [19] in the later X-ray synchrotron studies of nacre-like composites (Chapter 4). Alumina slurries were prepared with 4 wt.% PVA but varied solid loading from 10% to 40%. After bi-directional freeze casting at a cooling rate of 40 °C/min and using the one-step densification method, the alumina µL scaffolds were fabricated at 72% ceramic fraction. The densified ceramic scaffolds were then infiltrated with polymer and analysed by SEM imaging. **Fig.3-16** showed the microstructure of the µL scaffolds with various layer thicknesses under different solid loadings of alumina slurry. The SEM images were analysed by ImageJ and the results of ceramic wall thickness were illustrated in **Fig.3-16e**. Typically, alumina slurries with solid loadings from 10 to 40 vol.% generated the µL scaffolds with a wall thickness from 8 to 40 µm. Generally speaking, during freeze casting, slurry solid loading has a significant influence on morphologies, e.g. the lamellar thickness of

scaffolds where higher solid loading led to thicker lamellae and high ceramic fraction at the same time [1, 18].

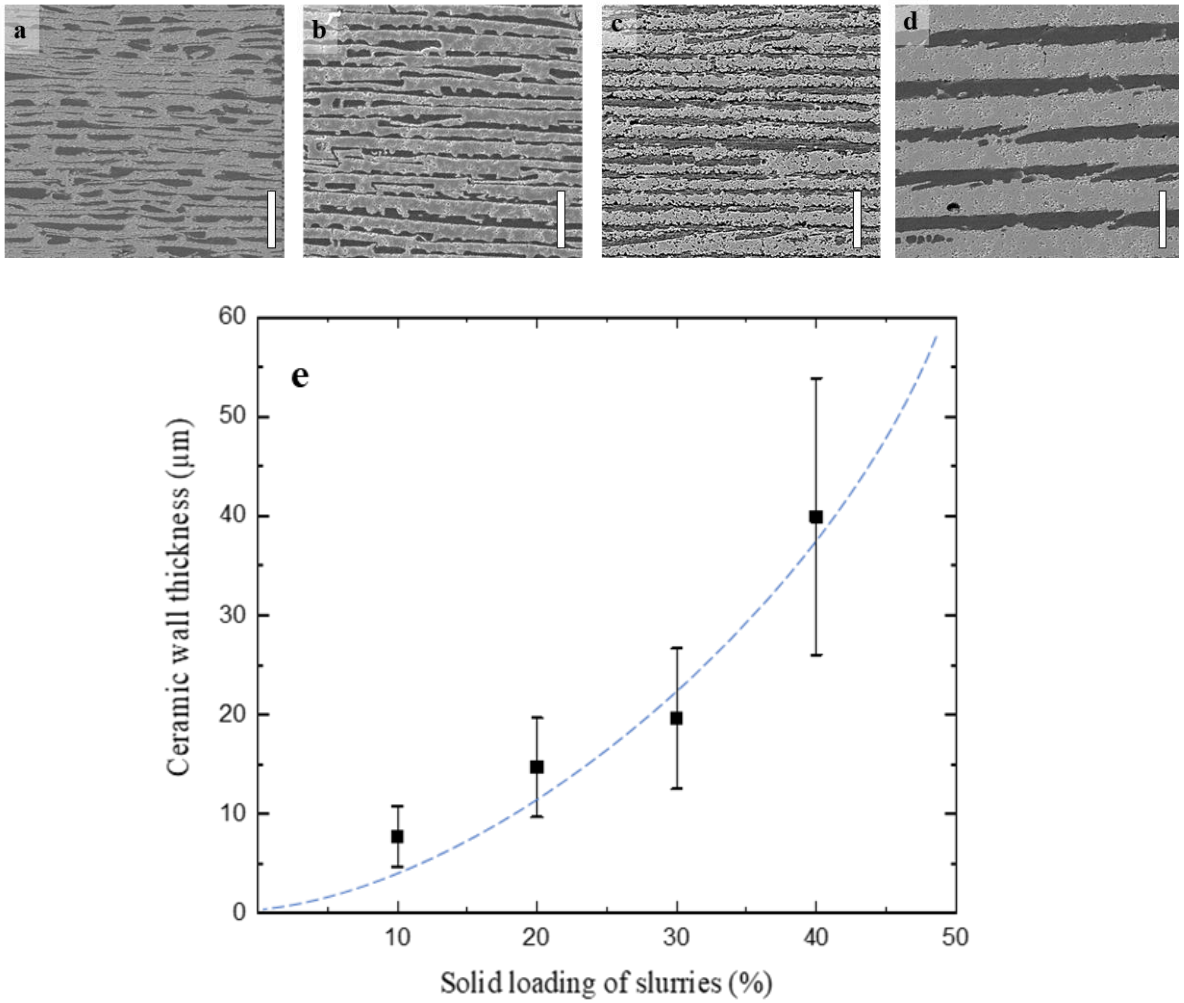

Fig.3-16 *SEM images of μL polymer-infiltrated alumina fabricated from 10%* ***a)****, 20%* ***b)****, 30%* ***c)****, and 40%* ***d)*** *slurries. The ceramic wall thickness in μL scaffolds were analysed and summarized by a plot of ceramic wall thickness vs. solid loading of slurries* ***e)****. Scale bars: 50 μm.*

3.3.4 Mechanical properties of ceramic scaffolds

To investigate the influence of different architectures on mechanical performance of the nacre-like ceramic scaffolds, compressive testing was conducted on the scaffolds with both μL and BM architectures fabricated using the one-step and two-step method, respectively. Because

both μL and BM scaffolds had highly anisotropic architectures, compressive tests were operated in two different directions: z- and x-direction (as shown **Fig.3-17**). Here, 'z-direction' is perpendicular to ceramic lamellae direction while 'x- direction' is parallel to ceramic lamellae direction. Two different types of ceramics (alumina and zirconia) were used to build up μL and BM scaffolds for compressive testing. All the nacre-like ceramic scaffolds were prepared at the same solid loading (10 vol.%), cooling rate (40 ℃/min) and with the same ceramic fraction (72 vol.%) and ceramic wall thickness (8 μm). The mechanical properties of compressive strength are summarised in **Fig.3-17**. Labels on samples with different architectures and testing directions are named in the following format: testing direction/architecture. For example, 'z-direction/BM' represents testing of the BM scaffolds in the z-direction.

As can be seen, for both μL and BM nacre-like scaffolds, compressive strength in the z-direction was higher than that in the x-direction. In particular, the BM alumina scaffolds exhibited a compressive strength at 72.9 MPa in the z-direction, which doubled the strength in the x-direction (36.5 MPa). Moreover, the compressive strength of the μL alumina scaffolds in the z-direction reveals ~15% improvement compared to the x-direction, increasing from 43.7 MPa to 50.9 MPa. This was also true for zirconia scaffolds that showed higher strength in the z-direction. The overall compressive strengths of zirconia scaffolds are superior to alumina scaffolds because the zirconia is inherently stronger than alumina.

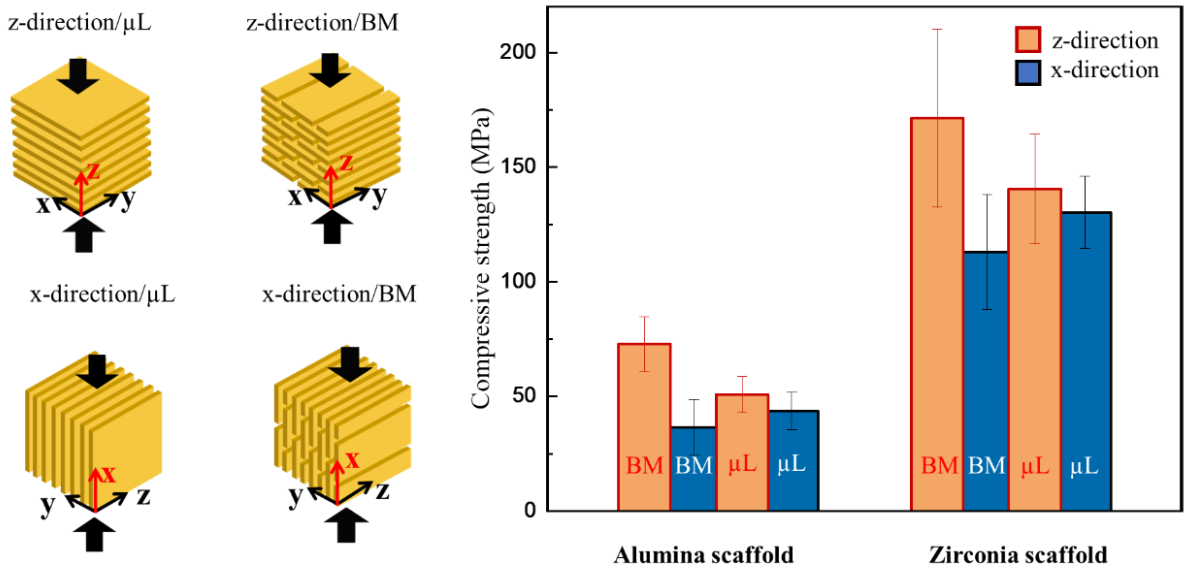

Fig.3-17 Compressive strength of nacre-like ceramic scaffolds with 72% ceramic fraction in different directions (x-direction and z-direction) and architectures (BM and µL).

According to the stress-strain curves of compressive testing on nacre-like alumina scaffolds illustrated in **Fig.3-18**, all curves reveal a stress plateaus before failure rather than brittle failure. It was difficult to find obvious linear elastic region from all materials thus no results of stiffness were obtained in compression tests. Apart from the µL scaffold in the x-direction, other samples exhibited extremely slow growing stress in the first ~4% strain because they underwent a densifying process during compressive testing.

As illustrated in **Fig.3-19**, the compression can be divided into two stages: the stage one was known as densifying process, where the distance between layers decreased under compressive loads because porosity in the lamellar structure was gradually reduced. In the stage two, the scaffolds started to withstand loads and then failed when reaching the maximum load. Here, only the BM scaffolds in both x and z-directions, and the µL scaffolds in the z-direction exhibited stage one densifying behaviour, resulting in slow stress increase in the beginning. On

the other hand, the µL scaffold in the x-direction withstood load from the beginning since the long and continuous lamellae were aligned in parallel to the compressive load direction.

For ceramic scaffolds with both µL and BM architectures, the compressive strain-stress curves along the x-direction illustrate some stepwise peaks before maximum stress, indicating the presence of crack deflections [20]. The fractured samples showed a flake-like structure, suggesting that ceramic walls tended to crush individually rather than collectively. In this case, ceramic layers are prone to delamination, leading to flake-like structure and relatively low compressive strength.

The results of mechanical testing (**Fig.3-17**) reveal that the scaffolds with different architectures exhibited different compressive strength. In particular, in the x-direction, the BM scaffolds had approximately 20% lower compressive strength compared to the µL scaffolds for both alumina and zirconia. This was because the ceramic layers in the µL scaffolds with longer ceramic walls offered better connectivity and stress-transfer, resulting in higher strength. However, in the z-direction, the BM scaffolds were approximately 30-40% stronger than the µL scaffolds. From the strain-stress curves (**Fig.3-18**), both µL and BM scaffolds displayed a similar failure behaviour because both scaffolds experienced a two-stage compressive failure. Nevertheless, the BM scaffolds crushed into a powder-like structure, while the µL scaffolds showed a diagonal crack (**Fig.3-19**). This may be attributed to a brick-sliding mechanism in the BM scaffolds as they are composed of individual ceramic bricks. Brick-sliding is a critical mechanism found in natural nacre [21] and artificial nacre-like materials [22-24]. As a result, the BM scaffolds underwent extended fracture during compressive testing and yielded high strength. By contrast, for the µL scaffolds, although the connectivity of ceramic walls traversing to the freezing direction prevented ceramic walls from buckling or shearing with each other when tested in the z orientation, the µL scaffolds with completely connected ceramic walls, leading to stress concentration.

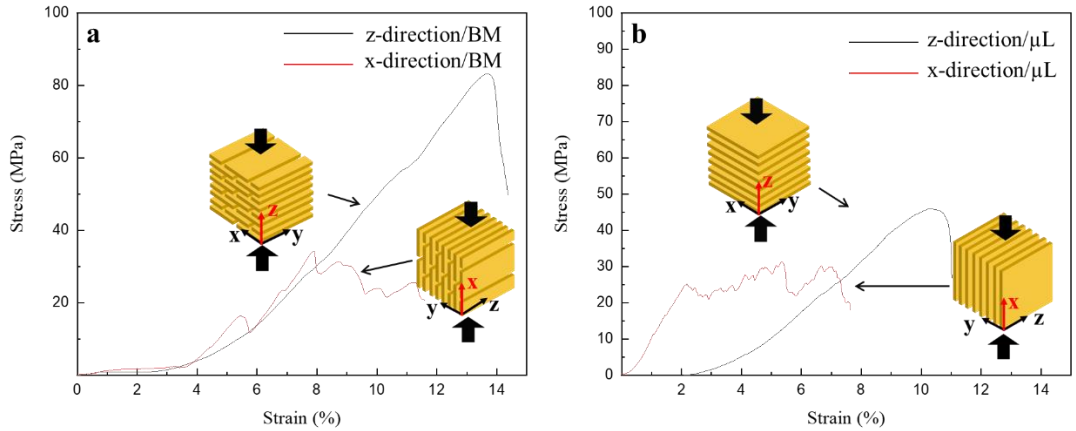

Fig.3-18 *The stress-strain curves of compressive testing on nacre-like alumina scaffolds. The testing was carried out in two different directions with two different architectures: BM* ***a)*** *and μL* ***b)****.*

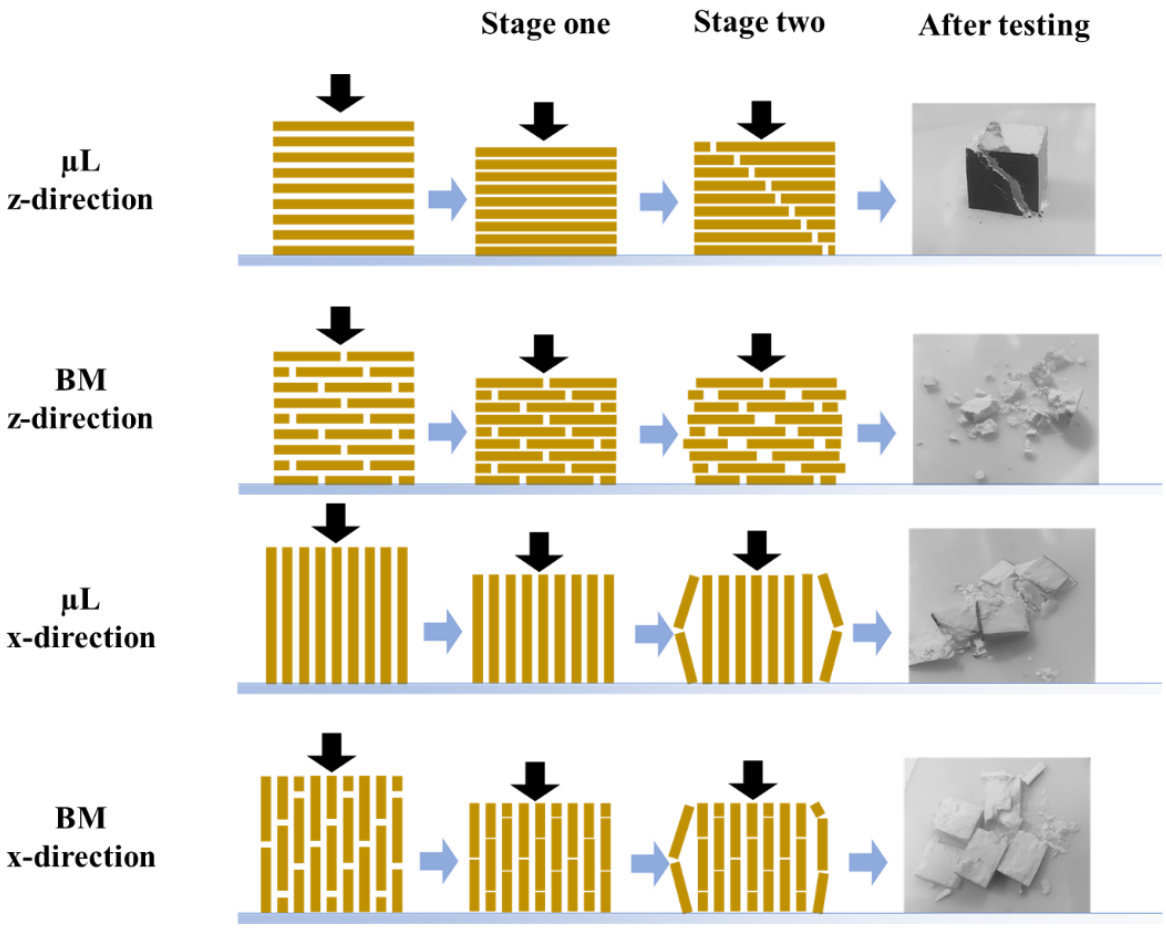

Fig.3-19 *Schematics show the compressive process of nacre-like alumina scaffolds and the fractured behaviours after compressive testing.*

3.4 Conclusions

To conclude, nacre-like BM and µL ceramic scaffolds were prepared via bi-directional freeze casting. Freezing ceramic slurries with optimum amount of dispersant produced highly aligned lamellae scaffolds with dendritic-like surface on one side. The dendritic-like surface could play a significant role in the formation of ceramic bridges during densification and the mechanical properties of the resultant composites (4.3.2.2.2). After densification from both one-step and two-step method, the final ceramic scaffolds exhibited nacre-like BM and µL architectures, depending on the densification method and processing conditions. Specifically, using the two-step method, the ceramic fraction and microstructure were manipulated as a function of the first-step sintering temperature in the BM ceramic scaffolds. Using the one-step method, ceramic scaffolds with a distinctive µL architecture were achieved by altering the binder content from 1% to 4%, where the scaffolds displayed different ceramic wall length from 200 to 2500 µm. The ceramic wall thickness, varying from 8 to 40 µm, was manipulated by the cooling rate and solid loading of slurries. The µL scaffolds with ceramic fractions up to 85% for alumina and 72% for zirconia were produced by uniaxial pressing at different compressive distance.

Without any polymer or metal infiltration, the nacre-like alumina and zirconia scaffolds showed high compressive strengths up to 171.3 MPa, depending on testing direction and architectures. With the chosen densification method and processing conditions, the as-prepared ceramic scaffolds with good mechanical properties and defined architecture could be employed for the fabrication of nacre-like ceramic/polymer and ceramic/metal composite materials in Chapter 4 and Chapter 5, respectively. The work in this Chapter laid foundation for further optimisation of mechanical properties of nacre-like composite materials for specific applications.

3.5 References

[1] A. Preiss, B. Su, S. Collins, D. Simpson, Tailored graded pore structure in zirconia toughened alumina ceramics using double-side cooling freeze casting, Journal of the European Ceramic Society 32(8) (2012) 1575-1583.

[2] J. Liao, H. Chen, H. Luo, X. Wang, K. Zhou, D. Zhang, Direct ink writing of zirconia three-dimensional structures, Journal of Materials Chemistry C 5(24) (2017) 5867-5871.

[3] S.P. Rao, S.S. Tripathy, A.M. Raichur, Dispersion studies of sub-micron zirconia using Dolapix CE 64, Colloids and Surfaces A: Physicochemical and Engineering Aspects 302(1) (2007) 553-558.

[4] S. Bhattacharjee, S.K. Swain, D.K. Sengupta, B.P. Singh, Effect of heat treatment of hydroxyapatite on its dispersibility in aqueous medium, Colloids and Surfaces A: Physicochemical and Engineering Aspects 277(1) (2006) 164-170.

[5] S. Algharaibeh, A.J. Ireland, B. Su, Bi-directional freeze casting of porous alumina ceramics: A study of the effects of different processing parameters on microstructure, Journal of the European Ceramic Society 39(2) (2019) 514-521.

[6] K. Lu, X. Zhu, Freeze Casting as a Nanoparticle Material-Forming Method, International Journal of Applied Ceramic Technology 5(3) (2008) 219-227.

[7] Y. Huang, H. Xiong, J. Zou, K. Zhou, D. Zhang, Ultralight porous SiC with attracting strength: Freeze casting of polycarbosilane/SiCp/camphene-based suspensions, Ceramics International 46(7) (2020) 9582-9589.

[8] F. Xue, K. Zhou, N. Wu, H. Luo, X. Wang, X. Zhou, Z. Yan, I. Abrahams, D. Zhang, Porous SiC ceramics with dendritic pore structures by freeze casting from chemical cross-linked polycarbosilane, Ceramics International 44(6) (2018) 6293-6299.

[9] S. Dhara, P. Bhargava, Influence of Nature and Amount of Dispersant on Rheology of Aged Aqueous Alumina Gelcasting Slurries, Journal of the American Ceramic Society 88(3) (2005) 547-552.

[10] H. Sarraf, J. Havrda, Rheological behavior of concentrated alumina suspension: effect of electrosteric stabilization, Ceramics Silikaty 51(3) (2007) 147.

[11] M.M. Porter, R. Imperio, M. Wen, M.A. Meyers, J. McKittrick, Bioinspired scaffolds with varying pore architectures and mechanical properties, Advanced Functional Materials 24(14) (2014) 1978-1987.

[12] Y. Zhang, K. Zhou, Y. Bao, D. Zhang, Effects of rheological properties on ice-templated porous hydroxyapatite ceramics, Materials Science and Engineering: C 33(1) (2013) 340-346.

[13] S. Deville, E. Saiz, A.P. Tomsia, Ice-templated porous alumina structures, Acta Materialia 55(6) (2007) 1965-1974.

[14] M.E. Launey, E. Munch, D.H. Alsem, H.B. Barth, E. Saiz, A.P. Tomsia, R.O. Ritchie, Designing highly toughened hybrid composites through nature-inspired hierarchical complexity, Acta Materialia 57(10) (2009) 2919-2932.

[15] H. Bai, F. Walsh, B. Gludovatz, B. Delattre, C. Huang, Y. Chen, A.P. Tomsia, R.O. Ritchie, Bioinspired Hydroxyapatite/Poly(methyl methacrylate) Composite with a Nacre-Mimetic Architecture by a Bidirectional Freezing Method, Advanced Materials 28(1) (2016) 50-56.

[16] A. Wat, J.I. Lee, C.W. Ryu, B. Gludovatz, J. Kim, A.P. Tomsia, T. Ishikawa, J. Schmitz, A. Meyer, M. Alfreider, D. Kiener, E.S. Park, R.O. Ritchie, Bioinspired nacre-like alumina with a bulk-metallic glass-forming alloy as a compliant phase, Nature Communications 10(1) (2019) 961.

[17] M. Sambasivam, R. White, K. Cutting, 12 - Exploring the role of polyurethane and polyvinyl alcohol foams in wound care, in: M.S. Ågren (Ed.), Wound Healing Biomaterials, Woodhead Publishing2016, pp. 251-260.

[18] V. Naglieri, H.A. Bale, B. Gludovatz, A.P. Tomsia, R.O. Ritchie, On the development of ice-templated silicon carbide scaffolds for nature-inspired structural materials, Acta Materialia 61(18) (2013) 6948-6957.

[19] Y. Okuda, M. Noda, H. Kono, M. Miyamoto, H. Sato, S. Ban, Radio-opacity of core materials for all-ceramic restorations, Dental materials journal 29(1) (2010) 35-40.

[20] K.H. Kim, D.H. Kim, S.C. Ryu, S.Y. Yoon, H.C. Park, Porous mullite/alumina-layered composites with a graded porosity fabricated by camphene-based freeze casting, Journal of Composite Materials 54(12) (2016) 1527-1534.

[21] F. Barthelat, H. Tang, P.D. Zavattieri, C.M. Li, H.D. Espinosa, On the mechanics of mother-of-pearl: A key feature in the material hierarchical structure, Journal of the Mechanics and Physics of Solids 55(2) (2007) 306-337.

[22] Z. Yin, F. Hannard, F. Barthelat, Impact-resistant nacre-like transparent materials, Science 364(6447) (2019) 1260.

[23] K.C. Datsiou, Bioinspired improvement of laminated glass, Science 364(6447) (2019) 1232.

[24] F. Barthelat, D. Zhu, A novel biomimetic material duplicating the structure and mechanics of natural nacre, Journal of Materials Research 26(10) (2011) 1203-1215.

Chapter 4

Nacre-like ceramic/polymer composites

Results in section 4.3.2.2.2 and 4.3.2.3 were published:

H. Wan, N. Leung, S. Algharaibeh, T. Sui, Q. Liu, H.-X. Peng, B. Su, Cost-effective fabrication of bio-inspired nacre-like composite materials with high strength and toughness, Composites Part B: Engineering 202 (2020) 108414.

4.1 Introduction

In the previous chapter (Chapter 3), nacre-like ceramic scaffolds were prepared by bi-directional freeze casting and densification with controllable microstructure and feature size. To obtain nacre-like ceramic composites with improved mechanical performance (high strength and toughness), ceramic scaffolds could be infiltrated with compliant phases. Polymers have been widely used to infiltrate into ceramic scaffolds to produce tough and strong composites [1]. For example, polymethyl methacrylate (PMMA), polyacrylic methacrylate (PLMA), and polyether urethane diacrylate-co-poly (2-hydroxyethyl methacrylate) (PUA-PHEMA) were individually infiltrated into nacre-like ceramic scaffolds and the resultant ceramic/polymer composites displayed remarkable mechanical properties, especially fracture toughness [2, 3]. In this chapter, the nacre-like ceramic scaffolds generated in Chapter 3 will be infiltrated with different polymeric compliant phases. The principal aim was to study the mechanical properties of synthetic nacre-like ceramic/polymer composites and their influencing factors including materials and fabrication processing parameters, thus flexural strength, compressive strength, stiffness, and fracture toughness (K_{IC} and *R*-curve) were evaluated. Since two different ceramic scaffolds were produced with two distinctive nacre-like architectures i.e. brick-and-mortar (BM) and micro-layered (μL) in Chapter 3, their corresponding composites will be discussed in two separate sections (4.3.2.1 and 4.3.2.2).

For BM architecture, ceramic scaffolds were infiltrated with PMMA and the effects of first-step sintering temperature in two-step densification method and silanization on mechanical properties were studied. The first-step sintering temperature was shown to manipulate microstructure and ceramic fraction of scaffolds as well as composites (Chapter3). Here, this section will mainly concentrate on the mechanisms underlying relationships between the first-step sintering temperature and mechanical properties of BM ceramic/polymer composites. As an important factor to influence the mechanics of composite materials, the interfaces played a significant role in natural biological materials (nacre, bone and wood) as reported by Barthelat *et al.* [4] This also inspired design strategies for synthetic biological materials. Therefore, the effect of interface on mechanical performance will be investigated. Silanization was an effective means to enhance the adhesion between ceramic and polymer [5], thereby the ceramic surface of scaffolds was modified by a silane coupling agent before infiltration of polymer. Here, the mechanism of silane coupling agent was to connect molecules between ceramic and polymer via covalent bonds to promote the interfacial bonding of composite materials. The silane-grafted ceramic surface was characterised via attenuated total reflectance (ATR)-Fourier-transform infrared spectroscopy (FT-IR) to ensure the successful silanization on ceramic.

For µL architecture, studies were carried out on mechanical performance dependence of microstructure (wall length, wall thickness, and ceramic fraction), polymer type [PMMA, copolymer of urethane dimethacrylate (UDMA)/triethylene glycol dimethacrylate (TEGDMA), polyurethane (PU) and epoxy resin], and ceramic type (alumina, zirconia). Considering that nacre's exceptional mechanical properties are attributed by its special layered architectures, adjustment on the microstructure of nacre-like composite materials offered effective ways to build up stronger and tougher materials. Therefore, for nacre-like composites, the effects of layer thickness [6], ceramic fraction [7], and aspect ratio [8] were widely studied. In addition,

the effect of constituents on mechanical properties of composites was also studied by simulation [9]. Herein, this work will focus on the ceramic/polymer composites with μL architecture and examine the relationships between mechanics and microstructure and composition.

Finally, the μL composites will compare with the BM composites (4.3.2.3). It is a classic competition between layered (lamellar) and BM architectures, recent studies have compared two architectures in zirconia/methacrylate resin [10], alumina/PMMA [6], and alumina/Zr-based bulk-metallic glass (BMG) composites [11]. Their results showed that the BM composites obtained better mechanical performance in most cases. However, the layered composites generally had a lower ceramic fraction, which made them not directly comparable. In this work, the novel one-step densification and conventional two-step densification methods were employed to produce μL and BM composites with the same ceramic fraction and ceramic wall thickness, which enabled the direct comparison of mechanical performance of nacre-like composites with only different architectures.

4.2 Materials and methods

4.2.1 Silanization

Before the silanization process, ceramic scaffolds were modified by piranha solution. The piranha solutions were prepared by adding hydrogen peroxide droplet into concentrated sulfuric acid slowly at 90 ℃. Hence, the ceramic scaffolds were immersed in piranha solution (15 vol.% H_2O_2, 15 vol.% H_2SO_4, 70 vol.% H_2O) at 90 ℃ for 20 min. The piranha solution an oxidizing agent with is a strong corrosive because it contains abundant extremely reactive atomic oxygen species, which can then chemically eliminate the organic contamination and generate hydroxyl groups on the ceramic surface during the piranha solution treatment (**Fig.4-1**) [6, 12, 13]. Afterwards, the ceramic scaffolds were then rinsed by deionised (DI) water under

low-power ultrasonic (50% power) for 15 min and 7-10 times, until the pH value of solution on ceramic surface is above 6. The purpose of the ultrasonication process was to ensure the removal of residue piranha solution that may remain inside the ceramic scaffolds.

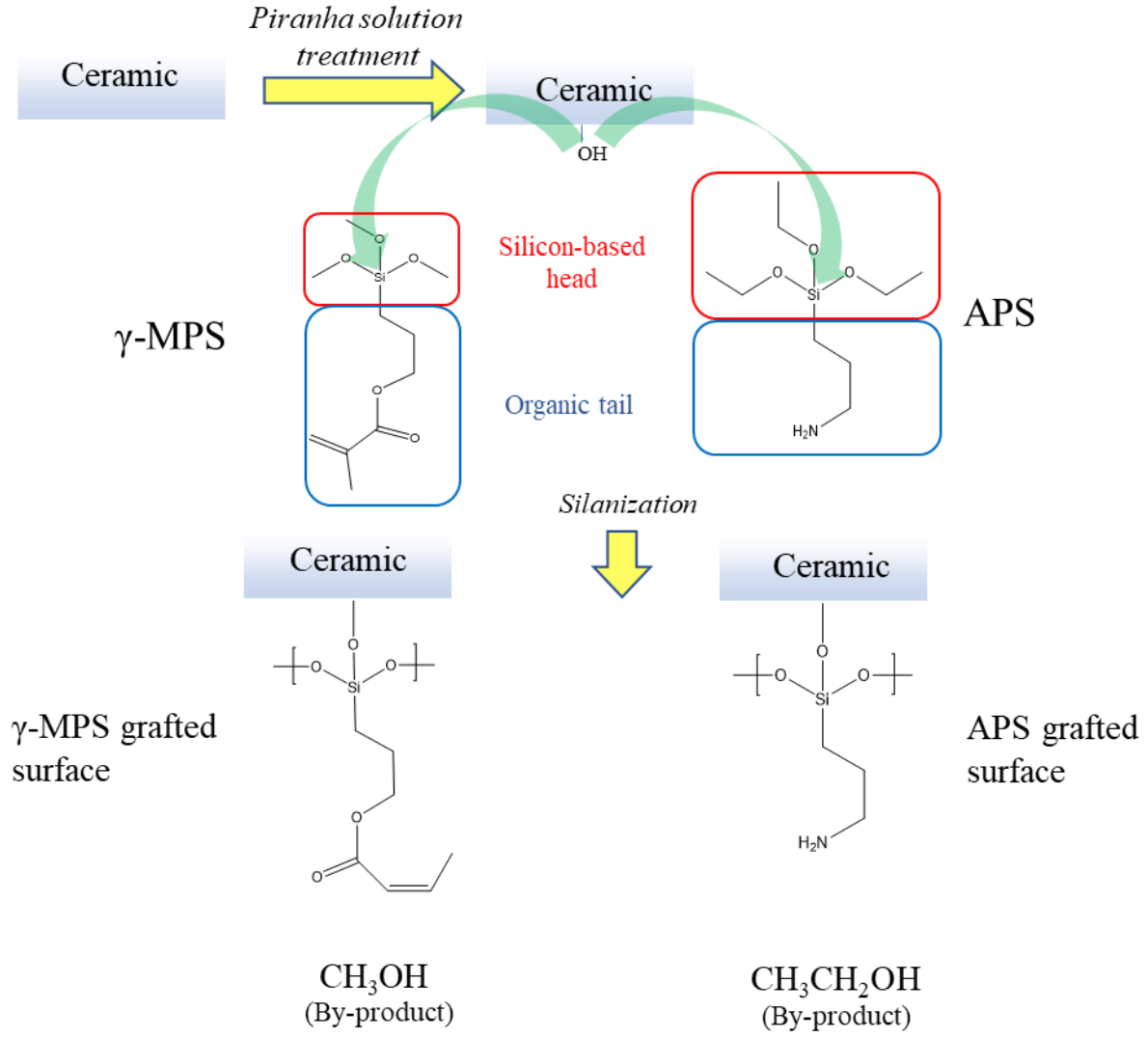

Fig.4-1 *The conceptual schematic diagram of piranha solution treatment (hydroxylation) and silanization of ceramic surface by γ-MPS and APS.*

Following on drying in oven at 90 ℃ for 4 hours, ceramic scaffolds were immersed into the solution of a silane coupling agent (50 vol.% silane, 50 vol.% acetone) for 12 hours for silanization. Two different silane coupling agents were used in this work i.e. 3-(Trimethoxysilyl) propyl methacrylate (γ-MPS) and 3-(Aminopropyl) triethoxysilane (APS)

(**Fig.4-1**). The silane coupling agent commonly acts as a sort of intermediary which bonds organic and inorganic molecules. The silane molecule consists of a 'silicon-based head' (red box) and an 'organic tail' (blue box) (**Fig.4-1**) which can connect with inorganic and organic phase, respectively. Specifically, the silicon-based head can link steadily to reactive groups on substrate surface (e.g. glass, metal and ceramic) via covalent bond. For instance, on ceramic surface, the -OH (hydroxyl group) generated during piranha solution treatment will react with the -Si-OR (R is $-CH_3$ for γ-MPS and $-CH_2CH_3$ for APS) on the head of silane molecule (green arrows) and then produce H-OR (by-product) and silane grafted ceramic surface as shown in **Fig.4-1**. After the grafting process, the ceramic scaffolds were rinsed with acetone to remove the by-product and unreacted silane coupling agents. On the other side of silane molecule, the organic tail commonly participates in crosslinking or polymerization of monomer/oligomers.

4.2.2 Polymer infiltration

Silane-grafted ceramic scaffolds were infiltrated into monomer and oligomers to complete fabrication of ceramic/polymer composites. During this process, polymerization and silane-polymer crosslinking reactions will occur simultaneously. Polymerisation is the process of linking monomer or oligomers molecules together in chemical reactions to form polymer chains or three-dimensional networks [14]. Meanwhile, the organic tail of silane will chemically link to monomers or oligomers by covalent bonds. Four different types of polymers were used here: PMMA, UDMA/TEGDMA, PU, and epoxy resin. According to literatures, γ-MPS was demonstrated to enhance the interface of the composites of ceramic/PMMA [5] and ceramic/UDMA/TEGDMA [15]. Moreover, APS was also used to enhance the interface between ceramic and polymers of PU [16] or epoxy resin [17].

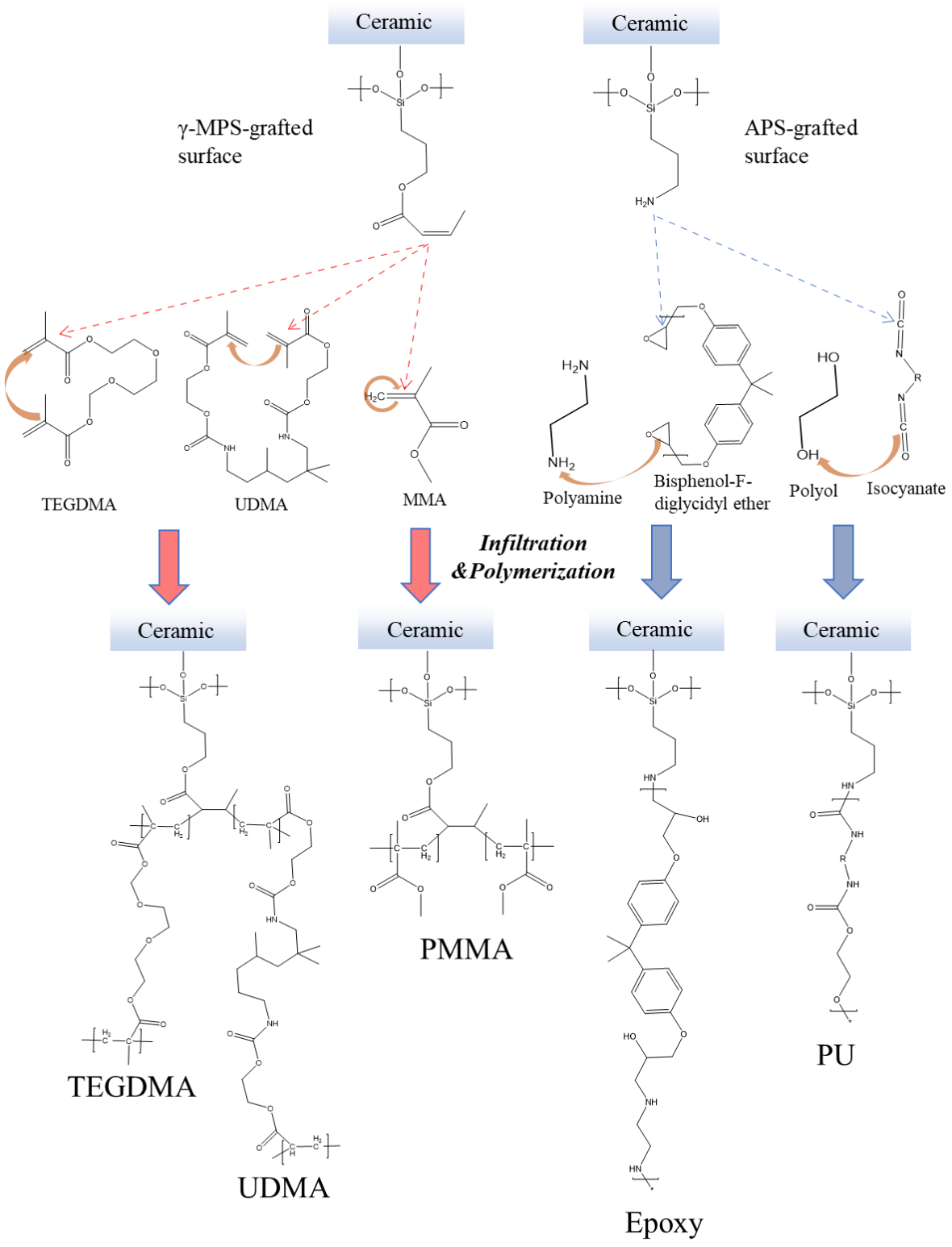

Fig.4-2 *The conceptual schematic diagram of polymerization and silane-polymer crosslinking reaction. The polymerization processes were highlighted by orange arrows. Reactions concerning γ-MPS and APS were highlighted by red and blue arrows, respectively.*

The chemical mechanisms of polymerization were shown in **Fig.4-2**. The methyl methacrylate (MMA), UDMA, and TEGDMA are vinyl-based monomers with similar functional groups of carbon-carbon double bonds (vinyl group), so theses polymers could be constructed through free radical polymerization based on vinyl group [18]. The vinyl groups were activated by free radicals (from initiator) and then reacted with the other vinyl groups resulting in connection of covalent bond. Moreover, the organic tail of γ-MPS containing a vinyl group will react with the free radical activated vinyl functional groups on MMA, UDMA, or TEGDMA during the radical-polymerization (**Fig.4-2**).

Monomers of the PU are composed of two components: formulated polyol (part-A) and isocyanate (part-B). However, the manufacturer did not provide the details of two components, therefore HO-CH_2-CH_2-OH (ethylene glycol) and O=C=N-R-N=C=O were used to represent polyol and isocyanate in **Fig.4-2**. The hydroxyl groups on polyol can react with isocyanate groups to form carbamate groups resulting in monomers connection, which is also named "urethane links". Therefore, PU with high molecule weight is formed by condensation reaction between isocyanate and polyol [19].

The starting materials of epoxy resin were composed of two parts: ethylenediamine (curing agents) and bisphenol-F-diglycidyl ether (epoxy oligomers). Amino on ethylenediamine can react with epoxide (the three-membered ring structure) functional groups on the epoxy oligomer to form covalent bonds. Hence, long-chain-length epoxy polymers are formed via step-growth polymerization of mediate-chain-length epoxy oligomer and ethylenediamine [20]. The APS-grafted substrates can link to both PU and epoxy resin. The organic tail of APS plays a role of polyol or ethylenediamine during polymerization of PU and epoxy, respectively. The -NH_2 (amino) on organic tail can also react with isocyanate and epoxides functional groups as shown in **Fig.4-2**. As a result, stable covalent bonds were formed between ceramic and polymers.

Consequently, to ensure the formation of chemical bonds between ceramic scaffolds and polymers in different ceramic/polymer systems, γ-MPS-grafted ceramic scaffolds will be infiltrated by PMMA or UDMA/TEGDMA; PU and epoxy resin will infiltrate into APS-grafted ceramic scaffolds.

4.2.2.1 PMMA

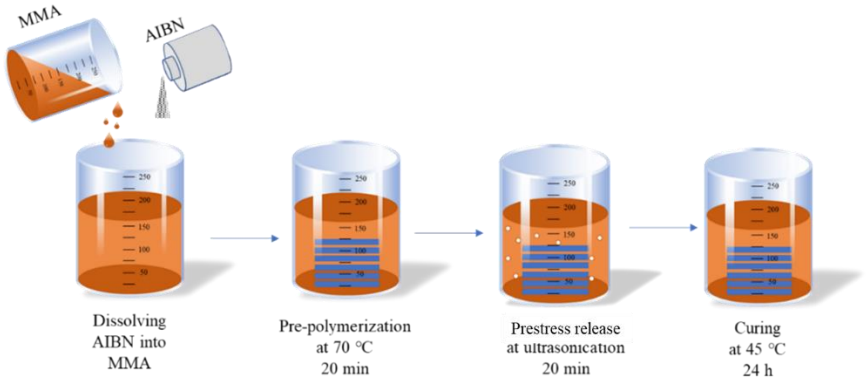

Fig.4-3 *Schematic of infiltration process of PMMA into ceramic scaffolds.*

Ceramic scaffolds were immersed into the solution of 0.5 wt. % azobisisobutyronitrile (AIBN, Sigma-Aldrich, UK) into MMA (Sigma-Aldrich, UK). The mixture was heated to 70 ºC where the AIBN (initiator) was activated to generate free radicals (2-cyanopropyl radicals) which then initiated the polymerization. The temperature was kept at 70 ºC/20 min for pre-polymerization until the MMA displayed a honey-like viscosity. The pre-polymerization is aimed to reduce prestress in the final ceramic/polymer composites. The monomer (MMA) is a kind of small-sized organic molecule, thereby the polymerization results in formation of massive covalent bonds and reduction of the intra-molecular spaces. It is apparent that the shrinkage strain developed during polymerization in composite might introduce stresses in polymer phase [21]. The prestress had an adverse effect on the mechanical properties of composites. Hence, MMA was pre-polymerized into mediate-chain-length polymer first and the prestress was then

released under ultrasonication for 20 min. Subsequently, the PMMA was cured in a water bath at 45 ºC for 24 hours. Finally, the composites were heated at 90 ℃/2 hours for annealing, following by slow cooling to room temperature to minimize thermally induced residual stresses.

4.2.2.2 UDMA/TEDGMA

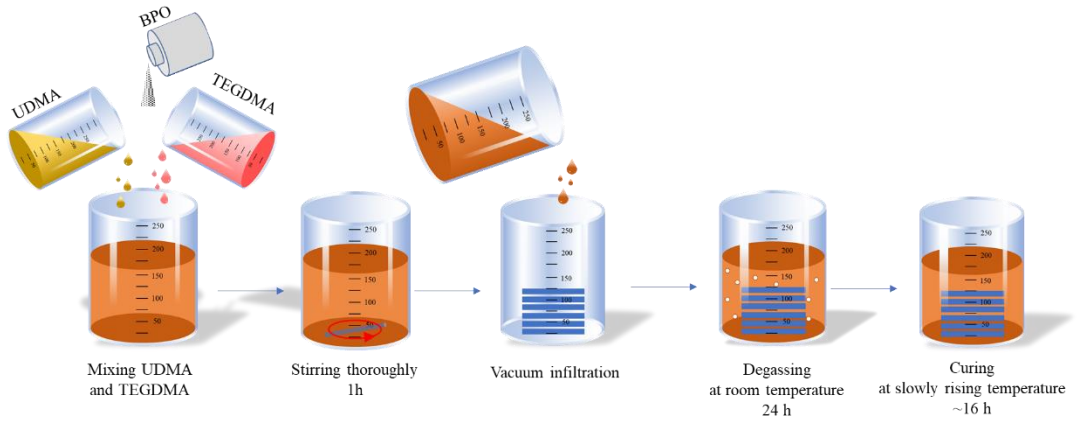

Fig.4-4 *Schematic of infiltration process of UDMA/TEDGMA into ceramic scaffolds.*

Initially, UDMA (oligomer, Sigma-Aldrich, UK), TEGDMA (monomer, Sigma-Aldrich, UK) and benzoyl peroxide (BPO, initiator, Luperox, Sigma-Aldrich, UK) were mixed at the ratio of 100:100:1 by weight. The mixture was magnetic stirred at room temperature for 1 hour until UDMA and TEGDMA homogenously mixed and BPO powder dissolved completely. Once the mixture was infiltrated into ceramic scaffold in a vacuum infiltration machine (Cast N' Vac 1000, Buehler, USA), the beaker was moved out of vacuum system and placed at room temperature for 24 hours allowing the air bubble escape. Afterwards, it was then transferred to an oven for heat treatment and curing process. The temperature of oven was programmed and rising slowly from 25 to 120 ℃ step by step according to previous work by Algharaibeh [15]. The time vs. temperature curve was illustrated in **Fig.4-5**.

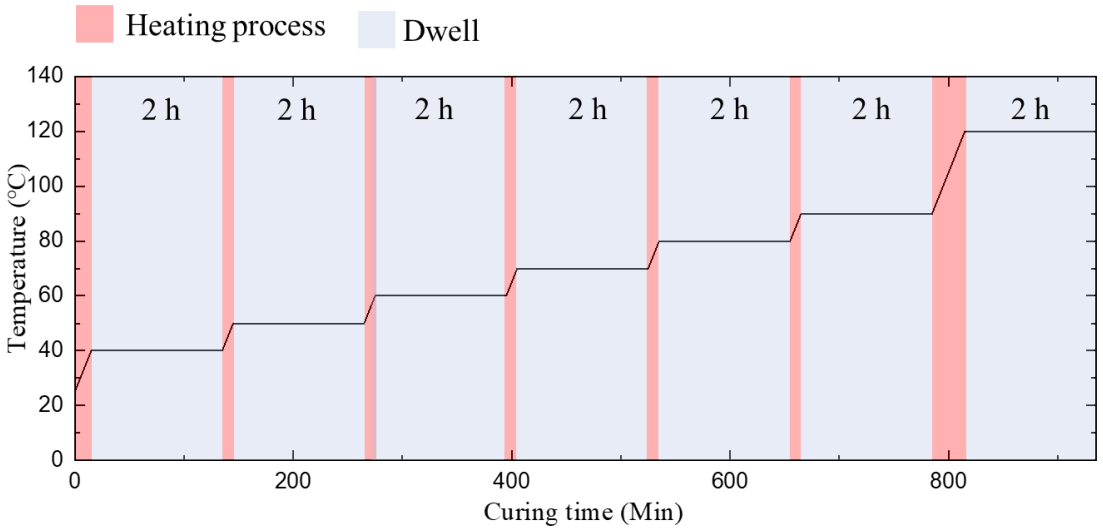

Fig.4-5 Temperature of heating treatment for UDMA/TEDGMA polymerization.

4.2.2.3 Epoxy

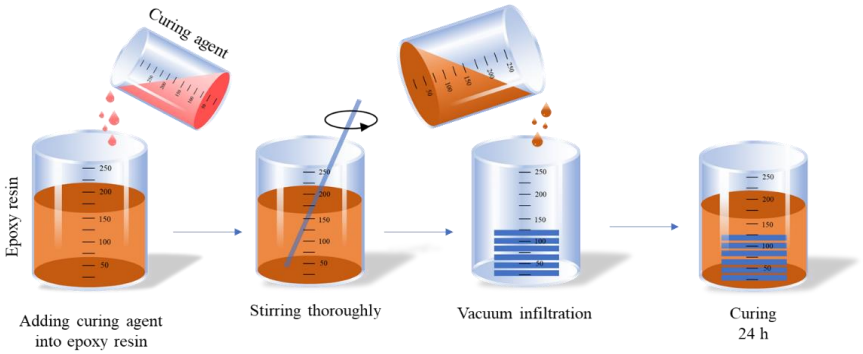

Fig.4-6 Schematic of infiltration process of epoxy into ceramic scaffolds.

14.3 wt. % of curing agent (SpeciFix-20 curing agent, Struers, Germany) was added into epoxy resin (SpeciFix resin, Struers, Germany) and stirred thoroughly by glass rod. When two parts were mixed completely, the mixture was infiltrated into ceramic scaffold in the vacuum infiltration machine, followed by curing at room temperature for 24 hours.

4.2.2.4 PU

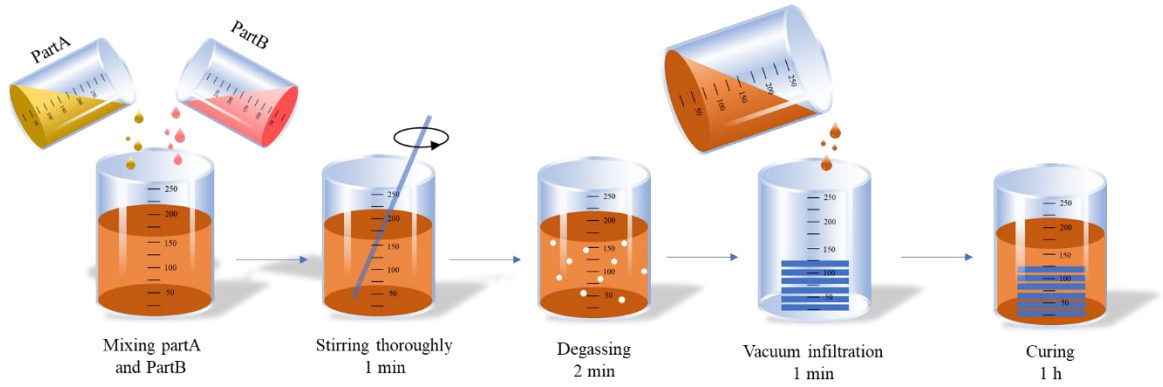

Fig.4-7 *Schematic of infiltration process of PU into ceramic scaffolds.*

The PU (Xencast P6, Easycomposite, UK) is composed of two components: part-A and part-B. Mixing and infiltration have to be done very quickly because the processing time before curing is less than 5 min once two parts are mixed. The bottles of both part-A and part-B were shaken thoroughly to dislodge sediment prior to mixing the two parts at a ratio 1:1 by weight. The mixture was vigorously stirred by a glass rod for 1 min and then transferred to the vacuum infiltration system to process degassing for 2 min under the vacuum. When the bubbles escaped, the mixture was poured on the ceramic scaffold slowly until immerse it (within 1 min). Finally, release the vacuum allowing the PU to cure at ambient temperature and pressure for 1 hour.

4.2.3 Microstructural and mechanical characterization

The microstructures of ceramic/polymer composite materials were characterised using scanning electron microscopy (SEM) (Quanta 400 – FEI Scanning Electron Microscope). Everhart-Thornley electron detectors (ETD) and back-scattering electron detectors (BSE) were both used to image the microstructure of composites. The *in situ* SEM (S3200N, Hitachi, Japan) and *in situ* radiographs (X-ray radiators, Diamond light source, UK) were used to observe and measure the crack propagation during mechanical testing operated by Deben stage (Deben, UK). The SEM images were statistically analysed by ImageJ to quantify the occurrence and

frequency of ceramic bridges connecting the ceramic layers. The number of ceramic bridges between adjacent layers were counted per unit area. Ceramic wall thickness was also measured based on the SEM images. Over three different images were used to estimate density of ceramic bridges and wall thickness.

Compressive strength of composites was tested on the rectangular specimens of 4 mm×4 mm ×6 mm where the compressive area was 4 mm×4 mm and height was 6 mm. Flexural strength of composites was evaluated by three-point bending on the rectangular specimens of 1.5 mm×2 mm×20 mm (span=12.5 mm). Fracture toughness K_{IC} and *R*-curves were measured by three-point-bending tests on single-edge notched bending (SEB) specimens with 1.5 mm×3 mm×20 mm (span=12.5 mm) and 2.5 mm×5 mm×25 mm (span=20 mm), respectively. All toughness tests satisfied the plane-strain and small-scale yielding requirements for valid K_{IC} measurement, as ASTM standards and all values represented an average of at least three measurements per configuration.

4.3 Results and discussion

4.3.1 Silane-grafted ceramic scaffolds

To confirm the silanization of the ceramic surface, silane-grafted alumina scaffolds were characterised by Fourier-transform infrared spectroscopy (FT-IR) at the region of 4000-500 cm^{-1}, pure silane coupling agent was used as the reference (**Fig.4-8**). As shown in **Fig.4-8a**, the spectrum of pure γ-MPS corresponded to $-OCH_3$ stretching bands at 2820 cm^{-1} which demonstrated the presence of functional groups of silicon-based head of γ-MPS. Meanwhile, the peaks at around 1630 cm^{-1} and 1720 cm^{-1} were assigned to stretching band of carbon-carbon double bonds and carbon-oxygen double bonds, respectively. C-H stretching bands was located at 2980 cm^{-1} relating to the $-CH_2CH_2-$ on silane molecule. The presence of characteristic peaks related to main functional groups identified the organic tail in the spectrum

of pure γ-MPS. Comparably, the spectrum of γ-MPS-grafted alumina displayed the characteristic peaks at 1630 cm^{-1}, 1720 cm^{-1}, and 2980 cm^{-1} indicating the existence of organic tail. However, the peak representing -OCH_3 at 2820 cm^{-1} in spectrum of pure γ-MPS disappeared in that of grafted alumina. It suggested that the -OCH_3 group disconnected from silicon-based head during silanization and then converted to methanol as a by-product which was removed in rinsing step. A wide band near 3400 cm^{-1} represented that there were still unreacted -OH on the alumina surface.

Fig.4-8b showed FT-IR spectra of pure APS and APS-grafted alumina scaffold. The characteristic absorption peaks at 2950 cm^{-1} and 2850 cm^{-1} were attributed to asymmetric and symmetric stretching vibrations of -CH_2; 1480 cm^{-1} and 1420 cm^{-1} assigned to C-H bending and C-N stretching vibrations, respectively. Differ from that of γ-MPS system, there was no obvious change between APS and APS-grafted samples because the peaks refer to -OCH_2CH_3 overlapped with peaks of –CH_2 at 2850 cm^{-1}. In addition, no wide band (near 3400 cm^{-1}) was found on APS-grafted surface, implying the -OH on the alumina surface was completed reacted with APS.

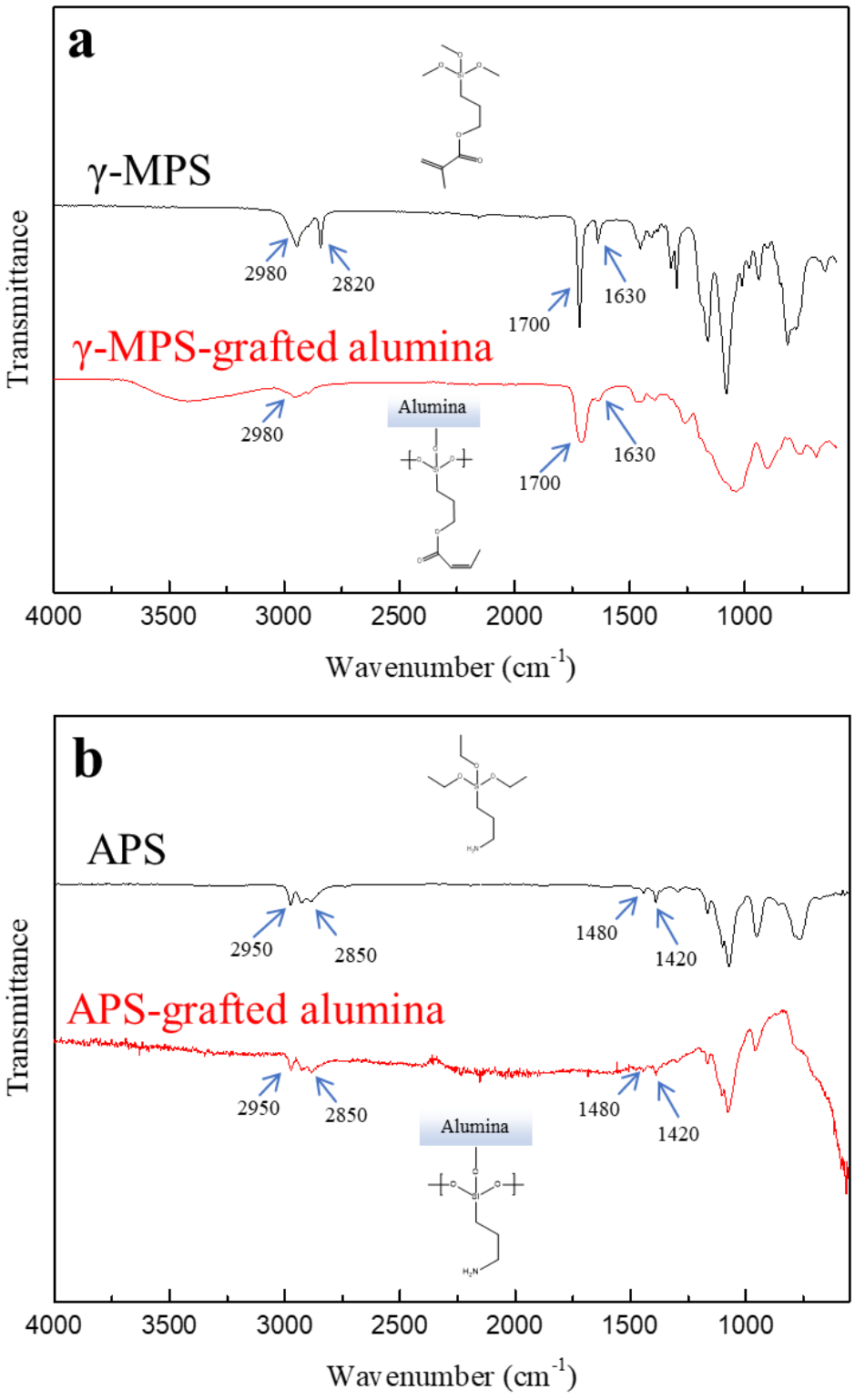

Fig.4-8 *FT-IR spectra of pure silane and silane grafted alumina for γ-MPS* ***a)*** *APS* ***b)*** *systems.*

As a result, it is clearly to see that both γ-MPS and APS have been confirmed to modify ceramic surface of scaffolds with functional groups of organic tails.

4.3.2 Mechanical properties of nacre-like ceramic/polymer composites

4.3.2.1 BM composites

In this section, nacre-like BM composites were prepared by infiltrating polymer (PMMA) into as-prepared BM ceramic scaffolds using a two-step method. Experiments were conducted to evaluate the effects of firs-step sintering temperature and silanization on mechanical properties of nacre-like BM composites which are presented in 4.3.2.1.1 and 4.3.2.1.2, respectively. The ceramic scaffolds prepared under different processing conditions are listed in **Table 4-1**.

Parameters studied	First-step sintering temperature		Silanization	
Ceramics	Alumina	Zirconia	Alumina	Zirconia
First-step sintering temperature (℃)	1250-1550	1150-1450	1550	1550
Second-step sintering temperature (℃)	1550	1550	1550	1550
Silanization (γ-MPS)	No	No	Yes	Yes

Table 4-1 *Manufacturing parameters of BM ceramic scaffolds before polymer infiltration.*

Two types of ceramics were used in this study: alumina and zirconia. According to Chapter 3, ceramic scaffolds with BM architectures were fabricated by the two-step densification method from scaffolds manufactured using bi-directionally freeze casting of ceramic slurries with 10 vol.% solid loading at 40 ℃/min cooling rate.

4.3.2.1.1 Effect of first-step sintering temperature

Fig.4-9 showed the mechanical performance of zirconia/PMMA composite materials prepared with different sintering temperature from 1150 to 1450 ℃. Both the load-displacement curves (**Fig.4-9a**) and fracture toughness K_{IC} (**Fig.4-9b**) were obtained by three-point bending on SEB specimens. Obviously, all samples displayed plasticity before failure, which meant the nacre-like BM architectures of all the samples exhibited the capability of stabilizing the crack propagation after the crack initiation. However, the crack resistance varied with the first-step sintering temperature. In the load-displacement curves (**Fig.4-9b**), samples sintered at relatively high temperatures in first-step sintering stage exhibited more gentle slopes and larger displacements before reaching the ultimate stress. For instance, samples sintered at 1350 ℃ and 1450 ℃ display pronounced ductility with more than doubled values of displacement (~0.1 mm) than those sintered below 1250 ℃. In terms of K_{IC}, samples with the lowest first-step sintering temperature (1150 ℃) showed the highest value of fracture toughness at 3.6 MPa $m^{1/2}$. When the first-step sintering temperature increased to1350 ℃, the K_{IC} dropped 67% to 1.2 MPa $m^{1/2}$. As the sintering temperature was further increased to 1450 ℃, the K_{IC} decreased slightly to 1.1 MPa $m^{1/2}$.

Fig.4-9c illustrates the correlation between sintering temperature and testing results of three-point bending (flexural strength and modulus) of composites. The results indicated that a rising first-step sintering temperature resulted in lower strength and modulus, where the tendency was similar to fracture toughness K_{IC} in **Fig.4-9b.** However, from the SEM image taken from fractured surface (**Fig.4-9d**), it was evidenced that the crack displayed typical toughening mechanisms during crack propagation: fractional sliding and pull-out, indicating that the composites were toughened by the nacre-like BM architectures.

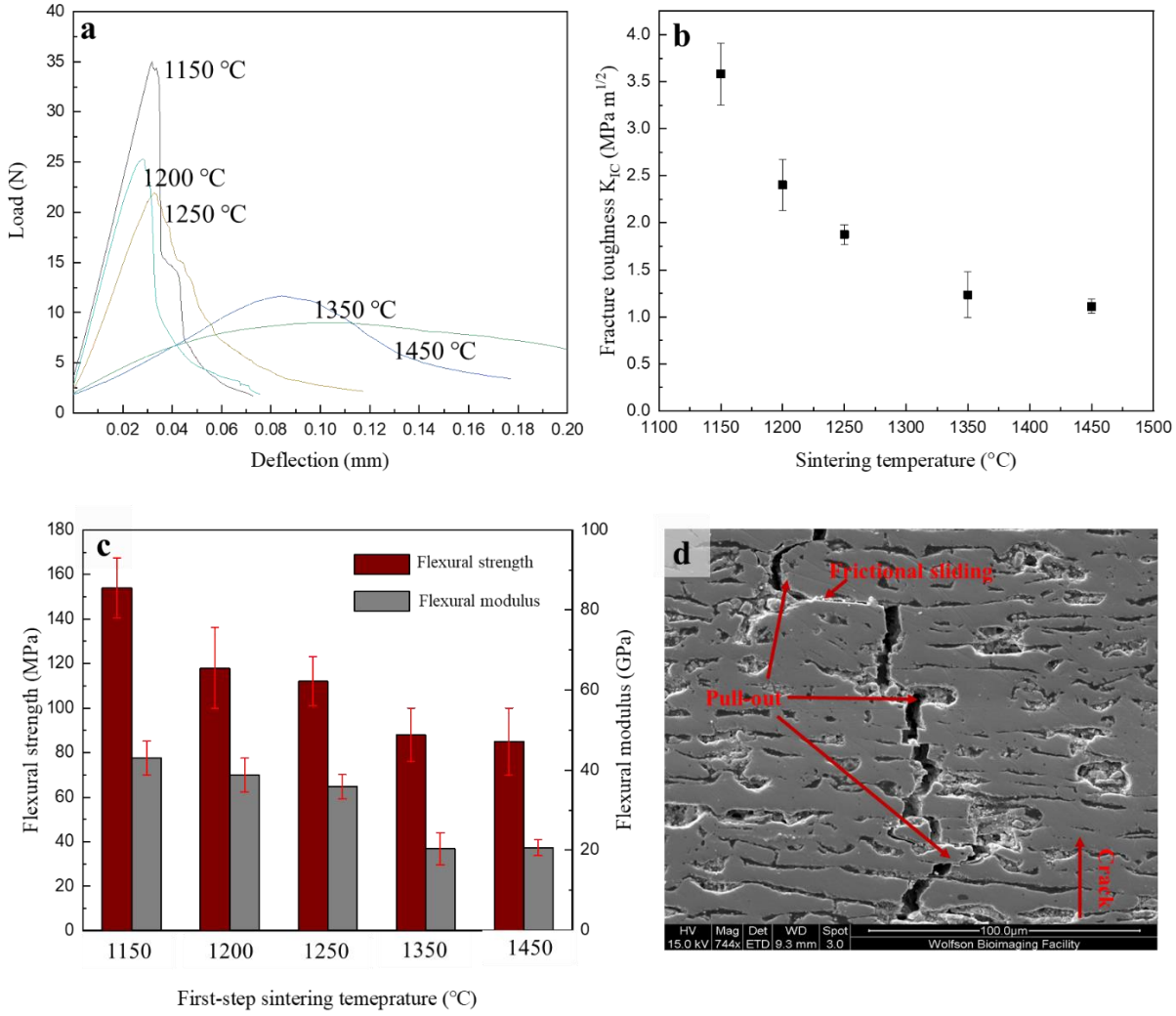

Fig.4-9 *Mechanical performance of the BM zirconia/PMMA composites with different first-step sintering temperature. Fracture toughness load-displacement curve* ***a)****, fracture toughness* K_{IC} ***b)****, and flexural strength and modulus* ***c)*** *were shown as the first-step sintering temperature from 1150 to 1450 ℃. The SEM image was taken after fracture toughness testing on a composite with firs-step sintering temperature of 1150 ℃* ***d)****.*

The first-step sintering temperature mainly affected two features of scaffolds (and resultant composites): ceramic fraction and microstructure. Previous results in 3.3.3.1 indicated that lower first-step sintering temperature led to higher ceramic fraction and more connections in ceramic scaffolds. In particular, the ceramic fraction decreased dramatically from 84.8% to

62.4% as the first-step sintering temperature was increased from 1150 to 1350 ℃. When the first-step sintering temperature continued increasing to 1450 ℃, the ceramic fraction slightly reduced to 58.1%. This tendency also corresponded to the mechanical properties of composites (fracture toughness K_{IC}, flexural strength and modulus); they decreased faster from 1150 to 1350 ℃ and slower from 1350 ℃ to 1450 ℃. At high ceramic contents, the mechanics of composites were enhanced because of the strong and stiff nature of ceramic (zirconia) which acted as a load-bearing phase. Meanwhile, higher ceramic content also led to lower polymer content with lower possibility to toughen composites intrinsically with the plasticity of polymer itself. Although the extrinsic toughening mechanisms normally contributed to the toughness during crack growth, they still had little effect on crack initiation [22]. Therefore, the fracture toughness (K_{IC}) of composites was also enhanced extrinsically via frictional sliding and pull-out (**Fig.4-9**). When the distance between ceramic layers (bricks) decreased as the ceramic fraction increases, there are higher possibilities of ceramic-ceramic layer sliding resulting in higher frictional force to resist crack propagating. In addition to layer sliding, the more ceramic bridges were formed which also enhanced the mechanics of the BM composite materials, this was likely achieved through efficient redistribution of stresses. The function of ceramic bridges in both natural nacre [23, 24] and nacre-like composite materials [25-27] was demonstrated to be a major mechanism of strengthening and toughening. Greco *at el.* investigated the relationship between volume fraction and microstructure (aspect ratio) of stiff phase on mechanical properties of nacre-like composites through computer simulations. Their conclusions were in good agreement with the results reported here, i.e. ceramic fraction and microstructures could stiffen, strengthen, and toughen the composites [28]. Therefore, when the first-step sintering temperature was lower, i.e. at 1150 ℃, BM zirconia/PMMA composites achieved higher flexural strength, modulus, and fracture toughness (K_{IC}) with exceptional toughening mechanisms. However, composites prepared at relatively higher first-step sintering

temperature displayed a better plasticity (ductility). A similar conclusion was drawn based on the BM alumina/PMMA composites by Algharaibeh from our group [15].

4.3.2.1.2 Effect of silanization

Fig.4-10 compared the mechanical performance of BM ceramic/polymer composites with and without silanization. It can be seen clearly that the silanization process effectively promoted the mechanical performances (flexural strength, compressive strength, flexural modulus, and fracture toughness (K_{IC})) of both alumina/PMMA and zirconia/PMMA composites. **Fig.4-10a** demonstrate that after silanization, the flexural strength for alumina and zirconia composites improved 50% and 250%, reaching 80 MPa and 179 MPa, respectively. For compression testing **(Fig.4-10b)**, the ultimate stress increased slightly from 176 MPa to 198 MPa as a result of silanization for alumina/PMMA composites; the zirconia/PMMA composites were 65% stronger after the grafting process where the compressive strength improved from 182 MPa to 297 MPa. Similar to strength, stiffness and fracture toughness were also altered owing to salination wherein the modulus improved slightly from 24 to 31 GPa for alumina/PMMA and from 22 to 24 GPa for zirconia/PMMA composites (**Fig.4-10c**); the fracture toughness K_{IC} significantly enhanced from 1.1 to 2.4 MPa $m^{1/2}$ and 1.2 to 3.7 MPa $m^{1/2}$ for alumina/PMMA and zirconia/PMMA composites, respectively (**Fig.4-10d**).

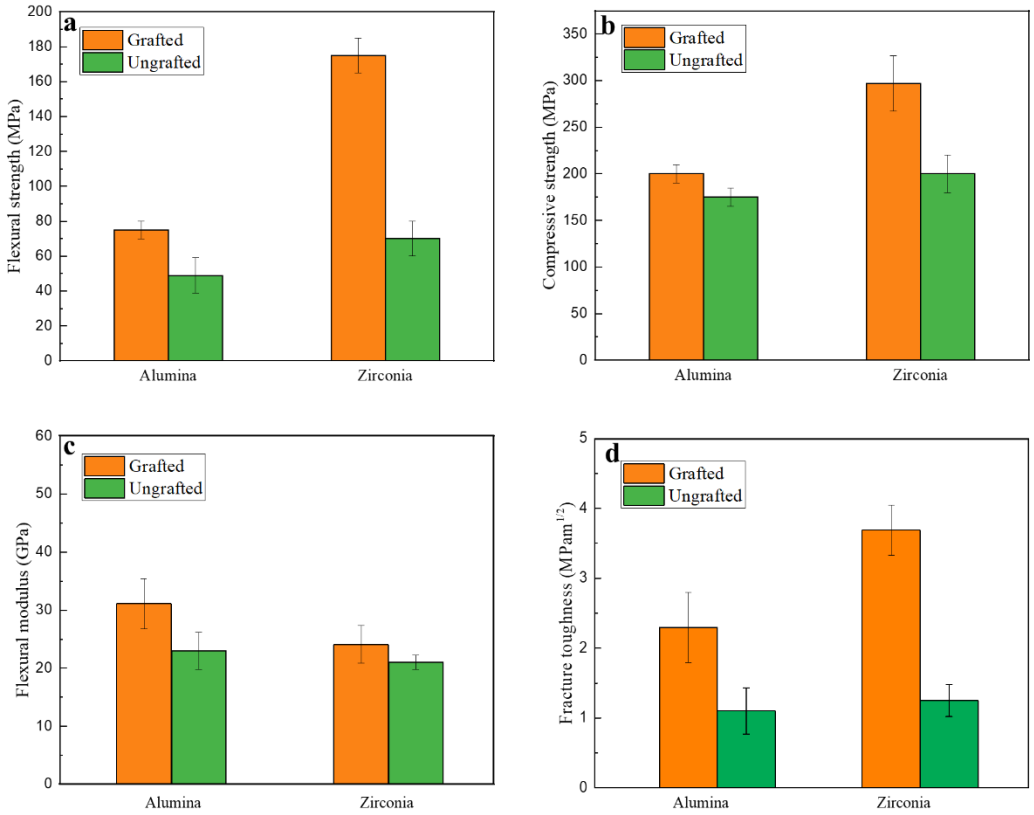

Fig.4-10 *Mechanical performance of BM alumina and zirconia/PMMA composites materials with or without silanization: Flexural strength* ***a)****, compressive strength* ***b)****, flexural modulus* ***c)****, and fracture toughness (K_{IC})* ***d)****.*

The improvements of mechanical performances might be attributed to the enhanced interface between ceramic and polymer phases. According to the SEM micrographs in **Fig.4-11,** grafted composites displayed a better cohesion between two phases compared to ungrafted composites where some obvious gaps or defects were found at the interface. It is well known that pre-existing gaps or defects have significant impact on the mechanical properties of materials. In addition, when the crack propagated in nacre-like composites, the stronger interface enables the organic layer to act as a viscoelastic glue to bear higher stress to prevent layer pull-out as in the natural nacre [29]. The effects of interface on mechanics of nacre-like composite were

also examined by simulation i.e. discrete element method (DEM) [30] and representative volume element (RVE) [9], both studies stated that increase of interface strength led to higher load bearing capacity, crack resistance, and stiffness of composites. Furthermore, the interfacial strengthening and toughening mechanisms could also be applied to other nacre-like BM composites [6, 31].

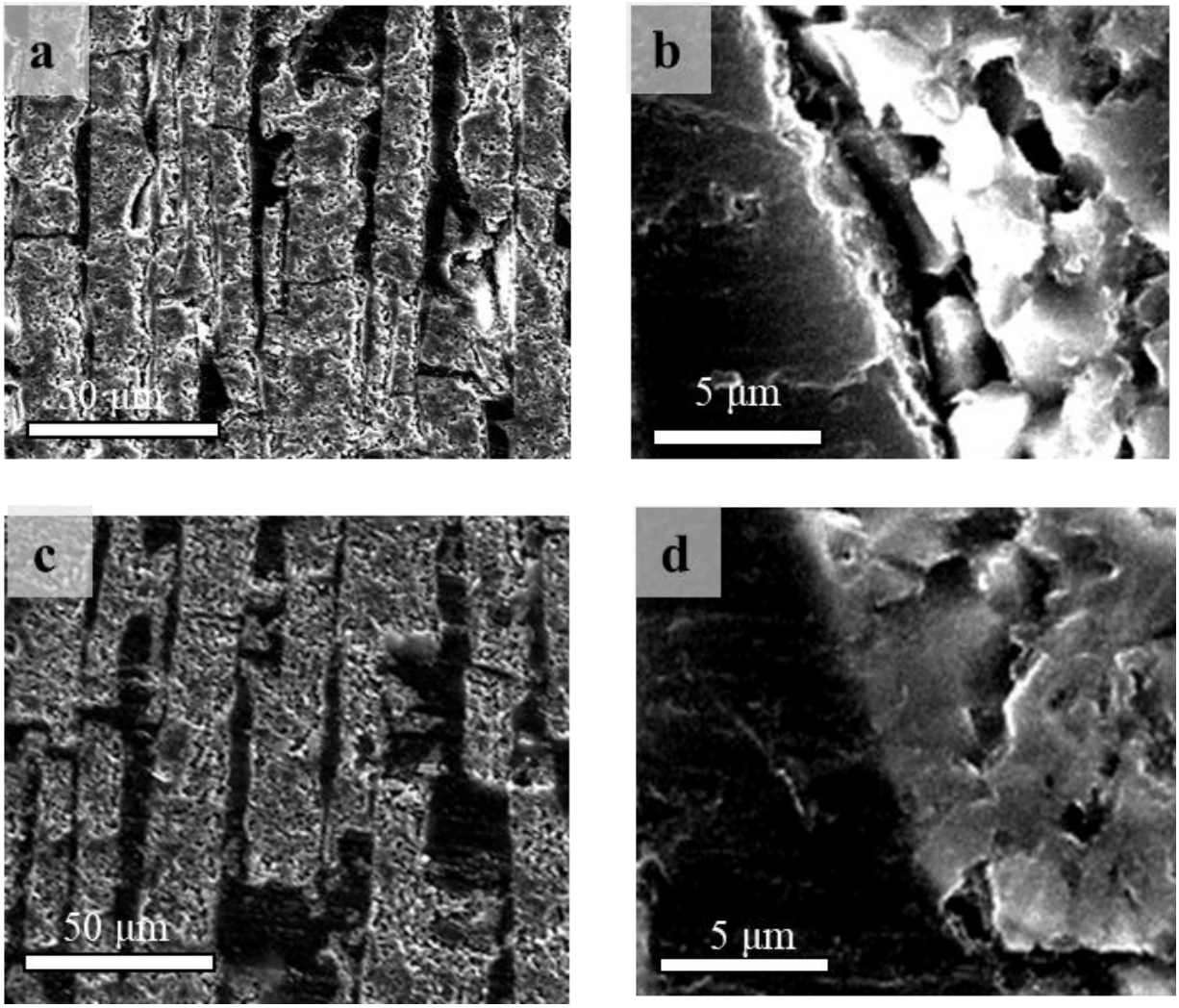

Fig.4-11 *SEM images of alumina/PMMA composites with* ***a)*** *and* ***b****) without* ***c)*** *and* ***d****) the grafting process.*

By comparing alumina/PMMA and zirconia/PMMA composites, it was apparent that zirconia-based composites were stronger but less stiff than alumina-based composites on both bending

and compression tests. It was demonstrated previously in 3.3.4 that the densified BM zirconia scaffolds obtained higher compressive strength than that of alumina. Differ from mechanical strength, the Young's modulus of alumina (389 GPa) was higher than zirconia (221 GPa). This implied that the ceramic phase did play a key role in load bearing capacity affecting mechanical properties of nacre-like ceramic/polymer composites.

Besides, it was also found that the grafting process not only strengthened but toughened zirconia/PMMA composites more significantly. While the strength and stiffness of alumina-based composite was improved less than 50%, the zirconia-based composite was improved 250% for flexural strength, and 65% for compressive strength. Specifically, fracture toughness improved two- and three-fold for alumina/PMMA and zirconia PMMA after grafting process, respectively. This suggested that the silanization of γ-MPS provided either more or stronger covalent bonds between polymer (PMMA) and ceramic (zirconia) surface.

4.3.2.1.3 Summary of BM composites

To conclude, when the BM ceramic/polymer composites were prepared at relatively lower first-step sintering temperature, they obtained higher ceramic fraction and higher microstructural integrity resulting in better mechanical performance. Meanwhile, the grafting process of silane coupling agents effectively promoted the mechanical performance of nacre-like BM composite materials. This was because that the silane coupling agents enhanced the interface by introducing chemical bonds between ceramic and polymers which led to reduced defects at the interface.

4.3.2.2 μL composites

In this section, all ceramic/polymer composites were produced via infiltrating polymers into μL ceramic scaffolds fabricated using a one-step method as described in 3.3.3.2. The processing parameters are listed in **Table 4-2**. The mechanical responses of composites were

evaluated to investigate the effects of these processing parameters and different microstructures. γ-MPS silanization was carried out for all the ceramic/polymer composites.

Parameters studied	Ceramic wall length	Ceramic wall thickness	Ceramic fraction	Polymer type
Ceramics	Zirconia	Alumina	Alumina	Alumina
Sintering temperature (℃)	1550	1550	1550	1550
Binder content (vol. %)	1-4	4	4	4
Ceramic wall thickness (μm)	8	8-40	8	8
Ceramic fraction (vol. %)	72%	72%	50-85%	72%
Polymers	PMMA	PMMA	PMMA	PMMA, UDMA/TED GEMA, PU, and epoxy

Table 4-2 *Manufacturing parameters of μL ceramic/polymer composites.*

Firstly, μL zirconia/PMMA composites were prepared from scaffolds with different binder contents where the ceramic wall length was altered. Then, alumina/PMMA were generated with various ceramic fraction and ceramic wall thickness. The reason why changes the zirconia into alumina is because the alumina/polymer composites prepared in this section will be characterized by X-ray radiography. However, the X-ray is hard to transmit through zirconia because of its high attenuation coefficient. Therefore, the present work will focus on alumina-

based composites and carry on the investigating impact of microstructure of µL ceramic/polymer composites. Finally, the role of the polymeric compliant phase in the mechanics of µL alumina composites was studied based on four different types of polymers.

4.3.2.2.1 Effect of ceramic wall length

According to 3.3.3.2.1, zirconia µL scaffolds were prepared via one-step method with altering binder content (1 wt.%, 2 wt.%, and 4 wt.%). The as-obtained scaffolds displayed a similar ceramic wall thickness (8 µm) and ceramic fraction (72%), but different ceramic wall length i.e. 200 µm, 500 µm, and 2500 µm for binder content of 1, 2 and 4 wt.%, respectively. Therefore, mechanical properties (flexural strength, modulus, and fracture toughness K_{IC}) of nacre-like µL zirconia/PMMA composites were evaluated to investigate the effect of ceramic wall length on mechanical performance of composites.

Fig.4-12 reveals the relations of binder content and mechanical properties of composites. Apparently, with higher binder content, mechanical properties of µL zirconia/PMMA composites significantly improved. When the binder content increased from 1 to 4 wt.%, the flexural strength was doubled from 136 to 274 MPa; flexural modulus increased from 29.8 to 42.1 GPa; fracture toughens K_{IC} also improved from 3.9 to 6.5 MPa $m^{1/2}$.

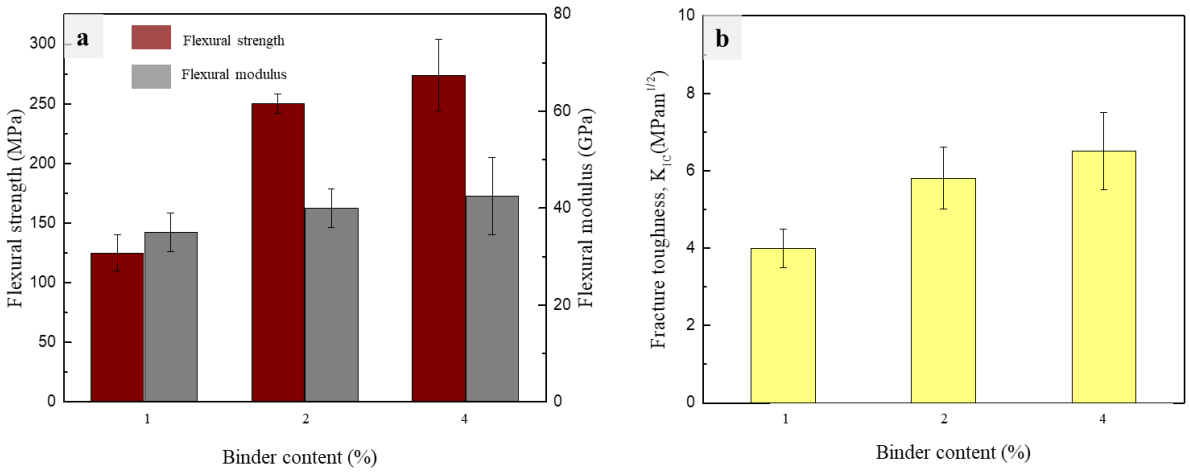

Fig.4-12 *Mechanical properties of µL zirconia/PMMA composites with various binder content: Flexural strength & flexural modulus* ***a)*** *and fracture toughness* K_{IC} ***b)***.

The improvement on mechanics may be attributed to the length of ceramic walls. As the ceramic wall elongated from short (250 µm) to mediate-length (500 µm), each ceramic layer obtained a better connection resulting in a better stress-transfer effect, which is known to enhance materials strength, stiffness and toughness for nacre-like composites [25, 26]. Nevertheless, as the ceramic wall length continues increased to 2500 µm, there was no further significant improvement in mechanics. This was because stress transfer already fully activated the long ceramic layer in composites with relatively high ceramic fraction (72%) [32], which was in agreement with the computer simulation. Greco *et al.* [28] stated that high aspect ratio of stiff phase (ceramic) resulted in a better stress transfer and load-bearing of nacre-like composites. It is noted that a similar effect was observed in BM composites which has been discussed in 4.3.2.3.

4.3.2.2.2 Effect of wall thickness and ceramic fraction

As described in 3.3.3.2.3, µL alumina scaffolds with the same wall thickness (8 µm) but different ceramic fraction (50-85%) were prepared with various compressive distance.

Meanwhile, µL alumina scaffolds were prepared at different wall thickness (8-40 µm) and same ceramic fraction (72%) by freezing slurries with different solid loading (10-40%) according to 3.3.3.2.3. All alumina scaffolds were grafted by γ-MPS and then infiltrated with PMMA to manufacture µL alumina/PMMA composites. Flexural strength of composites was measured by three-point bending on rectangular beams and fracture toughness *R*-curves were examined by three-point bending on SEB specimens. While single-value linear-elastic parameters based on crack initiation, such as K_{IC}, had traditionally been used to quantify toughness but they were difficult to represent the multiple extrinsic toughening mechanisms in the nacre-like materials [22]. Evaluation of fracture toughness requires nonlinear-elastic fracture mechanics to characterize the contributions from inelastic deformation, so the *R*-curve analysis were performed to characterize the fracture toughness associated with crack extension.

The results of three-point bending tests on µL alumina/PMMA composite materials are shown in **Fig.4-13**. The strength and stiffness of the µL composite materials is strongly dependent on the ceramic fraction and thickness of lamellar layers. The stress-strain curves for µL alumina/PMMA composites exhibited some degree of plastic deformation prior to failure, except for the sample containing 85 vol.% alumina, which displayed a brittle failure (**Fig.4-13a** and **c**). This may be attributed to the difference in their microstructure.

As can be seen in **Fig.4-13**, at the same ceramic wall thickness, composites with different ceramic fractions showed a similar failure strain (~0.35 %) but different stiffness and strength, where higher ceramic fraction results in higher flexural strength and modulus (**Fig.4-13b**). At the ceramic fraction of 72%, the µL composites with different ceramic layer thickness (from 8 to 40 µm) exhibited similar initial stiffness when strain < 0.05 %, but composites with thicker ceramic walls of 40 µm starts to yield earlier compared to those with thinner ceramic walls. Decreasing the ceramic wall thickness leads to a slight improvement in modulus, but flexural strength is improved around 80% (from 101 to 178 MPa) (**Fig.4-13d**).

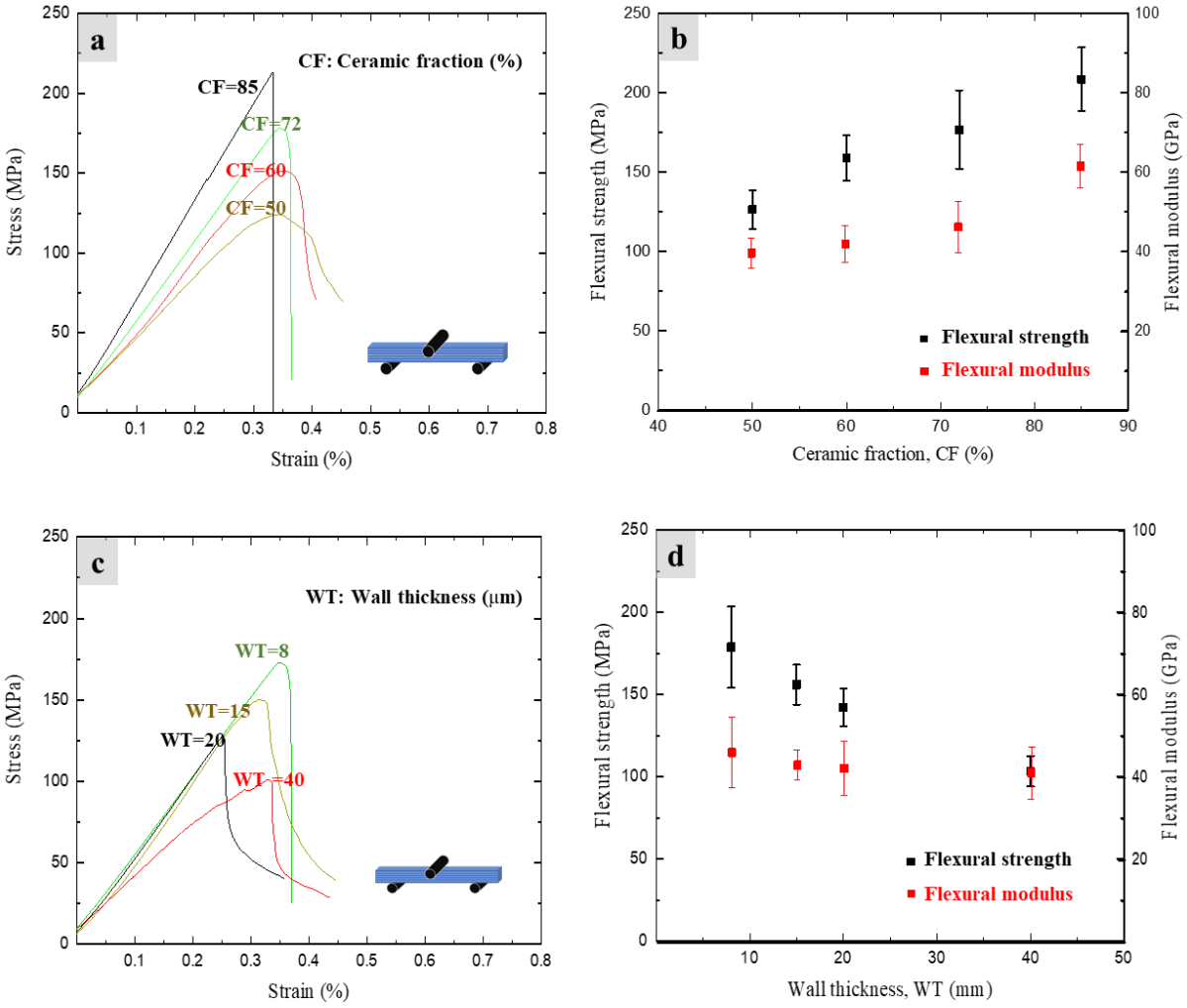

Fig.4-13 *Mechanical testing results of three-point bending on the μL alumina/PMMA composite materials including strain-stress curves* ***a)*** *&* ***c)*** *and average flexural strength* ***b)*** *&* ***d)****. Effects of ceramic fraction (at the same wall thickness of 8 μm)* ***a)*** *&* ***b)*** *and ceramic wall thickness (at the same ceramic fraction of 72 %)* ***c)*** *&* ***d)*** *on flexural behaviour. CF: ceramic fraction, WT: wall thickness.*

The *R*-curves were employed to evaluate the resistance to crack propagation. The loading-unloading curves were converted to relations between crack extension and fracture toughness K_J and all the *R*-curves were shown in **Fig.4-14**. According to the ASTM E1820 [33], while all

measurements are 'valid' before a = 0.25×b = 0.625 mm (where a is crack length and b is uncrack ligament before testing, b=2.5 mm), the results were 'invalid' above it. Hence, although the crack still propagates stably after this limit, this work will focus on the maximum ASTM "valid" toughness value at a=0.625 mm. The *R*-curves were shown in **Fig.4-14a** and **b** for composites with different ceramic fractions at the same wall thickness (8 μm) and ceramic wall thickness at the same ceramic fraction (72 vol.%), respectively.

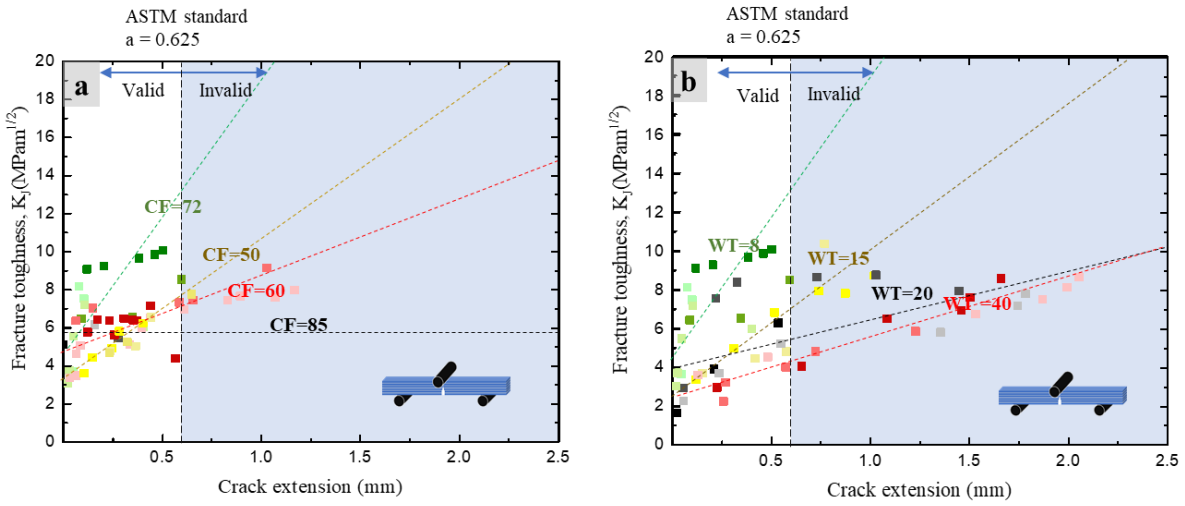

Fig.4-14 *Fracture toughness R-curves of the μL composite materials. Effects of ceramic wall thickness (at the same ceramic fraction of 72 vol.%)* ***a****) and ceramic fraction (at the same wall thickness of 8 μm)* ***b****) on R-curves behaviours. CF: ceramic fraction, WT: wall thickness.*

Similar to flexural strength, the fracture toughness K_J demonstrates a strong dependence on the ceramic wall thickness, where the stress-intensity factor K_J increases with the decrease of ceramic wall thickness (**Fig.4-14a**). When the ceramic wall thickness was 8 μm, most results reveal a rising *R*-curve where fracture toughness K_J increased when crack is extended, at a=0.625 mm, the 'valid' fracture toughness K_J reached 7.8, 7.2 and 12.5 MPa $m^{1/2}$ for 50, 60 and 72% ceramic fraction, respectively. However, the composite with 85 vol.% alumina failed catastrophically and illustrated a flat *R*-curve with a constant fracture toughness K_J at 5.8 MPa

$m^{1/2}$. This is not unexpected, previous studies showed that the fracture toughness (in energy terms) of nacre-like composites decreased when the volume fraction of polymer phase decreased because the soft polymer phase allowed more extensive plastic deformation. Nevertheless, for the µL composites, there are other competing toughening factors i.e. ceramic bridging and sliding.

The mechanical properties vary when the ceramic wall thickness is changed probably due to their microstructure and flaw density. It is known that the mechanical properties are sensitive to the size and number of flaws in ceramic phase. On the fracture surface in **Fig.4-15**, it can be seen that, compared to the thicker walls, the composite with thinner ceramic walls contains fewer flaws per unit area. Moreover, there is a bigger chance to find large pores within the thicker ceramic walls, which explains the negative impact to the strength, modulus, and fracture toughness.

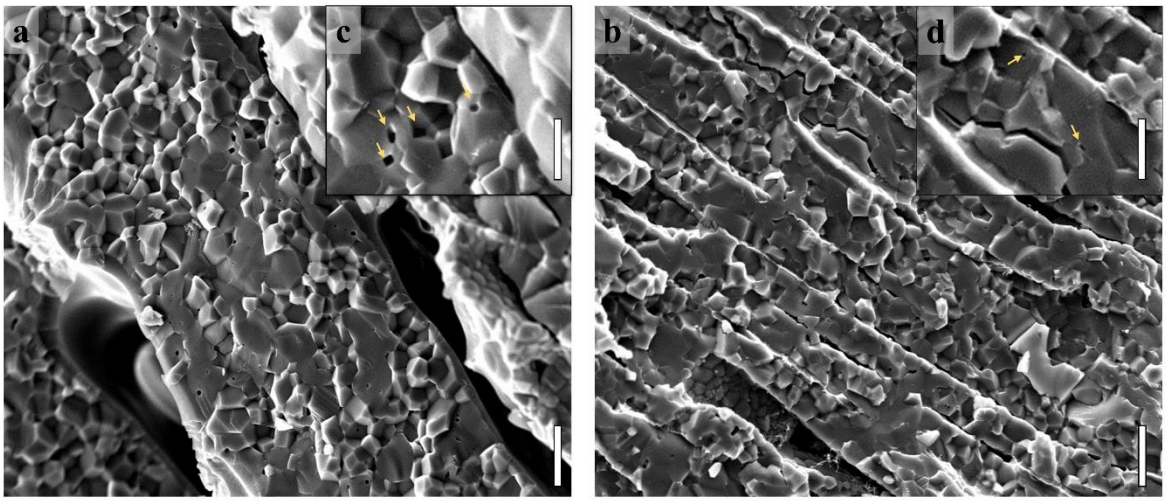

Fig.4-15 *Fracture surface of µL composite with 40 µm* ***a)*** *and 8 µm* ***b)*** *ceramic wall thickness. Larger and more closed pores were observed within the thicker ceramic walls as indicated by arrows in the inserts in* ***c)*** *and* ***d)****. Scale bars for* ***a)*** *and* ***b)****: 10 µm,* ***c)*** *and* ***d)****: 5 µm.*

On the other hand, the thinner ceramic walls can promote the strength and stiffness of nacre-like composites resulting from compensation of the effect of residue stresses. In polymer-infiltrated ceramic-based composites materials, residual stresses were produced during polymer infiltration and crosslinking. The residual stresses were considered to reduce strength of ceramic phase in terms of shear-lag model in Studart's work [25, 26]. In addition to defect reduction and strengthening in the composite with thinner ceramic layers, the microfracture-accumulating mechanisms may also significantly contribute to the effect of layer thickness on fracture toughness [34]. When the ceramic layer thickness was decreased, the amount of interface between the ceramic and polymer phases in the composites was increased. This can provide significant benefit to fracture toughness by having more micro-delamination, crack deflection, layer sliding, and pull-out, leading to more energy dissipation (**Fig.4-16**). Ultimately, the ceramic layer thickness was limited by the freezing rate and alumina particle size (~0.5 μm in the present work), it was found that faster freezing rate and lower solid loading may result in thinner ceramic walls [35]. However, it was heavily restricted by the freeze casting set-up and achievable sample size. In order to further optimise the microstructure and mechanical properties of the μL composite materials, it is worth using sinterable ceramic powders with nanoscale particle size or nanoplatelets in future work. This not only stops crack penetration through the strong ceramic layers but also diverts crack propagation along soft polymeric interfaces that facilitate progressive damages, resulting in both high strength and toughness.

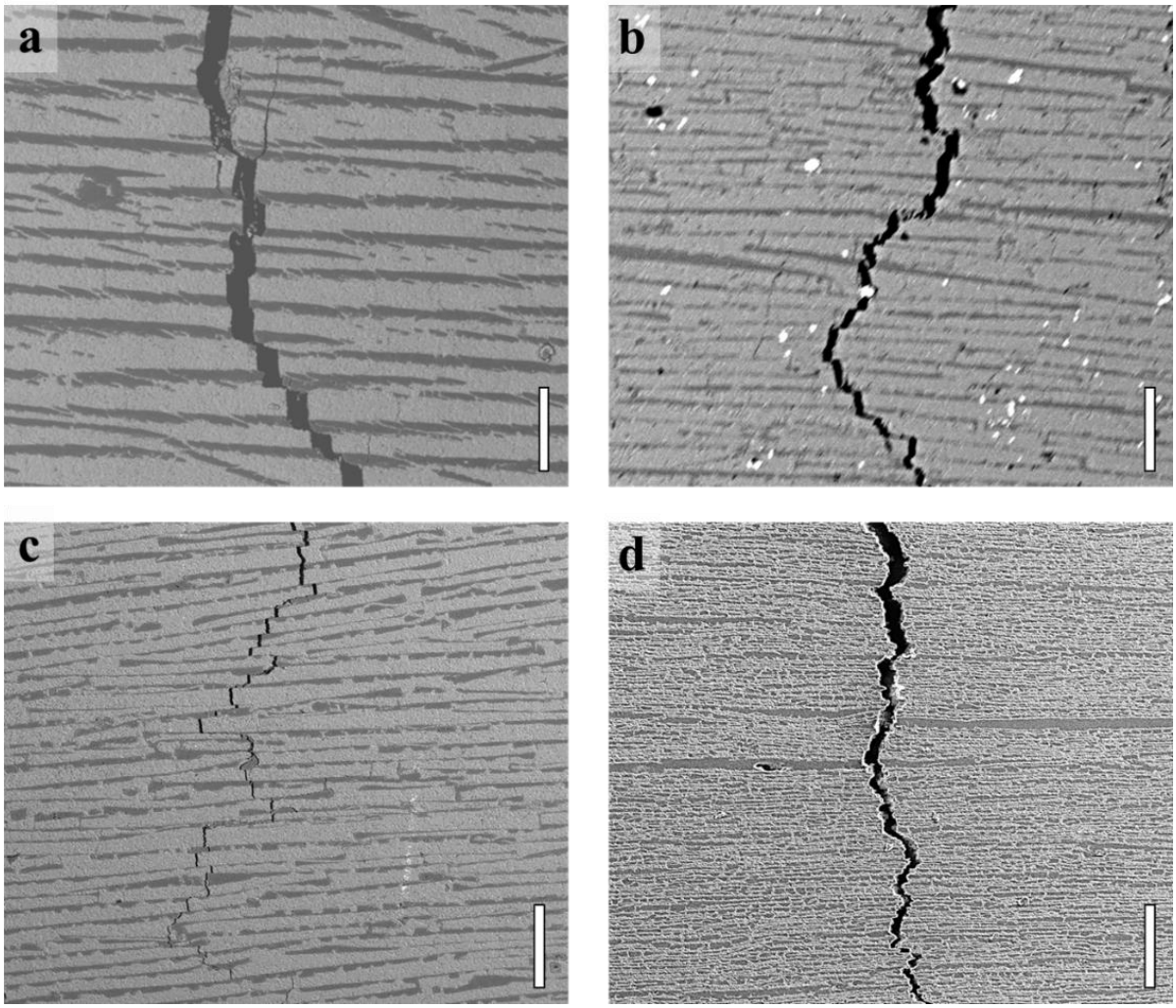

Fig.4-16 *SEM micrographs taken during the in situ R-curve measurements of µL alumina/PMMA composites (72 vol.%) with different wall thickness: 40 µm* ***a****), 20 µm* ***b****), 15 µm* ***c****), and 8 µm* ***d****). Note that the composites with thinner layer thickness display more ceramic layers resulting in more crack deflection hence more energy dissipation. Scale bar: 200 µm.*

In the one-step method, not only ceramic fraction, but also the morphology of ceramic scaffolds such as ceramic bridges, were directly affected by compression distance during uniaxial pressing. In careful examination of the microstructure of µL composites (**Fig.4-17)**, it becomes apparent that there is a correlation between ceramic bridges and ceramic fraction. The density of bridges, ρ_b is used to quantify the connections between layers. **Fig.4-17i** reveals that ρ_b increases drastically with the ceramic fraction, from ˜8 x10^8 to ˜100 x10^8/m^2 as the ceramic

fraction increases from 50 to 85 vol.%. The formation of ceramic bridges is due to asperities formed on the sidewalls of ceramic layers during freeze casting, which connect during pressing and sintering stages because of their high sintering activity. When the layer distance decreases, these asperities are more likely to form bridges.

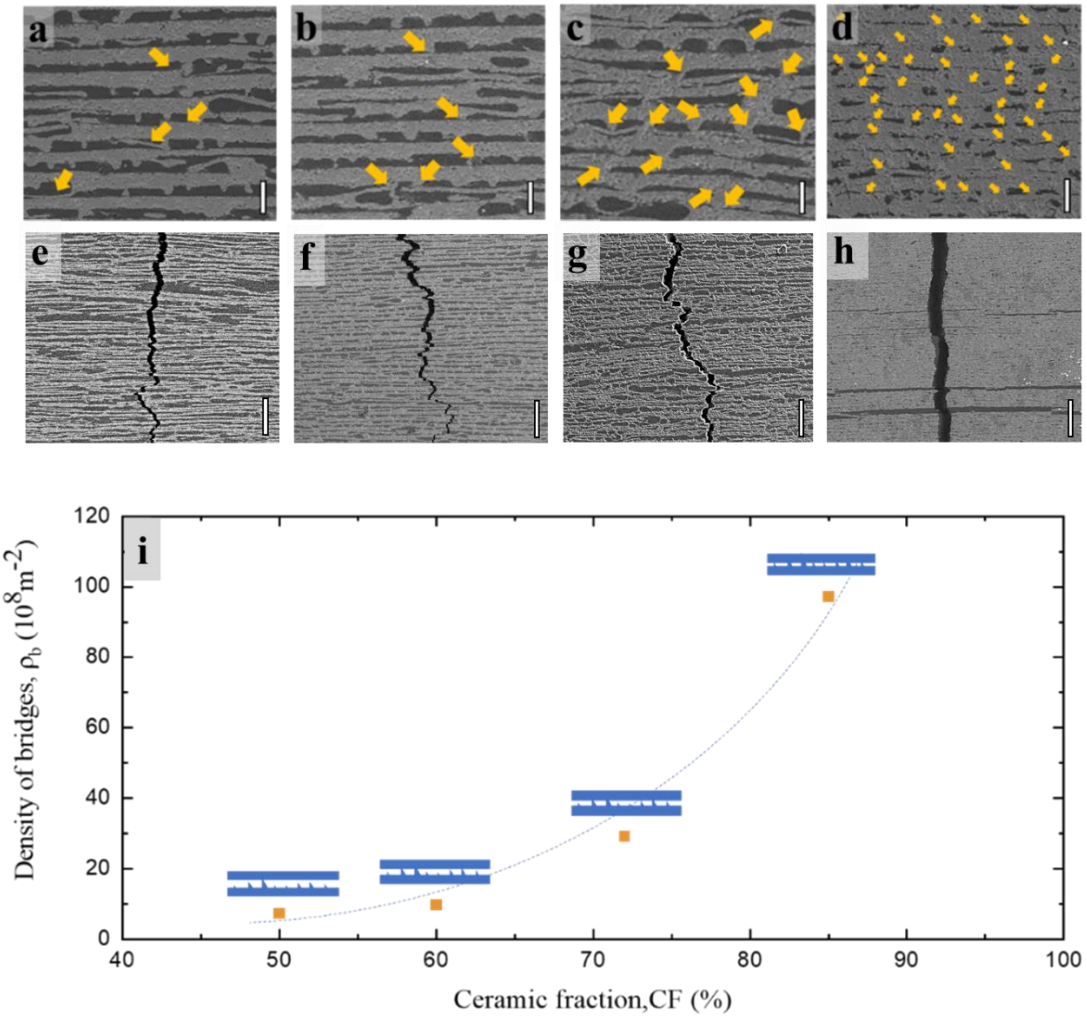

Fig.4-17 *Cross-section SEM micrographs of the µL composites produced from 10% slurry and pressed at an increasing compression distance, resulting in different ceramic fractions: 50% **a**), 60% **b**), 72% **c**) and 85% **d**). SEM micrographs taken during the R-curve measurements of µL alumina/PMMA composites with different ceramic fraction: 50% **e**), 60 % **f**), 72% **g**), and 85% **h**). **i)** is the plot of density of bridges (number of bridges per m^2) vs. ceramic fraction where the density of bridges was obtained from image analysis vs. ceramic fraction. Scale bars: 10 µm **a)**-**d**); 100 µm **e)**-**h**).*

It is well known that ceramic bridges play a key role in mechanical behaviours of nacre-like composites. Previous studies showed that, by introducing ceramic bridges in nacre-like composites [25-27], the strength, modulus, and toughness were enhanced concomitantly. The first role of ceramic bridges is stress transfer between layers. The stiff alumina bridges readily redistribute stresses over the connections between ceramic layers, and ceramic bridge breakage may also result in energy dissipation via deformation and fracture. During crack propagation, the nacre-like composite (both μL and BM) may lead to two possible fracture scenarios, i.e. bridge breakage with crack deflection and layer breakage without crack deflection. There is a competition between these two crack propagation paths depending on the relative strength of ceramic bridges and layers. If the stress transferred is lower than the bulk strength of ceramic layers, fracture requires pull-out of the stiff phase (ceramic) from the soft phase (polymer), leading to energy dissipation (**Fig.4-17e, f,** and **g**). By contrast, when the transferred stress exceeds the strength of the ceramic layers, fracture takes place within the stiff ceramic phase, resulting in a catastrophic failure of composites (**Fig.4-17h**). To quantify the effect of stress transfer provided by ceramic bridges in the μL composite materials, ceramic bridge density (ρ_b) between ceramic layers were estimated (**Fig.4-17i**). When fracture toughness increased from 7.8 MPa $m^{1/2}$ (for the 50% Al_2O_3 composite) to 12.5 MPa $m^{1/2}$ (for the 72% Al_2O_3 composite), the ceramic bridge density increased from 8 $x10^8$ to 35 $x10^8$ m^{-2}, more ceramic bridges provided larger energy dissipation during their breakage. On the other hand, when the bridges broke, the ceramic layers became disconnected; the bridges lost the efficiency of stress transfer, but the broken bridges can still act as asperities on the surface of ceramic walls which could enhance the frictional sliding of the individual ceramic layers. Nevertheless, when the ceramic bridges density exceeds 35 $x10^8$ m^{-2}, the fracture toughness drops down to 5.8 MPa $m^{1/2}$, meaning that the stress transfer surpassed ceramic layer strength, the crack went through the ceramic layers directly without much deflection (**Fig.4-17h**). The straight crack propagation in the 85%

sample where fewer ‘weak’ interfaces are present due to the close distance between ceramic layers and the formation of strong ceramic bridges.

Another factor is the frictional sliding between layers, one of the most important toughening mechanisms in natural nacre [36] and synthetic nacre-like composite [37]. This could be found in the present µL composites comprising >72 vol.% alumina. At a low ceramic fraction (<72 vol.%), the PMMA polymer phase is thick and separates each ceramic layer, the ceramic is rarely allowed to attach to the adjacent layers. In this case, the polymer is also a load-bearing phase offering extensive plastic deformation, contributing to the fracture toughness of composites. As the ceramic fraction increases, the spacing between ceramic layers reduces, the polymer layer becomes relatively thin or discontinued, it starts to act as a non-load-bearing lubricant which relieves stresses in the µL composites by offering frictional sliding between ceramic layers thereby increasing the crack resistance.

Consequently, in the composite material containing 50 vol.% ceramic, the compliant phase, polymer is load-bearing and allows extensive inelastic deformation. Therefore, the mechanical characterisation of toughness illustrates a rising *R*-curve and a valid K_J of 7.8 MPa $m^{1/2}$. When the ceramic fraction is increased to 60 vol.%, although extra ceramic bridges are formed, resulting in an increased contribution of extrinsic toughening, the fracture toughness K_J is slightly reduced because it contains less polymer which leads to inelastic deformation. As the ceramic fraction is increased further to 72 vol.%, more ceramic bridges are formed and the polymer phase starts to act as a stress-relieving ‘lubricant’, which is the main toughening mechanism in natural nacre [34], thus the toughness increases dramatically. However, if there are too many ceramic bridges as in the 85 vol.% composite where polymer loses its functions, becoming neither lubricant nor load-bearing phase, the composite failures catastrophically at the onset of crack initiation, albeit it is the strongest composite in this work. There is a trade-off between the surface roughness and bridges formed on ceramic layers or bricks in order to

achieve both high strength and toughness in nacre-like composites. The number of ceramic bridges or interfacial asperity between ceramic bricks should be controlled so long as they can still maintain the crack deflection along the 'weak' interface to have maximum energy dissipation. Otherwise, the composites will fracture in a brittle fashion. Therefore, it is possible to obtain both strong and tough nacre-like composites through synergistic actions of layered microstructure and appropriate interfacial properties such as ceramic bridges or micro-asperities and interfacial bonding. Theses strengthening and toughening mechanisms were also adopted to other nacre-like composites including ceramic/glass [29], hard glassy polymer/soft rubbery polymer [38], and graphene/metal or graphene/ceramic/metal [39, 40].

4.3.2.2.3 Effect of different types of polymeric compliant phase

µL alumina scaffolds with 72% ceramic fraction and 8 µm lamellar thickness were grafted by silane coupling agent as described in section 4.2.1 before infiltration with four different types of polymers to generate µL alumina/polymer composite materials. The strength of pure polymers was provided by the manufacturers or literatures (PMMA [41], UDMA/TEGDMA [42], Epoxy [43], PU [44]) and the Young's modulus of polymers were measured via ultrasound method. Flexural strength and modulus were examined by three-point bending tests on rectangular beams; fracture toughness *R*-curves were estimated by three-point bending on SEB specimens via monotonic loading mode. The *in situ* SEM was used to evaluate the crack extension.

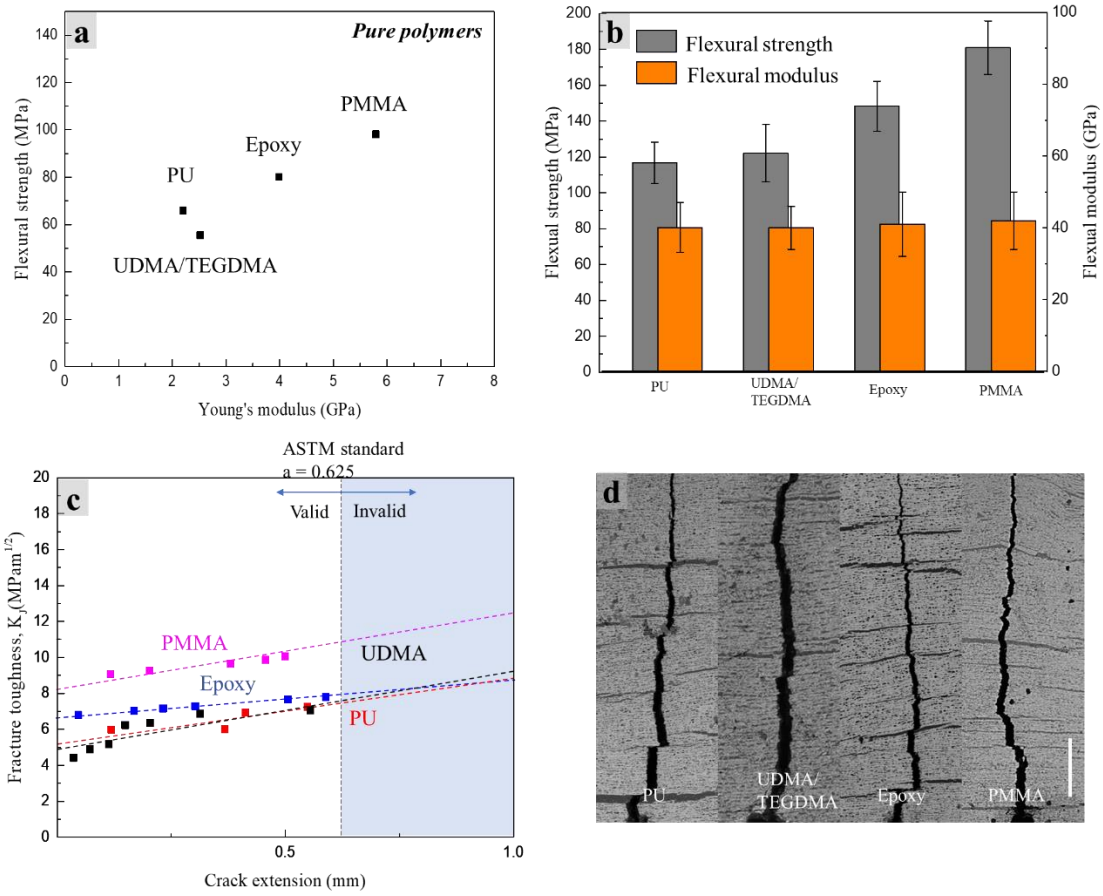

Fig.4-18 *Mechanical properties of pure polymers (PMMA, UDMA/TEGDMA, Epoxy, PU)* ***a)****. Flexural strength and modulus* ***b)*** *and R-curves* ***c)*** *of µL alumina/polymer composites with different types of polymers. Typical SEM micrographs of cracks during in situ R-curve measurements* ***d)****. Scale bar: 500 µm.*

It is clear from **Fig.4-18** that the mechanical properties of the µL composites are remarkably influenced by the choice of polymer used as the compliant phase. The mechanical responses of pure polymer were illustrated in **Fig.4-18a**, it suggests that the strength of polymer was ranged from 50 to 100 MPa and the modulus was ranged from 2 to 6 GPa. The µL alumina/polymer composites exhibited various flexural strengths in the range of 120 to 178 MPa. However, the modulus of composites keeps steady at approximately 40 GPa for different polymeric compliant phases, similar to those reported in literatures [6, 10]. This implied that the ceramic

phase dominated the stiffness of composites. The modulus of pure alumina (386 GPa) is two order of magnitude larger than that of pure polymers (2-6 GPa). The ceramic fraction was kept constant at 72% in this work hence the modulus did not fluctuate significantly with different polymers.

From the *R*-curves and SEM micrographs in **Fig.4-18c, d**, all composite samples exhibited typical energy dissipation mechanisms during crack extension, which is necessary to stabilize the crack growth and to obtain a rising *R*-curve. The *R*-curves reached a range of values of fracture toughness K_J from 6 to 11 MPa $m^{1/2}$ at ASTM limit (a=0.625 mm) for the µL composites with different polymeric compliant phases. As discussed previously, crack deflection in these composites is attributed to the nacre-like architecture of ceramic phase. The results also reveal that the strength and fracture toughness of µL ceramic/polymer composites are positively correlated with the mechanics of the polymers. For example, UDMA/TEGDMA and PU are two polymers with similar strength (60 MPa) and modulus (2.3 GPa) as shown in **Fig.4-18a**, their corresponding composites exhibited similar flexural strength (**Fig.4-18b**) and *R*-curve behaviours (**Fig.4-18c**). However, when the compliant phase is replaced by a stronger and stiffer polymer (epoxy), the flexural strength and fracture toughness (*R*-curve) is slightly improved. Likewise, when the strength and stiffness of compliant phase i.e. PMMA are further increased, µL alumina/PMMA composites demonstrate the highest toughness and strength.

There may be a few possible attributes to the enhanced strength and toughness of nacre-like µL composites. On the one hand, as the compliant phase in µL composites, the polymer act as a lubricant between ceramic walls, the stronger and stiffer lubricant could produce higher friction force during ceramic walls sliding, promoting crack-arresting mechanisms. On the other hand, the polymer phase with higher modulus and strength could effectively reduce stress concentrations within the µL ceramic scaffolds [2]. The results are in agreement with that reported by Niebel *et al.* [2], where the stress distributions of nacre-like BM ceramic/polymer

composites with various polymers were analysed by finite element (FE) model. Therefore, a strong and stiff polymeric compliant phase should be considered in designing nacre-like μL ceramic/polymer composites at a ceramic content of 72% to improve mechanical strength and fracture toughness.

4.3.2.2.4 Summary of μL composites

In summary, the mechanical properties of μL composites displayed both high strength and fracture toughness. The results have provided crucial information on how changes in the microstructure of the μL alumina/PMMA composites can influence their mechanical behaviours **(Fig.4-19)**. When the ceramic wall thickness became thinner (from 40 to 8 μm), the strength and toughness of the composites increased because the size and density of defects in ceramic phase decreased and microfracture-accumulating-mechanism was strengthened. Ceramic fraction made positive contribution to the flexural strength, but the fracture toughness varies when ceramic fraction is increased from 50 to 85 vol.%, with a maximum toughness at 72 vol.%. Both intrinsic and extrinsic toughening mechanisms affect the fracture toughness instantaneously as the volume fraction of constituent phase changes.

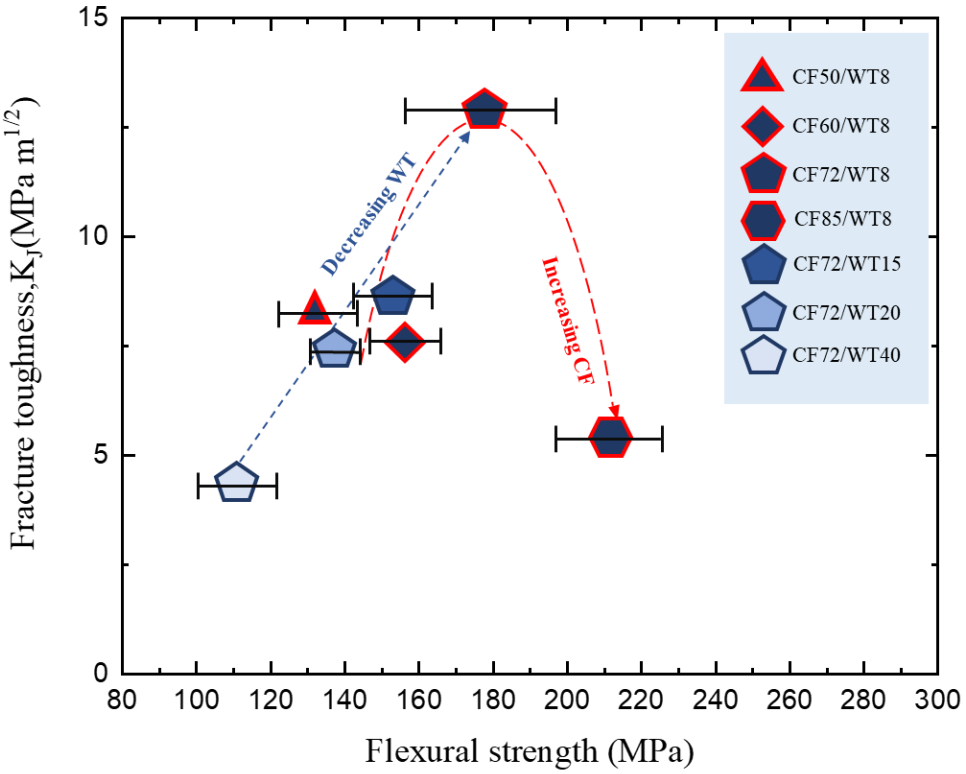

Fig.4-19 *Mechanical performance map of flexural strength vs. fracture toughness of the µL alumina/PMMA composites with different ceramic fractions (CF) and wall thicknesses (WT). The blue dash line indicates the increasing in wall thickness and the red dash line represent increasing alumina content.*

Furthermore, among four different types of polymers with various strength and stiffness, the PMMA with the highest value of strength and modulus apparently offers a new stress distribution and extrinsic toughening mechanism which result in a better mechanical behaviour in µL composites with 72% ceramic fraction.

4.3.2.3 µL vs. BM composites

Fig.4-20 showed the cross-section of nacre-like alumina/PMMA composite materials with µL and BM architectures, fabricated by the one-step and two-step method, respectively. Both have

the same ceramic fraction (72 vol.%), ceramic wall thickness (15 µm) and multi-layered structure with ceramic bridges between layers. However, the µL composite shows a better connectivity and more continuous ceramic walls (**Fig.4-20a** and **c**) compared to the BM composite (**Fig.4-20b** and **d**). In the BM composites, the length of ceramic layers is ranged from 20 to 690 µm, depending on the processing conditions. While the ceramic layers in the µL composites are almost continuous since the lamellar structure created in bi-directional freeze casting is well maintained in the one-step method. This will have significant implications to their corresponding mechanical properties.

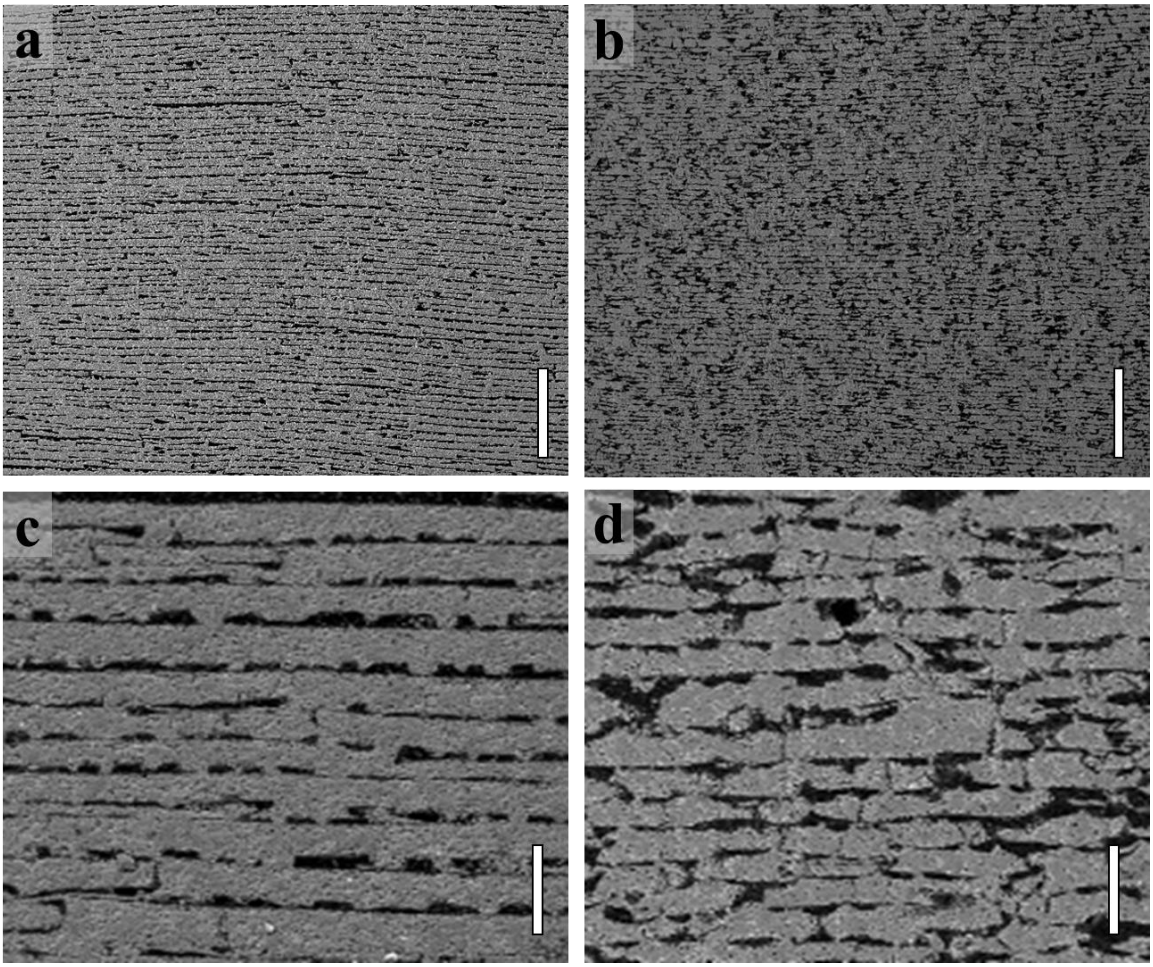

Fig.4-20 *SEM images of alumina/PMMA composite materials containing 72 vol.% alumina with different architecture:* ***a****),* ***c****) µL and* ***b****),* ***d****) BM, produced from the one-step and two-step method, respectively. Scale bar: 500 µm in* ***a****) and* ***b****); 50 µm in* ***c****) and* ***d****).*

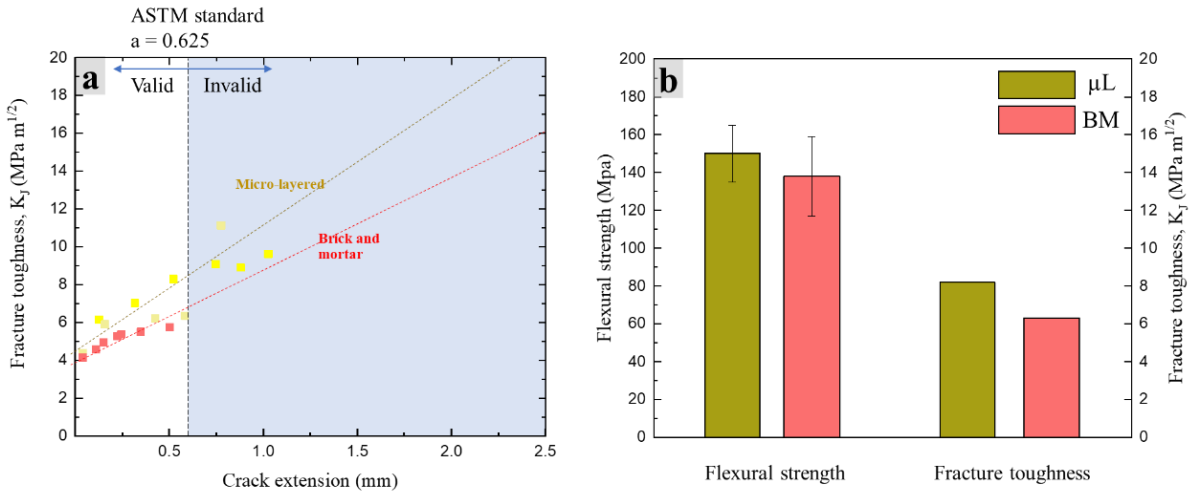

Fig.4-21 *Mechanical properties of nacre-like alumina/PMMA composites, both having 72 vol. % alumina and 15 μm lamellar thickness but with the μL and BM architecture, respectively. Fracture toughness R-curves* ***a)****, average of flexural strength and fracture toughness* K_J *(at a=0.625)* ***b)****.*

Fig.4-21 showed the comparison of mechanical properties of nacre-like composites with BM and μL. As can be seen from **Fig.4-21b**, the strength and fracture toughness K_J of the μL composites are approximately 15% higher than those of the BM composites owing to their distinct microstructure. The longer and more continuous ceramic walls in the μL composites have larger load-bearing capacity, thereby higher strength. As the *R*-curves illustrated in **Fig.4-21a**, both composites initiate at a similar point at around 4 MPa $m^{1/2}$ and displayed a rising toughness K_J. However, the μL composite shows a steeper slope for crack propagating as it has the load-bearing ceramic phase resulting in better capability of resisting crack propagation. Notwithstanding, although the crack geometries was varicose, they still show a typical crack deflection behaviour from the SEM images taken from surface (**Fig.4-22**) or the 2D X-ray radiographs transmitting the sample (**Fig.4-23**). This is because that ceramic layers in the μL composites are not perfectly flat and uniform in thickness during freeze casting, relatively

thinner part in each ceramic layer acted as a weak phase leading to crack attraction. Furthermore, it is reasonably assumed that the thinner parts of ceramic walls played a role of ceramic bridges and offered effective stress transfer between the 'ceramic bricks.' In this case, stresses will be predominantly transferred through these thinner parts (similar to mineral bridges in natural nacre) and redistribute stresses over the entire ceramic layers. Herein, the impact of stress transfer is less than the reinforcement effect, therefore the cracks preferred to deflect along the interface leading to energy dissipation. Consequently, the presence of certain ceramic bridges resulted in an improvement in both strength and fracture toughness, thereby the µL composites could be seen as the ceramic-bridges enhanced BM composites.

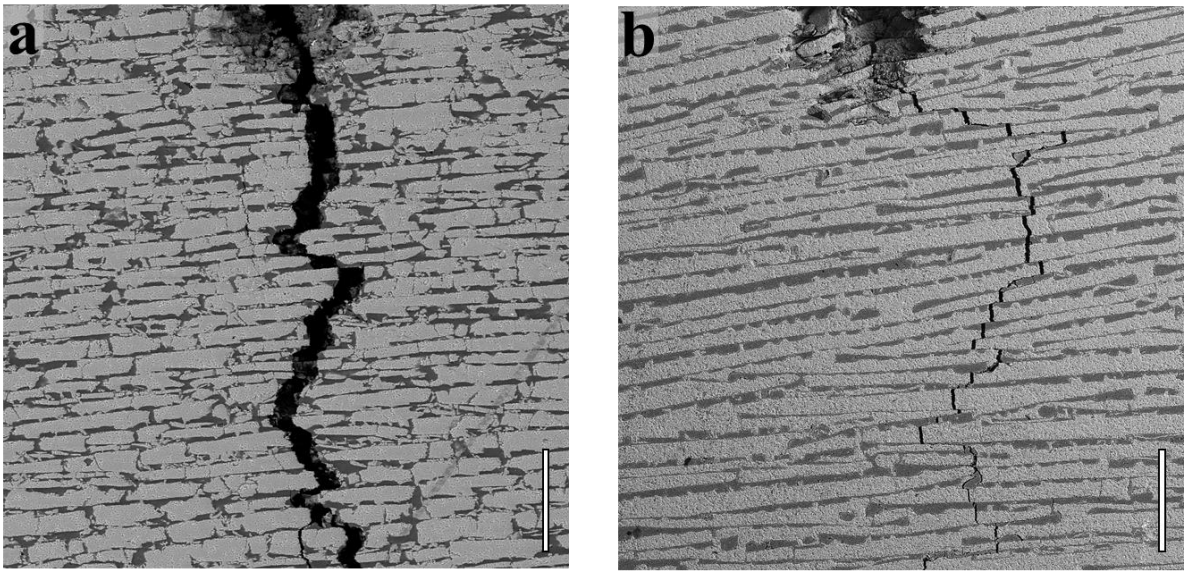

Fig.4-22 *SEM images taken after failure showing the crack propagation behaviour of nacre-like composite* ***a)*** *BM and* ***b)*** *µL, both composites exhibit similar toughening mechanisms: crack deflection, frictional sliding and 'pull-out'. Scale bars:* ***a)*** *and* ***b)****: 100 µm.*

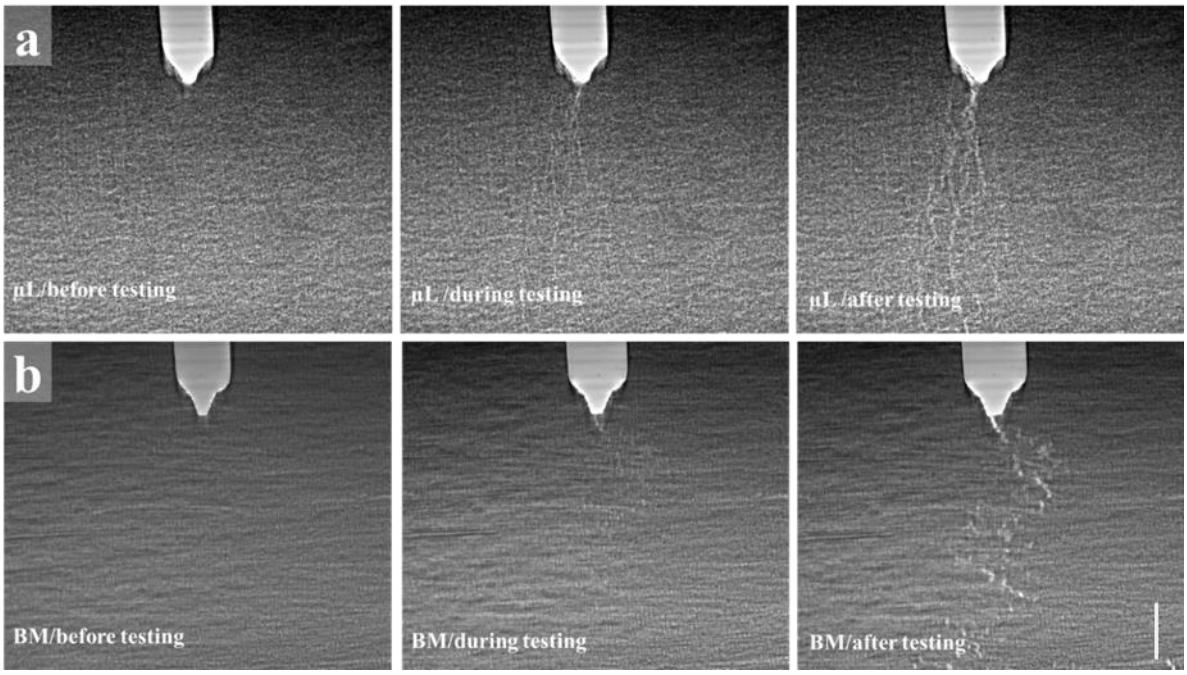

Fig.4-23 *2D X-ray radiographs of alumina/PMMA composites taken during fracture toughness on compact tension specimens. Scale bars: 250 μm.*

The motivation to design and fabricate a novel μL composite is inspired by the microstructure of natural nacre (**Fig.4-24**) which illustrates the assembling of mineral platelets and the narrow spacing between platelets filled by a biopolymer. As from the structural characterization of nacre, the typical spacing between mineral platelets is only several tens of nm [45]. Therefore, to mimic the microstructure of nacre, ceramic bricks in the nacre-like scaffolds should be densely packed with narrow gaps surrounded them from all directions. Thereby, this microstructure can potentially offer more chances of both frictional sliding and stress transfer, resulting in desirable mechanical properties of high strength and high fracture toughness. Launey *et al.* showed that, when applying an extra pressing process i.e. isostatic pressing, at a high pressure of 1.4 GPa, they effectively reduced the distance between ceramic layers and promoted the formation of inorganic (ceramic) bridges between the bricks after sintering resulting in high fracture toughness [6]. In both natural and synthetic nacre-like composites, the secret of such high toughness has been revealed as multi-crack initiation at a weak layer

followed by crack bridging in a tough layer [46]. Both experimental results and theoretical analysis suggested that the unique heterogeneous architecture in these composites improved toughness by creating property variations to slow down crack propagation and prevent crack penetration, as well as guiding cracks along weak interfaces to promote progressive damage [12].

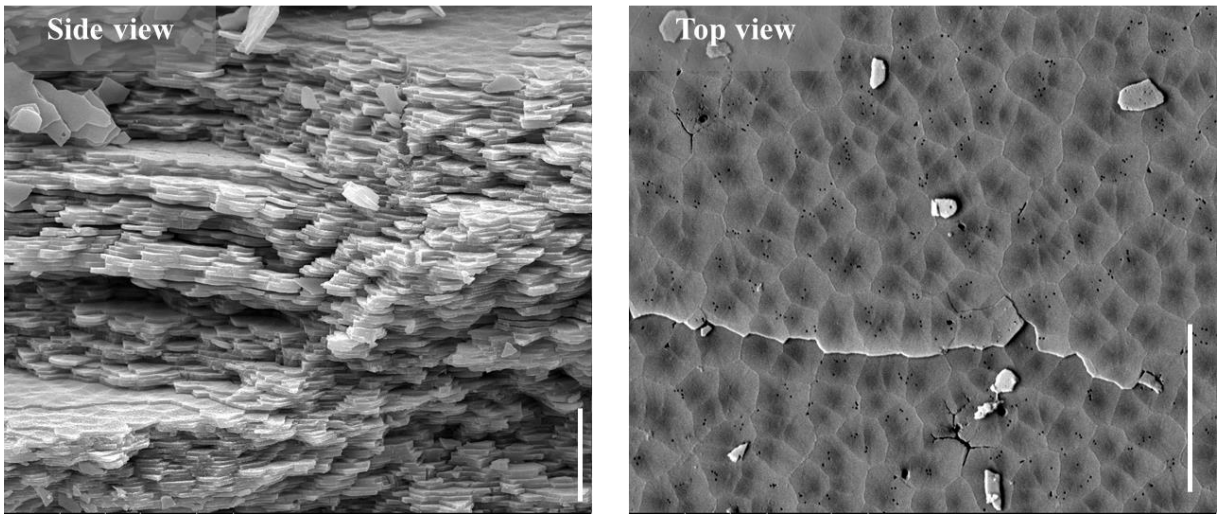

Fig.4-24 *SEM micrograph of natural nacre. Scale bars: 250 µm.*

4.4 Conclusions

In summary, nacre-like ceramic/polymer composite materials were fabricated via infiltrating different polymers (PMMA, UDMA/TEGDMA, epoxy resin, PU) into as-prepared nacre-like ceramic scaffolds. Composites were generated with different manufacturing parameters including sintering temperature, silanization, binder content, solid loading of slurries, compressive distance, selection of different polymer, and densification methods. Those parameters enabled us to fabricate composites with two distinct architectures (BM and µL) with variable ceramic fractions (50-85%), ceramic wall length (250-2500 µm) and ceramic wall thickness (8-40 µm).

Mechanical analysis with *in situ* observation demonstrated that it was possible to achieve a combination of good mechanical properties by the adjustment of microstructure of composites through the control of manufacturing parameters. It was revealed that the nacre-like ceramic/polymer composites with increasing crack resistance showed both intrinsic toughening mechanisms of plastic deformation in the polymer phase and extrinsic toughening mechanisms of ceramic layer pull-out, crack bridging, crack deflection and ceramic bridging [25]. For instance, first-step sintering temperature manipulated the ceramic fraction and microstructure resulting in BM composites with different amount of polymer and ceramic bridges. Silanization was shown to enhance the interface and reduce defects to resist layer pull-out. Higher binder content resulted in μL composites with longer ceramic walls, leading to better stress-transfer and improved crack resistance. Finer ceramic walls exhibited fewer defects and more ceramic layers, leading to higher crack resistance and more deflection behaviours. Higher ceramic fraction resulted in more ceramic bridges and higher frictions between layer-sliding, offering higher dissipating energy during crack propagation. However, when the ceramic fraction was above a threshold, i.e. >85 vol.%, ceramic bridges became predominant with diminished polymer phase alongside their unique deformation and crack deflection mechanisms, the μL alumina/PMMA composites displayed a brittle fracture behaviour, the nacre-like architectures lost its main function. When the PMMA was substituted with other polymers, μL alumina/polymer composites (at 72% ceramic fraction) still maintained the crack deflection. However, the mechanical strength and toughness of composites were dependent on polymers. Those with lower stiffness and strength such as PU and UDMA/TEGDMA significantly decreased the strength and toughness of composites. Finally, alumina/PMMA composites with the same ceramic fraction (72%) and wall thickness (15 μm) but with different architectures (μL and BM) were compared. Both μL and BM composites displayed rising *R*-curves because of their similar toughening mechanisms. However, their flexural strength and fracture

toughness (K_{JC}) were different owing to their difference in architecture. The BM composites fabricated by a two-step densification method had shorter bricks in each ceramic layer. Nevertheless, the μL composites fabricated by the one-step densification method exhibited a better structural integrity, leading to superior mechanical properties due to their better load-bearing and stress-distributing capacity. The most novel aspect of the one-step densification method developed in this work was that it was possible to produce the μL scaffolds with short inter-layer distance and even bridges to connect the ceramic bricks in continuous ceramic layers without the use of isostatic pressing at a high pressure and additional sintering stages. The performance results also clearly revealed that μL composites possessed distinct advantages over BM composites.

4.5 References

[1] J. Facenda, M. Borba, P. Corazza, A literature review on the new polymer-infiltrated ceramic-network material (PICN), Journal of Esthetic and Restorative Dentistry 30 (2018).

[2] T.P. Niebel, F. Bouville, D. Kokkinis, A.R. Studart, Role of the polymer phase in the mechanics of nacre-like composites, Journal of the Mechanics and Physics of Solids 96 (2016) 133-146.

[3] E. Munch, M.E. Launey, D.H. Alsem, E. Saiz, A.P. Tomsia, R.O. Ritchie, Tough, Bio-Inspired Hybrid Materials, Science 322(5907) (2008) 1516-1520.

[4] F. Barthelat, Z. Yin, M.J. Buehler, Structure and mechanics of interfaces in biological materials, Nature Reviews Materials 1(4) (2016) 16007.

[5] M. Abboud, M. Turner, E. Duguet, M. Fontanille, PMMA-based composite materials with reactive ceramic fillers. Part 1.—Chemical modification and characterisation of ceramic particles, Journal of Materials Chemistry 7(8) (1997) 1527-1532.

[6] M.E. Launey, E. Munch, D.H. Alsem, H.B. Barth, E. Saiz, A.P. Tomsia, R.O. Ritchie, Designing highly toughened hybrid composites through nature-inspired hierarchical complexity, Acta Materialia 57(10) (2009) 2919-2932.

[7] M. Grossman, F. Bouville, F. Erni, K. Masania, R. Libanori, A.R. Studart, Mineral Nano-Interconnectivity Stiffens and Toughens Nacre-like Composite Materials, Advanced Materials 29(8) (2017) 1605039.

[8] S. Askarinejad, N. Rahbar, Toughening mechanisms in bioinspired multilayered materials, Journal of the Royal Society Interface, 12 (2015) 20140855.

[9] F. Barthelat, Designing nacre-like materials for simultaneous stiffness, strength and toughness: Optimum materials, composition, microstructure and size, Journal of the Mechanics and Physics of Solids 73 (2014) 22-37.

[10] G. Tan, J. Zhang, L. Zheng, D. Jiao, Z. Liu, Z. Zhang, R.O. Ritchie, Nature-Inspired Nacre-Like Composites Combining Human Tooth-Matching Elasticity and Hardness with Exceptional Damage Tolerance, Advanced Materials 31(52) 1904603.

[11] A. Wat, J.I. Lee, C.W. Ryu, B. Gludovatz, J. Kim, A.P. Tomsia, T. Ishikawa, J. Schmitz, A. Meyer, M. Alfreider, D. Kiener, E.S. Park, R.O. Ritchie, Bioinspired nacre-like alumina with a bulk-metallic glass-forming alloy as a compliant phase, Nature Communications 10(1) (2019) 961.

[12] E.S. Fakunle, Z.P. Aguilar, J.L. Shultz, A.D. Toland, I. Fritsch, Evaluation of Screen-Printed Gold on Low-Temperature Co-Fired Ceramic as a Substrate for the Immobilization of Electrochemical Immunoassays, Langmuir 22(25) (2006) 10844-10853.

[13] L. Hallmann, P. Ulmer, F. Lehmann, S. Wille, O. Polonskyi, M. Johannes, S. Köbel, T. Trottenberg, S. Bornholdt, F. Haase, H. Kersten, M. Kern, Effect of surface modifications on

the bond strength of zirconia ceramic with resin cement resin, Dental Materials 32(5) (2016) 631-639.

[14] J.R. Ebdon, Introduction to polymers (second edition) R. J. Young and P. A. Lovell Chapman and Hall, London, 1991. pp. 443, price £16.95. ISBN 0-412-30640-9 (PB); ISBN 0–412–30630–1 (HB), Polymer International 27(2) (1992) 207-208.

[15] Fabrication and characterisation of biomimetic nacre-like ceramic/polymer composite a potential CAD/CAM dental material Algharaibeh, S. W. A. R. (Author). 24 Mar 2020
Student thesis: Doctoral Thesis › Doctor of Philosophy (PhD).

[16] H. Chen, D. Yang, Z. Guo, Dispersivity of modified ZnO and characterization of polyurethane/ZnO composites, Polymer Composites 35(2) (2014) 237-244.

[17] M.E. Connell, W.M. Cross, T.G. Snyder, R.M. Winter, J.J. Kellar, Direct monitoring of silane/epoxy interphase chemistry, Composites Part A: Applied Science and Manufacturing 29(5) (1998) 495-502.

[18] K. van Rijswijk, H.E.N. Bersee, Reactive processing of textile fiber-reinforced thermoplastic composites – An overview, Composites Part A: Applied Science and Manufacturing 38(3) (2007) 666-681.

[19] H. Janik, M. Sienkiewicz, J. Kucinska-Lipka, 9 - Polyurethanes, in: H. Dodiuk, S.H. Goodman (Eds.), Handbook of Thermoset Plastics (Third Edition), William Andrew Publishing, Boston, 2014, pp. 253-295.

[20] K. Hodd, 37 - Epoxy Resins, in: G. Allen, J.C. Bevington (Eds.), Comprehensive Polymer Science and Supplements, Pergamon, Amsterdam, 1989, pp. 667-699.

[21] H.H. Hamama, 19 - Recent advances in posterior resin composite restorations, in: A.M. Asiri, Inamuddin, A. Mohammad (Eds.), Applications of Nanocomposite Materials in Dentistry, Woodhead 2019 edition, pp. 319-336.

[22] M.E. Launey, R.O. Ritchie, On the Fracture Toughness of Advanced Materials, Advanced Materials 21(20) (2009) 2103-2110.

[23] S. Fan, B. Yilong, Mineral bridges of nacre and its effects, Acta Mechanica Sinica 17(3) (2001) 251.

[24] A.G. Checa, J.H.E. Cartwright, M.-G. Willinger, Mineral bridges in nacre, Journal of Structural Biology 176(3) (2011) 330-339.

[25] V. Naglieri, B. Gludovatz, A.P. Tomsia, R.O. Ritchie, Developing strength and toughness in bio-inspired silicon carbide hybrid materials containing a compliant phase, Acta Materialia 98 (2015) 141-151.

[26] M. Grossman, F. Bouville, K. Masania, A.R. Studart, Quantifying the role of mineral bridges on the fracture resistance of nacre-like composites, Proceedings of the National Academy of Sciences 115(50) (2018) 12698-12703.

[27] H. Zhao, Y. Yue, L. Guo, J. Wu, Y. Zhang, X. Li, S. Mao, X. Han, Cloning Nacre's 3D Interlocking Skeleton in Engineering Composites to Achieve Exceptional Mechanical Properties, Advanced Materials 28(25) (2016) 5099-5105.

[28] F. Greco, L. Leonetti, A. Pranno, S. Rudykh, Mechanical behavior of bio-inspired nacre-like composites: A hybrid multiscale modeling approach, Composite Structures 233 (2020) 111625.

[29] F. Bouville, E. Maire, S. Meille, B. Van de Moortèle, A.J. Stevenson, S. Deville, Strong, tough and stiff bioinspired ceramics from brittle constituents, Nature Materials 13(5) (2014) 508-514.

[30] K. Radi, D. Jauffres, S. Deville, C.L. Martin, Strength and toughness trade-off optimization of nacre-like ceramic composites, Composites Part B: Engineering 183 (2020) 107699.

[31] A. Dreyer, A. Feld, A. Kornowski, E.D. Yilmaz, H. Noei, A. Meyer, T. Krekeler, C. Jiao, A. Stierle, V. Abetz, H. Weller, G.A. Schneider, Organically linked iron oxide nanoparticle supercrystals with exceptional isotropic mechanical properties, Nature Materials 15(5) (2016) 522-528.

[32] P. Das, J.-M. Malho, K. Rahimi, F.H. Schacher, B. Wang, D.E. Demco, A. Walther, Nacre-mimetics with synthetic nanoclays up to ultrahigh aspect ratios, Nature Communications 6(1) (2015) 5967.

[33] ASTM E1820-17. Annual book of ASTM standards, ASTM International; 2017.

[34] H. Kakisawa, T. Sumitomo, The toughening mechanism of nacre and structural materials inspired by nacre, Sci Technol Adv Mater 12(6) (2012) 064710-064710.

[35] S. Algharaibeh, A.J. Ireland, B. Su, Bi-directional freeze casting of porous alumina ceramics: A study of the effects of different processing parameters on microstructure, Journal of the European Ceramic Society 39(2) (2019) 514-521.

[36] F. Barthelat, H. Tang, P.D. Zavattieri, C.M. Li, H.D. Espinosa, On the mechanics of mother-of-pearl: A key feature in the material hierarchical structure, Journal of the Mechanics and Physics of Solids 55(2) (2007) 306-337.

[37] H. Le Ferrand, F. Bouville, T.P. Niebel, A.R. Studart, Magnetically assisted slip casting of bioinspired heterogeneous composites, Nature Materials 14 (2015) 1172.

[38] Z. Jia, L. Wang, 3D printing of biomimetic composites with improved fracture toughness, Acta Materialia 173 (2019) 61-73.

[39] Y. Zhang, X. Li, Bioinspired, Graphene/Al2O3 Doubly Reinforced Aluminum Composites with High Strength and Toughness, Nano Letters 17(11) (2017) 6907-6915.

[40] Y. Zhang, F.M. Heim, J.L. Bartlett, N. Song, D. Isheim, X. Li, Bioinspired, graphene-enabled Ni composites with high strength and toughness, Science Advances 5(5) (2019) eaav5577.

[41] L. Acosta-Torres, A. Mendieta, R. Nuñez, M. Cajero-Juárez, V. Castaño, Cytocompatible antifungal acrylic resin containing silver nanoparticles for denture, International journal of nanomedicine 7 (2012) 4777-86.

[42] L.C. Nicolae, R.M. Shelton, P.R. Cooper, R.A. Martin, W.M. Palin, The Effect of UDMA/TEGDMA Mixtures and Bioglass Incorporation on the Mechanical and Physical Properties of Resin and Resin-Based Composite Materials, Conference Papers in Science 2014 (2014) 646143.

[43] D. Mathivanan, J. Siregar, D. Bachtiar, R. Rejab, T. Cionita, Effect of Fibre Loading on The Flexural Properties of Natural Fibre Reinforced Polymer Composites, Applied Mechanics and Materials 695 (2014) 85-88.

[44] Xencast, Manual of Xencast P6 Toughened Polyurethane Casting Resin 1kg Pack, Easycomposites (2020).

[45] X. Li, W.-C. Chang, Y.J. Chao, R. Wang, M. Chang, Nanoscale Structural and Mechanical Characterization of a Natural Nanocomposite Material: The Shell of Red Abalone, Nano Letters 4(4) (2004) 613-617.

[46] S. Kamat, H. Kessler, R. Ballarini, M. Nassirou, A.H. Heuer, Fracture mechanisms of the Strombus gigas conch shell: II-micromechanics analyses of multiple cracking and large-scale crack bridging, Acta Materialia 52(8) (2004) 2395-2406.

Chapter 5

Nacre-like ceramic/metal composites

5.1 Introduction

Nacre-like ceramic-based composites with micro-layered (μL) scaffolds infiltrated by a relatively soft compliant phase are projected to increase their strength and toughness. In Chapter 4, nacre-like ceramic/polymer composites exhibiting exceptional mechanical properties were achieved through careful manipulation of microstructure, architecture, and composition in order to imitate the specific features with the unique properties of nacre. Accordingly, the ceramic-based composites can also be strengthened and toughened when the polymeric compliant phase was replaced by a stronger and tougher metallic phase [1]. This chapter involves metal infiltration into μL ceramic scaffolds as a compliant phase to create the nacre-like ceramic/metal composite materials. Aluminium and magnesium alloys are widely used metal materials which are lightweight, strong, tough, corrosion resistant, as well as thermally and electrically conductive. Two types of alloys were used to represent aluminium alloy (5083) and magnesium alloy (AZ31) as their major components are Al and Mg, respectively. Two main composite systems were investigated i.e. alumina/aluminium and hydroxyapatite (HA)/magnesium.

Composites of ceramic/aluminium are normally produced by powder metallurgy and molten metal routes. However, using these methods, it is difficult to generate composites with complex architectures. To obtain structural ceramic/aluminium composites, ceramic scaffolds with a lamellar structure have been employed by pressure-assisted infiltration with molten alloys [2-4]. Nevertheless, the ceramic fraction of composites was limited (below 40%). In order to penetrate metal into scaffolds with smaller pore size as well as higher ceramic fraction (above

40%), the pressure applied for infiltration needs to be dramatically increased, which may deform or break the ceramic scaffolds during infiltration [5, 6]. Hence, the Lanxide process was developed to infiltrate metal into ceramic preform without external pressure and the resultant composite inherited the structure of the preform [7]. This technique is cost-effective as the infiltration process is driven by capillarity forces with the complete absence of external pressure. Therefore, types of ceramic and metal used are restricted depending on the wettability of ceramic to metal phases which plays a key role in this process. For example, it was reported by Rao *et al.* that alumina scaffolds could be infiltrated with alloy containing both aluminium and magnesium [8], because Mg in the aluminium alloy decreased the surface tension of molten aluminium alloy at high temperatures, resulting in improvement of wettability between alumina and aluminium alloy [8-10]. Use of nitrogen atmosphere in the process was also recommended to further improve the wettability [8]. For the preparation of alumina/aluminium composite materials here, Lanxide process was used which involves infiltration of aluminium alloy (5083) into alumina scaffolds with nacre-like μL architectures. After the completion of infiltration process, composite materials were tested for mechanical response with the ceramic fraction from 18% to 72%.

The second objective is to fabricate nacre-like biodegradable HA/magnesium implant materials using pressureless infiltration. Recent studies indicate that there is a high demand of biodegradable implants as orthopaedic biomaterials to eliminate the follow-up surgery of implants after bone healing [11]. The main features of the orthopaedic implant materials are not only to provide complete set of mechanical properties to support body structure but also to make it biocompatible with human tissues. Titanium-based alloys have been used as orthopaedic implant materials for many years because of their exceptional mechanical properties, biocompatibility, and corrosion resistance. Along with various advantages these materials also have some disadvantages e.g. titanium alloys are normally too stiff (with a

Young's modulus of 110 GPa) compared to human bone (20-30 GPa) therefore they show stress shielding effect to weaken or even damaging surrounding bone [12, 13]. Titanium alloy can also release toxic cations into blood which may lead to permanent physical irritation chronic inflammatory and impair human body's health [14]. Additionally, titanium implants are not biodegradable. They need to be removed after the bone healing process, especially for young patients. In order to address these problems, biodegradable implant materials with bone-matching stiffness are desirable. However, polymer-based biodegradable implants exhibited poor mechanical performances which restrict their uses for load-bearing implant applications [15, 16]. Mg-based materials were investigated as biodegradable implant materials because Mg has a lower Young's modulus (about 45 GPa) which is closer to that of bone than titanium, and can be gradually dissolved, absorbed and consumed at implanting location [17, 18] whereas Mg^{2+} cations released are not only harmless, but also accelerate the healing of bone tissues [19-21]. Recently, use of Mg alloys [22] as bone implants has shown a significant progress. Along with numerous positive aspects of these materials, rapid degradation of Mg and its alloy implant materials inside the human body is still a major obstacle hampering their use in the clinic. Fast degradation of Mg metal and its alloy will cause alkalization and hydrogen gas evolution which will affect local blood flow [23] and delay bone tissue integration [24]. To reduce the degradation rate of Mg, HA was considered to composed with magnesium. HA, as a natural bone constituent, is a bioactive ceramic material with excellent biocompatibility with human bone [25, 26]. HA can further promote the adhesion and differentiation to bone cells because of its excellent osteoconductive and osteoinductive properties [27, 28]. Pure HA material is not suitable to be used directly as load-bearing implants because it exhibited poor mechanical properties with low strength and toughness [29]. As a result, HA/magnesium composite was considered to be used as a promising biodegradable implant material as it can combine the advantages of both Mg alloys and HA. Therefore, HA/magnesium composites

were developed to improve the corrosive resistance [30], mechanical performance [31, 32] and degradation behaviour [33]. HA was also coated on implanted materials as a protective layer via a number of techniques including electrochemical deposition, sol-gel processing, spray and laser techniques [34-37]. However, in many cases, the coated samples exhibited undesired corrosion resistance, typically due to crack formation or poorly controlled morphologies of the HA coating layer [38]. Apart from coating, HA/magnesium composites were fabricated by extrusion of HA and Mg powders at 300-500 ℃ [39-42] or compaction-sintering process of powders [43, 44] where HA particles acted as the reinforcement phase dispersed within the Mg matrix. Nevertheless, the structural integrity of HA/Mg composites could not be retained after the degradation of Mg matrix. To prepare composites with biomimetic architecture, pressure-assisted infiltration was used to fabricate HA/magnesium composites with 3D HA network structure [45]. The molten magnesium alloy was infiltrated into 3D HA preforms with larger pores (500 μm), under 4-5 MPa pressure for a short duration (5 s), care was needed to preserve the porous structure of the HA preforms [45]. The resultant composites exhibited improved mechanical properties compared with the HA scaffolds alone.

In this work, the HA/magnesium composites with nacre-like μL architecture were prepared by pressureless infiltration of Mg alloy into nacre-like HA scaffolds in order to obtain biodegradable implant materials with good strength and toughness. However, from the previous studies, HA had a poor wettability with molten Mg which also reacted rapidly to produce MgO [46, 47] which might further prevent the Mg infiltration [48]. This reactivity problem indicated that the HA/magnesium composites were difficult to be prepared by pressureless infiltration of Mg directly into HA scaffolds. Interfacial modification was needed to improve the wettability which enabled pressureless infiltration between the alloy and ceramic phase [5]. Silica was introduced as a coating to promote the wettability of silicon carbide by molten magnesium alloys at high temperature [49-51]. Therefore, a similar approach

was adopted in this work. The μL HA scaffolds were coated with silica and then pressurelessly infiltrated with molten Mg alloy. The microstructure and composition of HA/magnesium composites were characterized. The mechanical responses were evaluated and compared with cortical bones and other implant materials.

5.2 Materials and method

5.2.1 Surface modification by silica suspension

A colloidal silica, Ludox (AS-30, Grace, UK) was utilized to form silica coating on HA scaffolds. Ludox is a 30% aqueous dispersion of colloidal silica with a particle size of 12 nm. It was commonly used to produce silica coating on ceramic surface to modify the chemical and mechanical properties of materials [52]. In this work, the HA scaffolds with μL architectures prepared by bi-directional freeze casting (Chapter 3) were modified and coated with silica nanoparticles. The HA scaffolds were infiltrated with Ludox in a vacuum casting impregnation system (Cast N` Vac 1000, Buehler, US). The container of HA scaffolds/Ludox was sealed to avoid solvent evaporation and then transferred at a dry, cool place for 12 hours allowing the silica nanoparticles uniformly diffuse into the scaffolds. Next, the HA scaffolds were dried and calcined at 600 ℃ for 12 hours in a Muffle furnace where the silica nanoparticles were fused mutually into coatings on the surface of HA scaffolds.

5.2.2 Pressureless infiltration

The as-prepared uncoated or coated HA scaffolds were then infiltrated with molten metals via a pressureless process. The infiltration was carried out in a tubular furnace as shown in Section 2.2.6. Here, two different alloys were used: aluminium alloy (5083) and magnesium alloy (AZ31). The preparation of different material systems requires different atmosphere, temperature, and reaction time as shown in **Table 5-1**. Prior to heating up, the tubular furnace was flowed with an inert gas (e.g. Ar or N_2) for 1 hour to replace air. The furnace was firstly

heated to 400 ℃ at a heating rate of 10 ℃/min then the temperature was held for 60 min allowing the reaction of getter and oxygen to reduce the possibility to form metal oxide on the surface of infiltrating metal (see **Fig.2-8**), which has negative impact to infiltration. The tubular furnace was then heated to infiltrating temperature and held for up to 180 min to complete the infiltration. Prior to opening the tubular furnace and collecting samples, the protective gas flowing was maintained until the tubular furnace was cooled down below 150 ℃.

Composite	Alumina/aluminium	HA/magnesium
Ceramic	µL Alumina	µL HA
Silica-coating	No	Yes
Ceramic fraction (%)	18-72	18
Metal (alloy)	5083	AZ31
Infiltrating atmosphere	N_2	Ar
Crucible	Alumina	Graphite
Infiltrating temperature (℃)	950	650-950
Infiltrating time (min)	180	10-180

Table 5-1 *The experimental conditions of pressureless infiltration for different composites.*

Before further microstructure and mechanical characterizations, samples were grinded using SiC sandpaper from #80 to #2000 finishing and polished using a cloth disk (MD-Nap, Struers, Denmark) with diamond pastes (1 µm) to obtain a smooth surface.

5.2.3 Microstructural characterization

The microstructure of materials was characterised by scanning electron microscope (SEM, Quanta 200F, FEI, US). The composition and elemental distribution were evaluated by X-ray diffraction (XRD, Bruker D8 Advance, US) and energy-dispersive X-ray spectroscopy (EDS, Jeol IT300, US).

5.2.4 Mechanical characterization

Compressive strength of composites was measured by compression tests on the rectangular specimens of 2 mm×2 mm×3 mm. Flexural strength of composites was evaluated by three-point bending on the rectangular beams with size of 1.5 mm×2 mm×25 mm (span=12.5 mm). Fracture toughness K_{IC} and *R*-curves were measured by three-point bending tests on single-edge notched bending (SEB) specimens with 1.5 mm×3 mm×20 mm (span=12.5 mm) and 2 mm×4 mm×20 mm (span=16 mm), respectively. *In situ* micro-CT (X-ray synchrotron, Advanced light source, Berkeley, US) was utilized to monitor the crack propagation during fracture toughness testing. The loading direction was perpendicular to the layers of μL architecture. The crack propagation length was estimated from 3D micro-CT tomography images reconstructed using Avizo as shown in **Fig.5-1.** Firstly, the 2D profile of cracks was obtained via slicing the 3D tomography along the crack direction into around ˜610 images (3 μm in distance per images). The first and last 30 images (~0.1 mm in distance) near the surface were excluded. Then the crack length was taken every 50 images (~0.15 mm in distance). The average value of all the measurements was defined as the crack length.

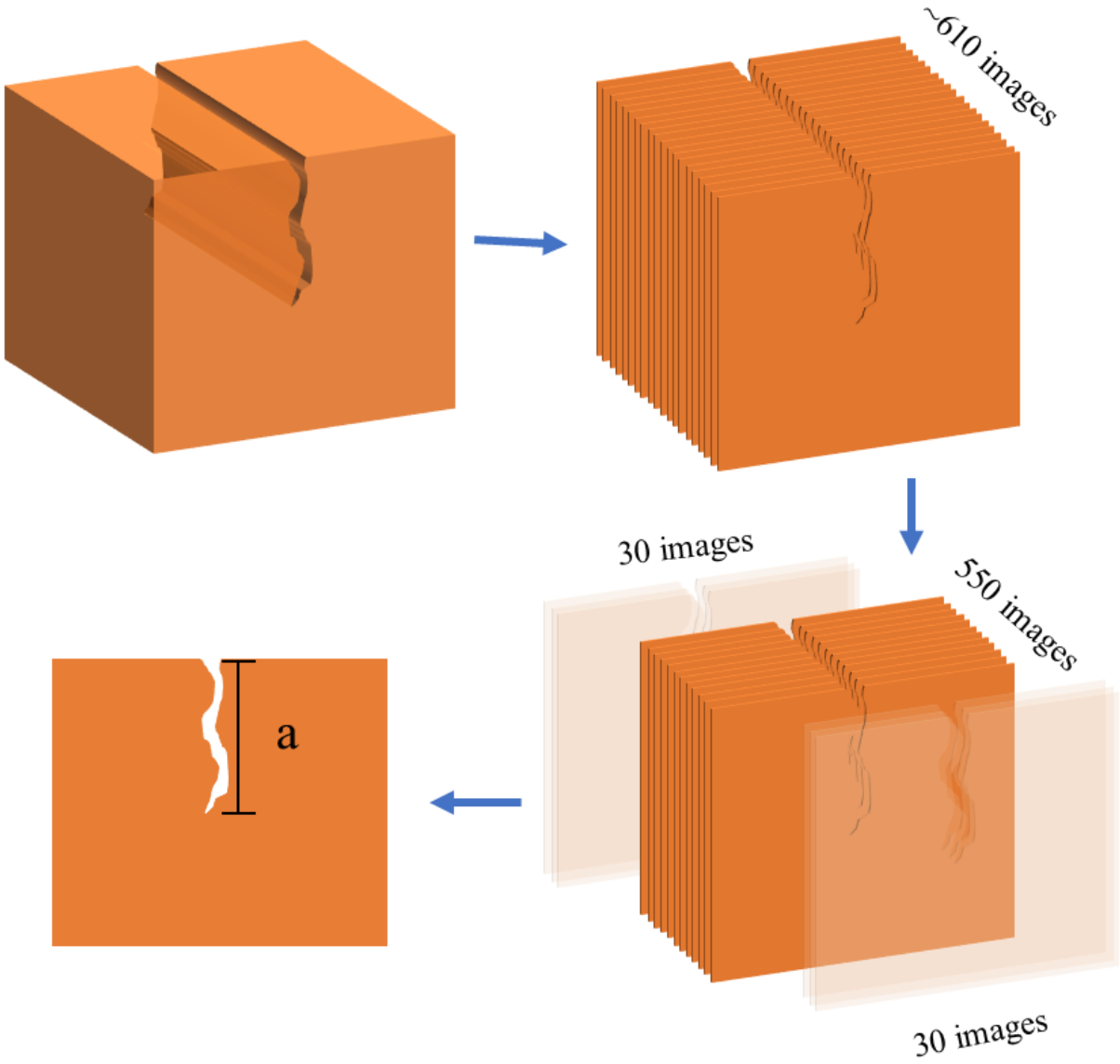

Fig.5-1 Estimation of crack length from a 3D tomography.

5.3 Results and discussion

5.3.1 Alumina/aluminium

Alumina/aluminium composites were prepared via pressureless infiltration of molten aluminium alloy (5083) into alumina scaffolds. According to 3.3.3, μL alumina scaffolds were produced with different ceramic fractions (18%, 50%, and 72%) by altering the compressive distance in the one-step method.

5.3.1.1 Microstructure and compositions

Fig.5-2a, b, and **c** demonstrated the microstructure of μL alumina/aluminium composites with various ceramic fractions. It can be seen that aluminium alloy infiltrated into ceramic scaffolds without damaging the μL architecture of scaffolds for all three samples but with various degrees of defects. As reported before, pressureless infiltration of aluminium alloy was dependent on the reactions between Mg, N_2, and Al [8-10]. The Mg in the alloy partially evaporated and reacted with N_2 to form a layer of Mg_3N_2 (5.1) on the surface of ceramic scaffolds. This Mg_3N_2 layer then reacted with the molten Al through a replacement reaction producing metal Mg and AlN (5.2).

$$3Mg + N_2 = Mg_3N_2 \quad (5.1)$$

$$Mg_3N_2 + 2Al = 3Mg + 2AlN \quad (5.2)$$

The metal Mg participated in cycling reaction with N_2 (5.1) [8] and the produced AlN layer has better wettability with the molten Al.

Combining (5.1) and (5.2):

$$2Al + N_2 = 2AlN \quad (5.3)$$

where the Mg acted as a catalyst in (5.3).

Fig.5-2 showed that composites with higher ceramic fraction have relatively more and larger defects at the interface. This was probably because of the different extent of reactions (5.1 & 5.2) during the infiltration of molten metal to ceramic scaffolds and formation of metal oxide during infiltration. Obviously, higher ceramic fraction meant narrower spacings between ceramic microlayers and smaller surface areas of molten aluminium alloy front exposed to N_2 in the ceramic scaffolds. The chances of N_2 to react with molten Al to form AlN were thus lower (5.3), which was less likely to improve the wetting and facilitate the Al infiltration. Besides, narrower spacings and smaller pores in scaffolds also meant that it was more difficult to replace air by N_2 completely when the tubular furnace was flowed with N_2 before

pressureless infiltration. In the following infiltration process, there was a higher possibility to form metal oxide by reacting with adsorbed air. The as-generated aluminium oxide on the surface of the molten aluminium alloy front was likely to prevent infiltration process. Hence, at higher ceramic fractions, the obtained composites produced more defects and larger flaws at the interface due to relatively poorer wettability and formation of metal oxide. This was also reflected in the measured densities of composites (**Fig.5-2d**). The difference between the real and theoretical densities of composites is more pronounced due to increased porosity in composites when the ceramic fraction increases. The theoretical density was calculated through RoM and the real density was measured by Archimedes methods.

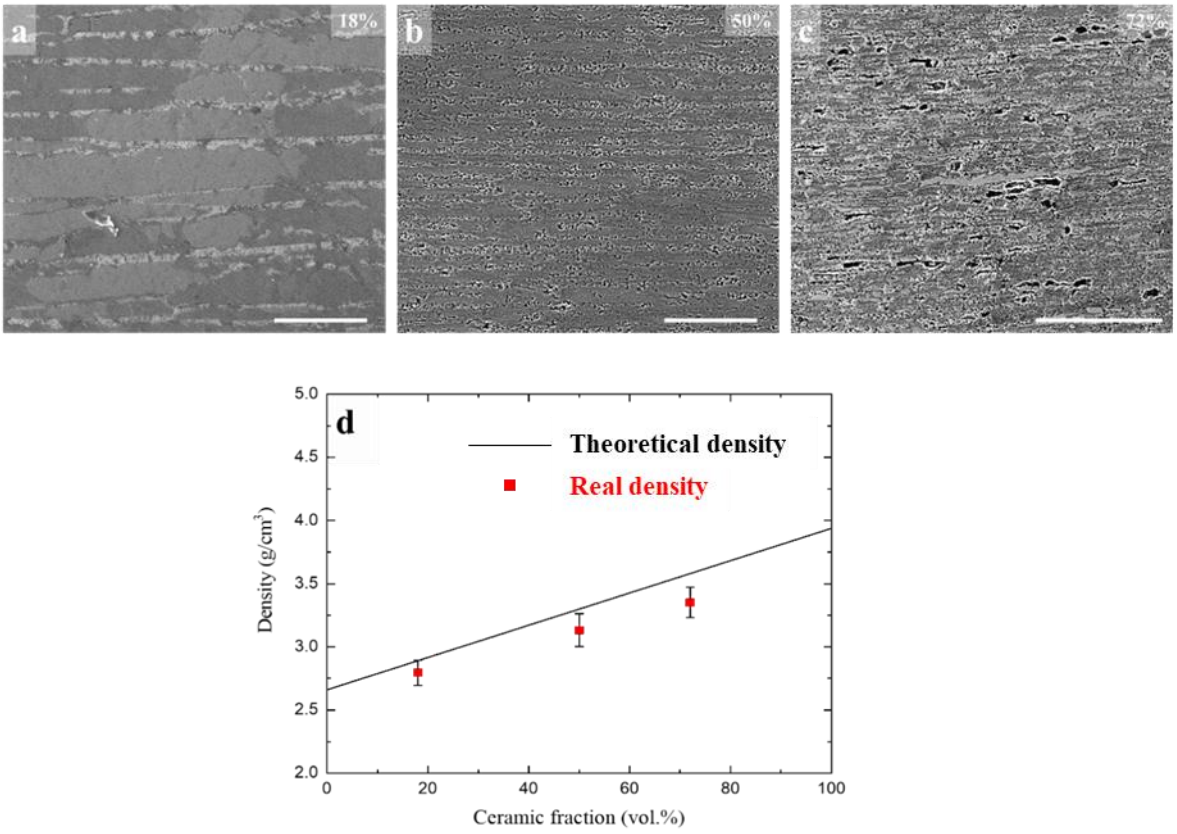

Fig.5-2 *SEM micrographs show the microstructure and defects distribution in alumina/aluminium composites (without silica-coating process) with ceramic fraction of 18%* ***a)****, 50%* ***b)****, and 72%* ***c)****. The theoretical densities was compared with real density* ***d)****. Scale bars for* ***a), b),*** *and* ***c):*** *100 µm.*

Because the alumina was chemically stable at the infiltrating temperature (950 ℃) [53], there should be no obvious changes in the composition of ceramic phase. However, the EDS results indicated that there were some Fe, Cr and Mn precipitates in the metal phase, apart from Al, C, O and Mg element, as shown in **Fig.5-3**.

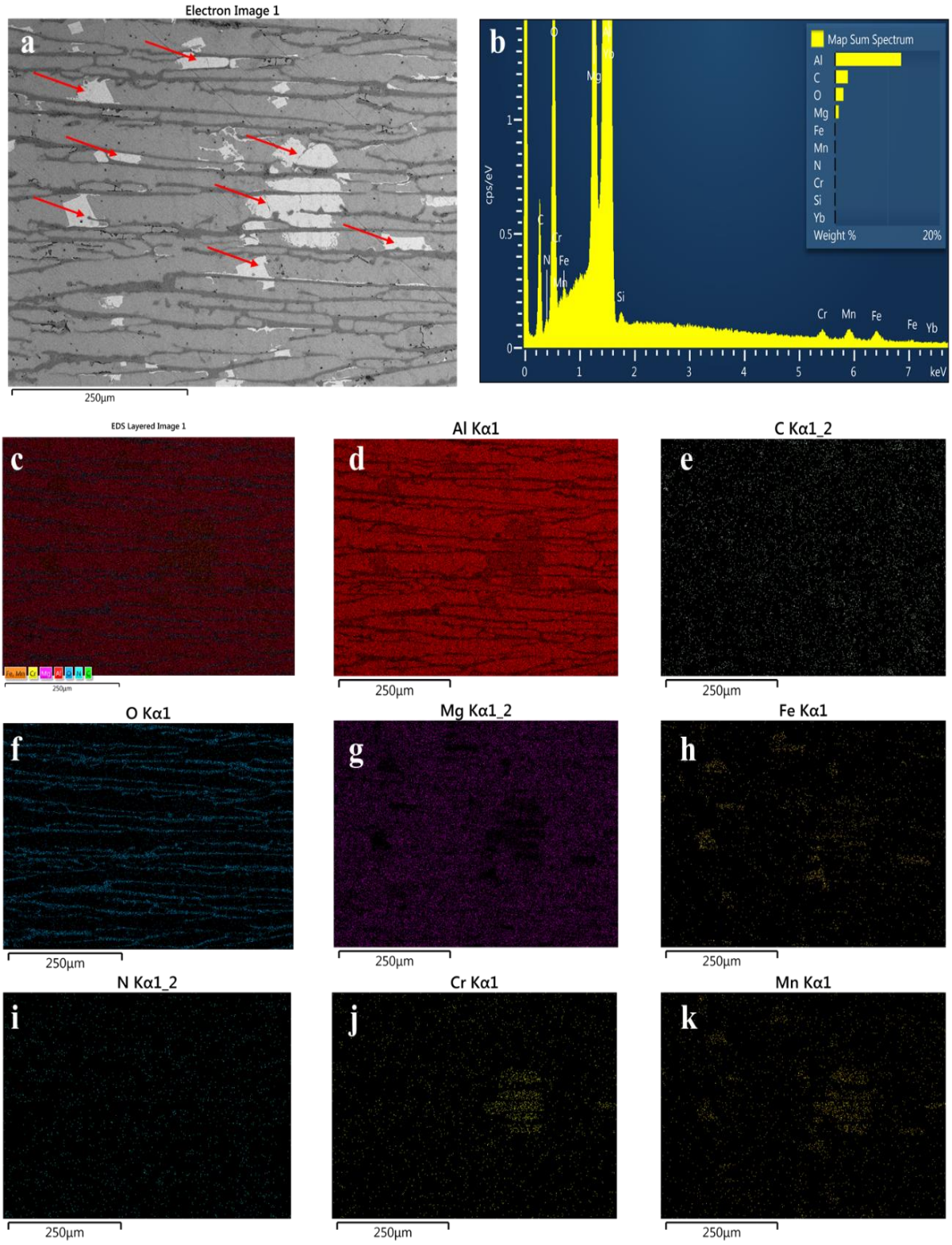

Fig.5-3 *SEM microstructures* ***a)****, elemental weight ratio spectrum* ***b)****, and elemental distribution maps for all* ***c)*** *and individual elements* ***d-k****) of µL alumina/aluminium composites with 18% ceramic fraction. The red arrows indicate the secondary phase.*

The SEM image in **Fig.5-3a** showed the microstructure and area for elemental analysis of alumina/aluminium composite. Obviously, the metal phase in the composite consists of two different phase-regions exhibiting various contrast in the SEM images i.e. primary phase (darker) and secondary phase (brighter). **Fig.5-3b** depicted an EDS spectrum acquired from the same area as the SEM image which revealed the existence and weight fraction of major elements including Al, C, O, Mg, Fe, Mn, N, and Cr. The distribution of those elements (**Fig.5-3d-k**) in this area is illustrated as EDS elemental maps, and all images are assembled in **Fig.5-3c**.

Elemental maps of Al and O are presented **Fig.5-3d** and **f**, respectively. It can be seen that Al is presented in both ceramic and metal phases, the metal phase exhibited higher weight ratio of Al since aluminium accounts for over 93% in the 5083 alloy. The O-rich area assigns to the alumina phase. C is evenly distributed in all area of the composite (**Fig.5-3e**). This suggests that the signals of C may be from the diamond nanoparticles trapped in relatively soft metal phase during polishing process using diamond suspension. Mg, the minor component of 5830 alloy (~5%), is uniformly distributed in the metal phase. The metal Mg played a significant role in the pressureless infiltration of aluminium alloy (5083) in N_2 atmosphere as shown in (5.1) and (5.2) where AlN was formed to promote wettability between ceramic and molten metal. The existence of AlN is confirmed by elemental map of N in **Fig.5-3i**. The other heavier metallic elements, such as Mn, Fe, and Cr enriches in the brighter phase (secondary phase) as presented in **Fig.5-3a** (highlighted by the red arrows). The secondary phase associated with heavier elements is known as the precipitate cluster, which is the pre-existing phase in the Al alloy (5083) [54, 55].

5.3.1.2 Mechanical properties

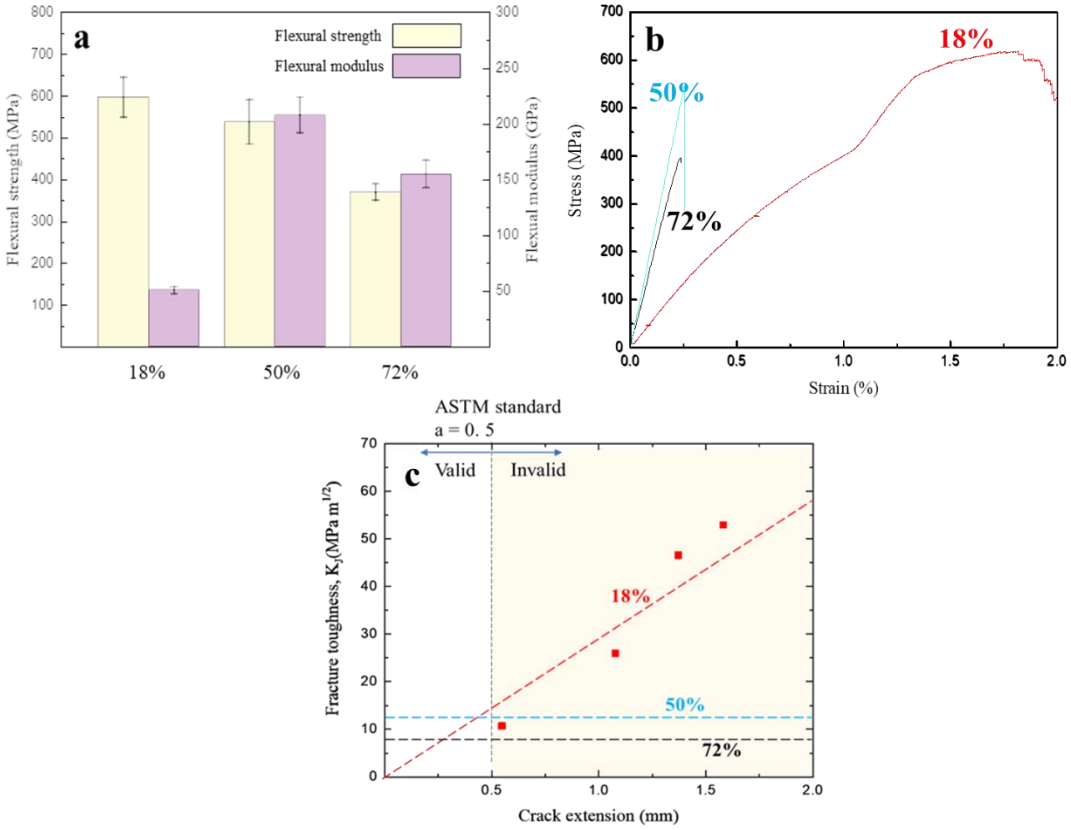

Fig.5-4 *Mechanical properties of µL alumina/aluminium composites with different ceramic fraction ranging from 18% to 72%: flexural strength and flexural modulus* ***a)****, strain-stress curves* ***b)****, and fracture toughness R-curve* ***c)****.*

The mechanical properties of the µL alumina/aluminium composites were markedly related to the ceramic fraction as shown in **Fig.5-4**. The flexural strength decreased from 596 MPa to 369 MPa as the ceramic fraction was increased from 18% to 72%. The flexural modulus of composites reached 51 GPa at 18% ceramic fraction. When the volume fraction of alumina was increased, the flexural modulus was increased to 207 GPa at 50% but dropped to 151 GPa at 72%. According to the strain-stress curves (**Fig.5-4b**) obtained from three-point bending tests, only the composite with low ceramic fraction (18%) showed inelastic deformation and strain

achieved ca. 1.8% at ultimate stress. The other two composites with higher ceramic fractions displayed a catastrophic fracture at the strain of ca. 0.25%. Furthermore, from the fracture toughness testing (**Fig.5-4c**), it was clear that only the composite with 18% ceramic fraction exhibited a rising *R*-curve and the fracture toughness K_J reached approximately 16 MPa $m^{1/2}$ at the ASTM limit (crack extension=0.5 mm). However, the crack could be further extended to 1.7 mm achieving a higher value of fracture toughness, $K_J \approx 50$ MPa $m^{1/2}$. In this case, the μL alumina scaffold was an additional phase in composites to reinforce the Al metal. Samples with ceramic fraction of 72% and 50% displayed flat *R*-curves with the values of K_{IC} being 12.6 MPa $m^{1/2}$ and 7.8 MPa $m^{1/2}$, respectively. Incomplete wetting/infiltration and resultant presence of defects within the composites with higher ceramic fractions are believed to attribute to their deteriorated mechanical properties.

5.3.1.3 X-ray tomography of crack propagation

In this work, the X-ray used to characterise alumina/aluminium composites was provided by synchrotron which is an extremely powerful source of X-ray. Therefore, images were produced with higher contrast and less noise. In contrast to the instantaneous cracking of composites with relatively high ceramic fractions (>50%), the composite with a lower ceramic fraction of 18% displayed stable crack propagation and rising crack resistance with the crack advancing. The crack in this composite was observed using X-ray micro-CT and the results were reconstructed into 2D profile and 3D tomography images as shown in **Fig.5-5**. The crack paths clearly showed a remarkable efficiency of the composite structure in resisting crack propagation. On many occasions, from top to bottom, typical extrinsic toughening mechanisms could be found in the 2D reconstructed crack profile including pull-out, crack bridging, multiple cracking (**Fig.5-5a**). Moreover, as shown in the perspective view with varying rotations (**Fig.5-5c** to **e**), the composite displayed a complex cracking profile in 3D space with the cracking paths continuously deflected/twisted along both in-plane (clockwise 60º) and out-of-plane

(anticlockwise 60º) directions. The crack consisted of multiple disconnected voids due to the crack bridging effects among the specimens in the perspective view. Apparently, the crack bridging connected uncrack ligament on the direction not only along (**Fig.5-5c**) but also perpendicular to (**Fig.5-5d**, and **e**) crack.

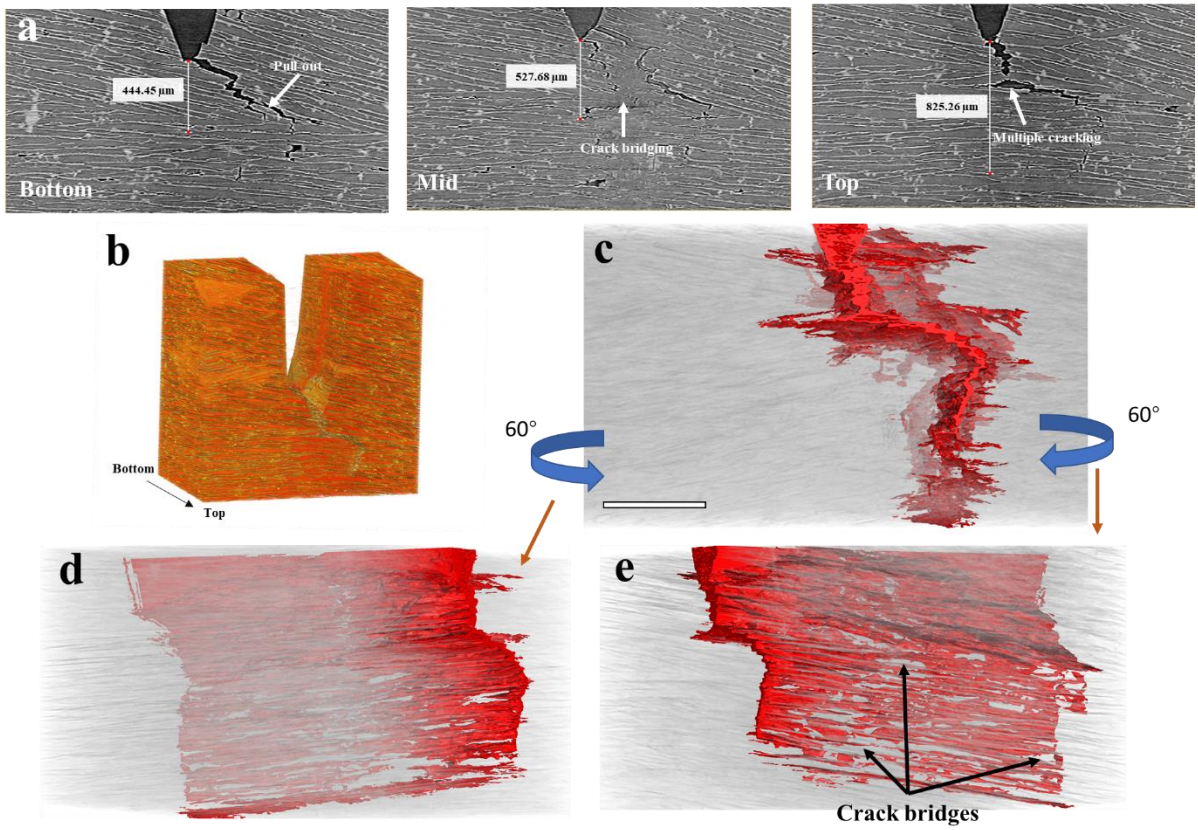

Fig.5-5 *Images of crack propagation taken using in situ micro-CT fracture toughness tests on µL alumina/aluminium composite with 18% ceramic content at load of 147N. Micro-CT 2D images of crack profile were taken from top, mid, and bottom* ***a)****; the corresponding 3D reconstruction of damaged specimen* ***b)****. The 3D perspective view of cracking profile was obtained by filtering out the signals from solids* ***c)****, which is then rotated both in-plane* ***d)*** *and out-of-plane* ***e)*** *directions. Scale bar: 500 µm.*

Moreover, it was possible to observe that the crack area was not homogenously distributed along the width of the testing specimen and the crack exhibited different geometries and length

at different positions. Here, crack length was measured in terms of the position of crack tips. Compared with the typical crack evaluation method using *in situ* SEM or optical microscope, the *in situ* micro-CT exhibited great potential to estimate the crack length. This method could obtain more information of crack inside the specimen which not only provided chance to observe toughening mechanisms (e.g. crack bridging) in multiple direction but eliminated border effects during crack length estimation. The border effect may cause error on measurements of the crack length and then fracture toughness K_J.

Although the *in situ* micro-CT provided more information inside materials, there were still challenges for this technique to compare with typical *in situ* SEM technique. Firstly, the choice of material was limited, X-ray was hard to transmit through materials with high attenuation coefficient (e.g. zirconia) to obtain clear images. The scanning speed of micro-CT (~1 min per image) was relatively slower than that of SEM (~500 ms per image) which meant videos could not be taken during mechanical testing however the samples could be scanned when the testing was paused or finished. Finally, the resolution of micro-CT (300 nm per pixel in this work) was much lower than that of SEM (normally 0.1-10 nm per pixel [56]), which may result in loss of details at nano- even micro-scale.

5.3.1.4 Toughening mechanisms

It can be seen from **Fig.5-4** that the μL alumina/aluminium composites with higher ceramic fractions of 50 and 72% resulted in flat *R*-curves due to their diminishing toughening mechanisms of crack bridging and multiple cracking. In the layered composites, the parameters that mostly control the mechanical performance are constituent mechanics and ceramic fraction. As the analyses on 3D and 2D images obtained using micro-CT, the main toughening mechanisms for μL composites are crack bridging, multiple cracking, and pull-out, which appeared only in composites with lower ceramic fraction (18%). According to computer simulations, in the case of high-aspect-ratio bricks, increasing mineral content promoted

stiffness and strength of nacre-like composites, but it was detrimental to crack bridging [1, 57, 58]. This result in accord with the fact associated to the μL composites here. In this work, the aspect ratio is fixed at a large value because the μL architecture naturally has ultralong ceramic layers, when the ceramic fraction > 50%, the crack bridging was eliminated. Apart from crack bridging, multiple cracking always presented when the ratio of layer thickness between ceramic and compliant phase above a critical value [59, 60]. Based on the modelling of a ceramic/metal system, Huang *et al.* [61] predicted that the metal layer should be more than 2.5 times thicker than the ceramic layer when the multiple cracking occurred. The model has also been applied to a layered alumina/aluminium composite by Ferraro *et al.* [54]. In present work, the μL composites with 18% ceramic fraction obtained metal/ceramic wall thickness ratio of ~4.5. When the ceramic fraction was increased from 50% to 72%, the wall thickness ratio was reduced from 1 to 0.39, respectively. The pull-out phenomenon was one of outcomes of multiple cracking. However, the critical ratio of thickness was determined by the mechanics of ceramic and compliant phase [59, 60], this was why the ceramic/polymer composites investigated in Chapter 4 still displayed these toughening mechanises when the ceramic fractions were > 50%. Moreover, as discussed previously in section 5.3.1.1, composites had more defects at high ceramic fractions which further reduced the capacity to resistant crack extension as well as fracture toughness.

5.3.1.5 Summary of alumina/aluminium composites

To conclude, μL alumina/aluminium composites were prepared via pressureless infiltration. The composites with various ceramic fraction displayed different microstructure, densities, strength, stiffness, and fracture behaviours. The pressureless infiltration was difficult to complete at high ceramic fractions producing defects at the interface, which had negative impact on mechanical performance of resultant composites. The micro-CT demonstrated a great potential to characterize fracture toughness and toughening mechanisms. However, only

the composite with 18% ceramic fraction exhibited the typical the toughening mechanisms of nacre-like composites because of defects, long ceramic wall, and low thickness ratio.

5.3.2 HA/magnesium

HA scaffolds were prepared via freezing 10% HA slurries under bi-directional cold filed at a cooling rate of 40 ℃/min. The as-obtained HA scaffolds were coated by silica and then infiltrated with magnesium alloy (AZ31) to prepare HA/magnesium composites.

5.3.2.1 Silica coating on HA scaffolds

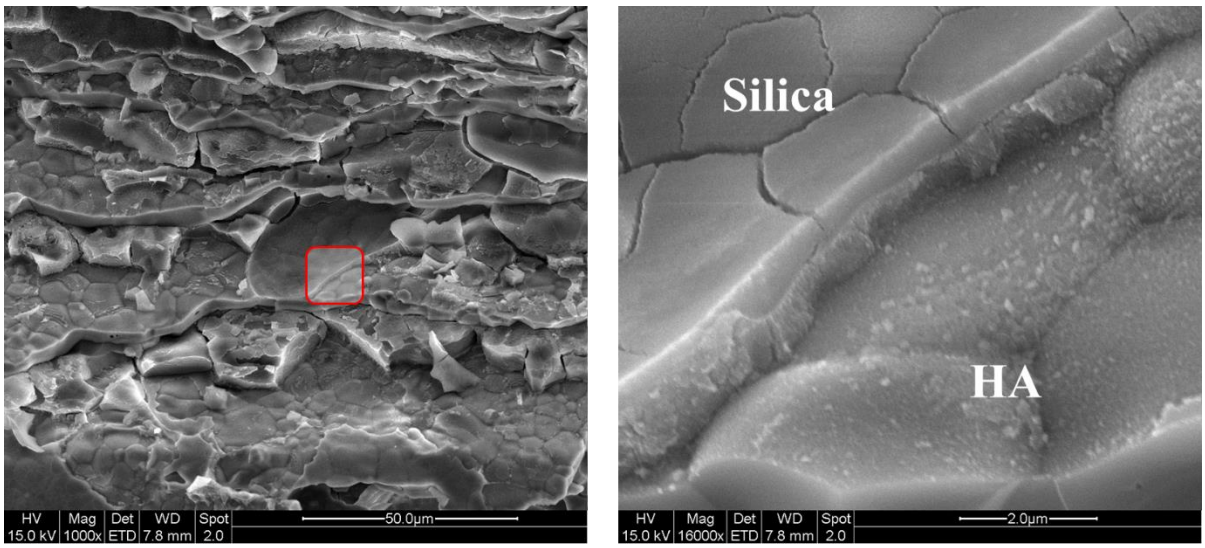

Fig.5-6 *Fracture surface of silica-coated HA scaffold.*

The silica-coated HA scaffolds were observed using SEM. As illustrated in **Fig.5-6**, SEM images revealed two different phases on the fractured surface of silica-coated HA scaffolds i.e. HA and silica. While the HA phase exhibited the typical grain structures of sintered ceramic, the silica phase displayed integral structures with multiple cracks. It can be seen that colloidal silica nanoparticles were fused together as silica layers or lump in the HA scaffold with a thickness <1 µm.

5.3.2.2 Pressureless infiltration of HA scaffolds with Mg

Silica coated HA scaffolds were infiltrated with AZ31 Mg alloy without external pressure at two different infiltrating temperatures (650 ℃ and 750 ℃) for different time (10-60 min) since the melting temperature of AZ31 was reported to be from 605 to 630 ℃ [62].

Time (min) / Temperature (℃)	10	20	30	60
650	No obvious infiltration	Infiltration completed	Infiltration completed	Violent reaction
750	Infiltrated but partially reacted	Infiltrated but partially reacted	Violent reaction	Violent reaction

Table 5-2 *Reactivity and outcome of pressureless infiltration of AZ31 into silica-coated HA scaffolds at various temperature and time.*

Table 5-2 lists the HA/Mg products after pressureless infiltration process. It can be seen that the silica-coated HA scaffolds were infiltrated with AZ31. However, their reactivity and infiltration ability were strongly dependent on temperature and duration. This indicated that the silica coating was the key to promote wetting and pressureless infiltration of AZ31 into HA scaffolds.

At the high temperature of 750 ℃, violent reactions occurred between HA and Mg, the silica coating facilitated infiltration but was unable to prevent such violent reactions. The resultant composites were severely distorted, even at a short duration of 10 min. However, at relatively low temperature of 650 ℃, the infiltration was possible without violent reactions at suitable duration (20-30 min). When the infiltrating time was too short (i.e.10 min), there seemed to be not enough time for Mg alloy to infiltrate into HA scaffolds. However, when the duration was

too long (i.e. 60 min), severe reactions between HA and Mg were observed again. To investigate the pressureless infiltration process and possible interactions between silica-coated HA and Mg, nacre-like HA/magnesium composites prepared at 650 ℃ for two different infiltration time (20 and 30 min) were characterised by SEM, EDS, and XRD. The mechanical responses (strength, modulus, and fracture toughness) of both composites were investigated.

5.3.2.3 Microstructure and composition of HA/magnesium composites

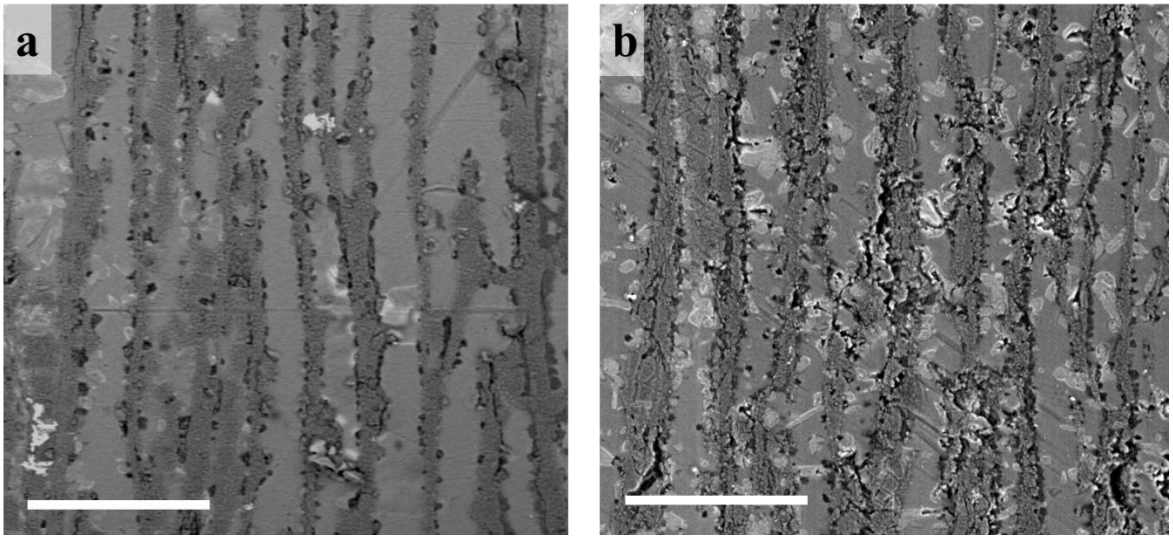

__Fig.5-7__ SEM images of HA/magnesium composites obtained from infiltration at 650 ℃ for 20 min __a)__ and 30 min __b)__. Scale bars: 100 µm

Fig.5-7 showed the microstructure of HA/magnesium composites. It can be seen that, in both composites, the ceramic scaffolds maintained the µL HA architecture after infiltration of molten Mg metal. In the Mg metal phase (light regime), some irregular new phases were generated. By contrast, composites with longer infiltration time (30 min) exhibited more pores and delamination, especially at the interface. The phase and composition of constituents were further investigated by EDS and XRD.

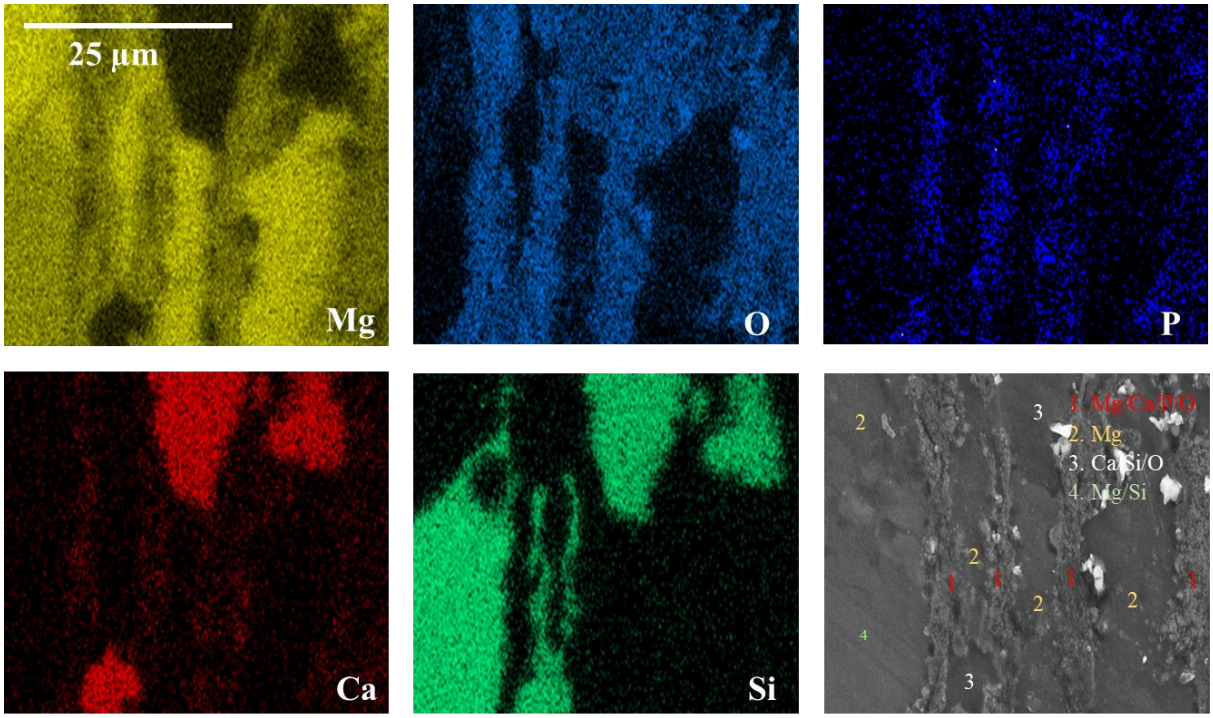

Fig.5-8 *EDS elemental mapping and SEM surface morphologies of HA/magnesium composites obtained from infiltration at 650 ℃ for 20 min.*

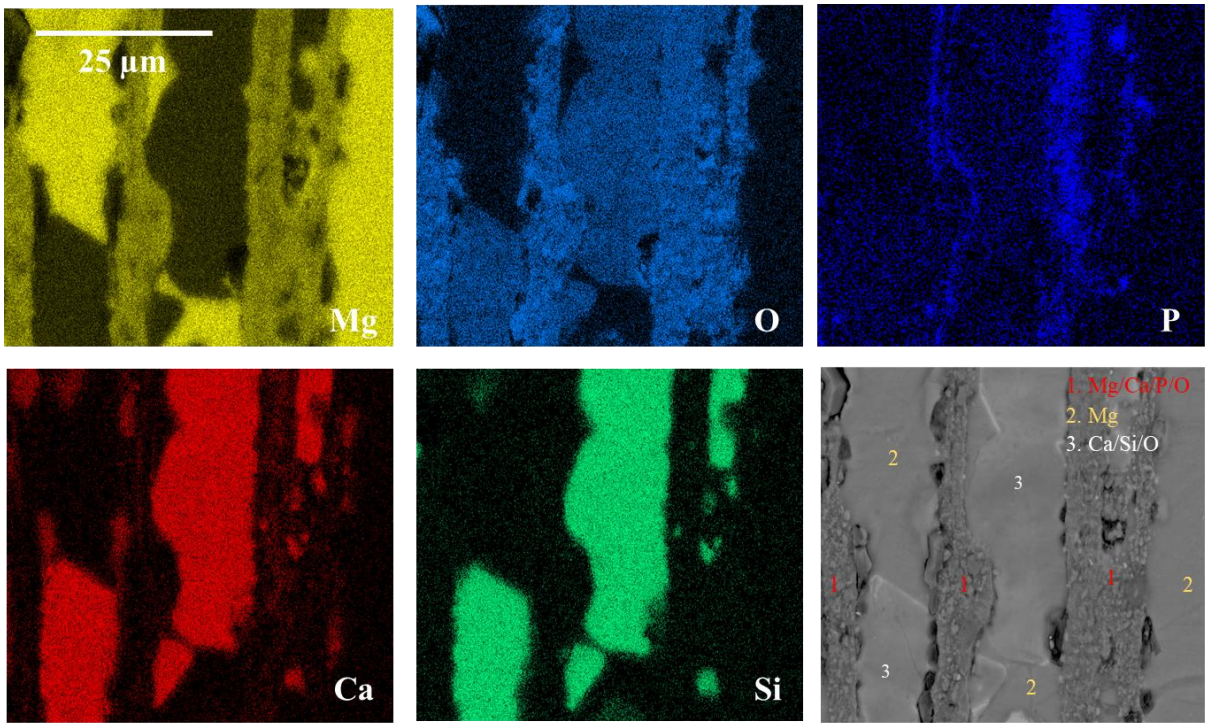

Fig.5-9 *EDS elemental mapping and SEM surface morphologies of HA/magnesium composites obtained from infiltration at 650 ℃ for 30 min.*

As can be seen from the EDS mapping and SEM images in **Fig.5-8** and **Fig.5-9**, it is apparent that, at infiltrating temperature of 650 ℃, composites show different composition. Obviously, the ceramic phase of HA was indicated by the regime **1** (red) in the SEM images, the layered structure was maintained fairly. However, the composition of HA was changed after pressureless infiltration process. Specifically, except for the main elements of HA (Ca, P, and O), additionally Mg was also observed in ceramic phase. The metal phase (Mg) was still present in the composites at the Mg-only position pointed out by regime **2** (yellow). Apart from metal and ceramic phases, another two different irregular lump phases were discontinuously distributed in the metal phase. The two new phases were composed of Ca/Si/O, and Mg/Si as illustrated in SEM images at regime **3** (while) and **4** (green), respectively. For instance, in the sample prepared at 20-min of infiltration (**Fig.5-8**), both of irregular lump phases embedded in the metal phase. In the sample processed at 30 min of infiltration (**Fig.5-9**), only one new phase was observed composed mainly of Ca, Si and O.

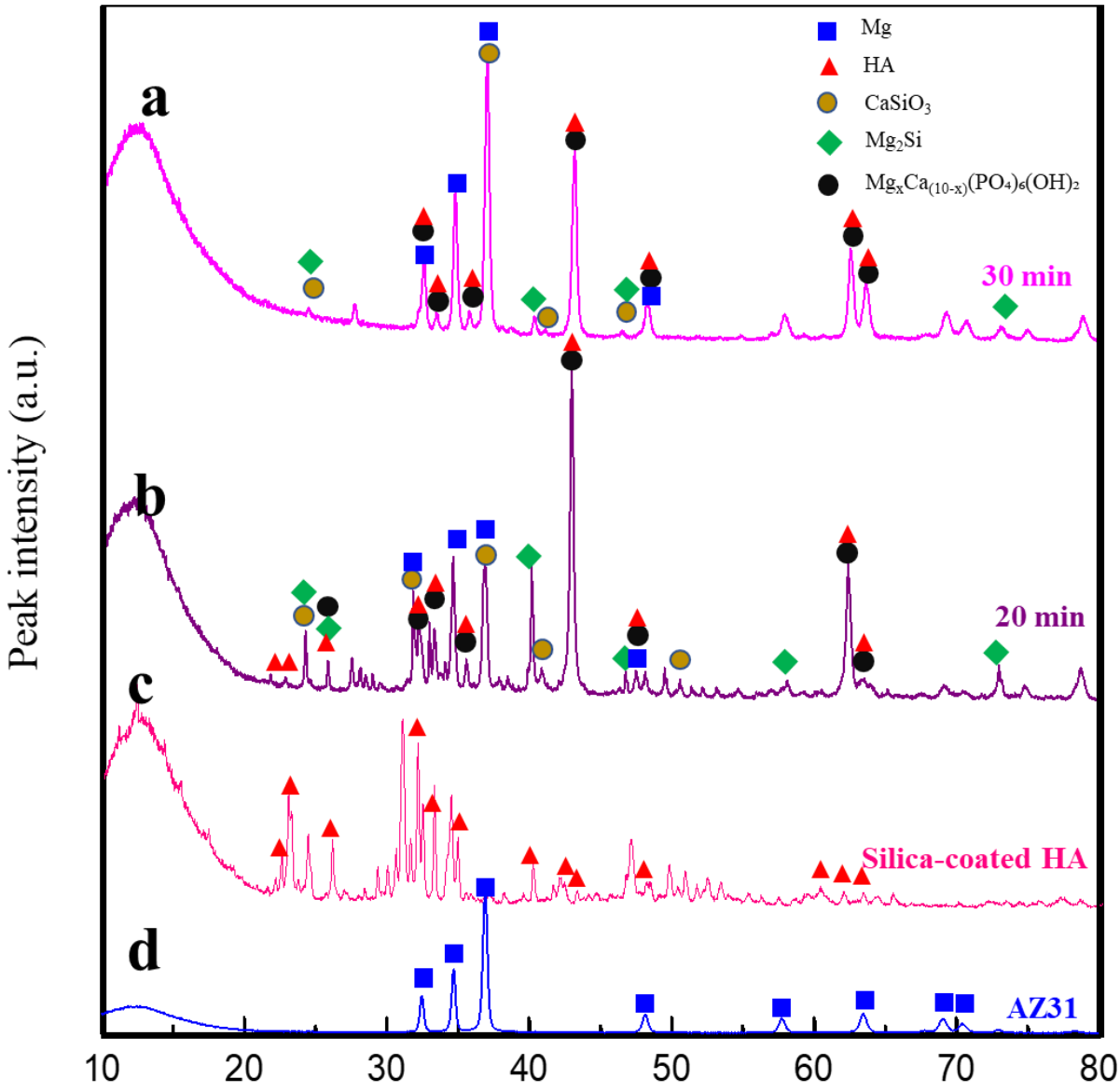

Fig.5-10 *X-ray powder diffraction patterns of HA/magnesium composites infiltration at 650 °C for 30 min* ***a)*** *and 20 min* ***b)*** *and raw materials of silica-coated HA* ***c)*** *and AZ31* ***d)***.

The composite materials of HA/magnesium and their raw materials were identified by powder XRD. Herein, all samples were grinded into fine powder before the characterisation using an XRD diffractometer. The spectra of powder XRD were obtained in the range of 10-80° (2 Theta) with a step time of 0.5 s and a step size of 0.02°. The powder XRD diffractometer was operated with Cu (Kα = 1.540600 Å) radiation.

All XRD patterns exhibited sharp peaks which suggests a good crystallinity in all composites and raw materials. The diffraction patterns of silica-coated HA scaffolds (**Fig.5-10c**) are in good agreement with the JCPDS (09-0432) of HA powder, indicating that the silica coating is mostly amorphous and has no effect on the crystallinity of HA. In the XRD spectrum of AZ31 (**Fig.5-10d**), the main characteristic peaks of Mg were observed. The AZ31 contains approximately 97% Mg and 3% Al. Sunil *et al.* [63] pointed out that, in AZ31 alloy, the Al was presented as the format of $Mg_{12}Al_{12}$ which is usually invisible in XRD spectrum of AZ31 because of its low content. **Fig.5-10a** and **b** identified the phases in the μL HA/magnesium composite materials infiltrated at 650 ℃ for 30 and 20 min, respectively. The XRD patterns verified the presence of AZ31, HA, Mg-substituted HA and other two phases. Comparing with XRD spectra of silica-coated HA (**Fig.5-10c**) and AZ31 (**Fig.5-10d**), both composite materials exhibited dominant peaks of Mg and HA indicating the presence of AZ31 and HA. However, the characteristic peaks of HA are overlapped with Mg-substituted HA. From previous studies, Mg can enter the HA lattice resulting in no changes in the crystallinity with a similar XRD pattern as HA [64, 65]. From the EDS results, the ceramic phase consisted of not only Ca, P, and O but also Mg. Thus, Ca in HA ceramic phase was partially substituted by Mg during infiltration and the ceramic phase was converted to $Mg_xCa_{(10-x)}(PO_4)_6(OH)_2$ where $0<x<10$. Besides Mg-substituted HA and Mg, new interfacial compositions were formed during reactions between HA, silica and AZ31. In addition, the EDS and XRD analysis also identified the formation of new phases i.e. Mg_2Si and $CaSiO_3$. All these peaks were present in the XRD pattern of composite processed at 650°C for 20 min. However, the peaks intensity of Mg_2Si in the XRD pattern was significantly weakened and Mg_2Si was also absent in the EDS mapping when infiltration time was increased to 30 min.

5.3.2.4 Interfacial reactions

In ceramic/metal composites showing reactive wetting, the interfacial compositions were affected by the chemical reactions occurred at interface between Mg metal and ceramic (silica coated HA). There were three stages of interfacial reactions during Mg infiltration at 650 ℃.

Stage one: when the molten Mg contacted with the silica on HA scaffolds, the following reactions occurred:

$$2Mg + SiO_2 = 2MgO + Si \quad (5.4)$$

$$2Mg + Si = Mg_2Si \quad (5.5)$$

Combining the two equations above:

$$4Mg + SiO_2 = 2MgO + Mg_2Si \quad (5.6)$$

In this stage, Mg reacted with SiO_2 and produced two new materials i.e. MgO and Mg_2Si. This reaction (5.6) was reported by Shi *et al.* [66]. The Mg_2Si generated in this stage played an essential role in promoting the wetting of magnesium alloy with silica-coated HA and then drove the pressureless infiltration. Furthermore, the as-obtained products from stage one, MgO and Mg_2Si participated more reactions in the **Stage two** and **Stage three**, respectively.

Stage two: MgO formed in stage one reacted with HA ($Ca_{10}(PO_4)_6(OH)_2$) as the following reactions:

$$xMgO + Ca_{10}(PO_4)_6(OH)_2 = xCaO + Mg_xCa_{(10-x)}(PO_4)_6(OH)_2 \quad (5.7)$$

$$CaO + SiO_2 = CaSiO_3 \quad (5.8)$$

Combining the two equations above:

$$Ca_{10}(PO_4)_6(OH)_2 + xMgO + xSiO_2 = xCaSiO_3 + Mg_xCa_{(10-x)}(PO_4)_6(OH)_2 \quad (5.9)$$

HA was converted into $Mg_xCa_{(10-x)}(PO_4)_6(OH)_2$ during the stage two (5.9). Here, MgO played the source of Mg^{2+} which was incorporated in the HA structure via replacement between Mg^{2+} and Ca^{2+}. The reason of this replacement reaction was that the Ca^{2+} vacancy site in HA was energetically more favourable for occupation of Mg substitution [64]. Recently, similar

Mg^{2+}/Ca^{2+} replacement reactions have been suggested in other studies such as HA/AZ31 in acid [67], HA/magnesium nitrate solution [68, 69], HA/magnesium chloride solution [70]. The calcium silicate ($CaSiO_3$) was formed by reaction between CaO and SiO_2 [71].

Stage three: Mg_2Si reacted with HA as the following reactions:

$$Ca_{10}(PO_4)_6(OH)_2 = H_2O + Ca_{10}(PO_4)_6O \quad (5.10)$$

$$Mg_2Si + 2H_2O = 2MgO + SiH_4\ (gas) \quad (5.11)$$

According to the condensation mechanism proposed by Mortier *et al.* [72], HA was possible to be partially condensed and produce H_2O under 700 ℃ (5.10). Mg_2Si could be seen as consisting of Si^{4-} ions which was reactive toward H_2O generating silane SiH_4 (5.11) [73, 74]. The by-product of MgO could participate in cycling reaction with SiO_2 as shown in (5.9). It was noticed that, when infiltration finished, the composite released a sharp and unpleasant smell. The smell was stronger when the infiltrating temperature was increased or the reaction time was longer, which indicated more reactions of stage three. It was difficult to characterize the gas emission in this project, but it was reasonable to speculate the gas released from HA/magnesium composite was SiH_4 which was known to have a sharp and unpleasant smell.

Therefore, there were three stages of reactions occurred during the infiltration of AZ31 into silica-coated HA scaffolds. It could be seen that SiO_2 was demonstrated to not only promote reactive wetting during pressureless infiltration but also act as a protective layer preventing direct reactions between HA and molten Mg [46, 47]. When the infiltration time was short e.g. 20 min, the reaction in stage one made a great contribution to facilitate pressureless infiltration, where the SiO_2 react with molten Mg to produce MgO and Mg_2Si increasing wettability between ceramic scaffolds and molten metal alloy. The formed MgO and Mg_2Si resulted in further reactions in stage two and stage three, respectively. In the stage two, the Ca^{2+} in ceramic phase (HA) was partially replaced by Mg^{2+} to generate Mg-substituted HA and CaO which then reacted with SiO_2 to produce $CaSiO_3$. However, the reactions in stage three were unwanted

where the ceramic phase was dehydrated as $Mg_xCa_{(10-x)}(PO_4)_6O$ and a flammable gas (SiH_4) was produced, depending on the reaction time. Thus, it was found $CaSiO_3$ Mg_2Si, Mg, Mg-substituted HA, and SiH_4 in the composites infiltrated within 20 min. When the reaction time was extended to 30 min, unwanted reactions in the stage three occurred consuming Mg_2Si and producing gaseous silane. Therefore, the intensity of Mg_2Si peaks in the XRD spectrum dropped significantly and the smell was noticeably stronger due to release of SiH_4. When the reaction time was further increased >30 min, the reactions in stage three played predominant role where the saline gas was further generated and the architecture of HA scaffolds was completely destroyed [46, 47].

5.3.2.5 Mechanical properties

The flexural strength and modulus of HA/magnesium composites and pure HA were evaluated by three-point bending tests on rectangular specimens; the compressive strength was measured by compression tests in rectangular specimens; the fracture toughness K_{IC} was measured by three-point bending on SEB specimens. It was found that the μL HA/magnesium composites achieved a remarkable bending strain to ultimate stress of 0.5% and 1.4% whereas the reference bulk HA exhibited a failure strain of 0.1% (**Fig.5-11a**). Composites also exhibited superior mechanical performance compared to the bulk HA (**Fig.5-11c**). Moreover, the fracture surface of composites prepared with 20-min infiltration time (**Fig.5-11b**) showed a typical pull-out behaviour after failure which was considered as the primary energy dissipating mechanism in nacre-like composites.

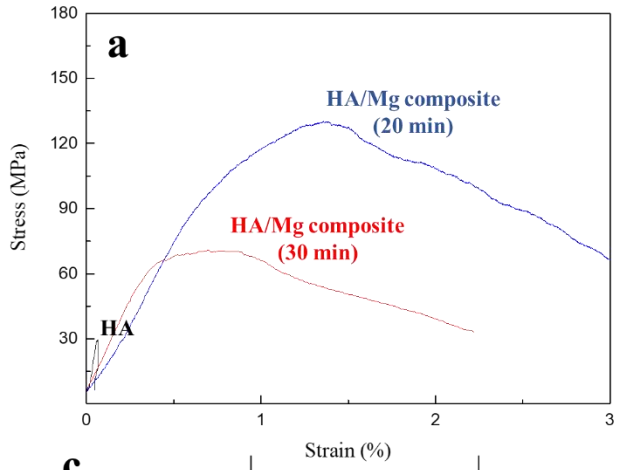

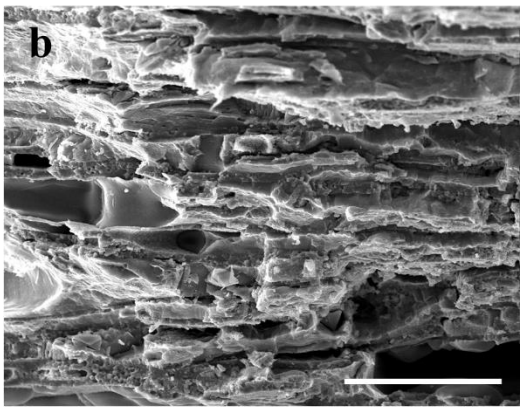

c

	Flexural strength (MPa)	Compressive strength (MPa)	Flexural modulus (GPa)	Fracture toughness, K_{IC} ($MPam^{1/2}$)
HA	28.44±1.12	135±33.2	45.01±4.65	0.76±0.21
HA/Mg composite (prepared in 20 min)	153.94±24.2	210.1367±16.6	12.41±2.66	5.36±0.85
HA/Mg composite (prepared in 30 min)	86.68±16.74	132.49±24.01	7.7±1.11	3.07±0.69

Fig.5-11 *Strain-stress curves of three-point bending tests* ***a)*** *and SEM images of fractured surface of the HA/magnesium composite (20min)* ***b)****. Summary of mechanical properties of bulk HA, HA/magnesium composites prepared at a duration of 20 min and 30 min* ***c).*** *Scale bar: 100 µm.*

It is obvious that the composite prepared at short time of 20 min has better mechanical proeprties compared to that prepared at a duration of 30 min. This could be attributed to the different compositions and residual stress generated during infiltration. As discussed above, when the reaction time was 30 min, reaction (5.11) in stage three became predominant to consume Mg_2Si and produce silane gas (SiH_4). The Mg_2Si was a strong and stiff material. The reduction of Mg_2Si content resulted in decreased mechanical properties of composites. Besides, the as-generated silane gas also affected the mechanical properties by introducing defects and residual stress or even debonding in the final composites (**Fig.5-7b**). The residual stress and defects were known to negatively affect the mechanical properties of composite materials.

5.3.2.6 Summary of HA/magnesium composites

HA/magnesium composites were fabricated via pressureless infiltration of AZ31 into silica-coated HA scaffolds at 650 ℃. Complex chemical reactions occurred during the pressureless infiltration. The extent of reactions was dependent on duration. Longer duration (30 min) resulted in more severe reactions, leading to poor mechanical properties of the resultant composites compared to short duration (20 min) because of the generation of gaseous silane product. However, all the reaction by-products (magnesium-substituted HA [75], $CaSiO_3$ [76, 77], Mg_2Si [78]) are still biocompatible. Therefore, the nacre-like HA/magnesium composites are worth a further investigation as biodegradable implant material.

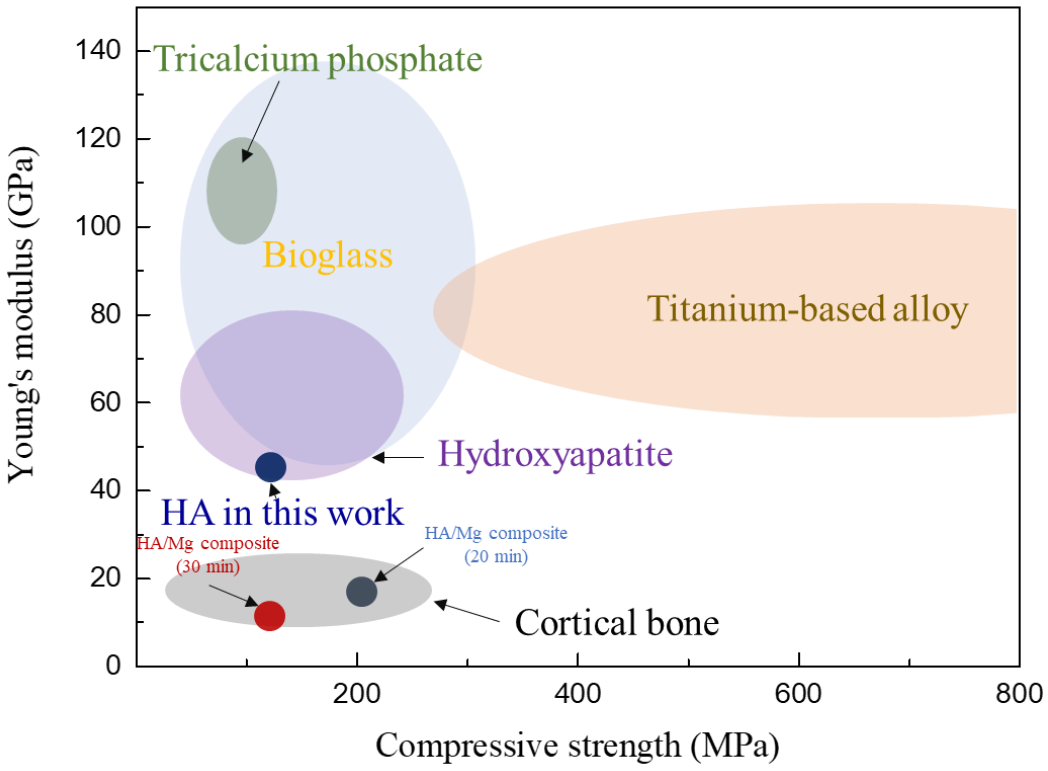

Fig.5-12 *Comparison of μL HA/magnesium composite with other commonly used bone-implant materials and cortical bones. The map of mechanical properties (stiffness and strength) of cortical bone [79], as-prepared HA/magnesium composite materials in this work and the other reported bone substitute materials: titanium-based alloy [80], Bioglass [81], tricalcium phosphate [82], and pure HA [83].*

Since bone is the second most transplanted tissue with 2.2 million bone-grafting procedures performed annually worldwide [84], there is a huge demand for customized bone substitutes for bone therapy. However, the most widely used implant materials such as stainless steel and titanium metals have various disadvantages with poor biocompatibility and mismatched mechanical properties with bone. Therefore, the major motivation of this work was to develop a biocompatible or biodegradable implant material with matched mechanical properties. It is demonstrated that the μL HA/magnesium composites exhibited comparable mechanical properties to natural cortical bone, with a compressive strength of 132-210 MPa and Young's modulus of 8-12 GPa (**Fig.5-12**)**.** Thus, the composites can reduce the stress shielding effect of the implants. Additionally, magnesium metal is biodegradable, the magnesium-based composites could offer a great potential as new biodegradable and biocompatible bone substitutes for orthopedic applications.

5.4 Conclusions

In this study, nacre-like μL ceramic/metal composites were prepared by pressureless infiltration of molten metals into as-prepared ceramic scaffolds. The pressureless infiltration was dependent on reactive wetting process allowing the penetration of molten metal in μL ceramic scaffolds with different ceramic fraction from 18% to 72%. The mechanical responses were demonstrated to be related to microstructure, ceramic fraction, and composition. Two different ceramic/metal systems were investigated i.e. alumina/aluminium and HA/magnesium.

The results on alumina/aluminium showed that mechanics of the composites were highly dependent on ceramic fraction. With a low ceramic fraction of 18%, the composite exhibited typical toughening mechanisms of nacre and a rising *R*-curve reaching the maximum fracture toughness K_J at 50 MPa $m^{1/2}$. However, composites with higher ceramic fractions (>50%) displayed poor mechanical performance due to the poor wetting of aluminium alloy with

alumina scaffolds and defects generated during metal infiltration. HA/magnesium composites were manufactured via pressureless infiltration of magnesium alloy AZ31 into silica coated HA scaffolds at low temperature (650 ℃) and short duration (<30 min). Silica coating was crucial to facilitate the infiltration as well as prevent the interactions between HA and magnesium alloy. Although it was inevitable that composites produced some new biocompatible phases i.e. magnesium-substituted HA, $CaSiO_3$, and Mg_2Si due to the reactions during infiltration, the mechanical properties of as-obtained μL HA/magnesium composites exhibited comparable and matched mechanical properties with cortical bones, indicating a great potential for their application in bone implants.

5.5 References

[1] M.R. Begley, N.R. Philips, B.G. Compton, D.V. Wilbrink, R.O. Ritchie, M. Utz, Micromechanical models to guide the development of synthetic 'brick and mortar' composites, Journal of the Mechanics and Physics of Solids 60(8) (2012) 1545-1560.

[2] F. Barthelat, D. Zhu, A novel biomimetic material duplicating the structure and mechanics of natural nacre, Journal of Materials Research 26(10) (2011) 1203-1215.

[3] S. Roy, A. Wanner, Metal/ceramic composites from freeze-cast ceramic preforms: Domain structure and elastic properties, Composites Science and Technology 68(5) (2008) 1136-1143.

[4] Y. Wang, P. Shen, R.-F. Guo, Z. Hu, Q.-C. Jiang, Developing high toughness and strength Al/TiC composites using ice-templating and pressure infiltration, Ceramics International 43 (2016).

[5] C. Garcia-Cordovilla, E. Louis, J. Narciso, Pressure infiltration of packed ceramic particulates by liquid metals, Acta Materialia 47(18) (1999) 4461-4479.

[6] A. Mattern, B. Huchler, D. Staudenecker, R. Oberacker, A. Nagel, M.J. Hoffmann, Preparation of interpenetrating ceramic–metal composites, Journal of the European Ceramic Society 24(12) (2004) 3399-3408.

[7] A.W. Urquhart, Novel reinforced ceramics and metals: a review of Lanxide's composite technologies, Materials Science and Engineering: A 144(1) (1991) 75-82.

[8] B.S. Rao, V. Jayaram, New technique for pressureless infiltration of Al alloys into Al2O3 preforms, Journal of Materials Research 16(10) (2001) 2906-2913.

[9] A. Klinter, G. Mendoza-Suarez, R. Drew, Wetting of Pure Aluminum and Selected Alloys on Polycrystalline Alumina and Sapphire, Materials Science and Engineering A 495(1) (2008) 147-152.

[10] A. Sangghaleh, M. Halali, Effect of magnesium addition on the wetting of alumina by aluminium, Applied Surface Science 255(19) (2009) 8202-8206.

[11] M. Prakasam, J. Locs, K. Salma-Ancane, D. Loca, A. Largeteau, L. Berzina-Cimdina, Biodegradable Materials and Metallic Implants-A Review, Journal of Functional Biomaerials 8(4) (2017) 44.

[12] L.-C. Zhang, L.-Y. Chen, A Review on Biomedical Titanium Alloys: Recent Progress and Prospect, Advanced Engineering Materials 21(4) (2019) 1801215.

[13] J. Lechner, S. Noumbissi, V. von Baehr, Titanium implants and silent inflammation in jawbone-a critical interplay of dissolved titanium particles and cytokines TNF-α and RANTES/CCL5 on overall health?, EPMA J 9(3) (2018) 331-343.

[14] K.T. Kim, M.Y. Eo, T.T.H. Nguyen, S.M. Kim, General review of titanium toxicity, International Journal of Implant Dentistry 5(1) (2019) 10-10.

[15] A.P. Gupta, V. Kumar, New emerging trends in synthetic biodegradable polymers – Polylactide: A critique, European Polymer Journal 43(10) (2007) 4053-4074.

[16] L.S. Nair, C.T. Laurencin, Biodegradable polymers as biomaterials, Progress in Polymer Science 32(8) (2007) 762-798.

[17] S. Farè, Q. Ge, M. Vedani, G. Vimercati, D. Gastaldi, F. Migliavacca, L. Petrini, S. Trasatti, Evaluation of material properties and design requirements for biodegradable magnesium stents, Matéria (Rio de Janeiro), 15 (2010) 96-103.

[18] M.P. Staiger, A.M. Pietak, J. Huadmai, G. Dias, Magnesium and its alloys as orthopedic biomaterials: A review, Biomaterials 27(9) (2006) 1728-1734.

[19] G. Song, Control of biodegradation of biocompatable magnesium alloys, Corrosion Science 49(4) (2007) 1696-1701.

[20] F. Witte, V. Kaese, H. Haferkamp, E. Switzer, A. Meyer-Lindenberg, C.J. Wirth, H. Windhagen, In vivo corrosion of four magnesium alloys and the associated bone response, Biomaterials 26(17) (2005) 3557-3563.

[21] F. Witte, J. Fischer, J. Nellesen, H.-A. Crostack, V. Kaese, A. Pisch, F. Beckmann, H. Windhagen, In vitro and in vivo corrosion measurements of magnesium alloys, Biomaterials 27(7) (2006) 1013-1018.

[22] C. Liu, Z. Ren, Y. Xu, S. Pang, X. Zhao, Y. Zhao, Biodegradable Magnesium Alloys Developed as Bone Repair Materials: A Review, Scanning 2018 (2018) 9216314.

[23] F. Witte, N. Hort, C. Vogt, S. Cohen, K.U. Kainer, R. Willumeit, F. Feyerabend, Degradable biomaterials based on magnesium corrosion, Current Opinion in Solid State and Materials Science 12(5) (2008) 63-72.

[24] N.-E.L. Saris, E. Mervaala, H. Karppanen, J.A. Khawaja, A. Lewenstam, Magnesium: An update on physiological, clinical and analytical aspects, Clinica Chimica Acta 294(1) (2000) 1-26.

[25] M.T. Fulmer, I.C. Ison, C.R. Hankermayer, B.R. Constantz, J. Ross, Measurements of the solubilities and dissolution rates of several hydroxyapatites, Biomaterials 23(3) (2002) 751-755.

[26] D. Tadic, M. Epple, A thorough physicochemical characterisation of 14 calcium phosphate-based bone substitution materials in comparison to natural bone, Biomaterials 25(6) (2004) 987-994.

[27] O. Gauthier, J.-M. Bouler, E. Aguado, P. Pilet, G. Daculsi, Macroporous biphasic calcium phosphate ceramics: influence of macropore diameter and macroporosity percentage on bone ingrowth, Biomaterials 19(1) (1998) 133-139.

[28] H. Yoshikawa, A. Myoui, Bone tissue engineering with porous hydroxyapatite ceramics, Journal of Artificial Organs 8(3) (2005) 131-136.

[29] W. Suchanek, M. Yoshimura, Processing and properties of hydroxyapatite-based biomaterials for use as hard tissue replacement implants, Journal of Materials Research 13(1) (1998) 94-117.

[30] Q.B. Nguyen, M. Gupta, T.S. Srivatsan, On the role of nano-alumina particulate reinforcements in enhancing the oxidation resistance of magnesium alloy AZ31B, Materials Science and Engineering: A 500(1) (2009) 233-237.

[31] Q.B. Nguyen, M. Gupta, Increasing significantly the failure strain and work of fracture of solidification processed AZ31B using nano-Al2O3 particulates, Journal of Alloys and Compounds 459(1) (2008) 244-250.

[32] H. Cay, H. Xu, Q. Li, Mechanical behavior of porous magnesium/alumina composites with high strength and low density, Materials Science and Engineering: A 574 (2013) 137-142.

[33] M. Habibnejad-Korayem, R. Mahmudi, H.M. Ghasemi, W.J. Poole, Tribological behavior of pure Mg and AZ31 magnesium alloy strengthened by Al2O3 nano-particles, Wear 268(3) (2010) 405-412.

[34] J.H. Gao, S.K. Guan, J. Chen, L.G. Wang, S.J. Zhu, J.H. Hu, Z.W. Ren, Fabrication and characterization of rod-like nano-hydroxyapatite on MAO coating supported on Mg–Zn–Ca alloy, Applied Surface Science 257(6) (2011) 2231-2237.

[35] H.X. Wang, S.K. Guan, X. Wang, C.X. Ren, L.G. Wang, In vitro degradation and mechanical integrity of Mg–Zn–Ca alloy coated with Ca-deficient hydroxyapatite by the pulse electrodeposition process, Acta Biomaterialia 6(5) (2010) 1743-1748.

[36] Y.W. Song, D.Y. Shan, E.H. Han, Electrodeposition of hydroxyapatite coating on AZ91D magnesium alloy for biomaterial application, Materials Letters 62(17) (2008) 3276-3279.

[37] M. Rahman, Y. Li, C. Wen, HA coating on Mg alloys for biomedical applications: A review, Journal of Magnesium and Alloys 8(3) (2020) 929-943.

[38] H. Hornberger, S. Virtanen, A.R. Boccaccini, Biomedical coatings on magnesium alloys – A review, Acta Biomaterialia 8(7) (2012) 2442-2455.

[39] E. Moradi, M. Ebrahimian-Hosseinabadi, M. Khodaei, S. Toghyani, Magnesium/nano-hydroxyapatite porous biodegradable composite for biomedical applications, Materials Research Express 6(7) (2019) 075408.

[40] F. Witte, F. Feyerabend, P. Maier, J. Fischer, M. Störmer, C. Blawert, W. Dietzel, N. Hort, Biodegradable magnesium–hydroxyapatite metal matrix composites, Biomaterials 28(13) (2007) 2163-2174.

[41] J. Kubásek, D. Vojtěch, J. Maixner, D. Dvorský, The effect of hydroxyapatite reinforcement and preparation methods on the structure and mechanical properties of Mg-HA composites, Science and Engineering of Composite Materials, 2017, p. 297.

[42] C. Zhao, F. Pan, H. Pan, Microstructure, mechanical and bio-corrosion properties of as-extruded Mg–Sn–Ca alloys, Transactions of Nonferrous Metals Society of China 26(6) (2016) 1574-1582.

[43] M.M.F. Aizat, M.R.N. Liyana, K.S. Khalijah, Fabrication of magnesium-hydroxyapatite composites targeted for biodegradable implant application, AIP Conference Proceedings 2030(1) (2018) 020082.

[44] Y. Su, D. Li, Y. Su, C. Lu, L. Niu, J. Lian, G. Li, Improvement of the Biodegradation Property and Biomineralization Ability of Magnesium–Hydroxyapatite Composites with Dicalcium Phosphate Dihydrate and Hydroxyapatite Coatings, ACS Biomaterials Science & Engineering 2(5) (2016) 818-828.

[45] B. Chen, K.-Y. Yin, T.-F. Lu, B.-Y. Sun, Q. Dong, J.-X. Zheng, C. Lu, Z.-C. Li, AZ91 Magnesium Alloy/Porous Hydroxyapatite Composite for Potential Application in Bone Repair, Journal of Materials Science & Technology 32(9) (2016) 858-864.

[46] A.K. Khanra, H.C. Jung, K.S. Hong, K.S. Shin, Comparative property study on extruded Mg–HAP and ZM61–HAP composites, Materials Science and Engineering: A 527(23) (2010) 6283-6288.

[47] Y.-H. Ho, K. Man, S. Joshi, M. Pantawane, T.-C. Wu, Y. Yang, N. Dahotre, In-vitro biomineralization and biocompatibility of friction stir additively manufactured AZ31B magnesium alloy-hydroxyapatite composites, Bioactive Materials 5 (2020) 891-901.

[48] L. Shi, P. Shen, D. Zhang, E. Dong, Q. Jiang, Wetting of (0001) α-alumina single crystals by molten Mg–Al alloys in the presence of evaporation, Journal of Materials Science 47(24) (2012) 8372-8380.

[49] T. Epicier, F. Bosselet, J. Viala, Microstructure of interfaces between a magnesium matrix and preoxidized silicon carbide particles, Interface Science 1(3) (1994) 213-221.

[50] T. Stephenson, Y. Le Petitcorps, J.M. Quenisset, Silica-aluminium alloy composites: a kinetic study, Materials Science and Engineering: A 135 (1991) 101-104.

[51] A. Bardal, Wettability and interfacial reaction products in the AlSiMg surface-oxidized SiC system, Materials Science and Engineering: A 159(1) (1992) 119-125.

[52] S. Suárez, R. Postolache, F.J. García-García, B. Sánchez, R. Rothon, A.M. Doyle, L. Tosheva, Silicalite-1 synthesized with geothermal and Ludox colloidal silica and corresponding TiO2/silicalite-1 hybrid photocatalysts for VOC oxidation, Microporous and Mesoporous Materials 302 (2020) 110202.

[53] P. Auerkari, Mechanical and physical properties of engineering alumina ceramics, Technical Research Centre of Finland Espoo1996.

[54] R. Goswami, G. Spanos, P.S. Pao, R.L. Holtz, Precipitation behavior of the ß phase in Al-5083, Materials Science and Engineering: A 527(4) (2010) 1089-1095.

[55] G. yi, B. Sun, J. Poplawsky, Y. Zhu, M. Free, Investigation of pre-existing particles in Al 5083 alloys, Journal of Alloys and Compounds 740 (2017).

[56] N. Raval, R. Maheshwari, D. Kalyane, S.R. Youngren-Ortiz, M.B. Chougule, R.K. Tekade, Chapter 10 - Importance of Physicochemical Characterization of Nanoparticles in Pharmaceutical Product Development, in: R.K. Tekade (Ed.), Basic Fundamentals of Drug Delivery, Academic Press2019, pp. 369-400.

[57] F. Barthelat, Designing nacre-like materials for simultaneous stiffness, strength and toughness: Optimum materials, composition, microstructure and size, Journal of the Mechanics and Physics of Solids 73 (2014) 22-37.

[58] F. Barthelat, R. Rabiei, Toughness amplification in natural composites, Journal of the Mechanics and Physics of Solids 59(4) (2011) 829-840.

[59] C. Ferraro, S. Meille, J. Réthoré, N. Ni, J. Chevalier, E. Saiz, Strong and tough metal/ceramic micro-laminates, Acta Materialia 144 (2018) 202-215.

[60] K.L. Hwu, B. Derby, Fracture of metal/ceramic laminates—I. Transition from single to multiple cracking, Acta Materialia 47(2) (1999) 529-543.

[61] Y. Huang, H. Zhang, The role of metal plasticity and interfacial strength in the cracking of metal/ceramic laminates, Acta metallurgica et materialia 43(4) (1995) 1523-1530.

[62] Goodfellow, datasheet, (2020).

[63] R.S. Buradagunta, K.V. Ganesh, P. Pavan, G. Vadapalli, C. Swarnalatha, P. Swapna, P. Bindukumar, G. Reddy, Effect of aluminum content on machining characteristics of AZ31 and AZ91 magnesium alloys during drilling, Journal of Magnesium and Alloys 4 (2016) 15-21.

[64] S. Lala, M. Ghosh, P.K. Das, D. Das, T. Kar, S.K. Pradhan, Magnesium substitution in carbonated hydroxyapatite: Structural and microstructural characterization by Rietveld's refinement, Materials Chemistry and Physics 170 (2016) 319-329.

[65] D. Laurencin, N. Almora-Barrios, N.H. de Leeuw, C. Gervais, C. Bonhomme, F. Mauri, W. Chrzanowski, J.C. Knowles, R.J. Newport, A. Wong, Z. Gan, M.E. Smith, Magnesium incorporation into hydroxyapatite, Biomaterials 32(7) (2011) 1826-1837.

[66] L. Shi, P. Shen, D. Zhang, E. Dong, Q. Jiang, Reactive wetting in liquid magnesium/silica and magnesium/silicon systems, Applied Surface Science 274 (2013) 124-130.

[67] S. Hiromoto, Self-healing property of hydroxyapatite and octacalcium phosphate coatings on pure magnesium and magnesium alloy, Corrosion Science 100 (2015) 284-294.

[68] E. Bertoni, A. Bigi, G. Cojazzi, M. Gandolfi, S. Panzavolta, N. Roveri, Nanocrystals of magnesium and fluoride substituted hydroxyapatite, Journal of Inorganic Biochemistry 72(1) (1998) 29-35.

[69] D. Predoi, S.L. Iconaru, M. Predoi, G. Stan, N. Buton, Synthesis, Characterization, and Antimicrobial Activity of Magnesium-Doped Hydroxyapatite Suspensions, Nanomaterials 9 (2019) 1295.

[70] A. Farzadi, F. Bakhshi, M. Solati-Hashjin, M. Asadi-Eydivand, N.A.a. Osman, Magnesium incorporated hydroxyapatite: Synthesis and structural properties characterization, Ceramics International 40(4) (2014) 6021-6029.

[71] P. HUDON, I.-H. JUNG, D.R. BAKER, Experimental Investigation and Optimization of Thermodynamic Properties and Phase Diagrams in the Systems CaO–SiO2, MgO–SiO2, CaMgSi2O6–SiO2 and CaMgSi2O6–Mg2SiO4 to 1·0 GPa, Journal of Petrology 46(9) (2005) 1859-1880.

[72] A. Mortier, J. Lemaitre, P.G. Rouxhet, Temperature-programmed characterization of synthetic calcium-deficient phosphate apatites, Thermochimica Acta 143 (1989) 265-282.

[73] D.R. Lide, CRC handbook of chemistry and physics, CRC press2004.

[74] K.A. Yasakau, M.L. Zheludkevich, S.V. Lamaka, M.G.S. Ferreira, Role of intermetallic phases in localized corrosion of AA5083, Electrochimica Acta 52(27) (2007) 7651-7659.

[75] T.-W. Kim, H.-S. Lee, D.-H. Kim, H.-H. Jin, K.-H. Hwang, J.K. Lee, H.-C. Park, S.-Y. Yoon, In situ synthesis of magnesium-substituted biphasic calcium phosphate and in vitro biodegradation, Materials Research Bulletin 47(9) (2012) 2506-2512.

[76] K. Okada, M. Tanuma, Y. Kameshima, A. Nakajima, S. Asai, M. Sumita, Bioactivity and mechanical properties of CaSiO3/high-density polyethylene (HDPE) composites prepared by a new surface loading method of CaSiO3 powder, Materials Research Bulletin 44(2) (2009) 298-305.

[77] H. Sun, S. He, P. Wu, C. Gao, P. Feng, T. Xiao, Y. Deng, C. Shuai, A Novel MgO-CaO-SiO2 System for Fabricating Bone Scaffolds with Improved Overall Performance, Materials 9(4) (2016).

[78] W. Jiang, J. Wang, W. Yu, Y. Ma, S. Guo, In-situ formation of a gradient Mg2Si/Mg composite with good biocompatibility, Surface and Coatings Technology 361 (2019) 255-262.

[79] M.J. Mirzaali, J.J. Schwiedrzik, S. Thaiwichai, J.P. Best, J. Michler, P.K. Zysset, U. Wolfram, Mechanical properties of cortical bone and their relationships with age, gender, composition and microindentation properties in the elderly, Bone 93 (2016) 196-211.

[80] C.E. Wen, Y. Yamada, K. Shimojima, Y. Chino, T. Asahina, M. Mabuchi, Processing and mechanical properties of autogenous titanium implant materials, Journal of Materials Science: Materials in Medicine 13(4) (2002) 397-401.

[81] G. Brunello, H. Elsayed, L. Biasetto, Bioactive Glass and Silicate-Based Ceramic Coatings on Metallic Implants: Open Challenge or Outdated Topic?, Materials (Basel) 12(18) (2019) 2929.

[82] W.L. Tham, W.S. Chow, Z.A.M. Ishak, The effect of 3-(trimethoxysilyl) propyl methacrylate on the mechanical, thermal, and morphological properties of poly(methyl methacrylate)/hydroxyapatite composites, Journal of Applied Polymer Science 118(1) (2010) 218-228.

[83] K.T. Chu, Y. Oshida, E.B. Hancock, M.J. Kowolik, T. Barco, S.L. Zunt, Hydroxyapatite/PMMA composites as bone cements, Bio-Medical Materials and Engineering 14 (2004) 87-105.

[84] P.V. Giannoudis, H. Dinopoulos, E. Tsiridis, Bone substitutes: An update, Injury 36(3, Supplement) (2005) S20-S27.

Chapter 6

Conclusions and future work

After billions of years of evolution, creatures in nature have possessed extraordinary structures and functions to survive severe conditions [1]. Natural composite materials such as nacre, tooth and bone have been developed as a source of inspiration and innovation to create a new class of bio-mimetic synthetic materials with superior performance over centuries. Currently, several studies have been investigating the synthetic materials with bio-inspired design, though it is still difficult to exactly replicate the architecture found in natural composite materials. For instance, nacre is one of the most promising biomineralized composite materials with nanoscale brick-and-mortar architecture. It was reported that nacres exhibited exceptional mechanical properties where the fracture toughness (in energy term) was thousands of times higher than that of single crystal of its constituents [2]. Inspired by this, research has been carried out to manufacture composites with bio-inspired nacre-like architectures utilizing multiple technologies, i.e. 3D printing [3], slip casting [4, 5], freeze casting [6-12]. In the present work, nacre-like composites were prepared by infiltrating polymeric or metallic compliant phase into ceramic scaffolds manufactured using bi-directional freeze casting. The mechanical responses of both the ceramic scaffolds and the composites were investigated. The strengthening and toughening mechanisms of biomimetic nacre-like composites were carefully analysed. Hence, the focus of this work was on how to manipulate the mechanical properties by fine tuning of bio-inspired nacre-like architectures, microstructure, and composition of composites. It demonstrated that it was possible to produce ceramic-based composite materials with exceptional mechanical properties. This chapter will summarise the main findings of this work and then suggest directions of future research.

6.1 Nacre-like ceramic scaffolds

Porous ceramics are employed in several application sectors to mitigate the issues associated with environment [13], biology [14], and energy [15]. The microstructure, including pore shapes, dimensions, orientations, distributions, and overall porosities, was primarily responsible for properties in these applications and was also a result of particular processing techniques and parameters [16]. It was noted that traditional processing methods such as foaming often lacked the control of microstructure, which was necessary to tailor the properties. In this work, a new technique was provided by combining bi-directional freeze casting and two densification methods (one-step and two-step), which was capable of producing the ceramic scaffolds with nacre-like architectures. This technique also exhibited the ability to tailor the architectures (BM and μL) and microstructure (ceramic integrity or linking bridges, wall thickness, wall length, and volume fraction) and the resultant nacre-like scaffolds displayed high compressive strength when loaded in two orthotropic directions. In addition to their application in preparing nacre-like composites by infiltration of compliant phase into ceramic scaffolds, future research of the nacre-like ceramic scaffolds can focus on studies of relationships between processing, structure and properties and development of more applications.

6.2 Nacre-like ceramic/polymer composites

Inspired by nature, nacre-like ceramic/polymer composites were produced by infiltrating polymers into as-prepared ceramic scaffolds. Both zirconia and alumina were employed as the ceramic phases; PMMA, UDMA/TEGDMA, PU, and epoxy resin were used as polymeric compliant phases. One of the most significant goals of this work was to analyse the mechanical response of these nacre-like ceramic/polymer composites with various architectures (BM and μL), microstructures, ceramic fractions, polymer phases and interfacial conditions in order to provide rational design of strong and tough ceramic composites. Essentially, nacre-like

ceramic/polymer composites were normally toughened by both intrinsic and extrinsic mechanisms with plastic deformation of polymer and crack deflections, respectively. The structural features of ceramic and polymer phases and their interface were demonstrated to affect those toughening mechanisms; the resultant mechanical properties of composites were enhanced by altering the stress distribution, defects density, ceramic bridges, load-bearing and lubricant effect. Moreover, the compliant phase made a great contribution to the mechanics of composites by affecting the stress distribution. In the end, μL composites exhibited superior mechanical response to BM composites at the same ceramic fraction and wall thickness owing to its improved stress-transfer effect.

Apart from the compliant phase, the choice of the ceramic phase is also worth further investigation. Nacre-like μL ceramic scaffolds were prepared with three types of ceramic i.e. alumina, zirconia, and hydroxyapatite (HA) where they displayed distinctive mechanics in the form of bulk material (**Fig.6-1a**). After infiltration of PMMA, the flexural strength and stiffness of ceramic/PMMA composites are strongly correlated to the ceramic phase as shown in **Fig.6-1b**. However, fracture toughness was not investigated due to the time constraint. In future work, it will be an interesting topic to investigate the effect of ceramic phase on fracture toughness of μL composite materials.

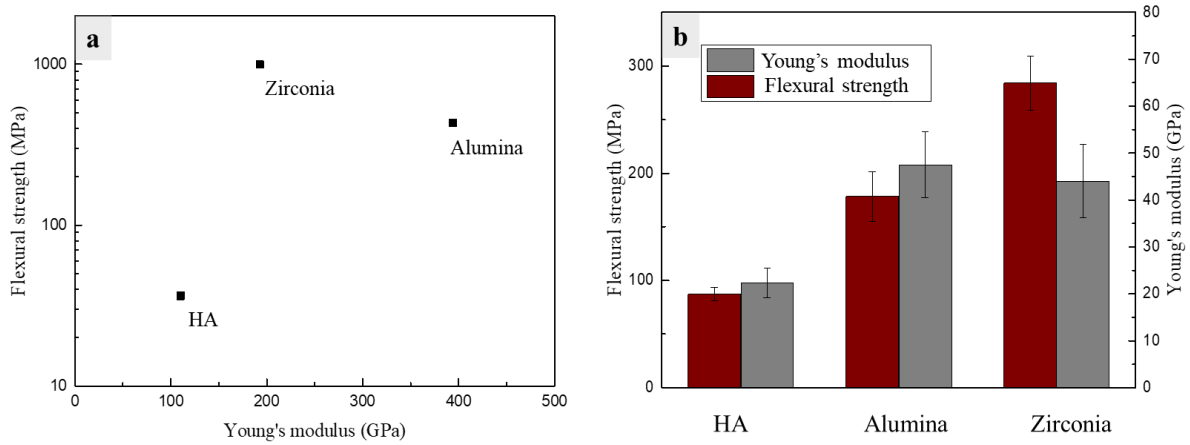

*Fig.6-1 Mechanical properties of pure ceramic **a)**. Flexural strength and modulus **b)** of µL ceramic/PMMA composites with different types of ceramics.*

6.3 Nacre-like ceramic/metal composites

The µL ceramic scaffolds were infiltrated with metals via reactive wetting and pressureless infiltration, and the resultant µL composites exhibit good mechanical properties. Careful control of interactions of metal alloys with atmosphere or scaffold coating was important to successfully infiltrate metals into ceramic scaffolds via improved reactive wetting. In the case of alumina/aluminium composites, the presence of N_2 gas was effective in promoting the wetting of aluminium alloy with alumina scaffolds, where N_2 interacted with Mg element in aluminium alloy (5083), forming a thin layer of Mg_3N_2 which facilitated the infiltration of aluminium alloy into alumina scaffolds. In the case of HA/magnesium composites, silica coating on the HA scaffolds played a key role in promoting the wetting that enabled the pressureless infiltration and preventing the violent reactions between molten magnesium alloy (AZ31) and HA scaffolds. Mg reacted with SiO_2 to produce Mg_2Si which improved the wetting and infiltration of molten Mg with HA scaffolds [17].

Using the one-step method, µL alumina/aluminium composites were manufactured with various ceramic fractions. The composites with a relatively high ceramic fraction (>50%) displayed poor mechanical performance with lower strength and brittle failure behaviour due to inferior infiltration of aluminium alloy into ceramic scaffolds. By contrast, the composites with low ceramic content (18%) showed a higher strength and fracture toughness but a lower stiffness. This difference was attributed to the pores and defects formed because of incomplete pressureless infiltration and wall thickness ratio of ceramic and metal in high ceramic content composites. The alumina/aluminium composites were toughened by not only intrinsic mechanisms of plastic nature of aluminium but also extrinsic mechanism of typical crack deflection, e.g. pull-out, and crack bridging. In addition, µL composites of HA/magnesium was also investigated as potential biodegradable implant materials [18]. The µL HA/magnesium composites were produced via a colloidal coating process of silica on HA scaffolds and subsequently pressureless infiltration of a magnesium alloy (AZ31). Albeit a few new biocompatible phases were formed during infiltration process, the resultant composites still exhibited a good combination of stiffness and strength which matches the mechanics of cortical bones.

Except for ceramic fraction, some more features of µL ceramic/metal composites can be further explored e.g. interface, composition, and microstructure. Understanding the contributions of these features to the toughening or strengthening mechanisms active in these bio-inspired materials is crucial for the development of stronger and tougher nacre-like ceramic/metal composites. For example, alumina/magnesium composites were briefly investigated via pressureless infiltration of a magnesium alloy (AZ31) into nacre-like alumina scaffolds. The composite displayed almost defect-free microstructure (**Fig.6-2a**). The three-point bending strain-stress curve exhibited a high flexural stress at 492 MPa and an excellent plastic deformation before failure as shown in **Fig.6-2b**. More optimisation and mechanical

characterization such as fracture toughness are needed to complete comparison between alumina/magnesium and alumina/aluminium composites.

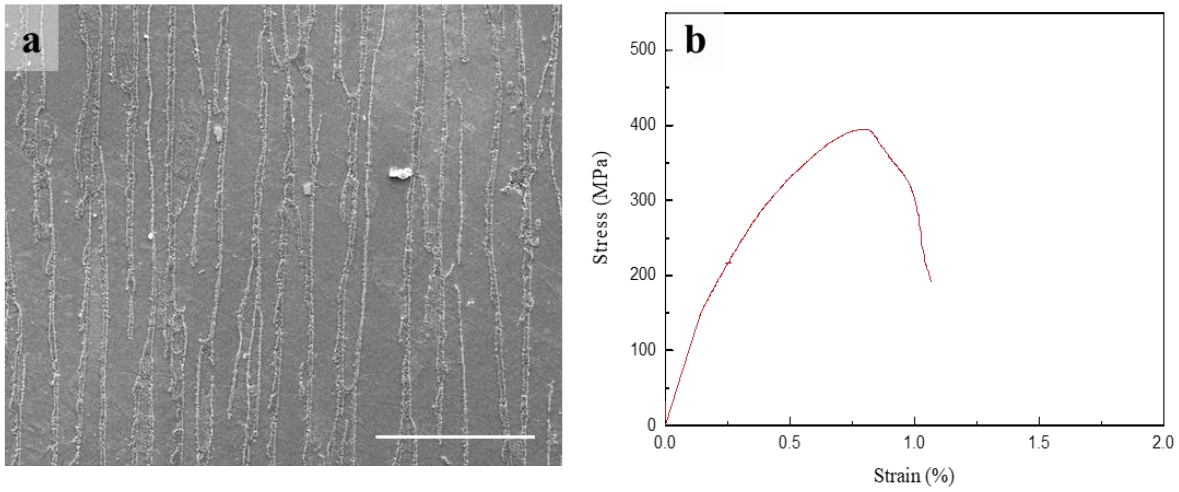

Fig.6-2 *SEM micrograph* ***a)*** *and strain-stress curve for three-point-bending test* ***b)*** *of a nacre-like alumina/magnesium composite.*

In addition, to assess the HA/magnesium composites as viable biodegradable implant materials, some of the key properties, i.e. biodegradability and biocompatibility should be investigated. Biodegradable rate and the biodegradation products of HA/magnesium composites should be fully evaluated in next step. To improve the corrosion resistance or biodegradability, Mg metal and its alloys were coated with HA and other materials e.g. biodegradable polymers to slow down the degradation rate [19-22]. Furthermore, multilayer system was investigated to further improve corrosive resistance [23, 24]. Here, the μL HA/magnesium composite is constructed with micro-layered structure of HA and Mg, which is inherently advantageous to achieve excellent corrosion resistance. On the other hand, the mechanical properties and biodegradability of HA/magnesium composites are highly dependent on the volume fraction of HA (or Mg) [25]. The one-step method developed in this work has demonstrated to be able to manipulate volume fraction of HA ceramic scaffolds. Therefore, the final μL HA/magnesium composites with tunable mechanical properties and degradability can be

prepared with desired ceramic fractions and properties in order to meet the requirements for different applications.

6.4 Future work

Currently, many nacre-inspired materials with different macroscopic dimensions and architectures have been demonstrated [26] and the most commonly reported nacre-like composites were the well-defined brick-and-mortar (BM) composites. By contrast, the μL composites investigated in present work have not been widely reported. To the best of my knowledge, the μL composites reported here are the first to be developed using such a cost-effective way from powder processing route. Future work should be more focused on nacre-like μL composites. As a new type of nacre-like composites, it is important to fundamentally understand how the structure features of μL composites affect their mechanical properties, what the optimal microstructural parameters are and how to control them in fabrication. Based on composites with μL architecture, future research work can be extended to the following three areas.

6.4.1 Computer simulation

Numerical analysis based on computer simulation is a powerful tool and widely used to predict the properties of structural materials and provide design guidance for fabrication and optimization of materials [27]. A recent research of computer simulation was conducted on the brick-and-mortar architecture [28]. Composites with ideal bricks were reacted and basic mechanical models were incorporated into an optimization scheme for the design of nacre-like composites. The newly developed nacre-like μL composites in this work are also worth further investigation by computer simulation. Unlike brick-and-mortar or typical layer-by-layer models, the μL architecture was assembled by ceramic layers with imperfect surface morphologies, which meant the ceramic layers were not absolutely flat or smooth due to micro-

asperities formed during freeze casting. The micro-asperities made a great contribution to mechanics of composites according to the results in Chapter 4. In addition, more mechanical properties and toughening mechanisms can be analyzed and clarified by computer simulation. For example, Poisson's ratio contributed to toughness of nacre [29]. Therefore, a new model of μL composites should be established to facilitate more accurate prediction about the properties of μL composites in future work.

6.4.2 Optimisation of microstructural features

Although some typical mechanics related features, i.e. interface, ceramic volume fraction, ceramic wall length and thickness were studied in this work, they are still worth being investigated more systematically. For example, this work qualitatively compared grafted and ungrafted composites. The results indicated that the grafting process was able to promote the interfacial bonding and strengthen the nacre-like composites. However, the μL alumina/PMMA composites with a high ceramic fraction (85%) exhibited a relatively low fracture toughness with a catastrophic failure behaviour because of the over-strengthened interface by ceramic bridges. To tackle this problem on high ceramic content composites, the interface can be chemically modified by reducing silane coupling agent to tailor the chemical bonding between ceramic and polymer phases. Under different reaction time or temperature, different amount of silane coupling agent can be grafted onto ceramic surface which can be quantitatively analysed by the X-ray photoelectron spectroscopy (XPS). After polymer infiltration, the mechanics of interface can be examined by micro-cantilever or push-out tests. As a result, the relationship between interfacial strength and mechanical properties of nacre-like composites can be established. Further investigation will focus on the effects of other factors such as wall thickness and length, ceramic fraction on the mechanical properties (strength, toughness, hardness, and Poisson's ratio, etc.) of nacre-like composites.

6.4.3 Application exploration

Because of their remarkable mechanical performance, nacre-like composites have shown a great potential for a range of applications in dental [4, 12], orthopaedic [10], and craniofacial implants [30]. With further improvement in mechanical properties, the nacre-like μL composites can also be designed as multifunctional materials for other engineering applications such as energy storage and thermal management. For instance, when the ceramic or polymer phase is carefully selected with thermally insulating or electrically conductive material, the resultant μL composites could also have such multifunctionalities in addition to excellent mechanical properties. The freeze casting was also suitable for scale up production because it is cost-effective and environmental-friendly . Therefore, the one-step densification method developed in present work paves a way for the design and fabrication of multifunctional nacre-like composite materials for various medical and engineering applications in future.

6.5 References

[1] C. Sanchez, H. Arribart, M.M. Giraud Guille, Biomimetism and bioinspiration as tools for the design of innovative materials and systems, Nature Materials 4(4) (2005) 277-288.

[2] X. Li, W.-C. Chang, Y.J. Chao, R. Wang, M. Chang, Nanoscale Structural and Mechanical Characterization of a Natural Nanocomposite Material: The Shell of Red Abalone, Nano Letters 4(4) (2004) 613-617.

[3] G.X. Gu, F. Libonati, S.D. Wettermark, M.J. Buehler, Printing nature: Unraveling the role of nacre's mineral bridges, Journal of the Mechanical Behavior of Biomedical Materials 76 (2017) 135-144.

[4] H. Le Ferrand, F. Bouville, T.P. Niebel, A.R. Studart, Magnetically assisted slip casting of bioinspired heterogeneous composites, Nature Materials 14 (2015) 1172.

[5] R. Libanori, D. Carnelli, N. Rothfuchs, M.R. Binelli, M. Zanini, L. Nicoleau, B. Feichtenschlager, G. Albrecht, A.R. Studart, Composites reinforced via mechanical interlocking of surface-roughened microplatelets within ductile and brittle matrices, Bioinspiration & Biomimetics 11(3) (2016) 036004.

[6] M.E. Launey, E. Munch, D.H. Alsem, H.B. Barth, E. Saiz, A.P. Tomsia, R.O. Ritchie, Designing highly toughened hybrid composites through nature-inspired hierarchical complexity, Acta Materialia 57(10) (2009) 2919-2932.

[7] V. Naglieri, B. Gludovatz, A.P. Tomsia, R.O. Ritchie, Developing strength and toughness in bio-inspired silicon carbide hybrid materials containing a compliant phase, Acta Materialia 98 (2015) 141-151.

[8] E. Munch, M.E. Launey, D.H. Alsem, E. Saiz, A.P. Tomsia, R.O. Ritchie, Tough, Bio-Inspired Hybrid Materials, Science 322(5907) (2008) 1516-1520.

[9] F. Bouville, E. Maire, S. Meille, B. Van de Moortèle, A.J. Stevenson, S. Deville, Strong, tough and stiff bioinspired ceramics from brittle constituents, Nature Materials 13(5) (2014) 508-514.

[10] H. Bai, F. Walsh, B. Gludovatz, B. Delattre, C. Huang, Y. Chen, A.P. Tomsia, R.O. Ritchie, Bioinspired Hydroxyapatite/Poly(methyl methacrylate) Composite with a Nacre-Mimetic Architecture by a Bidirectional Freezing Method, Advanced Materials 28(1) (2016) 50-56.

[11] A. Wat, J.I. Lee, C.W. Ryu, B. Gludovatz, J. Kim, A.P. Tomsia, T. Ishikawa, J. Schmitz, A. Meyer, M. Alfreider, D. Kiener, E.S. Park, R.O. Ritchie, Bioinspired nacre-like alumina with a bulk-metallic glass-forming alloy as a compliant phase, Nature Communications 10(1) (2019) 961.

[12] G. Tan, J. Zhang, L. Zheng, D. Jiao, Z. Liu, Z. Zhang, R.O. Ritchie, Nature-Inspired Nacre-Like Composites Combining Human Tooth-Matching Elasticity and Hardness with Exceptional Damage Tolerance, Advanced Materials 31(52) 1904603.

[13] M. Takahashi, R.L. Menchavez, M. Fuji, H. Takegami, Opportunities of porous ceramics fabricated by gelcasting in mitigating environmental issues, Journal of the European Ceramic Society 29(5) (2009) 823-828.

[14] J. Wang, W. Chen, Y. Li, S. Fan, J. Weng, X. Zhang, Biological evaluation of biphasic calcium phosphate ceramic vertebral laminae, Biomaterials 19(15) (1998) 1387-1392.

[15] S. Wang, X. Zhang, F. Kuang, J. Li, Y. Wang, R. Wang, Y. Wang, X. Lin, J. Li, Preparation and properties of a new porous ceramic material used in clean energy field, Journal of Materials Science & Technology 35(7) (2019) 1255-1260.

[16] E.C. Hammel, O.L.R. Ighodaro, O.I. Okoli, Processing and properties of advanced porous ceramics: An application based review, Ceramics International 40(10, Part A) (2014) 15351-15370.

[17] L. Shi, P. Shen, D. Zhang, E. Dong, Q. Jiang, Reactive wetting in liquid magnesium/silica and magnesium/silicon systems, Applied Surface Science 274 (2013) 124-130.

[18] F. Witte, F. Feyerabend, P. Maier, J. Fischer, M. Störmer, C. Blawert, W. Dietzel, N. Hort, Biodegradable magnesium–hydroxyapatite metal matrix composites, Biomaterials 28(13) (2007) 2163-2174.

[19] Y.W. Song, D.Y. Shan, E.H. Han, Electrodeposition of hydroxyapatite coating on AZ91D magnesium alloy for biomaterial application, Materials Letters 62(17) (2008) 3276-3279.

[20] S. Hiromoto, A. Yamamoto, High corrosion resistance of magnesium coated with hydroxyapatite directly synthesized in an aqueous solution, Electrochimica Acta 54(27) (2009) 7085-7093.

[21] R. Chaharmahali, A. Fattah-alhosseini, K. Babaei, Surface characterization and corrosion behavior of calcium phosphate (Ca-P) base composite layer on Mg and its alloys using plasma electrolytic oxidation (PEO): A review, Journal of Magnesium and Alloys (2020).

[22] S.A. Salman, K. Kuroda, M. Okido, Preparation and Characterization of Hydroxyapatite Coating on AZ31 Mg Alloy for Implant Applications, Bioinorganic Chemistry and Applications 2013 (2013) 175756.

[23] X.-J. Ji, L. Gao, J.-C. Liu, R.-Z. Jiang, F.-Y. Sun, L.-Y. Cui, S.-Q. Li, K.-Q. Zhi, R.-C. Zeng, Z.-L. Wang, Corrosion resistance and antibacterial activity of hydroxyapatite coating induced by ciprofloxacin-loaded polymeric multilayers on magnesium alloy, Progress in Organic Coatings 135 (2019) 465-474.

[24] L. Chen, C.-M. Tseng, Y. Qiu, J. Yang, C.-L. Chang, X. Wang, W. Li, A layer-by-layer assembled coating for improved stress corrosion cracking on biomedical magnesium alloy in cell culture medium, Surface and Coatings Technology 403 (2020) 126427.
[25] Z. Huan, J. Zhou, J. Duszczyk, Magnesium-based composites with improved in vitro surface biocompatibility, Journal of Materials Science: Materials in Medicine 21(12) (2010) 3163-3169.

[26] H. Zhao, Z. Yang, L. Guo, Nacre-inspired composites with different macroscopic dimensions: strategies for improved mechanical performance and applications, NPG Asia Materials 10(4) (2018) 1-22.

[27] H. Zhu, D. Balint, Z. Guo, Theoretical Analysis and Computational Simulation of Advanced Structured Materials, Advances in Condensed Matter Physics 2014 (2014) 367916.

[28] F. Barthelat, Designing nacre-like materials for simultaneous stiffness, strength and toughness: Optimum materials, composition, microstructure and size, Journal of the Mechanics and Physics of Solids 73 (2014) 22-37.

[29] F. Song, J. Zhou, X. Xu, Y. Xu, Y. Bai, Effect of a Negative Poisson Ratio in the Tension of Ceramics, Physical review letters 100 (2008) 245502

[30] G. Du, A. Mao, J. Yu, J. Hou, N. Zhao, J. Han, Q. Zhao, W. Gao, T. Xie, H. Bai, Nacre-mimetic composite with intrinsic self-healing and shape-programming capability, Nature Communications 10(1) (2019) 800.

Appendix: Publications, presentations and awards

Journal papers:

1. A paper was pulished from some results of Chapter 3 & Chapter 4 (as the lead writer)

Title: Cost-effective fabrication of bio-inspired nacre-like composite materials with high strength and toughness

Journal: Composite Part B: Engineering

Year:2020

Author: **Hongbo Wan**, Nathanael Leung, Sana Algharaibeh, Tan Sui, Qiang Liu, HuaXin Peng, Bo Su

2. The manuscript is ready to be published and the lead author (Sana Algharaibehae) is looking for a proper journal

Title: Fabrication and mechanical properties of biomimetic nacre-like ceramic/polymer composites for CAD/CAM dental restoration

Authors: Sana Algharaibehae, **Hongbo Wan**, Bo Su

3. The experimental sessions have finished and the lead author (Nathanael Leung) is writing the manuscript

Title: In situ synchrotron X-ray diffraction-based characterisation of deformation and fracture of novel bio-inspired dental composites

Authors: Nathanael Leung, Sana Algharaibeh, **Hongbo Wan**, Xiaodong Xu, Bo Su, Tan Sui

Conferrences:

1. The abstract has been accepted as a poster presentation on the topic “A novel nacre-like ceramic/polymer composites prepared by bi-directional freeze casting” in the 11th World Biomaterials Congress (WBC), December, 2020

Authors: **Hongbo Wan**, Nathanael Leung, Sana Algharaibehae, Tan Sui, Bo Su

2. The abstract has been accepted as a oral presentation on the topic “In situ study of the fracture toughening mechanisms of novel bio-inspired nacre-like composites.” in the 11th World Biomaterials Congress (WBC), December, 2020

Authors: Nathanael Leung, **Hongbo Wan**, Sana Algharaibehae, Bo Su, Tan Sui

3. The abstract has been submited as a poster/oral presentation on the topic “In-situ study of the fracture behaviour of bioinspired aluminia-based composites with differetn compliant polymer pahses” in the 23rd international conference on composite materials (ICCM23) August, 2021

Authors: Nathanael Leung, Urangua Jargalsaikhan, **Hongbo Wan**, Bo Su, Tan Sui

4. The abstract has been submited as a poster/oral presentation on the topic “Modeling the three-point bending of novel bioinspired dental crown composites” in the 23rd international conference on composite materials (ICCM23), August, 2021

Authors: Urangua Jargalsaikhan, **Hongbo Wan**, Nathanael Leung, Bo Su, Xu Song, Jianan Hu, Tan Sui